Searches for the Higgs Boson at the LHC Based on its Couplings to Vector Bosons

Zur Erlangung des akademischen Grades eines
DOKTORS DER NATURWISSENSCHAFTEN
von der Fakultät für Physik des
Karlsruher Instituts für Technologie (KIT) genehmigte

DISSERTATION

von

Dipl.-Phys. Christoph Hackstein
aus Calw

Mündliche Prüfung: 13. Mai 2011

Referent: Prof. Dr. G. Quast
Institut für Experimentelle Kernphysik

Korreferent: Prof. Dr. D. Zeppenfeld
Institut für Theoretische Physik

"It is a capital mistake to theorize before one has data. Insensibly one begins to twist facts to suit theories, instead of theories to suit facts."

Sir Arthur Conan Doyle, 'A Scandal in Bohemia'
The Adventures of Sherlock Holmes, The Strand Magazine (1892)

Searches for the Higgs Boson at the LHC
Based on its Couplings to Vector Bosons.

One of the primary goals of the Large Hadron Collider (LHC) is the search for the Higgs Boson. All Higgs searches rely heavily on Monte Carlo predictions of both the signal and background processes. These simulations necessarily include models and assumptions not derived from first principles. Especially the process of hadronization and the underlying event are only partially understood and differ strongly between different generators. As a result, the predictions can be wrong for special regions of phase space. Therefore, predictions by several programs should be compared to gain an estimate of the uncertainty of the observables considered.

In this work, two different Monte Carlo generators were compared in their predictions for a Higgs search in the Vector Boson Fusion (VBF) Higgs production channel with subsequent decay into W bosons that decay leptonically in turn. A significant difference in the description of both signal and background was found between the two generators.

As the Monte Carlo description of the Vector Boson Fusion topology exhibits large uncertainties, it is important to validate the predictions with data. One background process to the VBF Higgs production is the production of Z bosons with jets. This process has a large cross section and therefore it is possible to validate its Monte Carlo description with early LHC data. The data taken by the Compact Muon Solenoid (CMS) detector in 2010 amounts to 35.9 pb^{-1} which yields a sufficient number of Z boson events. The Monte Carlo description of these events was validated using the full CMS detector simulation. A good agreement between data and simulation could be found, making this process a first building block for the full VBF Higgs analysis.

If the Higgs boson is heavier than about 200 GeV, it will predominantly decay into a pair of vector bosons. In case the Higgs boson decays into muons via Z bosons its reconstruction is very precise, as muons can be measured with a high accuracy. However, the branching ratio of this decay is below 1%, resulting in a very small event yield. Including a Z boson decay into quarks leads to a drastically increased branching ratio, however this also strongly increases the amount of background events. A search strategy exploiting the fact that for Higgs boson masses above 350 GeV the Higgs decay products are boosted and therefore are collimated in a relatively small solid angle is presented.

In addition, this measurement allows to measure spin and $\mathcal{CP}$ quantum numbers of a found heavy resonance based on the angular distributions between the Z boson decay products.

Contents

Introduction

The scope of particle physics is the understanding of the elementary building blocks of nature and the forces between them. The continuous interplay between theory and experiment in this field led to the emergence of the Standard Model of particle physics.

The Standard Model of particle physics is a theory which describes three of the four known fundamental interactions between the elementary particles that make up all matter. It is a quantum field theory based on a $\mathrm{SU(3)_C \times SU(2)_L \times U(1)_Y}$ gauge symmetry yielding the gauge boson fields A^a_μ, W^i_μ and B_μ, corresponding to the gluon, the electroweak gauge bosons $\mathrm{W^\pm}$, Z and the photon. These gauge fields mediate the forces between the elementary particles. The matter content of the model consists of three generations of quarks and leptons. To date, experimental tests of the three forces described by the Standard Model have shown a very high degree of agreement.

However, the Standard Model falls short of being a complete theory of fundamental interactions, primarily because it does not include gravity, the fourth known fundamental force. In addition the Standard Model contains a large number of parameters such as masses and coupling constants that must be put into the theory "by hand", rather than being derived from first principles.

A problem arising from the description of the Standard Model as a gauge theory is the fact that the field quanta of the weak interaction, the W and Z bosons, have been found to be massive particles. Thus in order to preserve the gauge invariance of the theory, the Higgs mechanism has to be introduced. This part of the Standard Model has not been verified experimentally, since the Higgs boson, the field quantum of the postulated Higgs field, which is a neutral scalar field has not been discovered yet.

In addition, certain observables such as the anomalous magnetic moment of the muon, the decay rate of the rare decay $B_s \to \tau \nu_\tau$ and the $\mathcal{CP}$ violation in the $B^0_{\bar{s}}$-$\bar{B}^0_s$ mixing show deviations from the values predicted by the Standard Model. Furthermore the fact that neutrinos also possess mass is not incorporated in the theory yet. Many different theories have been put forward to explain these phenomena, however, no experimental justification has been found so far.

The tests of the Standard Model are performed at particle colliders. The main

tasks of the Large Hadron Collider at CERN[1] are the search for the Higgs boson and for physics beyond the Standard Model, a very challenging undertaking. On the one hand, the Higgs production cross section is quite low, so the Higgs signal has to be extracted from huge backgrounds. On the other hands, the mass of the Higgs boson is not yet known, which however strongly influences the possible Higgs decay channels. This means that for different Higgs masses distinct search strategies using different final states are needed.

All these searches rely on a detailed understanding of both the signal as well as the background processes. All analysis of LHC data relies on the predictions of Monte Carlo event generators. These simulations however contain many uncertainties, especially in the specific regions of phase space in which a Higgs search is performed. This makes an excellent understanding of the simulations used an exigency of all Higgs searches.

In Chapter 1 the Standard Model is discussed. The electroweak symmetry breaking offering an explanation for the origin of W and Z boson masses is presented. In addition, Quantum Chromodynamics and the description of particle interactions are summarized. Finally, the models used in event simulation for hadron-hadron collisions are depicted.

Chapter 2 gives an overview of the LHC and the CMS detector. The various sub-detector components as well as the trigger strategy are are presented.

In Chapter 3 the software used in this work for calculation of cross sections, simulation of events and analysis of data are described. In addition, the software framework utilized in the CMS collaboration for event generation and reconstruction is presented.

A very promising channel for Higgs search is Vector Boson Fusion as the special event topology of this channel allows for a good suppression of the background contributions. However, the exact nature of the event selection depends on an accurate understanding of the hadronic activity in the event. In Chapter 4 two different simulation programs are compared with respect to their prediction for both signal and backgrounds.

As the description of the Vector Boson Fusion topology is troubled by large systematic uncertainties, it is important to validate the backgrounds with data. A channel accessible even with a low amount of data is Z+jets. A comparison with first Z+jets events acquired during the LHC operations in 2010 is presented in Chapter 5.

Finally, a new search strategy for heavy Higgs bosons with masses above 350 GeV is presented in Chapter 6. This method uses the semi-leptonic decay channel $H \rightarrow ZZ \rightarrow 2\mu 2j$ which has a reasonable branching ratio. To suppress the large backgrounds this channel is plagued with, subjet methods are employed. The analysis shown is also suitable to distinguish the spin and $\mathcal{CP}$ properties of the heavy resonance found. This is shown for several benchmark scenarios.

---

[1] "Conseil Européen pour la Recherche Nucléaire"

Chapter 1

Theory

1.1. The Standard Model of Particle Physics

The Standard Model (SM) of elementary particle physics describes electromagnetism, the weak and the strong force, that govern the reactions between elementary particles. It is a quantum field theory[1], in which interactions between particles are described by the exchange of field quanta. The theory is based on the principle of gauge invariance.

The electroweak theory, proposed by Glashow, Salam and Weinberg [3] unifies electromagnetic [4] and weak [5] interactions. It is based on the gauge symmetry group $SU(2)_L \times U(1)_Y$ of weak left-handed isospin L and hypercharge Y. The introduction of this theory follows the presentation given in [6].

The strong interaction between the colored quarks and gluons is given by Quantum Chromo-Dynamics (QCD), based on the symmetry group $SU(3)_C$. The strong interaction will be presented in more detail in Sec. 1.3.

Matter particles are described in the Standard Model by two classes of fermions, the leptons and the quarks. Quarks are the constituents of protons and neutrons, whereas electrons and neutrinos are examples for leptons. Interactions between particles are in gauge theories treated as the exchange of bosons. The carrier of the electromagnetic interaction in Quantum Electro-Dynamics (QED) is the massless photon. The weak force, which is for example responsible for radioactive β decay, is mediated by the massive W and Z bosons. The massless gluons are the exchange particles of the strong interaction.

In the Standard Model fermions are spinor fields f. There are three generations of left- and right-handed chiral fermions $f_{L,R}$, where $f_{L,R} = \frac{1}{2}(\mathbb{1} \mp \gamma_5)f$. The left-handed fermions form weak isodoublets L_i and Q_i, the right-handed are weak

---

[1]For a detailed introduction see for example [1] and [2].

isosinglets e_{R_i}, u_{R_i} and d_{R_i}:

$$L_1 = \begin{pmatrix} \nu_e \\ e^- \end{pmatrix}_L \ , \ e_{R_1} = e_R^- \ , \qquad Q_1 = \begin{pmatrix} u \\ d \end{pmatrix}_L \ , \ u_{R_1} = u_R \ , \ d_{R_1} = d_R$$

$$L_2 = \begin{pmatrix} \nu_\mu \\ \mu^- \end{pmatrix}_L \ , \ e_{R_2} = \mu_R^- \ , \qquad Q_2 = \begin{pmatrix} c \\ s \end{pmatrix}_L \ , \ u_{R_2} = c_R \ , \ d_{R_2} = s_R \qquad (1.1)$$

$$L_3 = \begin{pmatrix} \nu_\tau \\ \tau^- \end{pmatrix}_L \ , \ e_{R_3} = \tau_R^- \ , \qquad Q_3 = \begin{pmatrix} t \\ b \end{pmatrix}_L \ , \ u_{R_3} = t_R \ , \ d_{R_3} = b_R$$

The fermionic hypercharge can be expressed in terms of the the weak isospin I_f^3 and electric charge Q_f:

$$Y_f = 2Q_f - 2I_f^3 \qquad (1.2)$$

$$\Rightarrow Y_{L_i} = -1 \ , Y_{e_{R_i}} = -2 \ , Y_{Q_i} = \frac{1}{3} \ , Y_{u_{R_i}} = \frac{4}{3} \ , Y_{u_{R_i}} = -\frac{2}{3} \ .$$

The neutrinos ν_i are assumed to be massless in the Standard Model, therefore they only appear with a left-handed component. Experiments have shown that neutrinos do have a non-vanishing mass, but the correct description of the neutrino masses is not yet clear. Only the quarks transform as triplets under $SU(3)_C$, whereas the leptons do not carry color charges.

In addition to the matter fields, there are the gauge fields that correspond to the spin-one bosons that mediate the interactions. Each of the three interactions in the Standard Model has its own fields.

First, there is the B_μ field corresponding to the generator Y of the $U(1)_Y$ group. In addition, the three fields $W_\mu^{1,2,3}$ correspond to the generators T^a $(a = 1, 2, 3)$ of the $SU(2)_L$ group. Finally, eight gluon fields $G_\mu^{1,\dots,8}$ in the sector of the strong interactions correspond to the eight generators of the $SU(3)_C$ group.

The resulting Lagrangian for the Standard Model without mass terms is

$$\begin{aligned} \mathcal{L}_{SM} = &- \frac{1}{4} G_{\mu\nu}^a G^{a,\mu\nu} - \frac{1}{4} W_{\mu\nu}^a W^{a,\mu\nu} - B_{\mu\nu} B^{\mu\nu} \\ &+ \bar{L}_i i D_\mu \gamma^\mu L_i + \bar{e}_{R_i} i D_\mu \gamma^\mu e_{R_i} \\ &+ \bar{Q}_i i D_\mu \gamma^\mu Q_i + \bar{u}_{R_i} i D_\mu \gamma^\mu u_{R_i} + \bar{d}_{R_i} i D_\mu \gamma^\mu d_{R_i} \ , \end{aligned} \qquad (1.3)$$

where the field strengths are given by

$$\begin{aligned} G_{\mu\nu}^a &= \partial_\mu G_\nu^a - \partial_\nu G_\mu^a + g_s f^{abc} G_\mu^b G_\nu^c \\ W_{\mu\nu}^a &= \partial_\mu W_\nu^a - \partial_\nu W_\mu^a + g_2 \epsilon^{abc} W_\mu^b W_\nu^c \\ B_{\mu\nu} &= \partial_\mu B_\nu^a - \partial_\nu B_\mu \ . \end{aligned} \qquad (1.4)$$

Here g_s, g_2 and g_1 respectively, denote the coupling constants of $SU(3)_C$, $SU(2)_L$ and $U(1)_Y$ and f^{abc} and ϵ^{abc} are the structure constants of $SU(3)_C$ and $SU(2)_L$.

The matter fields Ψ are minimally coupled to the gauge fields through the covariant derivative D_μ, which is for quarks defined as

$$D_\mu \Psi = \left(\partial_\mu - ig_s T^a_\mathrm{C} G^a_\mu - ig_2 T^a_\mathrm{L} W^a_\mu - ig_1 \frac{Y_q}{2} B_\mu \right) \Psi \ , \qquad (1.5)$$

where T^a_C, T^a_L and Y_q are the generators of the corresponding gauge groups.

This leads to a unique coupling between gauge fields V_μ and the fermion fields:

$$\text{fermion gauge boson coupling} \ : -g_i \bar{\Psi} V_\mu \gamma^\mu \Psi \ . \qquad (1.6a)$$

The non-abelian structure of the SU(2) and SU(3) groups yields self-interactions between their respective gauge fields V_μ:

$$\text{triple gauge boson coupling} \ : \ ig_i \mathrm{Tr}(\partial_\nu V_\mu - \partial_\mu V_\nu)[V_\mu, V_\nu] \qquad (1.6b)$$

$$\text{quartic gauge boson coupling} \ : \ \frac{1}{2} g_i^2 \mathrm{Tr}[V_\mu, V_\nu]^2 \qquad (1.6c)$$

The Lagrangian (1.3) for massless particles is invariant under local $\mathrm{SU(3)_C} \times \mathrm{SU(2)_L} \times \mathrm{U(1)_Y}$ gauge transformations. The gluons, the gauge bosons in the strong interaction, are indeed massless and it is possible to introduce $\mathrm{SU(3)_C}$ invariant mass terms for the quarks without additional fields.

In the case of the gauge bosons of the $\mathrm{SU(2)_L} \times \mathrm{U(1)_Y}$ it is not possible to introduce mass terms for the boson fields as a mass term $\frac{1}{2} M_V^2 W_\mu W^\mu$ would violate the gauge invariance. However, the gauge bosons of the weak interaction have found to be massive, so a theory of the weak interaction needs to contain gauge invariant mass terms. In addition fermion mass terms would also not be invariant under isospin symmetry transformations, since the left-handed component is part of an $\mathrm{SU(2)_L}$ doublet, whereas the right-handed component is a singlet.

While the electroweak and strong interaction part of the Standard Model has been tested to high precision and found to be in excellent agreement with data, the problem of gauge boson and fermion masses lead to the development of the Higgs-Brout-Englert-Guralnik-Hagen-Kibble mechanism of spontaneous symmetry breaking [7], or short the Higgs mechanism.

1.2. The Higgs Mechanism

In the Higgs mechanism, a scalar field with a special potential is postulated which allows for mass terms to arise from the coupling of particles to the Higgs field. The mechanism must generate masses for the three gauge bosons $\mathrm{W}^\pm$ and Z but not for the photon. Quantum electrodynamics, the description of the electromagnetic interaction, must be described by an exact symmetry. This means that the scalar field needs to provide at least three degrees of freedom for the gauge boson masses.

The simplest possibility with these constraints is a complex SU(2) doublet of scalar fields

$$\Phi = \begin{pmatrix} \phi^+ \\ \phi^0 \end{pmatrix} \quad Y_\phi = +1 \ . \tag{1.7}$$

Now the $\mathrm{SU(2)_L \times U(1)_Y}$ invariant terms for the scalar field need to be added to the standard model Lagrangian (1.3):

$$\mathcal{L}_S = (D^\mu \Phi)^\dagger (D_\mu \Phi) - \mu^2 |\Phi^\dagger \Phi| - \lambda |\Phi^\dagger \Phi|^2 \ . \tag{1.8}$$

In the case that $\mu^2 < 0$ the potential $V(\phi) = \frac{1}{2}\mu^2 |\Phi^\dagger \Phi| + \frac{1}{4}\lambda |\Phi^\dagger \Phi|^2$ has a minimum and the neutral component can develop a vacuum expectation value

$$|\langle \Phi_0 \rangle| = \sqrt{\frac{-\mu^2}{2\lambda}} \equiv \frac{v}{\sqrt{2}} \ . \tag{1.9}$$

Here $v^2 \equiv -\frac{\mu^2}{\lambda}$ is the non-zero vacuum expectation value (vev). The scalar field Φ can now be expressed by four elementary neutral scalar fields $\theta_{1,2,3}(x)$ and $H(x)$:

$$\Phi = \begin{pmatrix} \theta_2 + i\theta_1 \\ \frac{1}{\sqrt{2}}(v + H) - i\theta_3 \end{pmatrix} = e^{i\tilde{\theta}_a(x)\tau^a/v} \begin{pmatrix} 0 \\ \frac{1}{\sqrt{2}}(v + H(x)) \end{pmatrix} \ , \tag{1.10}$$

where τ^a denotes the Pauli matrices and H represents the Higgs field. It is now possible to perform a gauge transformation on this field to move to the unitary gauge

$$\Phi = \frac{1}{\sqrt{2}} \begin{pmatrix} 0 \\ v + H(x) \end{pmatrix} \ . \tag{1.11}$$

The vacuum now is not invariant under $\mathrm{SU(2)_L}$ transformations any more. However, it stays invariant under the QED $\mathrm{U(1)_Y}$ gauge transformations, therefore QED remains unbroken. This breaking of symmetry with the appearance of a vacuum expectation value is called "spontaneous symmetry breaking".

Now the dynamic term in the Lagrangian Eq. (1.8) can be expanded:

$$|D_\mu \Phi|^2 = \left| \left(\partial_\mu - ig_2 \frac{\tau_a}{2} \mathrm{W}_\mu^a - ig_1 \frac{1}{2} B_\mu \right) \Phi \right|^2$$
$$= \frac{1}{2}(\partial_\mu H)^2 + \frac{1}{8}g_2^2(v + H)^2 |\mathrm{W}_\mu^1 + i\mathrm{W}_\mu^2|^2 + \frac{1}{8}(v + H)^2 |g_2 \mathrm{W}_\mu^3 - g_1 B_\mu|^2 \ , \tag{1.12}$$

from which new fields can be defined:

$$\mathrm{W}_\mu^\pm = \frac{1}{\sqrt{2}}(\mathrm{W}_\mu^1 \mp i\mathrm{W}_\mu^2) \ , \ \mathrm{Z}_\mu = \frac{g_2 \mathrm{W}_\mu^3 - g_1 B_\mu}{\sqrt{g_1^2 + g_2^2}} \ , \ A_\mu = \frac{g_2 \mathrm{W}_\mu^3 + g_1 B_\mu}{\sqrt{g_1^2 + g_2^2}} \ . \tag{1.13}$$

Here A_μ and Z_μ have been defined to be orthogonal to each other. The terms bilinear in these fields correspond to their mass terms. The W and Z bosons acquired masses whereas the photon remains massless, as desired:

$$m_W = \frac{1}{2} v g_2 \ , \quad m_Z = \frac{1}{2} v \sqrt{g_1^2 + g_2^2} \ , \quad m_A = 0 \ . \tag{1.14}$$

The spontaneous breaking of the symmetry $\mathrm{SU(2)_L} \times \mathrm{U(1)_Y} \to \mathrm{U_Q}$ allows to absorb three of the degrees of freedom of the $\mathrm{SU(2)_L}$ doublet (1.7) to give the W and Z bosons masses. The additional degree of freedom is the physical Higgs field.

By introducing the $\mathrm{SU(2)_L} \times \mathrm{U(1)_Y}$ invariant Yukawa Lagrangian, the fermion masses can be obtained in a similar manner:

$$\mathcal{L}_{\text{Higgs}} = -\lambda_e \bar{L} \Phi e_R - \lambda_d \bar{Q} \Phi d_R - \lambda_u \bar{Q} \tilde{\Phi} u_R + h.c. \ , \tag{1.15}$$

where $\tilde{\Phi} = i\tau_2 \Phi^*$ and (1.15) holds for any generation.

The bilinear terms in the fermion fields now yield the fermion mass terms,

$$\mathcal{L}_{\text{Higgs}} = -\lambda_e (\bar{\nu}_e, \bar{e}_L) \begin{pmatrix} 0 \\ v + H(x) \end{pmatrix} e_R + \ldots = -\lambda_e (v + H) \bar{e}_L e_R + \ldots \ ,$$

resulting in

$$m_e = \frac{\lambda_e v}{\sqrt{2}} \ , \quad m_u = \frac{\lambda_u v}{\sqrt{2}} \ , \quad m_d = \frac{\lambda_d v}{\sqrt{2}} \ .$$

From (1.8) and using the relation $v^2 = -\mu^2/\lambda$, the Lagrangian of the Higgs field can be derived:

$$\mathcal{L}_H = \frac{1}{2} (\partial^\mu H)(\partial_\mu H) - \lambda v^2 H^2 - \lambda v H^3 - \frac{\lambda}{4} H^4 \ .$$

From this the Higgs mass can be found to be $m_H^2 = 2\lambda v^2 = -2\mu^2$ and the couplings to gauge bosons and fermions are in the convention of [6]

$$g_{Hff} = i \frac{m_f}{v} \ , \quad g_{HVV} = -2i \frac{m_V^2}{v} \ , \quad g_{HHVV} = -2i \frac{m_V^2}{v^2} \ .$$

The value of the vacuum expectation v can be determined from the W boson mass or the Fermi constant G_μ which can be measured in muon decays,

$$m_W = \frac{1}{2} g_2 v = \left(\frac{\sqrt{2} g^2}{8 G_\mu} \right)^{1/2} \to v = \frac{1}{(\sqrt{2} G_\mu)^{1/2}} \simeq 246 \text{ GeV} \ . \tag{1.16}$$

However, the mass of the Higgs boson itself is not determined by the formalism but remains a free parameter. From theoretical considerations, namely unitarity in perturbation theory [8] as well as triviality [9] and stability [10] bounds, an upper limit of $m_H < 650$ GeV can be derived. Experimentally, with the electroweak

precision data from the Large Electron Positron Collider (LEP) at CERN it is possible to exclude light Higgs boson masses and set a lower limit of $m_H > 114.3$ GeV [11] and recent results from the proton-antiproton collider Tevatron indicate an exclusion for 158 GeV $< m_{\mathrm{H}} < 173$ GeV [12].

To confirm the Higgs mechanism, the Higgs boson as a resonance has to be discovered and its couplings have to be measured in order to test whether the particle really has the properties associated with the Standard Model Higgs particle.

1.2.1. Decay of the Higgs boson

The Higgs couplings to gauge bosons and fermions are proportional to their masses. Therefore the actual branching ratio of the Higgs boson is strongly dependent on both the Higgs mass itself and the masses of the decay products. The Higgs boson will mostly likely decay into the heaviest particles accessible in phase space. Once the Higgs mass is fixed, all partial widths for different Higgs boson decays can be calculated. An overview of the branching ratio and width of the Higgs boson can be found in Fig. 1.1, a detailed summary of the currently available calculations is presented in [13].

A special case is the decay into massless particles, namely the decays $H \to \gamma\gamma$ and $H \to gg$. Since photons and gluons do not posses a mass, they do not couple to the Higgs boson directly. However, these decays can happen via a loop of massive particles, W bosons and heavy charged fermions for the Higgs decay into photons and heavy quarks for the Higgs decay into gluons.
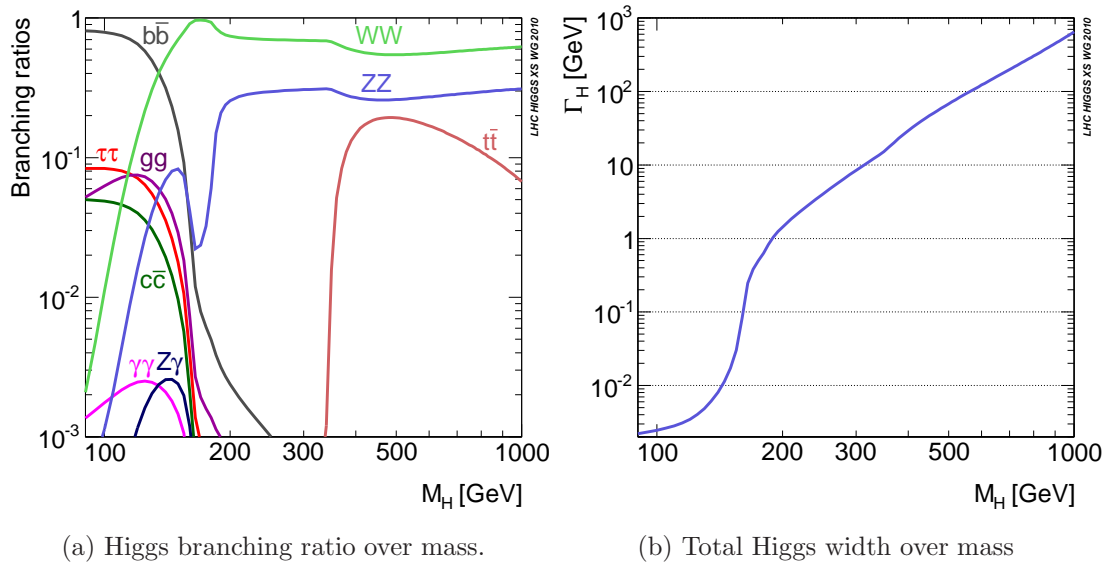

(a) Higgs branching ratio over mass.   (b) Total Higgs width over mass

Figure 1.1.: Dependence of the Higgs decay properties on m_{H}. Figures taken from [13]

For the lightest Higgs masses not excluded by LEP, the dominant decay is $H \to b\bar{b}$, which is however very hard to distinguish from background. To isolate
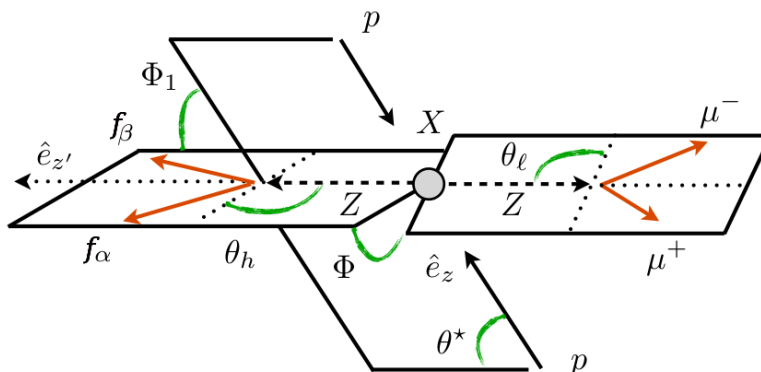
Figure 1.2.: The definition of the spin- and $\mathcal{CP}$-sensitive angles of Ref. [23] in $pp \to X \to \mathrm{ZZ} \to \mu^+\mu^- e^+ e^-$. Details on the definition of the angles are given in the text. An angle analogous to $tilde\Phi$ can be defined with respect to the muonic decay plane.

the signature of this decay the specific kinematic topology of the production process has to be taken into account in order to be able to suppress QCD multi-jet backgrounds. However, most Higgs searches in the light Higgs mass region concentrate mostly on the decay channels $H \to \tau\tau$ and $H \to \gamma\gamma$ as they are easier to separate from backgrounds.

At higher Higgs masses, the Higgs Boson width increases dramatically as more decay products are kinematically accessible. Around $m_\mathrm{H} = 160$ GeV the decay to a pair of W bosons becomes possible, which then dominates the branching ratio.

$\mathcal{CP}$ properties of the Higgs boson

It is possible to measure the $\mathcal{CP}$ properties of a heavy Higgs boson if it undergoes a four-body decay via two massive intermediate particles as for example gauge bosons or top quarks but also τ leptons.

The experimentally favored decay channel to determine $\mathcal{CP}$ and spin of a new massive particle X ($m_X \gtrsim 300$ GeV), coupling to weakly-charged gauge bosons, is the one into four charged leptons via $X \to \mathrm{ZZ}$ [14, 15, 16, 17, 18]. These "golden channels" [19] are characterized by extraordinarily clean signatures, making them experimentally well-distinguishable even if they only have small rates due to the small leptonic Z branching ratios.

The spin and $\mathcal{CP}$ properties are usually examined through correlations in the angular distribution of the decay products. There are several definitions throughout the literature for observables which contain the $\mathcal{CP}$- and spin-discriminating information in different ways.

A commonly used (sub)set of angles is given by the definitions of Cabibbo and Maksymowicz in [20], which originate from analogous studies of the Kaon system which can also be used for the Higgs system [14, 18, 21, 22].

A now widely used set of angles is defined in [23] as sensitive observables, which

also have been employed in a recent $X \to 4l$ investigation [17]. This introduction of these angles is taken from [178]. The definition of the angles is illustrated in Fig. 1.2: Let $\mathbf{p}_\alpha$, $\mathbf{p}_\beta$, and $\mathbf{p}_\pm$ be the three-momenta of the fermions f_α and f_β and the muons $\mu^\pm$ in the laboratory frame, respectively. In this definition one Z boson is assumed to decay into a pair of muons, whereas the other one decays into a pair of fermions in general. In the four lepton case, the second Z boson is taken to decay into electrons allowing for an unambiguous mapping of the decay products to the two Z bosons. This four lepton case provides a clean signal since muons and electrons can be measured with a reasonably good resolution in a detector. In addition this final state allows to clearly distinguish between the two leptons stemming from one Z boson through their charges which is measurable in a detector. However since the branching of the Z boson to a pair of leptons is only about 3% [24], the overall event yield is quite small. The hadronic decay on the other hand has a branching fraction of about 70%, with the drawback that it is not so straightforward to isolate the Z decay products from multi-jet backgrounds.

From these fermion momenta, the momenta of the Z bosons can be reconstructed

$$\mathbf{p}_{Z_h} = \mathbf{p}_\alpha + \mathbf{p}_\beta \,, \qquad \mathbf{p}_{Z_\ell} = \mathbf{p}_+ + \mathbf{p}_- \,, \tag{1.17a}$$

as well as the lab-frame momentum of the original resonance X

$$\mathbf{p}_X = \mathbf{p}_\alpha + \mathbf{p}_\beta + \mathbf{p}_+ + \mathbf{p}_- \,. \tag{1.17b}$$

In addition, the normalized unit vector along the beam axis is denoted by $\hat{e}_z$, and the unit vector along the ZZ decay axis in the X rest frame by $\hat{e}_{z'}$. The angles of Fig. 1.2 are then defined as follows

$$\cos\theta_h = \frac{\mathbf{p}_\alpha \cdot \mathbf{p}_X}{2\sqrt{\mathbf{p}_\alpha^2 \, \mathbf{p}_X^2}}\bigg|_{Z_h} \,, \qquad \cos\theta_\ell = \frac{\mathbf{p}_- \cdot \mathbf{p}_X}{2\sqrt{\mathbf{p}_-^2 \, \mathbf{p}_X^2}}\bigg|_{Z_\ell} \,, \tag{1.17c}$$

$$\cos\theta^\star = \frac{\mathbf{p}_{Z_\ell} \cdot \hat{e}_{z'}}{2\sqrt{\mathbf{p}_{Z_\ell}^2}}\bigg|_X \,, \qquad \cos\tilde{\Phi} = \frac{(\hat{e}_z \times \hat{e}_{z'}) \cdot (\mathbf{p}_\alpha \times \mathbf{p}_\beta)}{2\sqrt{(\mathbf{p}_\alpha \times \mathbf{p}_\beta)^2}}\bigg|_X \,, \tag{1.17d}$$

$$\cos\Phi = \frac{(\mathbf{p}_\alpha \times \mathbf{p}_\beta) \cdot (\mathbf{p}_- \times \mathbf{p}_X)}{2\sqrt{(\mathbf{p}_\alpha \times \mathbf{p}_\beta)^2 \, (\mathbf{p}_- \times \mathbf{p}_X)^2}}\bigg|_X \,, \tag{1.17e}$$

where the subscripts indicate the reference system, in which they are evaluated. More precisely, the so-called helicity angles θ_h and θ_ℓ are defined in their mother-Z's rest frame, and all other angles are defined in the rest frame of the particle X, where $\mathbf{p}_{Z_\ell} = -\mathbf{p}_{Z_h}$. It as also worth noting, that the helicity angles correspond to the so-called Collins-Soper angle of Ref. [25], evaluated for the respective Z boson.

1.2.2. Higgs production at the Large Hadron Collider

One of the aims of the Large Hadron Collider (LHC) at CERN, see Chapter 2.1, is the discovery of the Higgs boson. The overall picture for Higgs production at the LHC depends on the mass of the Higgs boson.
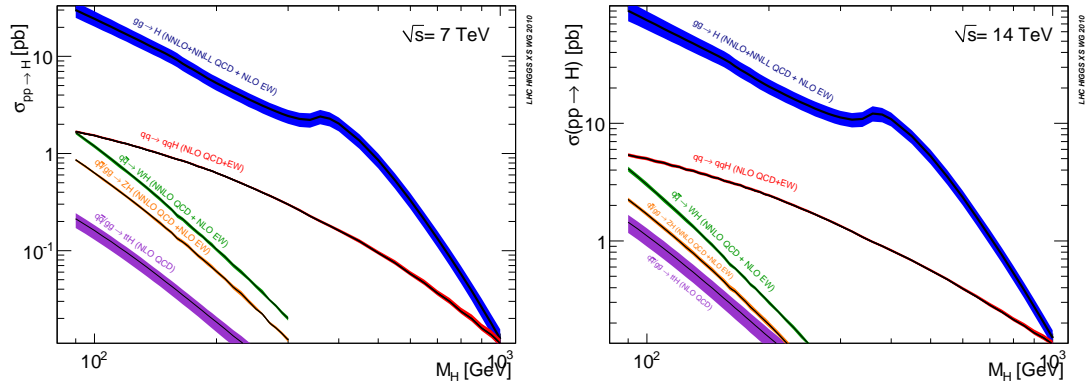
(a) Higgs production at 7 TeV c.o.m. energy   (b) Higgs production at 14 TeV c.o.m. energy

Figure 1.3.: Dependence of the Higgs production on m_H. Figures taken from [13].

In the case of a light Higgs, the production rate is high but the Higgs production processes suffer from large backgrounds whereas heavy Higgs bosons have smaller production cross sections with more manageable backgrounds.

There is only a limited number of production processes relevant for standard model Higgs production at the LHC. These are **gluon fusion** ($gg \to H$), **vector boson fusion** ($qq \to Hqq$ via W or Z exchange) and **associated production** with vector bosons or top quarks ($q\bar{q} \to VH$ or $gg, q\bar{q} \to t\bar{t}H$). The cross sections for these processes at the LHC are given in Fig. 1.3 for center-of-mass energies of 7 and 14 TeV. An overview of the currently available predictions for the Higgs cross section is given in [13] and [26].

Gluon fusion. The process $gg \to H$ via an intermediate heavy quark loop is for most of the allowed Higgs masses the dominant production mechanism. Only in the case of a very heavy Higgs boson Vector Boson Fusion is likely to be larger. This holds especially for center-of-mass energies $\sqrt{s}$ far above the threshold due to the increase of the gluon distribution, see Sec. 1.3.2, for small x. The leading order result is enhanced by the next-to-leading order contributions by $80 - 100\%$, depending on m_{H}, [27]. The gluon-Higgs interaction can be very well approximated by an effective Lagrangian obtained from integrating over the top quark loop and taking the top quark mass as infinite [28]
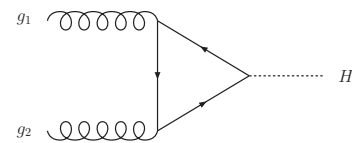
$$\mathcal{L}_{\mathrm{eff}} = -\alpha_s \frac{C_1}{4v} H G^{\alpha}_{\mu\nu} G^{\alpha\mu\nu} \,, \tag{1.18}$$
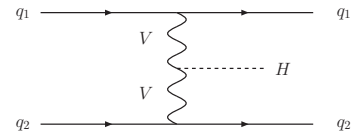
if the exact Born cross section with the full dependence on the top and bottom quark masses is used to normalize the result. Here v is the vacuum expectation value of the Higgs field and C_1 is the Wilson coefficient known at α_s^5 [29]. The exact and the approximate NLO cross sections differ less than 1% for light Higgs

masses below 200 GeV, and do not exceed 10% for masses up to 1 TeV. In this large m_{top} limit it is possible to calculate NNLO QCD corrections which lead to an additional increase of $10-15\%$ in the cross section [30]. In addition, three-loop virtual corrections to this process have been calculated, taking finite quark masses into account [31].

Combining all the available calculation for this process yields an increase by a factor of two in the inclusive cross section. The theoretical uncertainty from effects beyond NNLO is about 10%, showing a good convergence of the cross section with regards to the QCD corrections. The success in the QCD corrections has shifted the attention to electroweak corrections where important contributions come from 2-loop light-quark effects involving W and Z bosons. Their effect was found to give a further increase of 6% in the cross section from the $\mathcal{O}(\alpha) + \mathcal{O}(\alpha\alpha_s)$ terms [32].

All these results refer to the total cross section without any cuts. In a realistic analysis, the impact of higher order effects can depend crucially on the cuts imposed. It has been shown that while for the process $gg \to H \to \gamma\gamma$ radiative corrections are only marginally affected, the process $gg \to H \to \mathrm{WW} \to l\nu l\nu$ is strongly affected by these cuts which effectively remove almost the complete increase observed in the total cross section [33].

Vector Boson Fusion.   Although gluon fusion is the dominant process for Higgs production at the LHC, the contribution from vector boson fusion (VBF) becomes comparable for very large Higgs masses [34]. It can be visualized as elastic scattering of two quarks via the exchange of W and Z bosons. The next-to-leading order QCD corrections to these processes give only small enhancements of $5\% - 10\%$ [35]. The electroweak corrections also only yield a small contribution which decreases the total cross section by about 5% [36]. An approximative NNLO QCD calculation showed a further increase of only about 0.1% [37], decreasing the theoretical uncertainty from 5% to $1-2\%$. This fast convergence demonstrates that this channel is under excellent theoretical control.

In addition, once the Higgs boson has been found and its mass has been determined, the vector boson fusion processes will be of great importance in the measurement of its couplings to gauge bosons and fermions, since it allows for independent observation of different decay channels like $H \to \tau^+\tau^-$, $H \to \mathrm{WW}$, $H \to \gamma\gamma$ and so on.

The VBF processes can be measured quite precisely at the LHC since the estimated relative error in the cross section times decay branching ratio, $\sigma \cdot BR$ is in the range of $5\% - 10\%$ [38]. Together with the very accurate higher order corrections, this channel is understood very well.

A defining feature of VBF events in hadron-hadron collisions is the presence of two forward tagging jets, corresponding, at leading order, to the two outgoing quarks [39]. More on jet definitions can be found in Sec. 1.8. The scale of the

vent is given by the masses of the exchanged bosons, therefore the transverse momentum of the tagging jets is expected to be about half the mass of these bosons. Typically, one of the jets falls in the forward and one in the backward region of the detector. In case of more than two final state jets in the event, there are several possibilities to define the tagging jets. One would be to take the two jets with the highest transverse momentum, trying to ensure that the tagging jets are part of the hard scattering, another would be to take the two jets with the highest energy, which favors the very energetic forward jets typical for VBF processes.

In order to distinguish vector boson fusion events and especially the VBF Higgs boson signal from the background, hard cuts have to be applied on the Higgs boson decay products and the two tagging jets. The large rapidity separation of the two tagging jets is a very characteristic feature of this process, therefore this can be used to distinguish it from backgrounds. The decay products of the Higgs boson tend to fall into the "rapidity gap" between the two tagging jets.

Due to the fact that the exchanged particle in vector boson fusion is a color singlet state, there is no color connection between the final state jets. Thus there is no radiation of partons off the exchanged particles and therefore no jet activity in the central region stemming from the hard process. This allows the rapidity gap between the two tagging jets to be visible not only at the matrix element level but also in the hadronic final state. Results from Tevatron as well as next-to-leading order calculations show that a possible color singlet exchange in the one-loop level gluon fusion is suppressed by a factor of at least 10^{-2} [40].

As a result, in addition to the large separation of the two tagging jets, VBF events should not show much hard central jet activity. Imposing a *central jet veto* on events that pass the jet cuts is therefore a good way to further reduce backgrounds. The exact definition of this veto depends on the Higgs decay products under investigation as well as the experimental setup.

Associated production with vector bosons.

This process, Higgs + W, Z production, has only small cross sections but may be a useful channel to find light Higgs bosons decaying to $b\bar{b}$ or $\gamma\gamma$ since the weak boson can be used as a handle to identify the Higgs. The cross section for this process is larger at $p\bar{p}$ colliders than at pp colliders making it a dominant production process for a light Higgs at the Tevatron. The next-to-leading order QCD corrections increase the leading order cross sections by about 30%, [41], the NNLO QCD corrections give a further enhancement of $5-10\%$ [42]. NLO electroweak corrections were found to decrease the cross section by $5-10\%$, depending on the input parameter scheme [43].

Due to its small cross section and large QCD backgrounds, this process was deemed to be unimportant for the Higgs searches at the LHC. Recently, the process was brought back to attention by the possibility to use subjet techniques in order
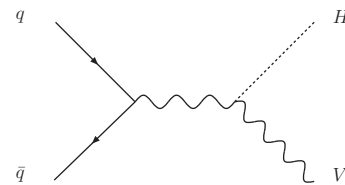
to separate the signal from its large backgrounds at the LHC in a boosted region [44].

Associated production with top quarks. As in associated production with vector bosons, a Higgs can be radiated off a top quark. This process offers the possibility to measure the top Yukawa coupling [45]. The cross section depends sensitively on the exact value of the top quark mass. Even though the top-Higgs coupling is large for the large m_t, the corresponding $Ht\bar{t}$ final state is heavy and therefore suppressed kinematically. The channel suffers from large backgrounds, particularly from $t\bar{t}b\bar{b}$ and $t\bar{t}jj$. The next-to-leading order calculations yield an increase of the cross section of about $20\% - 40\%$, [46]. This channel was also thought to be very hard to measure at the LHC but has regained interest with the application of subjet analysis which offer the chance to significantly reduce the combinatorial backgrounds [47].
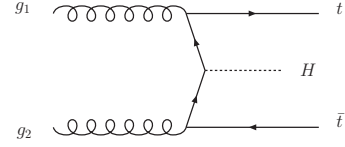
1.3. Quantum Chromodynamics

Experiments have shown that hadrons are not point-like particles but consist of particles called quarks, anti-quarks and gluons, the partons. The properties of these quarks gave rise to tight constraints on the nature of their interactions. Many different attempts for the description of this force, called the strong interaction, were tried, but the observed phenomena could only be satisfactorily described by a non- abelian gauge theory. The theory for the strong interaction is known as quantum chromodynamics, QCD.

A complete discussion of the features and verifications of QCD can for example be found in [48, 49], the brief overview over the most important features given here follows these introductions.

QCD is a non-abelian gauge theory with gauge group SU(3). SU(3) is a Lie group and so the generators of the group τ^a satisfy the corresponding Lie-algebra $su(3)$. For a more complete overview on the mathematical structure, see Appendix A.

Constructing a Lagrangian density that is invariant under local SU(3) transformations yields

$$\mathcal{L}_{\mathrm{QCD}} = \bar{q}(i\slashed{\partial} - m_q)q - g_s\bar{q}\gamma^\mu T^a q A_\mu^a - \frac{1}{4}F^{\mu\nu,a}F_{\mu\nu}^a \qquad (1.19)$$

$$\text{with } F_{\mu\nu}^a = \partial_\mu A_\nu^a - \partial_\nu A_\mu^a - g_s f^{abc} A_\mu^b A_\nu^c \ .$$

The difference to abelian theories, like quantum electrodynamics, QED, lies in the structure of the field strength tensor $F_{\mu\nu}^a$. In abelian theories the commutator of the fields vanishes by definition whereas in non-abelian theories the commutator yields additional terms leading to self-interactions of the gauge field. This also

means that the gauge bosons themselves carry the charge associated with the interaction.

1.3.1. Running Coupling and Confinement

The gauge bosons in QCD, the gluons, carry color charge themselves and therefore self-interact. This leads to significant differences between QCD and QED.

In QED the strength of the interaction is given by $\alpha = \frac{g^2}{4\pi}$. The observable charge however depends on the distance under consideration. A charge leads to a polarization of the vacuum which in turn gives rise to a screening effect. As a result, the observed charge is not constant any more but depends on the distance or the energy scale Q of the process, respectively. This is called the "running" of the coupling constant. In QED the strength of the coupling grows with increasing energy scale Q

$$\alpha(Q^2) = \frac{\alpha(\mu^2)}{1 - \frac{\alpha(\mu^2)}{3\pi} \log\left(\frac{Q^2}{\mu^2}\right)} \ . \tag{1.20}$$

Here μ denotes a reference scale at which α is known.

In QCD this screening effect is also present, since the quarks carry color charge as well as electric charge. Additionally, due to the self-coupling among the gluons there is also an anti-screening effect which is even stronger, so for small distances R and large Q^2 the coupling gets small. This phenomenon is known as *asymptotic freedom* [50]. For large distances however, the potential gets dominated by a term proportional to the distance R. This may be interpreted as the reason for *confinement*. Confinement explains why quark and gluon degrees of freedom are not observed as states which propagate over macroscopic distances. A rigorous proof of this effect has to rely on lattice QCD.

The development of the strong coupling constant in leading order can be described by

$$\alpha_s(Q^2) \equiv \frac{g_s^2(Q^2)}{4\pi} = \frac{\alpha_S(\mu^2)}{1 + \frac{\alpha_S(\mu^2)}{12\pi}(11N_C - 2N_f) \log\left(\frac{Q^2}{\mu^2}\right)} \tag{1.21}$$

where g_s is the coupling introduced in the QCD Lagrangian, N_C is the number of color charges and N_f the number of fermions.

Due to the decreasing coupling strength, it is possible to perform QCD calculations for high energetic reactions ($Q^2 \gtrsim 1$ GeV) in perturbation theory. On the other hand, for small energies $Q^2 \to 0$ calculations have to be non-perturbative. The energy scale at which α_S diverges is called Λ_{QCD} and has been estimated to be $\mathcal{O}(200$ MeV$)$. More qualitatively, Λ_{QCD} indicates the order of magnitude of the scale at which $\alpha_S(Q^2)$ becomes strong, thus the found value indicates a breakdown of perturbation theory for scales comparable with the masses of light hadrons.
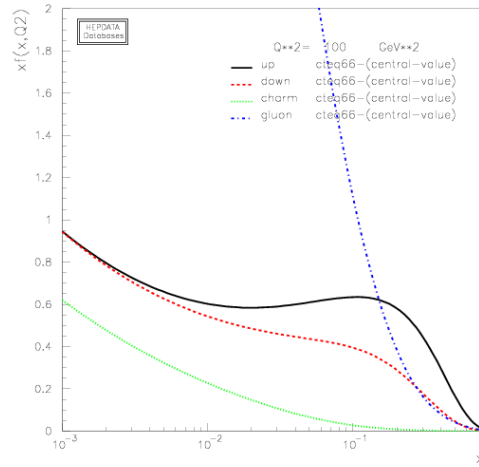
Figure 1.4.: Example of a PDF set, parton distribution functions from the CTEQ 6.6
            set. Figure created with [53].

1.3.2. Parton Distribution Functions

In the QCD parton model, a hadron entering a high energy reaction is viewed
as a collection of quasi non-interacting quarks, anti-quarks and gluons. This is a
direct consequence of the asymptotic freedom in QCD. The partons each carry a
fraction of the longitudinal momentum of the hadron with only small transverse
momentum. These hadrons are now described by Parton Distribution Functions
(PDFs) or structure functions. They give the probability density distributions for
the momentum fractions of the parton constituents

$$f(x)\mathrm{d}x = \mathcal{P}\left(x' \in [x, x + \mathrm{d}x]\right) \ , \tag{1.22}$$

where $f = q, \bar{q}, g$ are the quarks, antiquarks and gluons.

   PDF sets usually are derived from fitting deep inelastic and related hard scat-
tering data using parameterizations at low Q_0^2 ($\approx 1 - 7(\mathrm{GeV}/c)^2$) and evolving
these to higher Q^2.

   The most common framework for using PDF sets in calculations and event
generation is the LHAPDF library [51]. It provides a general interface to various
parton distribution functions by different authors. It is the successor of the CERN
PDFLIB library [52], which provided a standard `FORTRAN` interface.

   The typical format of the PDFs is a grid in x-Q^2 with a suitable interpolation
code provided by the PDF authors.

1.3.3. QCD Description of Particle Interactions

The QCD Lagrangian (1.19) can be used to obtain the Feynman rules correspond-
ing to the theory, from which in turn matrix elements can be calculated. These

together with an integration over the phase space of the process allow the calculation of cross sections.

In general, QCD is used to describe a reaction by ways of perturbation theory. This is a purely practical restriction since, with the exception of lattice gauge theory, there are no non-perturbative methods to calculate properties of QCD. Perturbation theory of course is only applicable if the strong coupling α_s is small.

Since the initial state in a hadron-hadron collider is not a beam of quarks or gluons, the particles described by the theory, but protons, the cross sections have to be convoluted with the parton distribution functions.

The general expression for a cross section is then given by

$$\mathrm{d}\sigma = \sum_{i,j} \iint \mathrm{d}x_1 \mathrm{d}x_2 f_i^{(A)}(x_1, Q^2) f_j^{(B)}(x_2, Q^2) \int \mathrm{d}\Phi \mathrm{d}\hat{\sigma}_{ij} \ ,$$

where the sum i, j runs over the partons in the incoming hadrons, the $x_{i,j}$ are the fractions of the incoming hadrons A, B momenta carried by these partons and Q^2 is the momentum transfer in the hard process. Finally, $\hat{\sigma}_{ij}$ is the cross section for the reaction with incoming partons i, j and $\mathrm{d}\Phi$ denotes the phase space integration.

The differential cross sections are typically divergent for small transverse momenta so a cutoff needs to be introduced. This indicates that perturbation theory does not provide an adequate description for small momentum transfers. This can be understood in the light of the running of α_S, as for small momentum transfers the strong coupling constant cannot be considered small anymore.

In close analogy to the renormalization process one can interpret the divergences as manifestations of an unphysical description. In the same manner as bare parameters like masses and couplings are not physically measurable, the partons entering the matrix-element calculations are asymptotic states and therefore not observable as well.

In conclusion, the description of a scattering process in QCD is divided into an infrared safe perturbative part and an infrared sensitive part. The scale separating the two parts is called the factorization scale μ_F. The quantities describing the non-perturbative parts of the process are on the one hand the PDFs describing the parton distributions in the incoming hadrons and on the other hand the fragmentation function describing the distribution of hadrons emerging from a parton.

In the case that, like in QCD, the soft and collinear divergences can be factorized from an infrared safe observable one can argue that, as in the renormalization, by evaluating the PDFs or fragmentation functions at a given scale μ_F the divergences can be subtracted. This leads to an evolution of the distributions between two scales which is calculable perturbatively, the Dokshitzer-Gribov-Lipatov-Altarelli-Parisi equations (DGLAP equations, [54]) for parton distributions (and analogous

equations for the fragmentation functions)

$$t\frac{\partial}{\partial t}f_\alpha(x,t) = \frac{\alpha_s(t)}{2\pi}\sum_{\alpha\to\beta\gamma}\int_x^1\frac{\mathrm{d}z}{z}P_{\alpha\to\beta\gamma}\left(\frac{x}{z}\right)f_\beta(z,t)\ , \tag{1.23}$$

where α,β,γ describe the partons, namely the gluons and the n_f quarks, and the $P_{\alpha\to\beta\gamma}$ are the regularized splitting functions, which can be obtained from perturbative QCD.

The DGLAP kernel $P_{g\to gg}$ or short P_{gg}, called gluon splitting function, is given by the color factor $C_A = 3$, the energy fraction z of the outgoing parton and the polarization of the gluons:

$$P_{gg}(z) = C_A\left[\frac{1-z}{z} + \frac{z}{1-z} + z(1-z)\right]\ . \tag{1.24a}$$

This splitting function can be obtained from the triple gluon vertex V_{ggg} in the QCD Lagrangian. It is divergent for $z\to 0$ or $z\to 1$ leading to enhancements associated with the emission of a soft gluon.

In the case of a gluon branching into a quark-antiquark pair $g\to q\bar{q}$ the spinor structure of the vertex has to be taken into account as well. The splitting function is then given by

$$P_{qg}(z) = T_R\left[z^2 + (1-z)^2\right]\ , \tag{1.24b}$$

where the color factor $T_R = 1/2$. Here no soft singularities appear ($z\to 0$ or 1).

For the branching where a quark emits a gluon, $q\to qg$, the splitting function P_{qq} is given by

$$P_{qq}(z) = C_F\frac{1+z^2}{1-z}\ , \tag{1.24c}$$

with the color factor $C_F = 4/3$. Here again the splitting shows a soft singularity as $z\to 1$ which is strongly dependent on the polarization, as only the amplitude for gluon polarization in the plane of branching develops this singularity.

These angular correlations can be measured in e^+e^- collisions, where the Bengtson-Zerwas-angle in fourjet-events, defined as the angle between the planes of the two hardest and two softest jets [55], is sensitive to these contributions. This is also a test for the non-Abelian nature of QCD.

1.3.4. Higher Order Matrix Elements

The simplest processes that can be imagined in a collider experiment are $2\to 2$ processes, at $\mathcal{O}(\alpha_S^2)$ for a QCD process. For more accurate predictions higher orders are needed. There are two possibilities for processes at $\mathcal{O}(\alpha_S^3)$. One is the *real emission*, where an additional parton is emitted and the resulting reaction is a $2\to 3$ process. This kind of process tends to be divergent for small parton energies or collinear emission. The other possible process when going to higher orders is the *virtual correction*, which is a $2\to 2$ process like the leading order but

with an internal particle loop. This process as well is divergent, however here the divergence is negative. The two types of divergences cancel exactly, leaving only finite terms. The combination of these two processes gives the next-to-leading order (NLO) corrections to the leading order (LO) $\mathcal{O}(\alpha_S^2)$ process.

This procedure can in principle be extended to even higher orders. For the next-to-next-to-leading (NNLO) order, graphs with two loops need to be evaluated. While the calculation for one-loop graphs is rather straightforward and well understood, it is not so easy for two-loop graphs, therefore only a limited number of inclusive processes has been calculated.

Going to higher orders in the real emission graphs only, the *Born level*, without any internal loops, is however comparatively easy to calculate. Here eight and more partons in the final state are possible, where the major limitation stems from the phase space generation of these particles. In order to avoid critical phase-space regions with possible divergences, these partons all have to be well separated and have a sufficiently high energy.

1.3.5. Jets and Observables

Quarks and gluons determine the dynamics of QCD reactions at high energies. However, due to confinement, these partons do not exist as free particles but only in bound states, the hadrons. Therefore a method to compare the final state of a QCD calculation, which consists of partons, and the final state of a corresponding experiment, consisting of hadrons has to be found. For this reason a *jet algorithm* is introduced, which is a procedure to classify any given final state according to the number of jets it contains. This measure must give cross sections which are free of soft and collinear divergences, just like total cross sections calculated in perturbation theory. An overview on the jet algorithms used in particle physics is given in Sec. 1.8.

More generally, every physical observable $\mathcal{O}_n$ must be collinear and infrared safe, so the following two properties must hold:

$$\mathcal{O}_n(p_1, p_2, \ldots, p_n) \xrightarrow{p_1 \parallel p_2} \mathcal{O}_{n-1}(p_1 + p_2, \ldots, p_n) \quad \text{collinear}$$

$$\mathcal{O}_n(p_1, p_2, \ldots, p_n) \xrightarrow{E_1 \to 0} \mathcal{O}_{n-1}(p_2, \ldots, p_n) \quad \text{soft}$$

From these criteria jet algorithms as well as event shapes can be constructed. While a jet algorithm will always find jets, a shape variable only measures some particular aspect of the shape of a hadronic final state. These shapes then characterize an event for example as pencil-like, planar, spherical etc. They also can be compared with theoretical predictions.

The concept of infrared safe observables is based on the reliability of perturbative predictions. Given that the coupling is small enough to justify perturbative calculations, finite predictions are possible. These require that for every parton emission a corresponding virtual correction is taken into account as well. In that

case the infrared singularities stemming from soft and collinear gluon emission cancel.

1.4. Parton Shower

In order to improve the predictions for cross sections and observables, more correction terms in perturbation theory have to be calculated. The complexity for higher order QCD calculations however increases roughly factorially with the order and the higher dimensional phase space gets arbitrarily complex. Thus, only a limited number of higher order terms for the most important signal and backgrounds have been calculated. In principle, the higher order terms in the perturbation series are assumed to become smaller with higher orders, but there are cases where the higher-order terms are enhanced for some phase space regions. As an example the emission rate for a branching $q \rightarrow qg$ diverges when the gluon either becomes collinear with the quark or when the gluon energy vanishes.

Instead of making precise predictions at a fixed order in perturbation theory one can try to get an approximate result in which enhanced terms are taken into account to all orders. The concept can be illustrated by a comparison of QCD and QED. In electrodynamics accelerated charges radiate photons whereas in QCD accelerated colors radiate and create gluons. As these also carry color they radiate as well, leading to a cascade of partons, the *parton shower* [56, 57]. The parton shower represents an approximative perturbative treatment of QCD dynamics above a given momentum transfer squared t, typically $\mathcal{O}(1 \text{ GeV}^2)$.

In a hard scattering process, the incoming and outgoing quarks must be on the mass shell, i.e. satisfy $p^2 = E^2 - \mathbf{p}^2 \approx m_q + \mathcal{O}(\Lambda_{\text{QCD}})$ at long timescales. However, the nearer the partons are to the hard interaction, the shorter is their timescale. Due to the uncertainty principle these nearer partons are more and more off-shell.

The parton shower converts highly virtual, primary partons associated with the hard process into low virtuality, final state partons. These final state partons are either of positive virtuality just prior to hadronization or partons with negative virtuality emerging from a beam hadron entering the hard scattering process. If the parton shower converts partons from the hard interaction to the hadronization scale, the branchings are *timelike* and the process is called final state radiation (FSR), for the conversion of partons from the incoming beam particle to the hard interaction, called initial state radiation (ISR), the partons undergo *spacelike* branching.

The generation of the incoming, space-like, and outgoing, time-like, parton showers is an iterative Markov branching process based on the use of the the DGLAP equations, Eq. (1.23), of the fragmentation functions. These equations sum up the leading effects of repeated parton branchings to all orders and thus improve the convergence of the perturbative calculation. The enhanced higher order terms appear for processes like soft gluon emission and the splitting of a gluon or a light quark into two almost collinear partons. These terms are

associated with large logarithms of the scale, thus the inclusion of these enhanced configurations is called the *Leading Log Approximation.*

However, the combination of higher order corrections in perturbation theory and the parton shower is not so straightforward. The problem is that both parton shower and higher order corrections predict additional external partons. It is now very important to avoid that parts of the phase space get sampled by both processes, which is denoted as double counting. For this, sophisticated algorithms have been invented, which are presented in Sec. 1.4.5.

1.4.1. Parton Branching

Collinear enhancements are associated with *parton branching* occurring on an incoming or outgoing line of a QCD Feynman diagram. The branchings are given by the splitting functions which can be calculated from the vertices in the QCD Lagrangian. They form the evolution kernels for the DGLAP equations as already described in Sec. 1.3.3.

For an outgoing parton the branching is timelike because then the momentum transfer t defining the scale of the process is greater than zero, $t > 0$. The opening angle for this branching can be calculated in terms of t, E and z, where z denotes the energy fraction of the outgoing partons b, c with respect to the energy of the incoming parton a, $z = E_b/E_a = 1 - E_c/E_a$.

For the case that the three partons are gluons, $g \to gg$, the additional radiation can be described by the splitting function Eq. (1.24a), a factor $1/t$ from the propagator of the incoming gluon, and the contribution of the polarization. Since the vertex factor is proportional to the opening angle θ and $t \propto 1/\theta^2$, the amplitude has a singularity proportional to $1/\theta$. This means that the amplitude for the emission of an additional parton in a process with n external particles in the small angle region the amplitude $|\mathcal{M}_{n+1}|^2$ can be factorized

$$|\mathcal{M}_{n+1}|^2 \sim \frac{4g^2}{t} P_{gg} |\mathcal{M}_n|^2 \tag{1.25}$$

where $|\mathcal{M}_n|^2$ is the amplitude for the process with n external particles.

To get the complete cross sections for the different possible splitting processes, the phase space for the n-parton final state $\mathrm{d}\Phi_n$ and the flux factor $\mathcal{F}$ have to be taken into account as well. The result is

$$\mathrm{d}\sigma_{n+1} = \mathrm{d}\sigma_n \frac{\mathrm{d}t}{t} \mathrm{d}z \frac{\alpha_s}{2\pi} P_{ji}(z) \ , \tag{1.26}$$

where P_{ji} is the appropriate parton splitting function.

As mentioned above, for multiple branchings the enhancement of higher order contributions is associated with multiple small angle parton emissions and is summed up by the DGLAP equations.

It is now possible to introduce regularized splitting functions and solve the DGLAP equations analytically via Mellin transformations. Alternatively, in order

to study more detailed features of the branching process and structure of the final state a numerical Monte Carlo approach can be used.

In an axial gauge the DGLAP equations correspond to a sum of ladder diagrams [58] whereas interference or crossed-rung diagrams give sub-leading contributions. This makes it possible to describe the process in the parton model language. To each parton there is a set of probabilities assigned for its possible branchings, including the possibility for no branching as well. The probabilistic evolution of a parton can now be described by a classical Markov process.

A problem for a straightforward implementation is the fact that the splitting kernels P_{ji} are singular. They have to be regularized, otherwise they can in principle yield arbitrarily high probabilities, i.e. well above one, which makes no sense in a probabilistic interpretation. In addition, it is not possible to evolve the DGLAP equations numerically with singular kernels. The regularization can be achieved by introducing suitable cut-offs on the soft gluon momenta providing correctly normalized branching probabilities. In an analytic calculation the regularization would be achieved due to the fact that the virtual and real emission divergences at a fixed order cancel, yielding infrared finite observables. In the same manner the subtraction terms here follow from unitarity and the infrared finiteness of inclusive observables.

1.4.2. Timelike Branching

To construct a time-like Monte Carlo algorithm for FSR, the Sudakov form factor is introduced:

$$\Delta_i(t, t_0^i) \equiv \exp\left[-\sum_j \int_{t_0^i}^t \frac{dt'}{t'} \int_{\epsilon(t')}^{1-\epsilon(t')} dz \frac{\alpha_s(t,z)}{2\pi} P_{ji}(z) \right] \qquad (1.27)$$

where the cut-off $z < 1 - \epsilon(t')$ is introduced to take the infra-red singularities into account.

The Sudakov factor sums up all possible branching processes $i \to j$, up to a cut-off t_0^i which is associated with the parton i. It can be interpreted as the probability that a parton evolves from the scale t down to the final scale t_0 without undergoing any resolvable branching. The definition of the Sudakov form factor introduces cut-offs $\epsilon(t')$. In addition, there is a lower cut-off on the parton virtuality $t_0^i \equiv (m_i + m_0)^2$, where m_i is the mass of the parton and m_0 a free parameter. These cut-offs together normalize the probability so that a statistical treatment of the branchings is possible. In a similar way as in a perturbative higher order calculation the divergences of real and virtual corrections cancel, the regularization in the splitting kernel cancel with the regularization in the Sudakov form factor.

Using this form factor, the evolution of the parton distribution $f(x, t)$ can be

described by an integral equation

$$f_i(x,t) = \Delta_i(t, t_0^i) f_i(x, t_0^i) + \int_{t_0^i}^t \frac{\mathrm{d}t'}{t'} \Delta_i(t, t') \int_x^{1-\epsilon(t')} \frac{\mathrm{d}z}{z} \frac{\alpha_s(t', z)}{2\pi} P_{ji}(z) f(x/z, t') \ .$$

$$(1.28)$$

Here the relations $\Delta_i(t_0^i, t_0^i) = 1$ and $\Delta_i(t, t_0^i)/\Delta_i(t', t_0^i) = \Delta_i(t, t')$ were used.

This set of inhomogeneous integral equations can be solved by repeated back substitutions, yielding a von-Neumann series solution, which forms the basis of the Monte Carlo implementation of final state time-like parton cascades:

$$\begin{aligned}
f_i(x,t) &= \Delta_i(t, t_0^i) f_i(x, t_0^i) \\
&+ \int_{t_0^i}^t \frac{\mathrm{d}t_1}{t_1} \Delta_i(t, t_1) \int_x^{1-\epsilon(t_1)} \frac{\mathrm{d}z_1}{z_1} \frac{\alpha_s(t_1, z_1)}{2\pi} P_{ji}(z_1) \Delta_j(t_1, t_0^j) f\left(\frac{x}{z_1}, t_0^j\right) \\
&+ \int_{t_0^i}^t \frac{\mathrm{d}t_1}{t_1} \Delta_i(t, t_1) \int_x^{1-\epsilon(t_1)} \frac{\mathrm{d}z_1}{z_1} \frac{\alpha_s(t_1, z_1)}{2\pi} P_{ji}(z_1) \int_{t_0^j}^t \frac{\mathrm{d}t_2}{t_2} \Delta_j(t_1, t_2) \qquad (1.29) \\
&\times \int_{x/z_1}^{1-\epsilon(t_2)} \frac{\mathrm{d}z_2}{z_2} \frac{\alpha_s(t_2, z_2)}{2\pi} P_{jk}(z_2) \Delta_k(t_2, t_0^k) f\left(\frac{x}{z_1 z_2}, t_0^k\right) \\
&+ \cdots \ .
\end{aligned}$$

This formula for the parton distribution has a direct probabilistic interpretation: the first term on the right-hand side is the contribution from configurations where no branching between the scales t and t_0 occurs, so the Sudakov form factor $\Delta_i(t, t_0^i)$ gives the probability for a parton i to evolve between these two scales without resolvable radiation.

The second term represents the case that the initial parton i evolves to an intermediate scale t_1 at which a resolvable branching $i \to jj'$ occurs. Parton j receives the fraction $z_1 > x$ of the momentum of parton i and evolves without further branching to its cut-off scale t_0^j.

The same holds for the further terms, where the contributions for additional resolvable partons are taken into account. The sum of all these configurations gives a solution to the DGLAP equations.

The implementation for this process in a Monte Carlo simulation is done by sampling the Markov process defined by the DGLAP equations. The process starts with an off-shell parton i of scale $t > t_0^i$ and the Sudakov form factors $\Delta_{i \to jj'}(t, t_0^i)$ are used to select an intermediate scale at which a specific branching $i \to jj'$ can occur. In case this scale is below t_0^i, the parton is set on mass-shell, $p_i = t_0^i$ and the evolution stops. In the case that a branching occurs, the momentum fraction of the daughter particles is selected by $\alpha_s(t, z) P_{ji}(z)$ and their scales t_j, t_j' are derived from t, z. This procedure is repeated until all particles are below the threshold t_0 and non-perturbative effects take over.

1.4.3. Spacelike Branching

Up until now only forward evolution was considered where an outgoing parton with timelike momentum emits further partons and moves to lower virtual mass-squared. This is a good method for timelike evolution like the final state of e^+e^- collisions.

For spacelike cascades it is more convenient to start by specifying the momentum fraction x_n of the partons entering the hard process that is used for the matrix element calculation. Evolving the parton backwards from the hard-scattering scale guided by the PDFs already used to choose the hard process to the low-scale incoming hadron gives in every case the desired final state of the cascade. Forward evolution would only in a few cases yield the right configuration and thus make a simulation rather inefficient.

However, it is not possible to use exactly the same description as for the forward evolution. The backward evolution from a given x_2 to a x_1 can yield unphysical configurations where $x_1 > 1$, corresponding to a parton that carries more than 100% of the incoming hadron momentum. These configurations have to be rejected and thus also lead to a low efficiency.

The correct description for backward evolution uses a modified form factor, taking the local parton density $f(x,t)$ into account when choosing the next value of the evolution variable t

$$\Pi_i(t, t_s^i; x) = \frac{f_i(x, t_s^i)}{f_i(x, t)} \Delta_i(t, t_s^i) \ . \tag{1.30}$$

This can be interpreted as the probability that the parton i in a hadron evolves from the scale t backwards to the scale t_s^i with the same momentum fraction x and without resolvable parton emission. This leads to the equation

$$
\begin{aligned}
1 = \ & \Pi_i(t, t_s^i; x) \\
& + \int_{t_s^i}^t \frac{\mathrm{d}t_1}{t_1} \int_x^{1-\epsilon_{j'}^s(t_1)} \frac{\mathrm{d}z_1}{z_1} \Pi_i(t, t_1; x) \frac{\alpha_s(t_1, z_1)}{2\pi} P_{ij}(z_1) \frac{f_{j/h}(\frac{x}{z_1}, t_1)}{f_{i/h}(x, t_1)} \Pi_j(t_1, t_s^j; x) \\
& + \int_{t_s^i}^t \frac{\mathrm{d}t_1}{t_1} \int_x^{1-\epsilon_{j'}^s(t_1)} \frac{\mathrm{d}z_1}{z_1} \Pi_i(t, t_1; x) \frac{\alpha_s(t_1, z_1)}{2\pi} P_{ij}(z_1) \frac{f_{j/h}(\frac{x}{z_1}, t_1)}{f_{i/h}(x, t_1)} \\
& \times \int_{t_s^j}^{t_1} \frac{\mathrm{d}t_2}{t_2} \int_{x/z_1}^{1-\epsilon_{k'}^s(t_2)} \frac{\mathrm{d}z_2}{z_2} \Pi_j\left(t_1, t_2; \frac{x}{z_1}\right) \frac{\alpha_s(t_2, z_2)}{2\pi} P_{jk}(z_2) \\
& \times \frac{f_{k/h}(\frac{x}{z_1 z_2}, t_2)}{f_{j/h}(\frac{x}{z_1}, t_2)} \Pi_k\left(t_s, t_s^k; \frac{x}{z_1 z_2}\right) \\
& + \cdots
\end{aligned}
\tag{1.31}
$$

The fractions of PDFs that accompany the splitting functions guide the evolution towards the correct parton content. This equation can now be interpreted as a
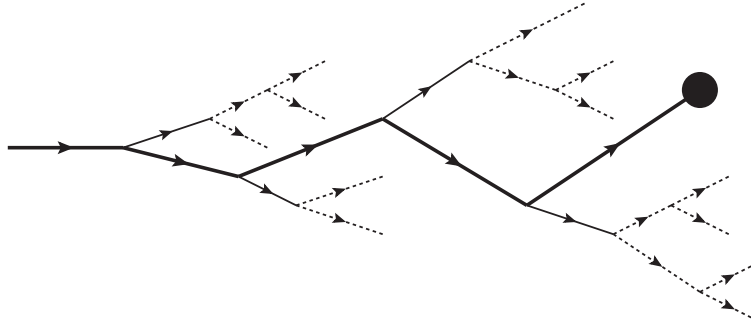
Figure 1.5.: Cascade of branchings. The thick line denotes main chain of partons that lead to the hard interaction,denoted by the dot, the other lines are partons that may recombine. Figure taken from [59].

normalized sum of the probabilities for all chains of branchings that take a given parton i at scale t back to an initial parton at scale t_s^i. The first term on the right hand side gives the probability that the parton evolved from t_s^i without resolvable emission, the second term gives the probability that the parton i evolved to t from the scale t_1 without resolvable radiation, where it had been produced in the branching of a parton b of momentum fraction x/z_1 which had come from the scale t_s^b without resolvable emission, and so on.

Even though the formulas for space-like and time-like branching look similar, their interpretation is different. While the time-like branching for the final state of a hard process occurs after the hard interaction took place, the space-like cascade in some sense already has happened before the hard interaction. It is possible to interpret the ISR as a virtual fluctuation in the proton. If no collision occurs the fluctuation collapses back, but in the case the highly virtual parton undergoes hard scattering, it cannot recombine with the partons in the cascade that lead up to its momentum configuration. Therefore a chain of branchings with increasing virtualities builds up the ISR shower, Fig. 1.5.

The numerical implementation of this backward evolution is similar to that in the timelike case. Given a parton i at scale t, the modified Sudakov form factor $\Pi_i(t, t_s^i)$ is used to select a branching scale. If this scale is below the cut-off, no resolvable branching is assumed to have occurred, the particle is set on mass-shell, $p_i = t_s^i$, and the branching stops. In case of branchings of the type $j \to ii'$ the momentum fractions are chosen according to $\alpha_s(t, z)P_{ij}(z)f_{j/h}(x/z, t)$. This procedure is repeated for j whereas i' undergoes timelike branching.

In the case of strange quarks entering the hard process, a minimum number of branchings has to occur in order to yield the correct flavors. This can be illustrated by considering for example the process $d \to dg$, $g \to s\bar{s}$. In case the scale is already below the cut-off scale before this amount of branchings has taken place, a non-perturbative model for this must be employed.

1.4.4. Coherent (Soft) Branching

So far only logarithmic enhancements stemming from soft-collinear and collinear enhancements have been considered. But there are also enhancements associated with soft gluon emission. This can be seen from the singularities in the small-angle parton splitting functions for soft gluon emission.

The emission of a gluon of momentum q from an external line with momentum p of a QCD Feynman graph gives a propagator factor

$$\frac{1}{(p \pm q)^2 - m^2} = \frac{\pm 1}{2p \cdot q} = \frac{\pm 1}{2\omega E(1 - v \cos \theta)} \tag{1.32}$$

where ω is the energy of the gluon, E and v the energy and velocity of the emitting parton and θ the angle of emission. In addition to the collinear enhancement for $\theta \to 0$ there is also one for $\omega \to 0$ for any velocity and angle.

This soft enhancement corresponds to a color factor times a universal, spin-independent factor of $F_{\text{soft}} = p \cdot \epsilon / p \cdot q$ in the amplitude, where ϵ is the polarization vector of the emitted gluon.

This enhancement factor in the amplitude for each external line implies that the cross section has a factor which is the sum over all pairs of external lines i, j

$$d\sigma_{n+1} = d\sigma_n \frac{d\omega}{\omega} \frac{d\Omega}{2\pi} \frac{\alpha_s}{2\pi} \sum_{i,j} C_{ij} W_{ij} \tag{1.33}$$

where $d\Omega$ is the solid angle of the gluon emission, C_{ij} a color factor and W_{ij} is the radiation function given in the case of massless partons by

$$W_{ij} = \frac{\omega^2 p_i \cdot p_j}{p_i \cdot q \, p_j \cdot q} = \frac{1 - \cos \theta_{ij}}{(1 - \cos \theta_{iq})(1 - \cos \theta_{jq})} \ . \tag{1.34}$$

The color weighted sum in the cross section is called the *antenna pattern* of the process.

The radiation function can be separated into two parts containing the leading collinear singularities for emissions from particles i and j, respectively,

$$W_{ij} = W_{ij}^{[i]} + W_{ij}^{[j]} \ , \tag{1.35}$$

$$\text{with} \quad W_{ij}^{[i]} = \frac{1}{2}\left(W_{ij} + \frac{1}{1 - \cos \theta_{iq}} - \frac{1}{1 - \cos \theta_{jq}}\right) \ . \tag{1.36}$$

This function has the property of *angular ordering*. Carrying out the azimuthal part of the angular integration, taking the parton i as reference direction yields

$$\int_0^{2\pi} \frac{d\phi_{iq}}{2\pi} W_{ij}^{[i]} = \begin{cases} \frac{1}{1 - \cos \theta_{iq}} & \text{if } \theta_{iq} < \theta_{ij} \\ 0 & \text{else} \end{cases} \tag{1.37}$$

This means that soft radiation in $W_{ij}^{[i]}$ is only emitted inside a cone of opening angle θ_{ij}. The same applies for the contribution $W_{ij}^{[j]}$ with i and j exchanged.

The angular ordering property is a coherence effect common to all gauge theories, in electrodynamics it accounts for the suppression of soft bremsstrahlung from electron-positron pairs, the *Chudakov effect*, which can also be explained heuristically by time-ordered perturbation theory.

In a suitable representation of the color algebra the color charges of the partons can be represented by vectors $\mathbf{Q}_i$ such that $\mathbf{Q}_i^2 = C_F$ for a quark, $\mathbf{Q}_i^2 = C_A$ for a gluon and $\mathbf{Q}_i^2 = 0$ for a singlet. With this, the color factor in the antenna pattern becomes $C_{ij} = -\mathbf{Q}_i \cdot \mathbf{Q}_j$.

For the case $e^+e^- \to q\bar{q}g$ with $\mathbf{Q}_i + \mathbf{Q}_j + \mathbf{Q}_k = 0$ this leads to

$$W = -\mathbf{Q}_i\mathbf{Q}_j W_{ij} - \mathbf{Q}_j\mathbf{Q}_k W_{jk} - \mathbf{Q}_i\mathbf{Q}_k W_{ik} \tag{1.38}$$

In case the partons i, j are close in angle, they form a system l with resulting net color charge $\mathbf{Q}_l = \mathbf{Q}_i + \mathbf{Q}_j = -\mathbf{Q}_k$. Using the above decomposition into leading collinear singularities and introducing the terms $\tilde{W}_{jk}^{[i]} = \frac{1}{2}(W_{ik}^{[i]} - W_{ij}^{[i]})$, W can be approximated as

$$W \simeq \mathbf{Q}_i^2 W_{ij}^{[i]} + \mathbf{Q}_j^2 W_{ij}^{[j]} + \mathbf{Q}_k^2 W_{lk}^{[k]} + \mathbf{Q}_l^2 \tilde{W}_{lk}^{[ij]} \tag{1.39}$$

This equation has a straightforward interpretation, each parton i, j and k radiates proportionally to its color charge squared. When two partons i and j are close in angle, their incoherent contributions are limited to cones of half-angle θ_{ij}. At larger angles, away from the direction of k, the coherent contribution is proportional to the combined color charge squared $\mathbf{Q}_l^2$ which is the same contribution as from an internal line with momentum $p_l = p_i + p_j$. So k is only able to resolve the net color charge $\mathbf{Q}_l$.

This treatment can be extended to higher orders, yielding the *coherent parton branching* formalism. This formalism allows to calculate soft gluon enhancement to all orders. The parton shower needs to be modified a little in order to impose angular ordering in the shower. Accordingly, partonic emissions are only allowed inside the cone specified by the previous emission. Instead of using the virtuality t as evolution variable, now

$$\zeta = \frac{p_b \cdot p_c}{E_b E_c} \simeq 1 - \cos\theta \tag{1.40}$$

is used for the branching $a \to bc$ with $\mathrm{d}t/t = \mathrm{d}\zeta/\zeta$. Imposing angular ordering on the shower algorithm then simply translates to $\zeta' < \zeta$ for successive branchings. An angular cut-off ζ_0 specifying the end of branching and removing infrared divergences has to be introduced as well, a good choice for this is $\zeta_0 = t_0/E^2$, keeping t_0 as minimum mass-squared.

Using also the appropriate splitting function P_{ba} instead of the soft approximation $\mathbf{Q}_a^2 d\omega/\omega$ the formalism treats both soft and collinear enhancement correctly. With this the formula for coherent branching becomes

$$\mathrm{d}\sigma_{n+1} = \mathrm{d}\sigma_n \frac{\mathrm{d}\zeta}{\zeta} \mathrm{d}z \frac{\alpha_s}{2\pi} \hat{P}_{ba}(z) \ . \tag{1.41}$$

The angular cut-off implies a more convenient evolution variable $\tilde{t} = E^2\zeta \geqslant t_0$. The angular ordering condition $\zeta_b, \zeta_c < \zeta_a$ for $a \to bc$ then reads

$$\tilde{t}_b < z^2\tilde{t}_a, \quad \tilde{t}_c < (1-z)^2\tilde{t}_a \tag{1.42}$$

$$\sqrt{\frac{t_0}{\tilde{t}}} < z < 1 - \sqrt{\frac{t_0}{\tilde{t}}} \tag{1.43}$$

Putting all this together, the coherent, angular-ordered Sudakov form factor is

$$\tilde{\Delta}_q(\tilde{t}) = \exp\left[-\int_{4t_0}^{\tilde{t}}\frac{\mathrm{d}t'}{t'}\int_{\sqrt{t_0/t'}}^{1-\sqrt{t_0/t'}}\mathrm{d}z\frac{\alpha_s(z^2(1-z)^2t')}{2\pi}P_{qq}(z)\right] \tag{1.44}$$

For large $\tilde{t}$ it falls more slowly than the original Sudakov form factor, which implies less branching due to the suppression of soft gluon emission.

1.4.5. Combining Higher Order Matrix Elements with Parton Showers

Matrix element calculations describe the production of particles to a fixed order while the parton shower adds the simulation of further emissions in the enhanced phase-space regions. Therefore going to a higher order matrix element including an additional particle includes also the corrections already included in the parton shower. Very often, the process of interest is an inclusive jet spectrum, that is the production of some objects X in association with several additional jets at matrix element level. To generate such a spectrum, the matrix element level for each process $X + n$ jets, where $n = 0, 1, \ldots$ up to the desired (or possible) number of external jets is calculated. However, combining this with a parton shower yields double counting since the hardest partons from the parton shower for low jet multiplicity matrix elements cover the same phase space region than the softest partons from the higher order matrix elements.

In addition, the overall normalization of distributions obtained with Monte Carlo simulations is not well-defined. The parton shower by construction does not affect the total cross section but merely the shape of distributions. One possible way to correct the normalization of Monte Carlo distributions is the usage of K-factors. A K-factor is defined as

$$K = \frac{\sigma^{\mathrm{improved}}}{\sigma^{\mathrm{MC}}} = \frac{\sigma^{\mathrm{NLO}}}{\sigma^{\mathrm{LO}}} .$$

It is crucial to note that when applying K factors for the normalization, the assumption is that it is possible to integrate over additional jets to obtain $\sigma^{\mathrm{improved}}$. The normalization of the Monte Carlo distributions then puts back these jets in the collinear approximation. From this it is clear that a more precise description is desirable.

To date, there are two different approaches for combining matrix element calculations with parton showers. The first is the matching of Born level matrix elements with different jet multiplicities, the second one is the merging of next-to-leading order merging.

Born Level Matching

There are currently two methods used as matrix level parton shower merging (MEPS) procedures, the MLM [60] scheme, a simplified version of the second one, the CKKW [61] method.

In the MLM scheme, which is implemented in the Monte Carlo generators ALP-GEN or MADEVENT, the generation starts with calculating the matrix elements for all the jet multiplicities of interest. These events are processed with a showering and hadronization generator, usually HERWIG 6 or PYTHIA 6 using LesHouches event files, see Sec. 3.3.2. The shower final state is then clustered using a jet algorithm, here a cone algorithm or a k_T algorithm can be employed, see Sec. 1.8. The jets with a transverse momentum larger than some $p_{\mathrm{T,cut}}$, typically $0.8 \times p_{\mathrm{T,min}}$ of the matrix element calculation, are then matched to the final state partons in the matrix element calculation. A jet is considered to be matched with a parton when their separation in the η-ϕ-plane is less than the jet radius used in the clustering. Once the jets are associated with the partons, all events where not every parton at matrix level is matched with exactly one jet at shower level are vetoed and discarded. In addition, for events with $n < n_{\max}$ outgoing partons, where $n_{\max}$ is the maximal number of external partons found in the sample, all events with more jets than partons are also discarded. These events are matched in an *exclusive* mode, that is the parton multiplicity in the matrix element has to be exactly the same as the jet multiplicity after the shower. The events with $n_{\max}$ external partons are matched in an *inclusive* mode, accepting also events with a jet multiplicity larger than $n_{\max}$ in the showered final state.

This method allows to combine final states with a different number of jets consistently without double counting. One thing to note is that the scale at which the parton shower starts has to be provided externally, it is typically chosen to be the hardest scale of the process.

The CKKW scheme is a more general way to combine parton showers with matrix elements, where instead of vetoing non-matching events a reweighting based on evolution using Sudakov logarithms is performed. This needs more information from the generation of the matrix element. A detailed introduction can be found in [62].

Next-to-Leading Order Merging

Merging NLO matrix elements with parton showers is more complicated than matching pure Born level matrix elements, as now the virtual correction and real emission matrix element in addition need to be considered.

There are currently two approaches to merging NLO calculations with parton showers, the MC@NLO [63] and the POWHEG [64] methods.

In the POWHEG (POsitive Weight Highest order Event Generator) approach, the correct treatment of the additional jets from the real emission is central. The basic idea is to generate the hardest emission first, using full NLO accuracy, and using a showering Monte Carlo generator to simulate the subsequent radiation. This works straightforward for a p_T ordered shower, which can be run with the transverse momentum of the real emission as starting scale. That way, all subsequent radiations will be softer, leaving the real emission as the hardest one. In the case of other evolution variables, this is not so straightforward. In an angular ordered shower, the first emission is unlikely to be the hardest one, so a different approach is needed, the *truncated* shower. The shower starts at the scale given by the angle of the hardest emission, evolving to smaller angles. That way not all possible emissions are included, namely the wide angle ones are missing. To include them, a second cascade starts at a scale given by the event and evolves until the evolution angle is at the value of the real emission. In this cascade, a veto is imposed on every radiation that is harder than the real emission. The combination of this vetoed, truncated shower with the first one allows a full description of the emissions.

In addition, the singular regions in the NLO calculation have to be identified and need to be separated to ensure the full cancellation of divergences.

The MC@NLO method uses a different method to avoid double counting and dealing with the counterterms needed for the full cancellation of divergences. It is described in detail in more detail in [62].

1.5. Hadronization

After the partons that were produced in the hard process far off mass shell have evolved in the parton shower, one is left with the final state of a cascade of partons, all near mass-shell at the cut-off scale t_0. The observable particles found in experiments however are hadrons, so the next step in the simulation of an event is the hadronization, where all the outgoing partons are combined into color neutral hadrons of a typical 1 GeV mass scale.

Since due to the running of the strong coupling α_S, perturbation theory does not work any more and non-perturbative techniques are far from providing enough understanding of confinement to allow the calculation of final state hadron distributions in jets from first principles, one has to resort to phenomenological models. A number of approaches for this have been tried with some success: the *Feynman-Field model* [65], the *Lund string model* [66], the *Cluster model* [67] and the *Statistical hadronization model* [68]. Currently, the string and the cluster model are most widely used in the available event generators and are described in more detail below.

The basic idea for most of the hadronization models used is some principle

derived from QCD quantities which then has to be extended by additional prescriptions and parameters. The huge amount of free parameters typically found in these models can be understood by considering the huge number of known hadrons with their specific properties like mass, spin, width and decay modes that are known today.

In principle, a model needs to provide the rules that can be applied iteratively on the partonic final state of the parton shower with its information about energy, momentum, flavor and other quantum numbers. The shower cut-off t_0 is an arbitrary parameter and not connected with hadronization, for which the intrinsic energy scale is presumably of $\mathcal{O}(\Lambda_{\mathrm{QCD}})$. Of course the outcome of the hadronization, i.e. the configuration of final state particles should not depend on the exact value of t_0. However, for an increased value of t_0 the shower terminates earlier and thus produces less partons with higher virtualities to hadronize. So ideally the hadronization model should as well have a parameter t_0 whose effect cancels when both the shower and the hadronization are combined. Unfortunately, this is generally not the case, in reality t_0 is an important tuning parameter chosen to simulate the correct amount of hadrons .

Hadronization is expected to be a local effect without involving large momentum transfers. So it seems reasonable that the hard process and the parton shower calculations are the dominant parts in determining the overall features of the process, like energy dependences, event shapes and other distinct features of the events. Nevertheless the effects of hadronization are not negligible, as can be seen from the results in e^+e^--collisions for event shape variables that are sensitive to out-of-plane activity [69].

1.5.1. The Lund String Model

The string model is motivated by the linear confinement of the QCD potential. A quark and an antiquark produced back-to-back that move apart lose energy to the color field between them. This field is supposed to collapse due to self-interactions into a color flux tube. This string-like configuration can be assumed to have a uniform energy per unit length, or string tension κ with $\kappa \approx 1$ GeV/fm, which corresponds to the description by confinement in QCD by a linear quark potential. Since the transverse size of the string $\langle r_\perp^2 \rangle = \pi/(2\kappa)$ is negligible, it is plausible to describe its dynamics by a massless, one-dimensional, relativistic string without transverse excitations. With this description, one obtains a Lorentz covariant and causal description of the energy flow due to linear confinement.

The string between a $q\bar{q}$ pair gains potential energy by the movement of the quarks. If the energy stored in the string gets sufficiently large, breaks due to spontaneous production of a $q'\bar{q}'$ pair can occur. The two new strings formed by the $q\bar{q}'$ and $q'\bar{q}$ pairs are color singlets as well and if their invariant mass is large enough, further breaks may occur. The string breaking ends when only short strings with an invariant mass in the hadron mass range remain. The equations of motion for strings then lead to so called 'yo-yo modes' in these strings, where the
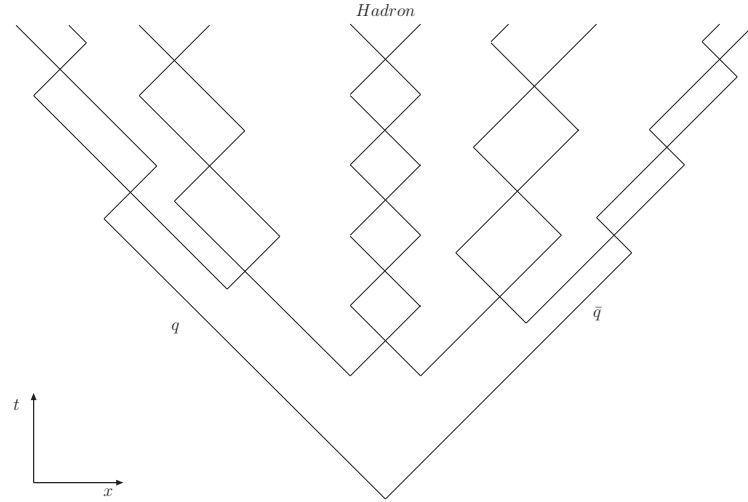
Figure 1.6.: Hadron production in the string model. One slowly right-moving fragment is highlighted, forming a hadron. The slowest hadrons form at the earliest times in the center.

$q\bar{q}$ pair, forming the endpoints of the string, seen from the string's center of mass frame, oscillates repeatedly outwards and inwards at the speed of light, passing through each other and transferring energy to and from the string [70].

To assign the transverse momentum distribution to the newly created $q'\bar{q}'$ pairs the model uses the idea of quantum mechanical tunneling. The probability for a string break to occur is given by Wilson's area decay law

$$\frac{\mathrm{d}P}{\mathrm{d}A} = P_0 e^{-P_0 A} \; , \tag{1.45}$$

where A is the space-time area within the backward light-cone of the point where the $q\bar{q}$-pair was created and P_0 is a constant. The position of the break-up point and the momentum of the fragment are related, $E = \kappa \Delta t$ and $p = \kappa \Delta x$. As a consequence, an average string fragment has $\langle \tau_{\mathrm{form.}}^2 (= t^2 - x^2) \rangle = 1/P_0$ and $\langle m_{\mathrm{string}}^2 \rangle = 2\kappa^2/P_0$ and therefore the slowest moving fragments form first, near the center of the string, yielding an inside-out pattern.

The tunneling also leads to a suppression of heavy quark production, $u : d : s : c \approx 1 : 1 : 0.3 : 10^{-11}$, so charm quarks and heavier quarks are very unlikely to be produced by the model.

In general, the string breaks are causally disconnected. Therefore the breaks can be performed in any order without affecting the result, so starting from the quark end inwards should yield the same final configuration than starting from the anti-quark end. This so-called 'left-right' symmetry constrains the fragmentation function $f(z)$ describing the fraction z of the energy and longitudinal momentum that the next string fragment will take out from the remainder. This function together with the tunneling probability provide tunable parameters for the model.

Meson production in the Lund model is now rather straightforward. It can

be depicted as a quark-antiquark pair connected by a string without any further breaking. Baryon production however is somewhat more difficult and not so well understood. In principle it can be pictured as a configuration with three quarks attached by strings to a common center in a direct extension of the meson case. The problem is how to achieve such a configuration starting with strings only connecting quarks and antiquarks. There are several different ways to do this, the most commonly used models are the *diquark* and the *popcorn* model. In the diquark model the string breaking is not imposed by a $q\bar{q}$ pair but by a $qq'\bar{q}\bar{q}'$ or diquark pair with the same color configuration as the endpoint quarks. Alternatively, in the popcorn model the string breaking is imposed by a quark-antiquark pair that has a different color configuration than the original pair. In that case, an anti-aligned, color triplet gluon field remains between the new quark-antiquark pair, inducing the possibility for further $q\bar{q}$ pairs to form which allows the string to break before the first virtual $q\bar{q}$ pair recombines. In both cases the remaining string fragment has a three-quark configuration and therefore a nonzero baryon number. The two models illustrate the ambiguity whether a baryon is regarded as a quark-diquark bound state or a three quark configuration.

For configurations with several final state partons, the model gets more complicated. In the case that gluons are present in the event, they enter as kinks on the strings. Each of these kinks carries localized energy and momentum, given by that of the initial gluon. These kinks in the string lead to changes in the angular distribution of the produced hadrons compared to a configuration without them. That means that gluons have two pieces of string attached to them, thus the ratio of gluon/quark string forces is two. This can be compared to the ratio of the color charge Casimir operators $N_C/C_F = 2/(1 - 1/N_C^2) = 9/4$, so gives a reasonable approximation. In the case of e^+e^- three jet final states the introduction of these kinks for the gluon jets yields an improved description of the experimental data. A second aspect of this treatment of gluons is that it makes infrared save matching with the parton shower possible, because the kink size depends on the transverse momentum of the gluons. Low energetic gluons produce only very small kinks on the string and therefore have only a negligible effect on the dynamics of the string.

There is an ambiguity about the various ways the strings can be spanned between the different possible endpoints given by the quarks and antiquarks and the kinks, given by the gluons. However, in the "leading color" or N^2 approximation, where $N = 3$ is the number of colors, it is always possible to arrange the partons in a planar configuration. In this configuration every parton has an equal and opposite color than its neighbor (or neighbors in the gluon case). It now seems most reasonable to stretch the string between the color connected neighbors. The planar approximation simplifies the calculations by discarding *nonplanar* graphs, i.e. graphs that cannot be drawn without any particle lines overlapping. These graphs are suppressed relative to the *planar* ones by powers of $1/N$, this corresponds to the above mentioned assumption that there are N^2 gluons instead of $N^2 - 1$.
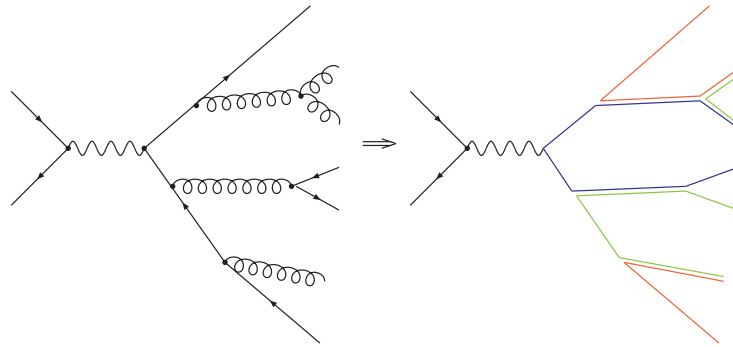
Figure 1.7.: Preconfinement. Quarks can be represented by one, gluons by two color
            lines.

The String model is a strongly physically motivated model which is very suc-
cessful in describing data. It is rather universal, once it is fitted to data from
e^+e^--collisions, there is not much freedom elsewhere to fit. The model yields
rather good predictions, every hadron described by the model uses one free pa-
rameter available for tuning. A possible drawback is that the model might hide
too much perturbative information, because the string formation in leading color
distorts the configuration.

1.5.2. The Cluster Model

The cluster model makes use of a property of the parton branching process called
preconfinement. The central idea is the formation of color singlet clusters of par-
tons stemming from the hard process and the subsequent parton shower. These
clusters then decay into hadrons. Preconfinement implies that pairs of color-
connected neighboring particles have the tendency to be arranged with limited
extension in both coordinate and momentum space. These color-singlet 'clus-
ters' have an asymptotic mass distribution that falls rapidly at high masses, is
asymptotically independent of the overall energy Q^2 and universal. In the planar
approximation, a gluon is represented by a color-anticolor pair, so the simplest
way for color-singlet clusters to form is by means of a non-perturbative low q^2 en-
hancement of the splitting of gluons into quark-antiquark pairs. This splitting is
relatively uncommon in the perturbative branching process, therefore it is usually
denoted as a "forced splitting". Neighboring quarks can then form color singlets.

   With the right approximation [72] for the $g \to q\bar{q}$ form-factor, it is possible to
include such an enhancement automatically such that all gluons will eventually
decay into quark-antiquark pairs.

   The mass spectrum of the formed clusters is again universal, peaking at a low
mass and falling off rapidly at high masses. The precise form is shaped by the
value assigned to the QCD scale Λ_{QCD}, the cut-off scale t_0 and also, though only to

a lesser extent, on the gluon-splitting mechanism. It is however independent of the center of mass energy of the collision. The spectrum is likely to represent a smeared version of "primordial resonances", formed in the early stage of confinement of real jets. Hence it seems reasonable to treat the cluster fragmentation as an averaged resonance decay with very simplified dynamics. This leads to a quasi-two-body decay, usually predominating for known resonances and branching ratios determined by density of states given by phase space times the spin degeneracy and does not include spin correlations, leading to isotropic decay. The reduced phase space for clusters decaying into heavy mesons and baryons is then sufficient to model the multiplicities of the various hadrons produced in e^+e^- collisions. So the probability for a cluster to decay into a given pair of hadrons h_1 and h_2 is given by

$$\mathcal{P}(Cl \to h_1 + h_2) = (2J_{h_1} + 1)(2J_{h_2} + 1)\, p(m_{Cl}, m_{h_1}, m_{h_2})\theta(m_{Cl} - m_{h_1} - m_{h_2})$$

where the J_i are the spin of the hadrons, m_i the masses, p the center-of-mass frame three-momentum in the two-body decay and the Heavyside function guarantees that the decay is allowed physically.

Even without the introduction of an adjustable fragmentation function, the energy and transverse momentum distributions of the hadrons agree quite well with experimental data. If soft gluon interference is taken into account the angular distribution in e^+e^- three-jet events is described effectually, as in the string model.

For very heavy clusters, typically $m_{Cl} > 4$ GeV, isotropic decay is an unreasonable assumption, so for these clusters an anisotropic fission mode is used. Since only a fraction of about 15% of the clusters lie beyond the fission threshold, the explicit form of the fission algorithm is not crucial and a simple one can be chosen, like the "symmetrical string breaking". This corresponds to a string with a given energy density between quark and diquark, which breaks in the middle by quark antiquark pair production, where the flavor of the produced pair is taken to be u, d, or s. This is repeated until all decay products are below the fission threshold, where the above mentioned cluster decay takes place. The threshold for cluster fission becomes a rather crucial parameter in this model, since even though only 15% of the clusters get split about 50% of the hadrons in the final state stem from these clusters.

For very light clusters which are too light to undergo two-body decay one assumes one-body decay and redistributes the excess momentum amongst neighboring clusters.

In case the clusters contain heavy quarks, namely c or b quarks, the decay model must be modified since the data of heavy flavor resonance multiplets is incomplete. The heavy quark is assumed to undergo free-particle β-decay, giving two hadronic clusters or a cluster and leptons. In the case of $b \to c$ the procedure is repeated on the charmed cluster. This model is rather crude but gives roughly correct multiplicities.

The cluster model implementation for a Monte Carlo simulation works as follows: For clusters formed of a quark-antiquark pair with flavors $q_1\bar{q}_2$ a third flavor

q_3 or d_3 is chosen randomly, where $q_3 = u$, d, or s and d_3 is one of the six di-quarks formed from these quarks. The decay products then are taken to be of flavor $q_1\bar{q}_3$, $q_3\bar{q}_2$ in the case of a two meson decay and $q_1 d_3$, $\bar{q}_2\bar{d}_3$ in the case of baryon-antibaryon decay. For the chosen flavor combinations, the possible decay products are taken from a list of resonances, weighted with the spin degeneracy $(2S + 1)$ of these resonances. For the chosen decay product, the available phase space is tested against a random number, if the test fails, the procedure starts again by choosing a new flavor q_3 or d_3 and selecting the possible decay products. In this procedure, the produced quark-antiquark or diquark-antidiquark pair is only used as a flavor label and does not have any dynamical role.

1.6. Underlying Event

In an $e^+ e^-$ collider both incoming particles fully enter the hard interaction and are either scattered or annihilated. As was discussed before, in a hadron collider only one parton per hadron enters the hard interaction whereas the rest of the hadrons is ignored in the description of the hard process.

For the complete picture it is however necessary to include the treatment of these *remnants*. Whereas for low energies one could use very simple approaches basically just ensuring confinement and the conservation of charge it becomes very crucial for higher collision energies, where the remnants can become very energetic and a more detailed treatment has to be used. Since the behavior of the proton remnants is dominated mostly by small momentum transfers, the relevant processes occur at non-perturbative scales, thus instead of analytical methods models have to be used.

While the basic physics of these remnants is assumed to be similar to that of soft hadronic collisions occurring in minimum bias data, there are significant differences when a hard scattering with high momentum transfer is present. The associated energy flow and charged particle density for events with a hard process is about a factor of 1.5 to 4 higher as in minimum bias events with the same collision energy. This "pedestal effect" was observed in jet events, boson production and Drell-Yan pairs [73].

While initial state radiation adds a Q^2 dependent amount of radiation, the dominant part of the activity stemming from remnant interactions saturates for sufficiently large Q^2 and will be called *soft underlying event* in this work.

A very simple approach to describing the underlying event is based on the *string hadronization*. Here the color information of the remnant is kept and the remnant particles thus can be connected to the rest of the event via strings which then can hadronize as usual.

Analogous to this in the *cluster hadronization*, the remnant can be treated as a cluster with a diquark flavor that then is treated like all the other clusters during hadronization.

This treatment of the proton remnants in the hadronization is very limited in its

predictions and does not model the actual behavior of the remnants as observed in experiments. Thus, this approach is only useful if the overall collision energy is small enough that the remnant has only very little energy and its effect is barely observed.

1.6.1. Parameterization of Experimental Data

In order to describe the behavior of the proton remnants, it is important to measure this effect and extract it from experimental data. One can then parameterize these data or derive models based on the findings from the data.

The parameterization of experimental data is the first widely used approach for a description of the underlying event. A very detailed implementation was developed by the UA5 collaboration. A Monte Carlo program fits the treatment of the soft underlying event to the data taken in the experiment [74]. The remnants can be turned into clusters that decay into a varying number of subsequent clusters with an average of sixteen clusters. These clusters are assumed to have a flat, central rapidity plateau with Gaussian tails and limited transverse momenta. These clusters then decay isotropically, with different functions determining charged multiplicity, particle composition, quantum number and energy-momentum conservation. The parameters for these distributions are taken from fits to experimental data.

Since these parameterizations are not supported by any further theory, they do not have much predictive power, especially with regards to extrapolations to higher energies.

An improvement to this employs a *Pomeron physics* based model [75, 76]. The basic unit of simulation here is a cut Pomeron giving rise to a chain of hadrons with a uniform rapidity and a Poissonian multiplicity distribution. The number and transverse momentum of these Pomerons can be adjusted for hard and soft scatterings according to fits to experimental data. The Pomerons are then fragmented in their respective center-of-mass frame with an independent fragmentation function taking the necessary energy dependence into account.

1.6.2. Multiparton Interactions

Another way of modeling the underlying event is via *multiparton interactions*, MPI, [77]. This model is based on the observation that the cross section of QCD $2 \to 2$ process diverges like $\mathrm{d}p_\mathrm{T}^2/p_\mathrm{T}^4$. In order to get a finite cross section, a lower cut-off $p_\mathrm{T,min}$ is introduced. The inclusive cross section $\sigma_\mathrm{int}(p_\mathrm{T,min})$ now reaches about 100 mb for $p_\mathrm{T,min} = 5$ GeV and 1000 mb for $p_\mathrm{T,min} = 2$ GeV. The expected *total* cross section σ_tot for LHC energies is however of the order 100 mb, where about a third of this cross section is related to elastic scattering and diffractive events not containing any jets.

This behavior can be understood by the fact that due to asymptotic freedom a proton at high energies can be regarded as a bunch of more or less free partons.

Therefore, in each collision, several more or less independent interactions can occur. An event with n interactions above $p_{\mathrm{T,min}}$ then counts for each interaction for the inclusive cross section $\sigma_{\mathrm{int}} = \sum n\sigma_n$, whereas it only counts once for the total cross section $\sigma_{\mathrm{tot}} = \sum \sigma_n$. Therefore $\sigma_{\mathrm{int}} > \sigma_{\mathrm{tot}}$ is not an unphysical statement but merely a sign that $\langle n \rangle > 1$, i.e. there are more than one parton-parton interaction per collision.

Since the multiple scatterings are taken to be independent of each other, a Poissonian distribution of the number of scatterers m can be assumed:

$$P_m = \frac{(\langle n(b,s) \rangle)^m}{m!} \exp(-\langle n(b,s) \rangle) \ . \tag{1.46}$$

This also includes the possibility for the several interactions to occur even if $\sigma_{\mathrm{int}}(p_{\mathrm{T,min}}) < \sigma_{\mathrm{tot}}$.

Energy-momentum conservation of course forbids the scatterers to be completely independent of each other, but the Poissonian distribution serves as a good starting point.

The mean number of interactions depending on the impact parameter b and s is taken to be

$$\langle n(b,s) \rangle = \mathcal{L}_{\mathrm{partons}} \otimes \sigma_{\mathrm{int}} = \frac{A(b)}{P_{\mathrm{res}}} \sigma_H^{\mathrm{inc}}(s) \tag{1.47}$$

where $\mathcal{L}_{\mathrm{partons}}$ is the parton luminosity, $A(b)$ a function specifying the parton distributions depending on the impact parameter, $P_{\mathrm{res}} \approx 1/300$ a parameter describing the $\rho-$meson dominance and σ_H^{inc} is the *inclusive* cross section.

There are now several possibilities to simulate the scatterers. One approach is to order the generation in the transverse momentum of the scatterers, another to have them completely independent, only imposing energy-momentum conservation afterwards.

Since the outgoing particles in the MPI model are partons, they have to be showered by the parton shower. This means that the implementation has to be done in the same step as the shower in order to treat the outgoing partons properly.

Here it is possible to combine both additional scatterers and partons from the shower. If both the scatterings and the initial state radiation are ordered in transverse momentum, the two can be combined, mixing the splittings from the shower with the scatterings in decreasing transverse momentum. The resulting *interleaved* description allows for a more consistent description of the partonic content at the various scales.

In addition to the multiparton interactions, the description of the underlying event needs to treat the low energy remnants. Considering that the number of scatterers would go to infinity as $p_{\mathrm{T,min}} \to 0$, it is obvious that a certain cut-off is needed. This can also be understood from the scattering processes themselves. Each scattering cross section is calculated using perturbation theory. This however only works under the assumption of free parton initial states existing at positive and negative infinity. Therefore for the calculation of the additional

scatterers confinement of the initial hadrons needs to be taken into account as well. Perturbation theory can only be applied down to

$$p_{\mathrm{T,min}} \simeq \frac{\hbar}{r_p} \approx \frac{0.2 \text{ GeV} \cdot \text{fb}}{0.7 \text{ fb}} \approx 0.3 \text{ GeV} \simeq \Lambda_{\mathrm{QCD}} \ . \tag{1.48}$$

This breakdown can be explained by considering the behavior of a soft parton. The corresponding transverse wavelength will be large enough to allow for one phase across a complete hadron. That means that the parton will only see the coherent sum of all color charges, which is zero since a hadron is a color singlet. To properly take the structure of a hadron into account the lower cutoff needs to be somewhat larger than the value derived in Eq. (1.48). Taking the average separation of a color and its anti-color into account requires a value of $p_{\mathrm{T,min}} \approx 2$ GeV. This also is in agreement with the value needed to describe Tevatron data.

1.7. Decays

The simulation of the matrix elements often has final state particles that are not stable. For example on-shell gauge bosons whose decay is not incorporated in the calculation of the hard process and τ leptons who are short lived are only measured through their decay products. Therefore these decays need to be simulated as well in an event generator.

In addition heavy particles from beyond the standard model physics can decay through complex decay chains which are characteristic for the theory and therefore need to be understood in detail. Furthermore, not only the correct decay modes are of interest, but also their angular relations, since these are dominated by the spin correlations in the decay chain.

It is therefore desirable to incorporate the full decay matrix element where available, as for example in the decay of the τ lepton and top quark and be able to keep spin correlations from the production until the final state of decay chains.

In the case of τ leptons very elaborate programs incorporating the decay are available [78, 79]. For decay chains of heavy particles, there exists formalism to treat the spin correlations and widths properly [80].

Furthermore in electroweak decays the radiation of photons can be important for the detailed description of final state kinematics. This can be simulated according to the YFS formalism [81]. In addition to the soft photon corrections to the leptonic Z boson decay, which is incorporated in [82], there is also the possibility to include a complete photon cascade [83].

In addition to the decay of intermediate resonances, most of the hadrons produced in hadronization have a short lifetime, the real final state of an experiment therefore consists of the decay products of these particles. An event generator must thus include a step in which these decays are taken into account. Since the decays as well as the hadronization can not be simulated analytically, measured values of decay widths, branching fractions and lifetimes are stored in tables and

the event generator chooses a decay channel with the weight according to the corresponding branching fraction.

The phase space for these decay processes is rather complicated, especially if the final state consists of a very large number of particles with non-negligible masses. To deal with this, special algorithms have been developed, like the MAMBO algorithm [84, 85]. In this algorithm, the N body final state momentum configuration is generated by using an exponentially damped phase space integration for the process and then boosting and rescaling it to reach overall energy-momentum conservation.

Furthermore, the implementation of possible decay modes is not just a straightforward integration of the decay tables measured in experiments and provided by the Particle Data Group. The measured branching ratios for rare decays do not necessarily sum up to one or disagree between experiments. Also not all possible entries of $SU(3, 4, 5)$ multiplets have been observed. In addition, the treatment of excited baryons can affect the description of normal baryons.

From this it is obvious that a careful treatment of the decays is needed including the tuning of the complete decay chains in order to get physically meaningful results. A widely used package to perform decays of B hadrons is `evtgen` [86], which was tuned extensively to the data provided by the Belle and Babar experiments. In addition, generators include their own decay models and tables, a very detailed description is done for example in HERWIG++, which employs a database with the available decay modes allowing a detailed documentation [87].

1.8. Jet Definitions

As described in the previous chapters, the final state of a reaction with outgoing partons consists of a huge amount of hadrons and their decay products. The hadrons stemming from the showering and hadronization of the matrix element partons however will most likely lie close to each other, close to the original parton, as described in the parton shower. It is now possible to recombine the four-momenta of the hadrons in such a bundle by the use of a "jet algorithm".

The role of the algorithm is to associate clusters of final state objects into jets such that the kinematic properties of the jets can be related to the corresponding properties of the partons in the hard process. Thus, the jet algorithm gives a direct insight into the process at QCD level. As a result, a good jet algorithm should not exhibit large differences in the properties of jets at parton level to the jets at hadron or calorimeter level.

Jet algorithms start from a list of fourvectors referred to as "protojets" that can be the momenta of calorimeter cells or particle tracks in an experimental study, the output of hadrons in a full event simulation or the partons in a perturbative QCD calculation. A jet definition must be able to specify a jet configuration unambiguously, both in a theoretical calculation and in experimental data analysis.

Many qualitative features of hadron production can be described by the intuitive

jet definition of "a large amount of hadronic energy/activity in a small angular region" but for a detailed qualitative analysis a more precise definition is needed. A proper algorithm should satisfy the following set of conditions [88]:

Fully specified: All the steps should be fully specified so that the jet selection, the kinematic variables and all possible corrections are clearly and completely defined. Additional algorithms like preclustering, splitting or merging must as well be specified completely.

Theoretically well behaved: In QCD calculations, all observables must be infrared and collinear safe in order to cancel infrared divergences. Also important for jet algorithms in hadron colliders is longitudinal boost invariance because in that case the center of mass of the individual parton-parton collision is normally boosted with respect to the hadron-hadron center-of-mass.

Detector independence: The outcome of the algorithm should not depend strongly on the detector specifications like segmentation or resolution and not amplify the effects of resolution smearing and angle biases.

Straightforward implementation: The algorithm should be easy to implement for perturbative calculations and experimental data, as well as provide an efficient use of computer resources.

In principle a jet algorithm works in two steps. In the first step, the actual **jet algorithm**, it selects a set of particles which are typically close to each other in the y-ϕ-plane and then in a second step combines their momenta to form the momentum of a jet according to a specific **recombination scheme**.

There are essentially two classes of jet algorithms, **cone-type** [89] and **clustering** [90] algorithms.

1.8.1. Cone-Type Algorithms

In cone-type algorithms a jet of radius R consists of the particles whose trajectories point into in a given area $A = \pi R^2$ of the $y - \phi$ space and the axis of the cone coincides with the jet direction defined by the the E_{T} weighted centroid of the particles in the cone. Here E_T is the transverse energy, $E_{\mathrm{T}} = E \sin \theta$. Jets are then defined by maximizing the amount of energy which can be covered by such cones.

A problem for the cone algorithm arises from the fact that nothing in the algorithm prevents the cones from overlapping, so that particles may belong to several jets at once. While it is no problem to have particles which do not belong to any jet, the case where particles are not assigned to jets unambiguously has to be avoided, else the energy of these particles would be counted multiple times. This can be resolved by adding a procedure in the algorithm specifying how to split or merge overlapping cones.

A further drawback for the cone-type algorithms is the amount of computing time needed to find all stable cones. In order to save computation time, the iteration used to search for the stable cones in experimental data starts with the cones centered about the most energetic particles, the *seeds*. For all particles in a seed cone, the E_{T} weighted centroids are calculated and used as centers for new cones. This is iterated until the cone is stable. However, such a seeded algorithm is not stable under the emission of soft or collinear gluons [88]. The presence of soft gluons can change the outcome of the jet finding because it can change the cone axis and prevent merging when in a configuration without soft gluons merging would have taken place or vice versa.

It is however possible to prevent this. The SIScone algorithm [91] is a fast seed-less algorithm that identifies all distinct circular enclosures, also called distinct cones, where distinct means having a different particle content. A full estimate on the number of calculations to be undertaken by this algorithm can be found in [91], with about $\mathcal{O}(N^2 \ln N)$ calculations it is much lower than the brute force implementation and in the range of the midpoint implementation of a cone algorithm with seeds.

1.8.2. Clustering Algorithms

In clustering algorithms the particles are assigned to jets in an iterative way, starting on a list of "protojets" consisting of the final state objects of interest. The algorithm is based on a distance measure d_{ij} between two protojets h_i and h_j. Two protojets that are classified as closest by this distance measure are clustered into a new protojet, and then removed from the list. The algorithm then starts again with the updated list of protojets. It also determines when, for a particular protojet, the joining should cease, in which case that protojet is labeled a "jet" and is removed from the list of protojets and not manipulated further.

The k_{T} Algorithm

1. For every protojet h_k compute the resolution variable d_{kB}. It has the property that, in the small angle limit, it reduces to the squared relative transverse momentum of the protojet with respect to the beam direction. The actual definition for d_{kB} may differ depending on the process considered. For hadron-hadron collisions the most common choice is the $\Delta\mathcal{R}$ scheme, where $d_{kB} = p_{T,k}^2 \cdot R$, with R as a dimensionless parameter, playing a radius-like role defining the extent of the jets.

2. For every pair h_k and h_l of protojets calculate the resolution variable d_{kl}. It has the property that in the small angle limit it reduces to the squared relative transverse momentum of the two protojets. Again there are several possible choices for this variable, in the $\Delta\mathcal{R}$ scheme it is $d_{kl} = \min(p_{T,k}^2, p_{T,l}^2) \cdot R_{kl}^2$, where $R_{kl}^2 = (y_k - y_l)^2 + (\phi_k - \phi_l)^2$. This definition corresponds to the one used in cone algorithms.

3. Find the smallest value $d_{\min}$ among the d_{kB} and d_{kl}.

   - if a d_{kl} is the smallest value, remove h_k and h_l from the list of protojets and combine them into a new protojet with momentum $p_{(kl)}$ according to a recombination scheme. Again there are several possible schemes, for example the E-scheme corresponding to vector addition of the four-momenta. This is a good choice because it is an exact way of merging and also favorable with regards to simplicity.

   - If a d_{kB} is smallest, object h_k is defined to be a jet and removed from the list of protojets.

4. Repeat until all objects have been included in jets.

In step 2, it is possible to include an additional parameter d_{cut} [92] and check if $d_{\min} > d_{\mathrm{cut}}$. In that case, all remaining objects are classified as jets and the algorithm is complete. This so called "exclusive mode" separates the hard final state explicitly from the soft beam remnants, the $d_{\min}$ defines the hard scale of the process. This can be done in two ways, either a fixed d_{cut} (and therefore scale) is used to find the jets with $p_{\mathrm{T},i}^2 > d_{\mathrm{cut}}$, or the d_{cut} is set in each event, defined by the $d_{\min}$ obtained after clustering the list of protojets into a given number of final state jets.

Without this stopping parameter, the resulting "inclusive mode" bears a similarity with the cone algorithm and is a good choice for hadron-hadron colliders.

Recently, this definition of the k_T algorithm has been extended by modifying the resolution variables d_{kl} and d_{iB}. This lead to several new jet algorithms with different properties. All off these definitions can be parameterized via

$$d_{ij} = \min\left[p_{\mathrm{T}i}^{2n}, p_{\mathrm{T}j}^{2n}\right] R_{ij}^2 \ , \quad d_{iB} = p_{\mathrm{T}i}^{2n} R_{\mathrm{eff}}(p_{\mathrm{T}i})^2 \ , \tag{1.49}$$

where $n = 1$ and $R_{\mathrm{eff}}(p_{Ti}) \equiv R_0 = const.$ for the k_T algorithm. Modifications in these two values now lead to different jet algorithms.

The Cambridge-Aachen Algorithm Based on the geometrical considerations that lead to the fastjet implementation, see [93], this variation of the k_T algorithm has been proposed [94]. Here the recombination parameter from (1.49) is set to $n = 0$ and $R_{\mathrm{eff}}(p_{Ti}) \equiv R_0 = const.$, so this jet definition is purely geometrical, based on *angular ordering*. The advantage of this algorithm is the reduced amount of "junk jets", jets that stem from soft particles and not the hard process and the limited growth of these objects once formed.

The Anti-k_{T} Algorithm The anti-k_T algorithm [95] takes the idea of the Cambridge-Aachen algorithm further by setting $n = -1$ and $R_{\mathrm{eff}}(p_{Ti}) \equiv R_0 = const.$ This means that while the k_T algorithm clusters soft particles first, the anti-k_{T} algorithm starts with the hardest particles. The resolution variable d_{ij} between a hard and a soft particle will be dominated solely by the transverse momentum

of the hard particle and their R_{ij}-separation. The d_{ij} of a pair of similarly soft particles will be much larger, thus soft particles will cluster with hard particles faster than they will cluster with each other. In total, this will yield jets with a very cone-like structure, with the splitting and merging done by the algorithm itself.

Variable ΔR Algorithms This class of jet algorithms is based on a further generalization of (1.49) by setting $R_{\text{eff}}(p_{\text{T}i})$ to a function in $p_{\text{T}i}$ instead of a constant [96]. This can be motivated by considering resonance decays into jets, where the shower of hadrons is boosted and will very likely fall in a circular cone with fixed angular size. In general, the cone size of the jet is assumed to vary like $\Delta R \propto 1/p_{\text{T}}$, which leads to the simplest variable ΔR algorithms, the "variable radius" (VR) algorithms with

$$R_{\text{eff}}(p_{\text{T}}) = \frac{\rho}{p_{\text{T}}} \ .$$

where ρ is a dimensionful constant. This definition of R can be combined with $n = 0$ and $n = -1$, thus one can get a "VR" version of the the anti-k_{T} and the Cambridge-Aachen jet algorithms. It was shown that these VR algorithms tend to get a better mass reconstruction for heavy resonances and, with jet identity cuts, a better signal-to-background ratio.

1.8.3. Jet Analysis

In a typical hadron-hadron collision a jet will not only contain the particles stemming from the initial parton but will also acquire contributions from the underlying event, detector noise and pile-up, adding energy and transverse momentum. This of course makes measurements less precise. In addition, the internal structure of a jet can be useful to gain information its content and origin. A lot of work has recently gone into the detailed analysis of jets, aiming at a deeper insight into the properties of jets and a more precise description of the physics processes taking place.

Jet Area

Since the additional activity from underlying event and pile-up is supposed to be independent of the hard process and can be assumed to be uniformly distributed, it is possible to measure it. From these measurements one can then derive a correction factor for jets. This correction factor is however dependent on the spatial extension of the jet in the detector, its *catchment area*, so the area covered by the jet has to be known. While a cone jet has an obvious geometrical extension, this is not so straightforward for a jet obtained by a clustering algorithm. This makes jet energy corrections for this kind of jets difficult.

A useful definition to assign the catchment area of jets proposed in clustering algorithms has been proposed in [97] and revived in [98]. The idea is to add extremely soft particles, so-called "ghosts" to the protojets and determine the region where they are clustered in jets as the catchment area of the jet. In principle, there are two ways of doing this, resulting in two different definitions:

- The **passive area** is scanning one ghost particle over the whole rapidity-azimuth region and determining the area in which it is clustered into a given jet. This is a measure of the susceptibility of the jets to contamination from an UE with pointlike structure.

- The **active area** is obtained by adding a dense coverage of ghosts and counting the number of these ghosts into a given jet. This measures the susceptibility of the jet to an UE with uniform, diffuse structure.

There is a difference in these two definitions, since the ghosts in the active area definition can cluster among themselves and thus change the borders of the jet areas.

Mass Drop

Distinguishing the jets produced by the decay of heavy resonances from backgrounds can be very hard since QCD and $t\bar{t}$ backgrounds typically are several orders of magnitude larger in cross section. A possibility to improve background rejection is to look for boosted resonances only. The angular separation R_{ij} of the two quarks from the decay can roughly be described by

$$R_{ij} \simeq \frac{1}{\sqrt{z(1-z)}} \frac{m_{\text{Res.}}}{p_{\text{T}}} , \quad (p_{\text{T}} \gg m_{\text{Res.}}) , \tag{1.50}$$

where $m_{\text{Res.}}$ is the mass of the resonance and $z, (1-z)$ are the momentum fractions of the two quarks.

To resolve these special angular scales, the Cambridge-Aachen algorithm is applied to the final state of the event using this value of R, typically a value of $R = 1.0 \dots 1.2$, it is possible to cluster most of the decay products into one jet, a so-called *fat jet*.

A hard jet found by the algorithm then is analyzed for a *mass drop* condition [44]. This is done by iteratively decomposing the fat jet:

1. The last clustering step of jet j is undone and the two subjets j_1 and j_2 are labeled such that $m_{j_1} > m_{j_2}$.

2. If there is a significant mass drop $m_{j_1} < \mu m_j$ and the splitting is not too asymmetric, $y = (\min(p_{\text{T},j_1}^2, p_{\text{T},j_2}^2))/(m_j^2) \cdot \Delta R_{j_1,j_2}^2 > y_{\text{cut}}$, then j is taken to stem from a heavy resonance and the algorithm finishes.

3. Otherwise j_1 is redefined as j and enters step 1. If there are no more clusterings to be undone, the algorithm ceases.

With this procedure it is possible to distinguish jets from heavy resonance decay from pure QCD jets, where the mass drop condition is rather seldomly fulfilled. In addition, one can find additional mass scales in the jet in case the heavy resonance decayed into a lighter one, for example a top quark decaying into a b quark and a W boson, in which case one of the subjets might correspond to the W boson.

Jet Filtering

Jet filtering is a generic method to remove contamination stemming from the underlying event and pile-up. Filtering takes a jet already found by another jet algorithm with typically a large R parameter and reclusters the constituents using a significantly smaller R parameter. Typically a Cambridge-Aachen or k_T algorithm is used for this. The algorithm then clusters the jet constituents into so-called *subjets*. In the end, only the hardest subjets are recombined into a *filtered jet*. The other subjets are assumed to stem from the underlying event and other sources not related to the resonance. The number of subjets allowed depends on the process under investigation, typically one for each parton from the supposed resonance decay and one additional to allow for hard final state radiation.

Since jet filtering needs information on what to look for, it is often used in combination with the mass drop condition mentioned above. After the mass drop condition is met, the constituents of the two subjets j_1, j_2 are reclustered using a jet algorithm with a jet radius $R = \frac{1}{2}\Delta R(j_1, j_2)$. This combination of mass drop and jet filtering is supposed to remove the additional activity that gets clustered into the fat jet due to its large radius.

The technique has been proposed for top quark searches [171] as well as to improve the search for the Higgs boson especially in the associated production with vector bosons [44] and top quarks [47].

Jet Pruning

Jet pruning [99] was proposed as an improvement to jet filtering aiming to remove the soft QCD contributions in the jet most likely stemming from the underlying event. Considering a recombination $1, 2 \rightarrow p$ it is useful to consider the following variables:

$$z \equiv \min(p_{\mathrm{T},1}, p_{\mathrm{T},2})/p_{\mathrm{T},p} , \quad \theta \equiv \Delta R_{12} .$$

Recombinations occurring at large θ are very likely to appear in heavy resonance decays, typically in the final recombination whereas small θ as well as small z recombinations are typically representing the QCD showering of the decay products or pure QCD jets. Even recombinations with a large-angle and small z that can occur in resonance decays will unlikely result in an accurate description of the decay since in that case the decay will be very asymmetric making it unlikely that the parent particle is accurately reconstructed. These large-angle and small z recombinations can also stem from soft radiation and the underlying event.

To remove these soft, large-angle recombinations, the *pruning algorithm* was introduced. It is applied to a jet from bottom up by re-running the jet clustering without searching for a particular number of subjets.

1. The algorithm is re-run on the set of input objects from the original jet, checking for the following condition in each recombination:

$$z < z_{\text{cut}} \quad \text{and} \quad \Delta R_{12} > D_{\text{cut}} \ .$$

2. If this condition is met, the protojets are not merged but the softer protojet is discarded and the algorithm continues. The resulting jet is the *pruned jet*.

The minimum angle D_{cut} can be chosen to be $D_{\text{cut}} = m_J/p_{\text{T}_J}$ for both k_{T} and CA algorithm, where m_J is the mass and p_{T_J} is the transverse momentum of the initial jet. Smaller values of D_{cut} removes more of the QCD radiation thus degrades the mass resolution whereas bigger values yield a loss in efficiency.

The value for z_{cut} typically varies like $z = 0.05 \ldots 0.15$, where smaller values are used with the CA algorithm and since the k_{T} algorithm orders the recombinations partly in z, the pruning needs to be more aggressive and larger values are employed.

Jet Trimming

Jet trimming [101] is motivated by the fact that the jet radius ideally should be large to capture all emission of the initial objects. However, jets with large radius will also collect a huge amount of radiation from the underlying event, pile-up etc. so typically one tries to find an optimal value as a compromise and extracts an average amount of activity based on the area of the jets. As in the case of jet filtering and pruning, jet trimming aims at removing soft contributions from jets in order to improve the resolution in reconstruction. The algorithm runs as follows:

1. All protojets are clustered into jets using any clustering algorithm. The resulting jets are called the *seed jets*.

2. The constituents of each seed jet are reclustered into subjets, using a possibly different jet algorithm with a radius R_{sub} that is smaller than that of the seed jet.

3. The resulting subjets are discarded in case $p_{\text{T,subjet}} < f_{\text{cut}} \cdot \Lambda_{\text{hard}}$, where f_{cut} is a fixed dimensionless parameter and Λ_{hard} is a hard scale depending upon the kinematics of the event.

4. The remaining subjets are assembled into the trimmed jets.

The jet definition used in step 1 is rather irrelevant for the trimming procedure, using the CA, anti-k_T or VR algorithm are good choices in order to capture most of the resonance decay products.

The jet definition used in step 3 however is quite crucial, the best choice is the k_T algorithm since the subjets found by this algorithm tend to share the energy between the subjets best.

The scale choice for Λ_{hard} is non-trivial, comparable with the scale choice for matrix element calculation. Possible values are the transverse momentum of the seed jet or the effective mass of the event $H = \sum p_{\text{T}}$. The value for f_{cut} has to be optimized and adjusted to the value for Λ_{hard}, typical values are $f_{\text{cut}} = 0.03..0.05$.

An interesting feature of the trimming procedure is the large decrease in the jet area of the trimmed jets, which can amount to more than 90%. This improves the overall jet energy scale uncertainty, since with the smaller jet area less radiation from the underlying event and pile-up have to be subtracted.

Chapter 2

The CMS Experiment

2.1. The Large Hadron Collider

The Standard Model of particle physics has been tested to a very high precision and is considered to be an effective theory up to energy scales around $\Lambda \approx 1$ TeV. To search new physics beyond the Standard Model and test the validity of the SM at higher energies, colliders which provide the collision energy corresponding to the energy regions of interest are needed. To this end, the Large Hadron Collider (LHC) was designed to reach energies no other accelerator attained before. It is a two-ring superconducting hadron collider located at CERN, Geneva and is installed in the existing 26.7 km tunnel that was constructed for the CERN Large Electron Positron (LEP) machine [102]. The design energy of the two counter-rotating proton beams of the LHC is 7 TeV each, resulting in collisions with a center-of-mass energy of 14 TeV. The major aim of the LHC is to provide under-standing of the electroweak symmetry breaking as well as verifying SM parameters and searching for physics beyond the Standard Model.

The design of the LHC follows from the limitations given by the size and shape of the LEP tunnel. This tunnel is divided into eight segments in which the acceleration and the focussing and beam guidance take place. Between these sectors are the nominal interaction points where the beams can be crossed to make them collide. Only at four of these eight points the beams actually collide, to keep the beam disruption at a minimum.

At LEP, the main limiting factor for the center-of-mass energy was the synchrotron radiation emitted by the accelerated electrons when guided on their circular paths. Protons, with their much larger mass compared to electrons, suffer much less from synchrotron radiation, allowing to reach much higher energies with the same bending radius.

The LHC storage ring is only the last step in a long chain of accelerator stages. Fig. 2.1 shows an overview of the accelerator complex used in the LHC program. Further details of the accelerator complex beyond the scope of this work can be found in the LHC design reports, [103, 104, 105].
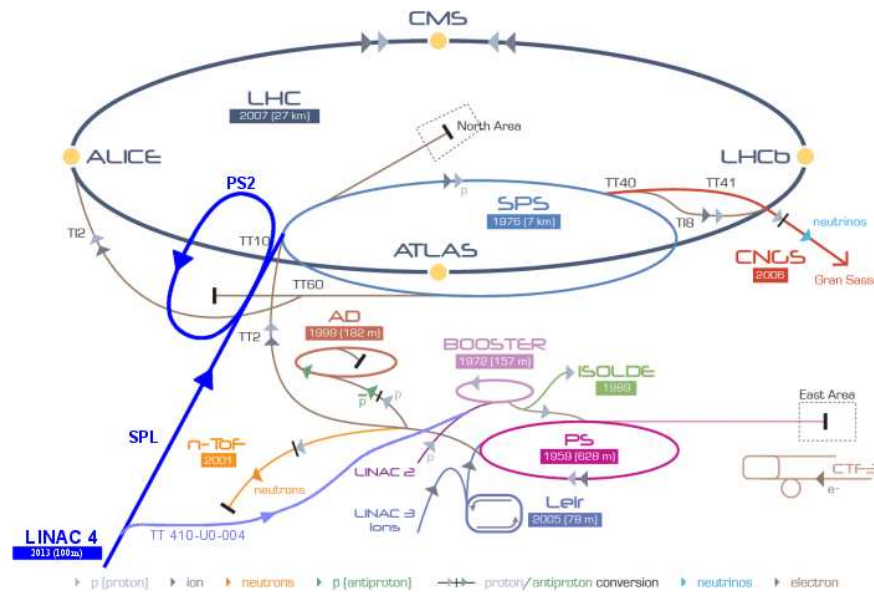
Figure 2.1.: Overview over the different accelerators at CERN from the proton injection
             via different accelerator stages up to the collision in the final step in the
             LHC ring.

The LHC was designed to collide either protons or heavy ions, namely lead,
at the given interaction points. In a first step, protons or lead ions are created
in a source. The proton production starts with the ionization of hydrogen gas
through a Radio Frequency Quadrupol (RFQ) duoplasmotron which is able to
provide a charged ion beam of 750 keV. This beam is then accelerated with a
linear accelerator, the LINAC2 and passes through a carbon foil at the end of the
machine. The foil strips off all orbiting electrons leaving a pure proton beam at
an energy of 50 GeV and a current of 180 mA.

This beam then passes through two circular accelerators, the Proton Syn-
chrotron (PS) and Super Proton Synchrotron (SPS). These two accelerators were
the predecessors of the LHC, both built as storages rings and used as pre-accelerators
for their suitors after energy upgrades. These two rings in steps pre-accelerate the
protons to 450 GeV before they are injected into the LHC main ring.

The LHC consists of more than one thousand magnets, all employing super-
conductive wirings. The acceleration is done by superconductive radio frequency
cavities, whereas dipole magnets able to generate a 8.3 T magnetic field are used
to bend the beam on the circular ring. In addition, other magnets like quadrupoles
are used to focus and squeeze the beams. To reach the superconducting regime of
the used materials, the magnets are cooled down to a temperature of $-271\,°C$. To
cool down such a large installation to these extreme conditions, an advanced cryo-
genic system is used which exploits the properties of liquid helium, for example
the suprafluidity.
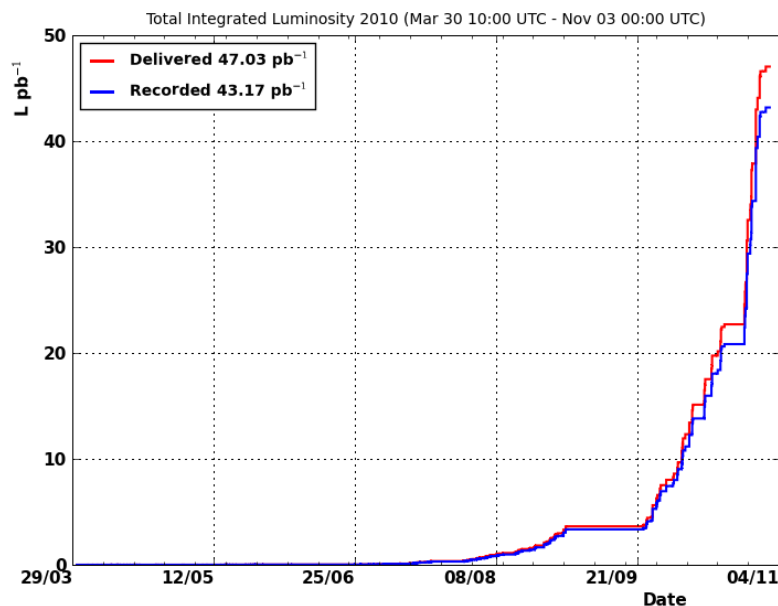
Figure 2.2.: The plot shows the maximum luminosity reached by the LHC up to the end of November 2010, i.e. the complete luminosity collected so far in the 2010 *pp* collisions. Taken from [106].

Another important parameter at the LHC beside the particle energy is the *Luminosity*. It is a measure of the amount of particles in the beam being able to collide. The luminosity is proportional to the number of events of a certain process, making it possible to relate event rates and interaction cross sections. The design luminosity of the LHC is unprecedented for a proton machine: 10^{34} cm^{-1} s^{-1}. This quantity can be calculated as a first approximation by the formula

$$\mathcal{L} = \frac{N^2 k f \gamma}{4\pi \epsilon_n \beta^\star} \, F \tag{2.1}$$

where N is the number of particles in each of the k circulating bunches, f the revolution frequency, $\beta^\star$ the value of the betatron function at the crossing point and ϵ_n the emittance corresponding to a one σ contour of the beam, contracted by a Lorentz factor γ. F is a reduction factor due to the crossing angle between the beams. In order to achieve high luminosities, the LHC beam is designed to contain a high number of bunches, up to 2808, filled with $\approx 10^{11}$ protons each, which collide with a high frequency of 40 MHz with well focussed beams, i.e. small emittance and $\beta^\star$. Due to the large number of protons per bunch, a major drawback of the LHC running at the high design luminosity is the number of about 20 concurrent collisions within one bunch crossing. This effect is called *pile-up* and complicates the precise reconstruction and measurement of events, making discoveries more challenging.

The main machine parameters (design values) are listed in Table 2.1.

Machine Parameter	Value for pp collsions	Dimensions
Energy per nucleon	7	TeV
Dipole field at 7 TeV	8.33	T
Design Luminosity	10^{34}	cm^{-2} s^{-1}
No. of bunches	2808	–
No. particles per bunch	1.15×10^{11}	–
Bunch separation	25	ns
β-function at IP	0.55	m
Relativistic gamma facto γ_r	7460	–
RMS beam radius at IP	16.7	μm
RMS bunch length σ_z	7.95	cm
Luminosity lifetime	15	h
Number of collisions/crossing	≈ 20	–

Table 2.1.: Some of the nominal machine parameters relevant for the LHC detectors.

2.1.1. LHC Start and Incident

The LHC operation started in 2008, with the first beam cycling on september 10. However, before any collisions could occur, an accident happened delaying the operations. On september 19, 2008 during powering tests of the main dipole circuit, an electrical fault in the bus between magnets developed a resistive zone. This caused an electrical arc, which punctured the liquid-helium containment. Once the cooling layer was broken, the helium flooded the surrounding vacuum layer where the pressure was too large for the relief discs serving as regulating valves to hold them back. The large pressure was sufficient to break the magnets surrounding the connection from their mountings. In addition to the damage done in the vicinity of the broken connection, a large part of the accelerator was contaminated with soot.

More information on the accident can be found in the official press release by the CERN management [107] and the detailed technical report [108].

In the repair period following the incident the monitoring system of the currents in the magnets and the emergency valves for the helium were extended. As only half of the beam pipe could be heated up to room temperature, not every magnet could receive the upgraded valves. As a consequence, the maximal energy for the first running was reduced to a centre-of-mass energy of $\sqrt{s} = 7$ TeV. This energy was chosen such that the splines connecting the magnets are able to withstand the corresponding currents needed to circulate the beam even if they should loose superconductivity in a similar accident as in september 2009.

Nonetheless, even at half its design energy, the LHC provides collisions with

the highest energy ever reached in a collider experiment.

The luminosity in turn was necessarily smaller as the design specifications demanded as well. The high luminosity aimed at needs a very detailed understanding of the complete injection chain and storage ring, so it was not expected to reach the design values within the first year of LHC operations. Operations started with one bunch of protons per beam but the number of bunches could be increased to 248 per beam, yielding a luminosity of $1.01 \cdot 10^{32}$ cm^{-2} s^{-1}.

The luminosity collected by the CMS experiment in the LHC operations between march and november 2010 is shown in Fig. 2.2. The effect of the additional bunches per beam can be directly seen in the large increase at the end of the running period.

2.1.2. The LHC Experiments

There are six experiments situated in four underground caverns located around the main ring. The design of these detectors was driven by the challenges posed by the large energy and luminosity of the LHC.

The extremely high interaction rate with only a small amount of the events being of interest requires a fast and efficient data acquisition system as well as a fast response of the order of $20 - 25$ ns to resolve particles coming from two subsequent collisions. The large number of particles in the final state of a collision requires detectors with a fine granularity.

The large flux of high energetic particles due to the high luminosity poses a further major challenge for the detector systems. Radiation doses of up to 10 kGy per year for the detector components closest to the beam are expected. A detector that is able to operate over the whole running period of the LHC expected to be 10 to 20 years requires radiation hard electronics and materials.

There are two general purpose experiments, ATLAS (A Toroidal LHC ApparatuS) [109] and CMS (Compact Muon Solenoid) [110], covering a broad range of measurements and searches. The other four experiments, ALICE (A Large Ion Collider Experiment) [111], LHCb (LHC beauty) [112], LHCf (LHC forward) [113] and TOTEM (TOTal Elastic and diffractive cross section Measurement) [114] are dedicated to specific analyses.

ALICE was designed for the analysis of heavy-ion physics with the goal to study the so-called quark-gluon plasma, a type of strongly interacting hadronic matter. The main aim of LHCb is to perform precision measurements of B mesons to study the B oszilations and search for new physics. LHCf is a small experiment located in the ATLAS underground cavern, 140 m off the interaction point. It aims at measuring the amount and energy of neutral pions in order to validate models for ultra-high-energy cosmic rays. TOTEM is based in the CMS cavern and aims at measuring the total cross section in proton-proton collisions and studying elastic scattering and diffractive processes. To measure particles very close to the beam pipe it employs so-called "Roman Pots", special vacuum chambers that host the detector and are directly connected to the beam pipe. Four pairs of these pots

are located near the interaction point.

2.2. The Compact Muon Solenoid Experiment

The Compact Muon Solenoid (CMS) detector is one of the general-purpose detectors used at the LHC at CERN. The overall design was driven by the environment conditions at the LHC with its large flux of particles and high bunch crossing frequency. A benchmark requirement which was posed in the design process is the proof of electroweak symmetry breaking through the discovery of a Higgs boson. The large diversity of Higgs decay modes depending on the Higgs boson mass makes this a very interesting benchmark. As hadronic final states are suffer from large QCD backgrounds and the limited accuracy in jet mass resolution, a clear focus of CMS lies in the detection of final states containing isolated leptons or photons, even though the branching fractions for these final states are smaller. This results in the requirement for an excellent muon tracking system covering a wide range of momenta and providing a good dimuon mass resolution. The electromagnetic calorimeter has to yield a similar precise mass resolution for diphoton and dielectron masses as well as an accurate energy resolution.

A further region of interest is the search for supersymmetry. A very important aspect in the models containing so-called R-parity conservation is a large amount of missing transverse energy $\not{E}_{\mathrm{T}}$ in the final state. A good measurement of the missing transverse energy relies on a hermetic coverage of the hadronic calorimeter and a good dijet mass resolution.

In addition, QCD effects, electroweak and flavor physics, B-hadron decays, lepton flavor conservation surveys as well as precise measurements of CKM matrix elements will be of interest. These precision studies require in addition a precise tracking system to achieve a good momentum resolution of charged particles, efficient track reconstruction abilities and vertex reconstruction.

The name of the detector implies some of its major design criteria. Figure 2.3 shows a perspective view of the CMS detector. It can be seen that the magnet and the embedded muon system define the overall dimensions, resulting in a compact design. The dominant feature is a superconducting solenoid with a length of 13 m, an inner diameter of 6 m and a homogeneous magnetic field of 3.8 T inside the solenoid. The onion-like layout of the detector provides an almost hermetic coverage around the main interaction point. Several subdetector components required for the measurement of different kinds of particles and their properties are arranged in a layered structure forming a central barrel enclosed by two flat endcaps. The detector has a total length of 21.6 m and a diameter of 14.6 m with a total weight of 12500 t.

The return field is led by layers of iron in which four muon stations are integrated to allow a good muon identification and resolution over a wide range of momenta and solid angles as well as good dimuon mass resolution.

The bore of the superconducting magnet is large enough to allow for the inner
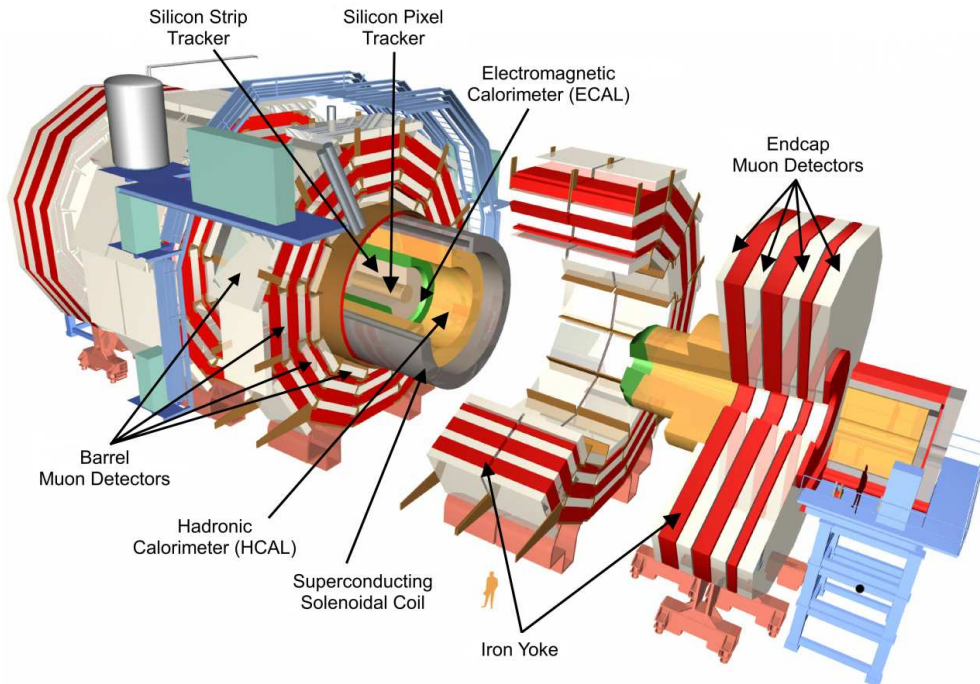
Figure 2.3.: Overview of the CMS detector.

tracking system and calorimetry inside. Good charged-particle momentum resolution and reconstruction are achieved by the all-silicon inner tracking system which also includes pixel detectors enabling efficient triggering as well as τ and b-tagging.

The electromagnetic calorimeter (ECAL) consists of lead tungstate crystals with a coverage of pseudorapidities up to $|\eta| < 3$. It allows for a precise measurement of diphoton and dielectron masses over a wide solid angle, π^0 identification as well as efficient photon and lepton isolation at high luminosities.

The ECAL is surrounded by the hadron calorimeter which was designed to have a good missing-transverse-energy and dijet-mass resolution, requiring hermetic coverage of the hadron calorimeter with a fine lateral segmentation.

Figure 2.4 shows a segment of the CMS detector with the paths of different particles in the magnetic field and their interactions with the different detector components.

The CMS detector had been ready for data-taking before the crash in 2008 and the time of the LHC repairs and upgrade was used to calibrate and align the muon and tracking system by using cosmic muons to a high precision [115]. When data taking started with the first collisions in 2009, the full detector proved to be extremely well calibrated and ready for data taking.
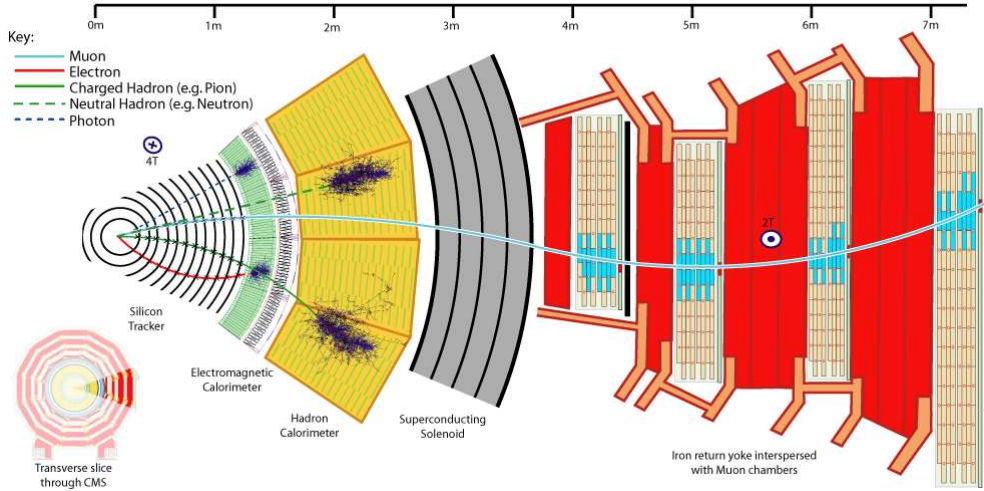
Figure 2.4.: Segment of the CMS detector in the r-ϕ plane.

2.2.1. Coordinate Conventions

The coordinate system of the CMS experiment has its origin in the center of the detector at the primary interaction point. The x-axis points radially towards the center of the LHC ring, the y-axis points vertically upwards. The z-axis is parallel to the beam line with the positive direction pointing towards the Jura mountains. The azimuthal angle ϕ is measured from the x-axis in the $x - y$ plane, the polar angle θ is measured from the $z-$axis. As in hadron collisions the center-of-mass system is not neccesarily at rest in the lab frame, particle physics relies on the rapidity instead, which is a Lorentz invariant quantity. It is defined as

$$ y = \frac{1}{2} \ln \left(\frac{E + p_z}{E - p_z} \right) \ . \tag{2.2} $$

For massless particles the rapidity equals the easier to calculate pseudorapidity η given by

$$ \eta = - \ln \left(\tan \frac{\theta}{2} \right) \ . \tag{2.3} $$

As the center-of-mass in a collision is usually not at rest, with some of the outgoing particles going in the forward direction where they cannot be detected, it is not possible to exploit overall momentum conservation. It is however possible to measure the amount of activity transverse to the beam, which must be conserved as well and can be measured quite precisely. Therefore, the transverse momentum p_{T} which is defined as $p_{\mathrm{T}}^2 = p_x^2 + p_y^2$ is used to characterize the momentum of a measured object. The angular distance between two particles observed from the origin of the coordinate system is $\Delta R = \sqrt{(\Delta\phi)^2 + (\Delta\eta)^2}$.

2.2.2. Superconducting Solenoid

The superconducting solenoid for CMS provides a 3.8 T field in a cylinder of 6 m diameter and a length of 12.5 m. The flux is returned through a 10000 t return yoke consisting of 5 wheels and 2 endcaps.

The solenoid consists of 4 layers of winding and has a cold mass of 220 t. At 3.8 T, the magnet will have a stored energy of 2.6 GJ. Due to the high ratio between stored energy and cold mass (11.6 kJ/kg) a large mechanical deformation of about 0.15% occurs when energized. The winding of the coil consists of a stabilized reinforced NbTi conductor.

The return yoke consists of 11 large elements, 5 barrel wheels and 6 endcap disks. The wheels consist of 4 concentrical layers of steel, enabling the integration of the muon system inside the return yoke.

2.2.3. The Pixel Detector and Tracking System

At the center of the detector lies the inner tracking system [116]. It is designed to measure the trajectories of charged particles emerging from the interaction point as well as to provide a precise reconstruction of secondary vertices from the decay of short-lived particles. The trajectories or *tracks* are reconstructed from the hits of the particles in several layers of silicon detectors.

Once the LHC is operated at its design luminosity of 10^{-24} cm^{-2} s^{-1} and energy of 14 TeV there will be about twenty collisions with a total of $\mathcal{O}(1000)$ particles per bunch crossing, i.e. every 25 ns. This intense particle flux is challenging for a fast and precise reconstruction of the tracks and their attribution to the correct bunch crossing. These features imply a high power density of the on-detector electronics which therefore require efficient cooling. In order to avoid multiple scattering, bremsstrahlung, photon conversion and nuclear interactions as much as possible, the tracking system should keep to the minimum of the material used to reduce these interactions. On the other hand the system needs to be cooled, resulting in additional hardware in the inner tracking region, so a compromise between the two demands needs to be found.

In addition, the tracker must be able to withstand the strong radiation without damage and remain operational for the expected LHC lifetime of about ten years. With the all-silicon approach employed by the CMS experiment it is possible to combine radiation hardness, fine granularity and fast response in the tracker component.

The tracking system has a cylindric shape with a total length of 5.8 m and a diameter of 2.5 m surrounding the interaction point. It is placed completely in the homogeneous magnetic field of the solenoid, providing an excellent resolution. The tracking system consists of about 198 m^2 of active silicon material with an acceptance up to a pseudorapidity of $|\eta| < 2.5$.

A schematic overview over the inner tracking system is given in Figure 2.5. It consists of two components, a silicon pixel detector in the center, surrounded by
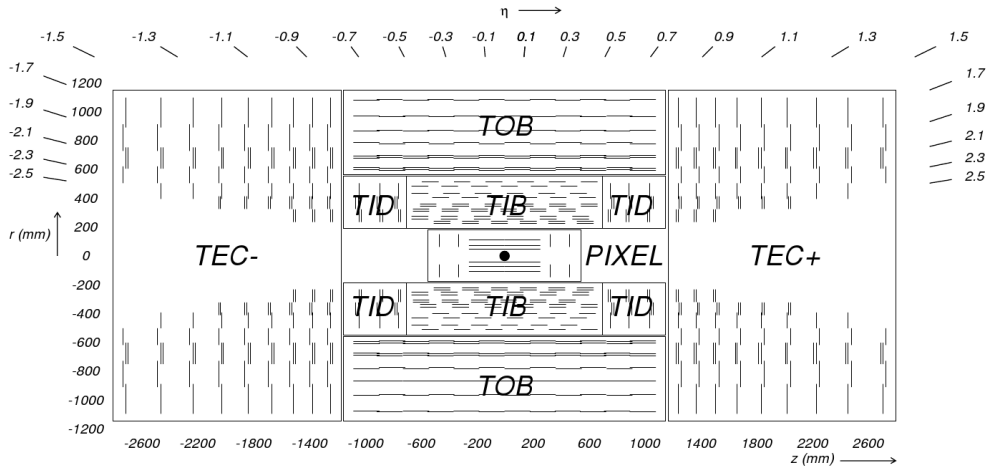
Figure 2.5.: Overview of the inner tracking system.

a silicon strip detector.

Silicon Pixel Detector

The silicon pixel detector is the inner part of the tracking system, closest to the interaction point. It consists of three barrel layers with a cell size of $100 \times 150 \ \mu m^2$ in r-ϕ and z respectively as well as two endcap disks. The cylindric layers are arranged concentric around the beam pipe at radii of 4.4 cm, 7.3 cm and 10.2 cm. The endcap disks with a radial size of ≈ 6 to 15 cm are placed on each side of the barrel layers at $z \pm 34.5$ and $z \pm 46.5$ cm.

The pixel detector delivers three high precision space points on almost each charged particle trajectory in the covered pseudo rapidity range of $-2.5 < \eta < 2.5$. In total the pixel detector covers an area of about 1 m^2 and has 66 million pixels. It provides a small impact parameter resolution which is important for a good secondary vertex reconstruction. The fine granularity in r-ϕ and z makes a three dimensional secondary vertex reconstruction possible. The pixel system has a zero-suppressed read out scheme with analog pulse height read-out. This yields an improvement for the position reconstruction through charge sharing and also helps to separate signal and noise hits. The modules on the endcap disks are positioned in a turbine-like geometry to enhance charge sharing.

Silicon Strip Detector

The silicon strip detector, also denoted *tracker*, consists of single sided p-on-n type silicon micro-strip sensors. It occupies the radial region between 20 cm and 116 cm and is divided in three different subsystems.

The Tracker Inner Barrel and Disks (TIB/TID) is placed directly around the silicon pixel detector. It consists of four barrel layers and three disks at each end and extends in radius towards 55 cm. It can deliver up to four r-ϕ measurements

on a trajectory with a single point resolution between 23 μm and 35 μm.

The TIB/TID is surrounded by the Tracker Outer Barrel (TOB). It consists of six barrel layers up to a radius of 116 cm and extends in z between ± 118 cm, the same length as TIB and TID together. The TOB can provide up to six additional r-ϕ measurements with a single point resolution between 35 μm and 53 μm.

Beyond the z range of the TOB lie the Tracker EndCaps (TEC+ and TEC-, the sign indicates the orientation along the z axis). They cover the range of 124 cm $< |z| <$ 282 cm and 22 cm $< r <$ 113.5 cm. Each TEC consists of nine disks, each carrying up to seven rings of detectors providing up to nine ϕ measurements per track.

The typical cell size in the Tracker is about 10 cm $\times$ 80 μm for the intermediate range of 20 cm $< r <$ 55 cm and 25 cm $\times$ 180 μm for the outer region where 55 cm $< r <$ 110 cm. This increased length leads to a higher strip capacity and therefore an increased electronic noise. To keep a good signal to noise ratio well above 10, the outer cells are thicker than the ones in the inner detector.

This overall Tracker layout ensures that at least ≈ 9 hits will be detected for a track anywhere in the range of $|\eta| < 2.4$ with at least 4 of them being two-dimensional measurements.

2.2.4. The Electromagnetic Calorimeter

Electrons, positrons and photons passing through matter interact with the material through bremsstrahlung and pair production, creating in turn new photons and electron-positron pairs. For high energetic initial particles, the newly created particles in turn can interact with the material and produce even more particles and so on, yielding an *electromagnetic shower*, a cascade of photons, electrons and positrons. Via Compton scattering and the photoelectric effect, these particles can interact with the electrons in the detector material and deposit their energy in the calorimetry system.

The electromagnetic calorimeter (ECAL) in CMS is a hermetic homogeneous calorimeter consisting of a barrel part and two endcaps. The barrel part consist of $61,200$ lead tungstate (PBWO$_4$) crystals whereas each endcap is made of 7324 crystals. A schematic overview of the ECAL is given in Fig. 2.6. The use of high density crystals allows for a fast and radiation resistant calorimeter with fine granularity. One of the driving criteria in the design was the capability to detect the decay of the Higgs boson into two photons which requires a very precise spatial and energy resolution.

Lead tungstate has a high density (8.28 g/cm^3), short radiation length ($X_0 = 0.98$ cm) and small Molière radius (2.2 cm). With these characteristics it is possible to construct a compact calorimeter with a fine granularity. The scintillation decay time of these production crystals is of the same order of magnitude as the LHC bunch crossing time, about 80% of the light is emitted in 25 ns.

The barrel region of the ECAL (EB) extends over the pseudorapidity range $|\eta| < 1.479$. It has a 360-fold granularity in ϕ and a $(2 \times 85)-$fold one in η. The
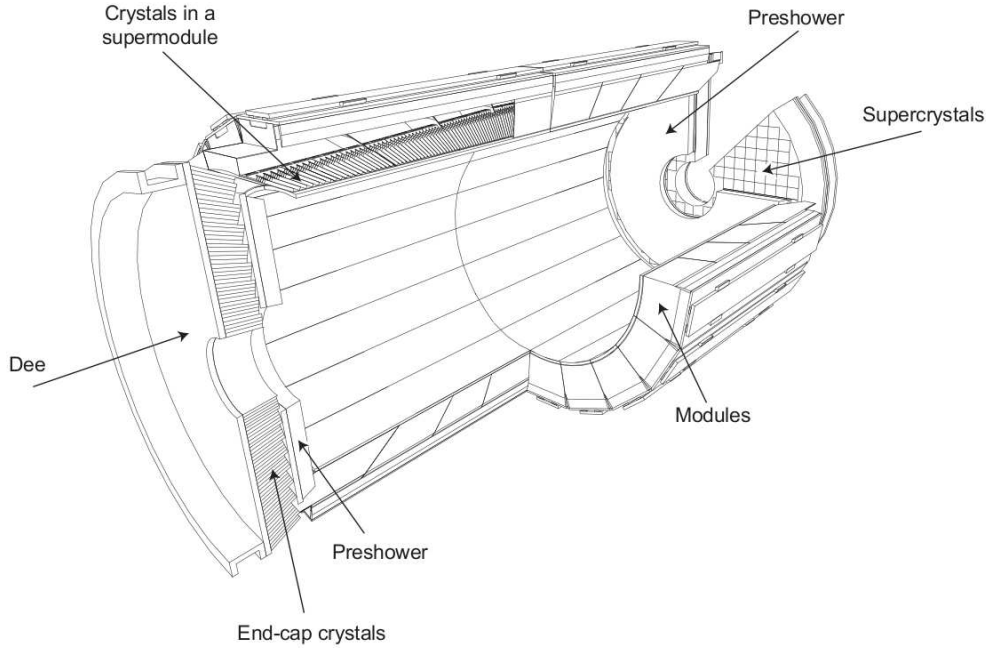
Figure 2.6.: Overview of the electromagnetic calorimeter.

crystals have a tapered shape, slightly varying with their position in η. The crystal cross section corresponds to approximately 0.0174×0.0174 in η-ϕ corresponding to 22×22 mm^2 at the front face and 26×26 mm^2 at the rear face. The crystal length is 230 mm, corresponding to $25.8 \cdot X_0$. The crystal alignment follows a quasi-projective geometry so that their axes yield small angles with respect to the vector from the nominal interaction vertex. An overview over the structure of the electromagnetic calorimeter is given in Fig. 2.6.

The endcaps (EE) cover the pseudorapidity range $1.479 < |\eta| < 3.0$. Each endcap is divided into two halves, the so-called *Dees*. The crystals in the EE are arranged in a rectangular grid in the x-y-plane and have a front face cross section of 28.62×28.62 mm^2 and a rear face cross section of 30×30 mm^2. Their length is 220 mm, corresponding to $24.7 \cdot X_0$.

For the actual detection of the electromagnetic shower, photodetectors are used. They need to be fast, radiation tolerant and must be able to operate in the 3.8 T magnetic field. Due to the small light yield of the crystals, an amplification of the emitted light is required, in addition the readout should be insensitive to particles traversing the crystals. The different magnetic field and different level of radiation in the EB and the EE suggested the usage two different approaches for the photodetectors. In the barrel part avalanche photodiodes are used whereas vacuum phototriodes are employed in the endcaps.

In addition to the endcaps, the Preshower detector is installed in the forward region of the ECAL, covering pseudorapidities of $1.653 < |\eta| < 2.6$. Its aim is to identify neutral pions in the endcaps and helps in the identification of electrons

against minimum ionizing particles. The Preshower detector consists of two layers, lead radiators that initiate electromagnetic showers from incoming photons and electrons with silicon strip sensors placed behind each radiator to measure the deposited energy and the transverse shower profile. The Preshower is 20 cm thick with radiation lengths of $2 \cdot X_0$ respectively $1 \cdot X_0$ for the two planes. This means, that 95% of the single incident photons start showering before the second sensor plane. Each silicon sensor measures 63×63 mm^2 and the whole Preshower detector needs to be aligned very precisely with the endcaps to get an accurate combined measurement and use this information for triggering.

2.2.5. The Hadronic Calorimeter

Hadrons are much heavier than electrons and therefore pass through the electromagnetic calorimeter without much interaction. The exact reconstruction of hadron jets is crucial for many searches at the LHC as well as the reconstruction of apparent missing transverse energy associated with neutrinos or exotic particles.
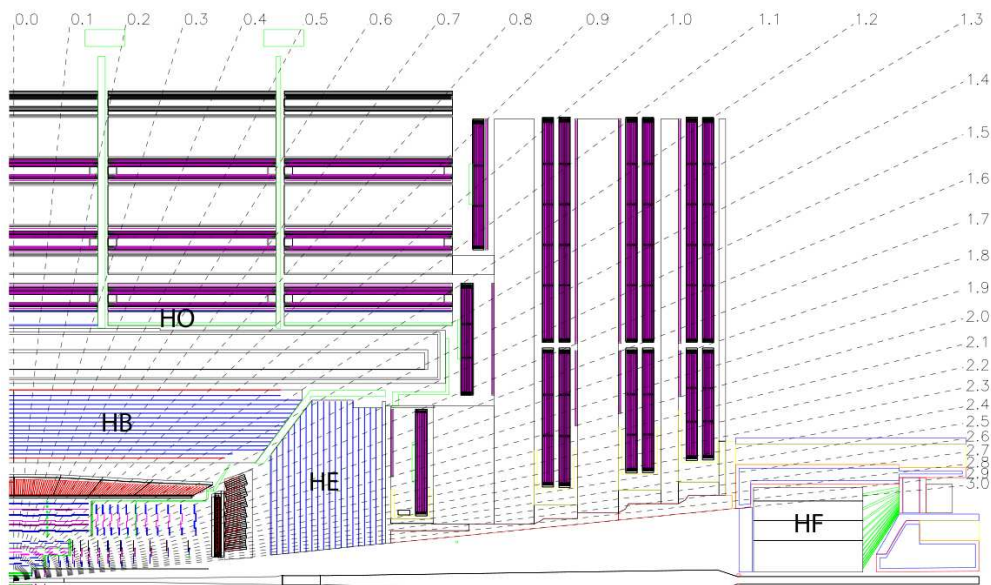
Figure 2.7.: Overview of the hadronic calorimeter and its position with respect to the muon system.

Fig. 2.7 shows the position of the hadronic calorimeter (HCAL) in a longitudinal view of the CMS detector. The HCAL barrel and endcaps are located outside the tracker and electromagnetic calorimeter system. The complete hadronic calorimeter consists of the Hadron Barrel (HB) and Hadron Outer (HO) parts in the central region, two endcaps (HE) and two forward (HF) calorimeters close to the beam pipe outside the muon system.

The Hadron Barrel calorimeter covers a pseudorapidity range $|\eta| < 1.3$ and is composed of 36 identical azimuthal wedges. These wedges are constructed from

flat brass absorber plates aligned parallel to the beam axis, the innermost and outermost plates are made of stainless steel to increase the structural strength. Each wedge in turn is segmented into four azimuthal angle sectors. Between the brass plates are layers of plastic scintillator, divided into 16 η sectors, resulting in a segmentation of 0.087×0.087 in the η-ϕ plane. The absorber consists of a 40 mm thick steel plate in the front, followed by eight 50.5 mm-thick and six 65.5 mm-thick brass plates and one 75 mm thick steel back plate. In between these absorber layers are 3.7 mm thick plastic scintillators. The read-out in the barrel calorimeter is done by using hybrid photodiodes. Due to the fact that the HB is limited in its radial extension between the outer extent of the electromagnetic calorimeter at $r = 1.77$ m and the inner radius of the magnet coil at $r = 2.95$ m, an additional *tail catcher*, the Hadronic Outer calorimeter is placed outside the solenoid to complement the HB.

The endcaps cover a pseudorapidity range of $1.3 < \eta < 3$, which corresponds to 13.2% of the solid angle, a region containing about 34% of the particles produced in the final state. The radiation level at full LHC luminosity is very large for the forward rapidity regions and amounts to about 100 kGy after 10 years of operation. To withstand the large radiation level as well as cope with the high counting rates and fulfill the mechanical requirements C26000 cartridge brass was chosen as the material for the calorimeter. The design of the absorber follows that of the barrel, here 79 mm thick brass plates are intersected with 9 mm gaps for the scintillators. The overall geometrical design was driven by the need to minimize the cracks between HB and HE rather than by optimizing for single-particle energy resolution, since the resolution of jets in the HE will be limited by pile-up and magnetic field effects anyway. The granularity of the scintillator cells in the η-ϕ-plane is 0.087×0.087 for $|\eta| < 1.6$ and about 1.7×1.7 for $|\eta| \geqslant 1.6$. The photodetectors used in the endcaps are multipixel hybrid photodiodes (HPDs) since they have a low sensitivity to magnetic fields and a large dynamic range.

In the central rapidity region, the combined stopping power of EB and HB does not provide sufficient containment for hadron showers. In order to gain an adequate sampling depth for this region, the Hadron Outer calorimeter (HO) extends the calorimeter outside the solenoid. The solenoid is used as an additional absorber equal to $1.4/\sin\theta$ interaction lengths thus its purpose is to identify late starting showers and to measure the shower energy deposited after HB. The design of the HO follows the design of the return yoke, which consists of five rings with a length of 2.536 m. Since the absorbing material is very small in the central rapidity region, the central ring of the HO consists of two layers of scintillators on either side of a 19.5 cm thick piece of iron, at radial distance of 3.82 cm and 4.07 cm, respectively. The other rings have each one scintillating layer at a radial distance of 4.07 m. The HO is limited by the structures needed to stabilize the return yoke and muon system as well as the cryogenic "chimneys" needed for the cooling system. The sizes and positions of the tiles in the HO are supposed to follow the layers of the HB to make towers of a granularity of 0.087×0.087 in the η-ϕ plane.

The effect of shower leakage has a direct consequence on the measurement of missing transverse energy. It has been show from detector simulations that the inclusion of the HO yields a much more precise reconstruction of high energetic jets and therefore better understanding of the missing transverse energy.

The Hadron Forward calorimeters (HF) cover the rapidity region of $3 < |\eta| < 5.2$. They are located at $z = \pm 11.2$ m from the interaction point. On average, 760 GeV per proton-proton interaction at design energy will be deposited into the two forward calorimeters, peaking at highest rapidities. At $|\eta| = 5$ the HF will experience around 10 MGy after an integrated luminosity of $5 \cdot 10^5$ pb^{-1}. This presents a considerable challenge to the calorimeter and the HF was constructed with the foremost aim to survive in this high radiation environment for at least one decade. Each HF is essentially a cylindrical steel structure with an outer radius of 130 cm. It consists of 5 mm thick grooved plates with quartz fibers inserted into these groves as detecting material. The quartz fibers consist of a fused-silica core and a polymer hard-cladding. The detector is divided into two longitudinal segments. Half of the fibers extend over the full depth of the absorber, 165 cm which corresponds to approximately $10 \cdot \lambda_I$. The other half starts at a depth of 22 cm from the front end of the detector. This separation allows to distinguish between showers stemming from electrons and photons from those stemming from hadrons.

2.2.6. The Muon Detector

Muon detection is a very powerful tool for separating interesting processes from the large background at the LHC. Muons can be detected relatively easy and they are less affected than electrons by radiative losses in the tracker material.

As the name of the detector already suggests, a robust muon measurement with a wide angular coverage was a central theme from the earliest design stages of the CMS experiment. The muon system has three functions: muon identification, the measurement of their momentum and event triggering [119].

The shape of the CMS muon system was driven by the necessity to integrate it into the return yoke of the solenoid magnet, therefore it consists of a cylindrical barrel section and two planar endcaps. The overall active detection plane extends over roughly $25,000$ m^2.

The barrel covers a pseudorapidity region $|\eta| < 1.2$. Here the neutron-induced background is small, the muon rate is low and the magnetic field is uniform due to its containment in the steel return yoke. The return yoke consists of five layers of steel and the four stations of drift tube (DT) chambers used for muon detection in the barrel region are interspersed among these plates. The innermost three stations each contain 8 chambers, the first half measure the muon coordinate in the r-ϕ plane, the second half measure the z direction. The outermost station does not contain the z-measuring chambers. The number of chambers and their orientation were chosen to provide a good efficiency for combining muon hits into one single muon track and in order to provide an excellent time resolution for

bunch crossing identification.

The endcap regions in the muon system cover a pseudorapidity region $0.9 < |\eta| < 2.4$. Here the detection suffers from higher muon rates, higher backgrounds and a large, non-uniform magnetic field. In order to provide a good measurement with fast response time, fine segmentation and radiation resistance, the endcaps use cathode strip chambers (CSC). There are four stations of CSCs in each endcap, the chambers are positioned perpendicular to the beam axis and positioned between the flux return plates of the magnet. The cathode strips in each CSC run radially outward to provide a measurement of the r-ϕ bending plane, the anode wires run approximately perpendicular to the anodes and are read out to obtain a measurement of the η component and beam-crossing time of a muon.

Due to the overlap between barrel and endcaps, the muon system covers the full pseudorapidity region $|\eta| < 2.4$ without acceptance gaps. Thus, muon identification is ensured over a range corresponding to $10° < \theta < 170°$. The reconstruction efficiency is typically $95 - 99\%$ except for $|\eta| = 0.25, 0.8$, corresponding to the regions between two wheels, and $|\eta| = 1.2$, the transition between the barrel and the endcaps.

Both, DT and CSC subsystems can trigger on the transverse momentum (p_{T}) of muons with good efficiency and high background rejection. Due to the uncertainty on the eventual background at full LHC energy and luminosity, an additional, independent trigger system was implemented. This system consists of resistive plate chambers (RPC) and is installed in both, the barrel as well as the endcap regions. The RPCs provide a fast, highly-segmented trigger with a sharp p_{T} threshold over a large region $|\eta| < 1.6$. They are double-gap chambers that are operated in avalanche mode ensuring good operation at high rates. They provide a fast response with a good time resolution but a coarser spatial resolution as the other detection systems used.

In total, six layers of RPCs are embedded in the barrel muon system, two in each of the innermost two stations and one in each of the last two stations. The doubling in the innermost layers allows triggering of low-p_{T} muons that stop before reaching the outer layers. In the endcaps, each of the first three stations contains a plane of RPCs.

The muon system was tested and calibrated in combination with the inner tracking system to a high precision using cosmic muons in the CRUZET and CRAFT runs which took place before the scheduled start of the LHC in 2008 and especially during the repair phase after the incident in 2009.

2.2.7. The Forward Detectors

To study phenomena in the very forward region additional detector systems are in place. One is the Centauro And STrange Object Research (CASTOR) detector, designed to cover a pseudorapidity range $5.2 < \eta < 6.6$. It is located at 14.38 m from the interaction vertex, its position with respect to the other subsystems can be seen in Fig. 2.8. The detector consists of quartz-tungsten crystals and therefore
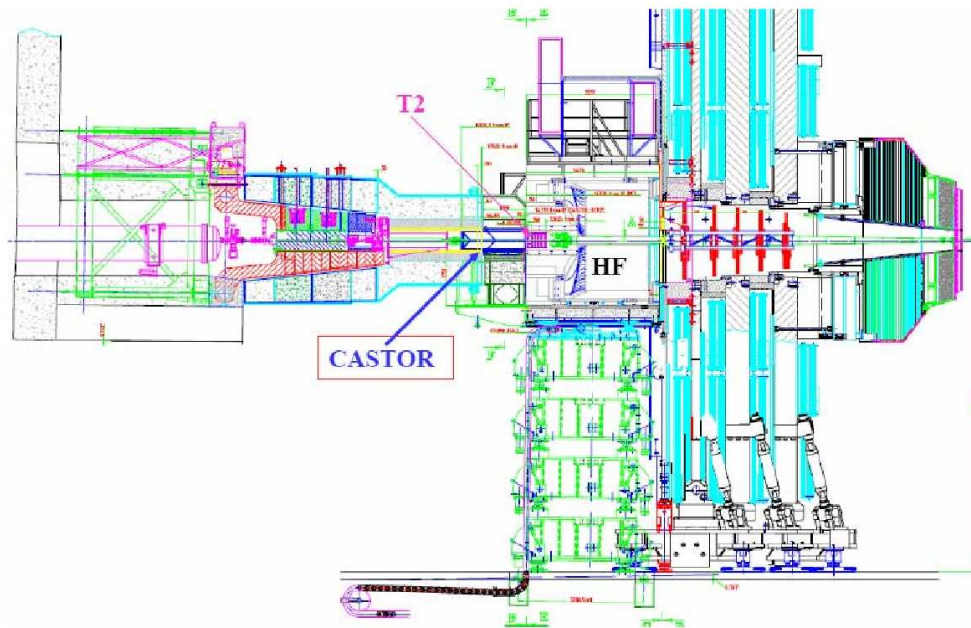
Figure 2.8.: Position of the CASTOR calorimeter.

has a fast response, compact detector dimension and high radiation hardness, all features needed in the very forward region. The layers of tungsten and silica quartz have a thickness of 5.0 mm and 2.0 mm respectively for the front part, designed to measure electromagnetic cascades and 10.0 mm and 5.0 mm respectively for the back part, designed to measure hadronic cascades. The plates are inclined 45° with respect to the beam axis in order to maximize the Cherenkov light output. While CASTOR does not have any granularity in pseudorapidity and only a twelve-fold granularity in ϕ, it still does provide a good resolution over the longitudinal length of the shower, allowing for an observation of the time-dependence of the shower.

To study even higher rapidity ranges, the Zero Degree Calorimeter (ZDC) covering $|\eta| \geqslant 8.3$ have been proposed. They will be located between the two LHC beam pipes at approximately 140 m on each side of the CMS interaction point and will give more detailed insight into diffractive events in proton-proton collisions as well as heavy ion studies. However, the ZDC have not been installed yet.

2.2.8. Trigger and Data Acquisition

At the nominal luminosity, collisions take place at a frequency of 40 MHz, i.e. one every 25 ns. Since every event has a size of ≈ 1.5 MB, the total flux of data would amount up to 60 TB/s. It is not feasible to process, and above all, store this amount of data taking currently available network and storage technologies into account.

To reduce the amount of data to a manageable size, a two level trigger system is used by CMS [120]. A schematic overview of this system can be found in Fig. 2.9.

The Level-1 (L1) trigger relies on onboard electronics and aims at a fast rejection
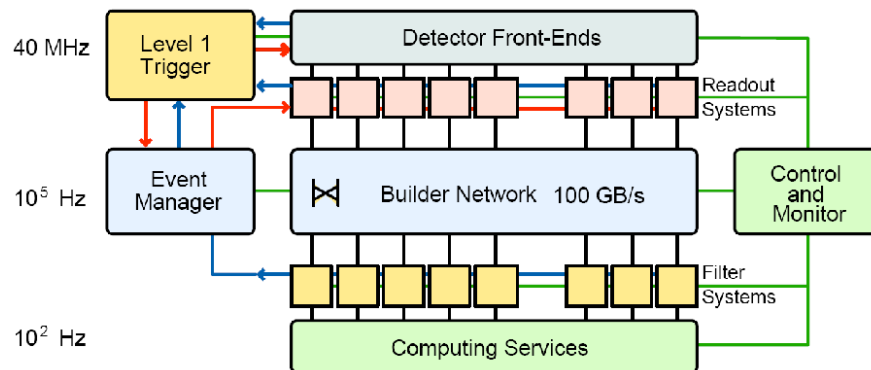
Figure 2.9.: Overview of the CMS trigger system.

of events, whereas the high level trigger (HLT) [121] investigates reconstructed events that have passed the L1. This data reduction has been carefully designed to avoid a biased selection. Since the triggering it is an inherent selection procedure for every physics analysis, this is a crucial point regarding the requirements for the trigger thresholds.

The L1 reduces the event rate from 40 MHz to 100 kHz. It was designed to decide within 3 μs whether to reject or keep an event. In order to achieve this goal, the trigger was implemented in custom hardware directly built into the detector, close to the corresponding read-out channels.

The decision is based on data from the calorimeter and the muon system. Bucket-brigade circuits are used to cache information from the inner parts of the detector to allow potential muons to traverse the detector and trigger the decision to pass the event on to the HLT. The calorimetric information is evaluated locally and then passed on to the Global Calorimetric Trigger, which calculates jets and checks for electron and photon candidates. The Global Muon Trigger processes information from the three kinds of muon chambers in which already proto-tracks are reconstructed. A proto-track is the combination of several hits in the muon system into one possible trajectory of a particle moving though the detector. The combined information is then passed to the Global Trigger, uses the low level information to to calculate composite objects such as jet multiplicities and missing transverse energy.

Once accepted by the Level-1 trigger, the events are filtered through the HLT system. It consists of a farm of about a thousand commercial processors and has access to the information coming from the whole detector. As it is completely software based, it is very flexible to be adjusted to different running conditions of the detector. The time spent for the analysis of one single event is of the order of one second. Each processor runs the same HLT software code to reduce the Level-1 output rate of 100 kHz to 150-200 Hz. All raw data is transferred to the main CERN computing center and will be kept for the whole running time of the experiment.

In conclusion, CMS faces challenges not only in terms of the physics programme, detector operation and maintenance, but also in terms of the acquired data volume and the computing infrastructure required to process it. Datasets and resource requirements are at least an order of magnitude larger than in previous experiments.

Chapter 3

Programs

The analysis of LHC events relies crucially on the predictions of Monte Carlo event generators. There are on the one hand matrix element generators, incorporating the theories under investigation. On the other hand there are event generators for showering and hadronization, that simulate the transition from the parton level information of the matrix element to a measurable final state.

In addition, there is a multitude of algorithms needed for reconstruction and analysis of data as well as helping with the simulation itself.

This chapter describes the tools used in this work.

3.1. Matrix element generators

For the simulation of matrix elements, various generators are available. There are generators for tree level predictions as well as generators incorporating next-to-leading order calculations.

The Program `vbfnlo`

`vbfnlo` [122] is a fully flexible partonic Monte Carlo program for vector boson fusion, double and triple vector boson production processes at NLO QCD accuracy. In case of the vector boson fusion process the NLO electroweak contributions are available as well. Additionally, the program provides the simulation of CP-even and CP-odd Higgs boson production in gluon fusion associated with two jets at leading order QCD with the full top- and bottom-quark dependence in a two-Higgs-doublet model. Several models for anomalous couplings of Higgs and vector bosons are implemented as well as a Warped Higgsless extra dimension model.

The amplitudes are calculated by means of helicity amplitudes using HELAS [123]. The Monte Carlo integration and stratified sampling is done with a modified version of VEGAS [124] using an optimized phasespace for up to seven final state particles. Arbitrary cuts can be specified as well as various scale choices, both

fixed or dynamical renormalization and factorization scales are available. Any currently available parton distribution function set can be used through the LHAPDF library [51]. For processes implemented at leading order, the program is capable of generating event files in the Les Houches Accord (LHA) format, described in Sec. 3.3.2. In the phase space regions which are accessible at hadron colliders, VBF reactions are dominated by t-channel electroweak gauge boson exchange. Therefore, s-channel exchange contributions and kinematically suppressed fermion interference contributions [125, 126] are disregarded within `vbfnlo`. The subsequent decay of the Higgs boson is simulated either including width effects or by using the narrow width approximation. For the decay into two leptons, full width effects are available, for the $H \to W^+W^-$ and the $H \to ZZ$ modes, full off-shell effects and spin correlations of the decay leptons are included. Details of the calculation can be found in [34]. ¡

MadGraph/MadEvent

MADEVENT [127] is a program suite to calculate tree level matrix elements automatically. At its core, it uses MADGRAPH II which finds all contributing Feynman graphs for a given initial and final state together with the desired number of different couplings. In addition, it is also possible to require certain intermediate particles or to exclude such explicitly.

After MADGRAPH has found all contributing graphs to the specified process, the code needed to calculate the matrix elements is generated. This is done by using the HELAS subroutines employing helicity amplitudes.

The generated code then can be used to simulate events. MADEVENT can perform the full matrix element calculation using the code created with MADGRAPH and using VEGAS to perform the phase-space integration. The simulation can either just calculate the cross section using specified cuts or produce event samples in Les Houches event files. It is possible to use parton distribution functions provided by the LHAPDF library.

MADEVENT allows to easily compare different physics scenarios, from the Standard Model to various new physics scenarios. These are stored as "models", which provide the particles and their couplings for the matrix element creation. A special case is the "`heft`" model. It incorporates an effective field theory for the coupling $gg \to H$ which in the standard model only is possible through a heavy quark loop. It is however possible to calculate an effective coupling in the limit $m_t \to \infty$. The `heft` model is an implementation of this effective field theory thereby allowing for the generation of the most important Higgs production process at the LHC.

In addition, MADEVENT contains many other tools. MADANALYSIS can be used to generate distributions based on matrix elements in the generated Les Houches files with arbitrary cuts. It is further possible to manipulate the information in the event files, by decaying heavy resonances or adding different decay channels to already existing ones.

There is a direct interface to PYTHIA 6 which automatically transfers the matrix

element information to obtain hadron level events. These can in addition enter a parameterized detector simulation which can give an estimate of the finite detector resolution on the generated final state.

The program can be used on a local desktop computer, on a batch farm or using several CPU cores at once. In addition, also a web interface for process generation and, to a smaller extent, even online event generation is available.

The latest development includes a rewrite of MADGRAPH using the python programming language making use of many modern optimizations which allows a much faster process generation.

3.1.1. MCFM

MCFM [128], Monte Carlo for FeMtobarn processes, is a parton-level Monte Carlo program for next-to-leading order predictions for a wide range of different processes at hadron colliders.

Among the implemented processes are the production of vector bosons in association with jets, vector boson pair production in various scenarios, different Higgs production channels and top quark pair and single top production.

MCFM allows for a wide variety in the choice of the input parameters, be it the definition of the electroweak coupling or scale choices. It is possible to use built-in PDF sets or link against the LHAPDF library to be able to use any of the PDF sets available within.

The program is not only able to calculate cross sections including various cuts but also can yield histograms for any observable. In addition, it can provide weighted n-tuples containing the four-vector information of the outgoing particles in the event. It is also possible to get an unweighted n-tuple output, however this is extremely limited and inefficient.

3.2. Showering and Hadronization generators

There are several different implementations of parton shower and hadronization models. In addition, the matching of higher order matrix elements and parton showers is incorporated in special programs.

3.2.1. PYTHIA

`PYTHIA 6.4` [129] is a multi-purpose showering and hadronization Monte Carlo event generator. It is written in `FORTRAN` and includes a huge variety of physics processes and phenomenological models. The code provides a huge list of matrix element calculations for both standard model and new physics scenarios. In addition, matrix elements from external generators using Les Houches event files can be processed, see Sec. 3.3.2.

There are two possibilities for the simulation of initial- and final-state radiation. One implementation is based on a virtuality (Q^2) ordered DGLAP evolution and a newer one is based on ordering in transverse momentum (p_T). The latter was introduced to yield harder jets in the final state, as events generated with the virtuality ordered shower tended to have too soft hadronic activity.

The hadronization is modeled by the Lund string model, indeed the `JETSET` program which contained the original implementation of this model was merged together with `PYTHIA`, which at that time only implemented QCD matrix elements.

`PYTHIA` offers three choices for the description of the underlying event, depending on the chosen parton shower evolution. The 'old model' is the first implementation of the multiparton interactions in `PYTHIA` and to be used in conjunction with the virtuality ordered shower.

The 'intermediate model' was introduced to give a more sophisticated description of correlations in flavor, color, longitudinal and transverse momentum between the beam remnants and the external partons of the hard process that initiate the shower. This model uses the virtuality ordered shower as well and allows for individual showering of each scatterer present in the interaction, which was not possible with the old model.

The 'new model' combines the improvements introduced in the intermediate model with the p_T ordered parton shower. The multiple interactions, which are also ordered in transverse momentum are interleaved with the parton shower evolution yielding an overall ordering of emissions from shower and multiple interactions.

`PYTHIA` also provides a variety of analysis routines which allow for the study of jet observables and event shapes.

There are efforts towards a complete reimplementation of `PYTHIA` using C++. A first attempt under the name of `Pythia 7` provided a generic framework for event generation but then was discontinued. The proof-of-concept framework was then developed further and renamed to `ThePEG`, "Toolkit for high-energy Physics Event Generation" [135]. Currently, a second attempt under the name of `Pythia 8` is under way which is supposed to replace the `FORTRAN` version in the near future.

3.2.2. The Program Herwig++

Herwig++ [130] is a general-purpose Monte Carlo event generator. It is the successor of the highly successful `HERWIG` event generator used during LEP/HERA and Tevatron [131].

New theoretical ideas for the LHC make major changes necessary but since the original event generator evolved into a large-scale programming process, this is rather difficult to attain. Therefore a new approach was made to redevelop the original program in the object-orientated programming language C++, using a more flexible structure to include current and future developments wherever possible.

The main features of Herwig++ include initial- and final-state QCD evolution using an angular-ordered parton shower with improved treatment of mass effects and Lorentz invariance properties. To accomplish this the parton shower used in `HERWIG` that uses the evolution variable

$$\tilde{q}^2 = \frac{p_{\mathrm{T}}^2}{z^2(1-z)^2} = \frac{q^2}{z(1-z)}$$

was changed to a shower algorithm based on quasi-collinear splitting introduced in [133]. This required new definitions of z and p_{T} [132] to obtain invariance under boosts along the jet direction and the evolution variable was changed to

$$\tilde{q}^2 = \frac{q^2 - m^2}{z(1-z)} = \frac{p_{\mathrm{T}}^2}{z^2(1-z)^2} + \frac{m_i^2}{z^2(1-z)} + \frac{m_j^2}{z(1-z)^2} + \frac{m^2}{z(1-z)} \,,$$

where m is the mass of the incoming parton and $m_{i,j}$ are the masses of the two outgoing ones.

This new shower algorithm aims especially for an evolution down to zero p_{T} radiation from massive particles, thus avoiding the 'dead-cone' and the overlap in the soft region of the 'final state + gluon' phase space that appeared in the shower used in the `FORTRAN` program. To avoid a 'dead' region of phase space not covered by the parton shower due to the choice of evolution variables, hard matrix element corrections are applied, thus taking the most important sub-leading higher-order corrections into account. Additionally the azimuthal angle φ is not chosen randomly but as a result of planned azimuthal spin correlations [134].

The hadronization in HERWIG++ is modeled by the cluster model based on non-perturbative gluon splitting that was described in section 1.5.2. This follows closely the implementation in the `FORTRAN` version, but with an improved algorithm for the cluster decay implemented to resolve known problems.

The description of the underlying event in HERWIG++ is based on an eikonal model for multiple partonic scatterings. The implementation is general so in addition to the soft interactions it is also possible to simulate double parton scattering where two or more hard interactions take place in the same proton-proton interaction. Alternatively, there also exists an implementation of the UA5 parameterization for the underlying event which can be used as an alternative to the eikonal model.

HERWIG++ also provides a sophisticated model of hadron and tau decays using matrix elements to determine the momenta of the decay products for many decay modes including a detailed treatment of spin correlations and off-shell effects.

HERWIG++ is based on `ThePEG` [135], a toolkit for implementing physics models of event generation. `ThePEG` provides a general structure of event generation in terms of abstract base classes for the different tasks appearing in the simulation of an event. The implementation of different models is then done by creating classes that inherit from the respective base classes and implementing sets of pre-defined virtual functions.

ThePEG is organized as a repository for the various C++ libraries with the implementations of the individual models. To use the program, the needed libraries are loaded and configured via special commands.

3.2.3. POWHEG

POWHEG BOX [136] is a framework for implementing NLO calculations in shower Monte Carlo programs according to the POWHEG method, see Sec. 1.4.5. It incorporates a library where the included processes are made available to the users. It can be interfaced with Monte Carlo programs that are able to process Les Houches event files, see 3.3.2.

The event generation works in two steps, first the NLO calculation at parton level is performed where the cross section is calculated and the kinematics of the particles involved in the hard process are written into a Les Houches file along with the information needed for matching. In a second step these Les Houches files are processed by programs linking against PYTHIA and HERWIG 6. These programs use one of these two showering generators to simulate full events from the parton level events in the Les Houches files while steering the parton shower according to the information on the hardest emission obtained from the matrix element calculation.

The currently implemented processes are vector-boson production including decay, vector boson production plus one jet including decay, single top production, Higgs production in gluon fusion and in vector boson fusion, jet pair production, heavy quark pair-production and W^+W^- plus dijet production.

3.3. Analysis software

For the reconstruction and analysis of LHC events special algorithms are needed. In addition, special data formats for transferring event information between different steps in the event simulation and analysis are required.

3.3.1. The Fastjet Package

FastJet [137] is an implementation for various jet algorithms. Its name stems from the fact that it was the first fast $(N \ln N, N^2)$ implementation of the longitudinally invariant k_T algorithm. The library is written in C++ and implements the k_T [138], inclusive Cambridge/Aachen [94] and anti-k_T [139] jet algorithms.

The package provides a class of Lorentz four-vectors which can be initialized with the momenta of the input objects of the jet algorithm, the protojets. This collection is then passed to the jet finding class which recombines the jets and provides their four-momenta in the same format as the input.

There is a wide range of various jet algorithms available as plug-ins, including MidPoint and SISCone cone algorithms, specific implementations used in experi-

ment as well as e^+e^- algorithms. In addition, it is possible to calculate jet areas by the introduction of ghost particles.

The jet finder class provides the complete reconstruction history thus allowing for subjet analysis. For this several external plug-ins are also available like filtering, trimming and pruning, see section 1.8.3.

3.3.2. Event Data Formats

An important task in the event simulation with Monte Carlo generators is the transfer of the results from one step to the following. There are several steps where this is important.

The first one is the transfer of matrix element information from a matrix element generator (MEG) into a showering and hadronization generator (SHG). For this, the Les Houches accord was defined.

The second step where information needs to be transferred is after showering and hadronization. The full output of the respective generator needs to be available for the detector simulation as well as for the analysis at hadron level. The HepMC event record was introduced to accomplish this.

In addition, the data associated with an event as measured in a collision needs to be stored along with information about the reconstruction and the conditions at the time of the data taking. For this, CMS utilizes the Event Data Model (EDM).

The Les Houches Accord

The events created in a MEG do not have physically measurable final states, since the output contains quarks and gluons which are not color singlet states. So in order to get a full event simulation, a second program has to be used, a SHG. To transfer the results from a matrix element generator, a specific file format is used that is defined in the Les Houches Accord [140, 141].

The communication between a MEG and a SHG like HERWIG++ occurs at several stages of a full event simulation.

First, at initialization basic parameters about the experiment and the calculation have to be transferred as well as information about the considered processes. Additionally, "meta information" needs to be conveyed, how to deal with the weights and information about the used MC, settings used in the creation and so on.

Then the data for every created event has to be transferred as well in order to provide the SHG with the information needed to perform the simulation of the shower and hadronization. This includes the parameters for the event like scales, the weight and the couplings as well as information about the particles at the matrix element level.

Normally, different parts of the SHG are used to read these informations, so there are two common blocks used for this. Their form is similar to the old `HEPEVT`

common blocks used to transfer information about SHG final states to detect or simulation or analysis programs. The `HEPRUP` block stores the run information needed at initialization such as center-of-mass energy, scales and cross sections, whereas the `HEPEUP` block stores the information about the individual events.

The information from the common blocks is stored as plain numbers in an ASCII file following a fully specified order. These common blocks are grouped by the use of XML [142] tags. A full description of the information in the common blocks and the file format can be found in Appendix B.

The HepMC Event Record

HepMC [143] was designed to provide a generic event record for high energy reactions. It is written in C++ and uses object orientation. The applications of the event record can be twofold. On the one hand, it serves as a "container class" for storing events after generation and handing them either into a dedicated analysis code or detector simulation. On the other hand, the event record can be used as a framework, for example when passing the output from one step in the simulation to a different tool to perform the next step. This is especially used for external decay packages like `tauola` [78] and `EvtGen` [86], which simulate the decay of τ leptons and B hadrons respectively, taking spin information and the large set of possible decay chains into account.

Usually, the particle content of a Monte Carlo generated event follows a tree-like structure. For each particle the "mother" from which it radiated or is a decay product and the "daughters" are known. The HepMC event record follows this by using a graph structure for the organization of the event data. The vertices of this graph stand for the steps where a change in the event occurred, for example a parton shower branching and has informations about the incoming and outgoing particles in this step. The particles themselves are represented by lines connecting their production vertex with their decay vertex.

All the information in the graph can be easily accessed via special iterators. Among the data stored are the four-momentum, flavor, charge, etc. of the particles in the event, in addition information about various flow patterns like color flow and spin density matrices can be included.

The Event Data Model (EDM)

The basic processing unit in the CMS software model is the event. It corresponds to a recorded bunch crossing or a simulated collision from Monte Carlo. Each "event" consists of a C++ object container that can hold both raw detector output, be it from a real collision or a simulated event. In addition, reconstructed physics objects and general information such as for instance the configuration of the software used to produce the data present in the event or the event number are stored. The event is passed from one step to the next during the data processing, where all or part of the objects accumulated in the events can be written to ROOT

files exploiting the tree technology. Furthermore, additional conditions have to be stored on an Interval-of-Validity (IOV) basis, like information on malfunctioning detector components or alignment constants. To access these informations, for example from databases, a special mechanism, the EventSetup system is used.

To increase transparency, several well defined configurations, called data-tiers, exist that contain events after a certain processing step:

RAW contains all detector readout information, including technical trigger bits and metadata. Typically, a RAW file has a size of about 2 MB per recorded event.

RECO contains reconstructed physics objects such as jets or muons obtained from single hits in the muon chambers. The detector information that was used to reconstruct these high-level objects is also available. Since much of the original RAW information is omitted, RECO files are only about one third of the size of RAW files per event.

AOD (Analysis Object Data) contain only minimal content required for particular analyses, obtained from RECO by applying filters. AOD are produced to fit the needs of the end user with special requirements concerning physics content. This results in smaller files of about 0.1 MB per event, which are easier to handle.

3.3.3. ROOT

ROOT [144] is an object oriented framework written in C++. It was designed to assist in the analysis and presentation of large amounts of data and is widely used in the high energy physics community. ROOT is a successor of the Physics Analysis Workstation (PAW) [145], that was written in FORTRAN.

The data in ROOT is defined as a set of objects, and specialized storage methods are available giving direct access to the separate attributes of the selected objects, without the need of processing all information in the data. ROOT includes histograming methods, curve fitting, function evaluation, minimization, graphics and visualization classes to allow the setup of an analysis system that can query and process the data interactively or in batch mode, as well as a general parallel processing framework, PROOF, aimed at providing a faster way to analyze large amounts of data.

There are four different ways in which ROOT can be used. First, as a standalone C++ program linking against the needed ROOT libraries, second using the built-in command line C++ interpreter, called CINT as well as a python interpreter, pyroot and finally an interactive way using a graphical interface.

The system can also benefit from large computing clusters or multi-core machines by using the parallelization approach PROOF.

3.3.4. CMSSW

The common software framework of the CMS collaboration is called CMSSW [146]. It has a highly modular structure based on the Event Data Model using a collection of software packages. CMSSW contains services taking care of calibration, simulation and detector alignment together with modules for the reconstruction. The architecture of CMSSW foresees one single executable, the same for the analysis of Monte Carlo and data samples or reconstruction and event visualization, called cmsRun. CMSSW contains many plug-in components that encapsulate units of precise event-processing functionalities in form of algorithms. The configuration files storing the steering parameters and running order for cmsRun are contained in a configuration file, interpreted at runtime and written in the Python programming language.

The typical work flow of analyzing an event starts from a source. This can either be a file with recorded CMS data as well as Monte Carlo events or on-the-fly generation of Monte Carlo events. Producers read the event content and process it to add physics objects to the event. Filter modules evaluate the properties of objects in the event and return a boolean value that can be used to stop the execution of the modules chain and skip to the next event. A defined output which can contain event information in either EDM or other formats is finally written to disk. Analyzers can be used to study the properties of an event and write some user specified output, e.g. a histogram.

Jet reconstruction in CMS

An important task in the reconstruction of events is the jet finding, as described in Sec. 1.8. In events, different kinds of objects can serve as inputs for the jet clustering algorithms. On Monte Carlo level, usually the four-vectors of all stable particles are clustered into jets, leading to "generator particle jets".

In a full event, the obvious choice for the jet constituents are energy deposits in the calorimeters. The position and energy content of the calorimeter towers is used to define the input objects for the algorithm, resulting in so-called "calorimeter jets". Calorimeter jets are especially robust as they rely only on low-level detector information.

A further possible input for jet algorithms are tracks as reconstructed by the tracking detector. Obviously this collection only contains information about charged particles and therefore these "track jets" do not contain the full energy of the event. However, since tracks do not suffer from response problems, track jets are well suited for precise measurements especially of low transverse momentum charged activity.

The excellent CMS tracking detector allows to introduce a new approach for jet finding, using reconstructed particles as input. Information from the tracking detector, the calorimeters and the muon system are taken into account to reconstruct several different types of particles. These are photons, charged hadrons, neutral hadrons, muons and electrons. The reconstructed objects then serve as

input for the jet finding. The resulting "particle flow" jets are expected to have an improved energy response and resolution compared with the calorimeter jets.

As both calorimeter and particle flow objects are not able to account for the complete energy of the jets, a number of corrections to the transverse momenta of the jets are necessary. The CMS collaboration uses a factorized multi-level approach in which only some of the corrections are mandatory, while others can be applied if a particular analysis requires them. The seven levels are in detail:

- Level 1: Offset correction: Corrects for pile-up and electronic noise [147].

- Level 2: Relative correction: Flattens the jet response in pseudo-rapidity [148].

- Level 3: Absolute correction: Corrects to particle level as a function of p_T [149].

- Level 4: EMF correction: Optional correction for variations of the electromagnetic energy fraction [150].

- Level 5: Flavor correction: Optional correction for different response of light and heavy quark and gluon initiated jets [151].

- Level 6: UE correction: Optional correction for underlying event contributions [152].

- Level 7: Parton level corrections: Optional correction from particle to parton level [153].

A detailed discussion of these corrections and their derivation can be found in [154].

Muon reconstruction in CMS

Muons are measured in CMS in the silicon tracker and the muon system. The muon reconstruction software produces three kinds of muon objects: With the information provided by the muon system alone, so-called *standalone muons*, or in combination with the tracking device input *global muons* and *tracker muons*.

In a first step, muon tracks are reconstructed from the information of the muon system. First, track segments are obtained from the measured drift times in the muon chambers. The segments from the innermost layer are used as seeds for the following muon reconstruction. A Kalman-filter procedure is used to construct and successively improve the muon trajectory by taking reconstructed track segments from the adjoining chambers into account. This also incorporates the uncertainties on the different track measurements. The energy loss of the muons and scattering in the material between the chambers as well as the inhomogeneous magnetic field are taken into account. The muons reconstructed in this manner are the standalone muons.

The global muon reconstruction extends the trajectories of the previous stand-alone reconstruction and matches them with hits in the silicon tracker considering the energy loss and multiple scattering in the detector material, especially in the solenoid and the calorimeter. The extrapolation of the trajectory defines a region of interest within the tracking detector. All hits within this region are used to reconstruct local tracks. This design is called "regional reconstruction" and implies important savings in term of CPU resources needed since not the complete information of the tracker is analyzed. If these tracks are compatible with track from the muon system, a global fit combines the information of the muon chambers and the tracking system into a final muon that is then called *global muon*.

Muons with a transverse momentum in the TeV range are characterized by a significant energy loss in matter and originate severe electromagnetic showers in the muon system. A determination of the trajectories based only on the hits in the tracking detector and the innermost muon detector layer yields information about muon bremsstrahlung and other energy loss mechanisms. This information improves the reconstruction of muons with large transverse momenta.

In an alternative approach, muons are reconstructed beginning with reconstructed tracks in the silicon tracker system. In the same way as before they are propagated, now outward to the muon system, and the candidates are matched to locally reconstructed tracks if available. A final combined fit then yields so-called *tracker muons*. The approach resembles the global muon reconstruction but avoids possible mismatches of muon tracks with tracks in the tracking system. Analyses typically require a successful reconstruction using both methods.

Chapter 4

Higgs search in Vector-Boson Fusion

As described in chapter 1.2.2, the Vector Boson Fusion process is an important channel for Higgs production at the LHC.

The distinguishing feature of the VBF signal is the separation between the two tagging jets and the fact, that the Higgs decay products fall in this so-called "rapidity gap". In the case of a leptonic Higgs decay, it is possible to make full use of this specific structure to suppress QCD dominated backgrounds by applying a central jet veto. However, the signal then suffers from small branching ratios. In addition, the Higgs decay into a pair of electrons or muons is negligible, therefore only the Higgs decay into vector bosons V with subsequent decay into leptons, $H \to VV \to 4l$, offers a sizeable cross section. The overall branching fraction for this channel is nonetheless small, even though the Higgs branching into vector bosons is very large for Higgs masses around 160 GeV, since the branching ratios for vector bosons into leptons are in the percent level, 3% for Z and 10% for W bosons per lepton flavor [24]. These branching ratios suggest the channel $H \to W^+W^- \to \ell^+\nu_\ell\ell'^-\bar{\nu}_{\ell'}$ as promising for an analysis.

4.1. The $H \to W^+W^- \to \ell^+\nu_\ell\ell'^-\bar{\nu}_{\ell'}$ Channel

A detailed study for this process has been performed at matrix element level in [155, 156] and has been repeated in [157] including the full detector simulation of the CMS experiment. However, the event selection in VBF processes depends on many dynamical features of the jets in the signal process. The effect of parton shower, hadronization and underlying event on these features has to be studied by comparing different models for these steps in order to see if the specific event topologies are affected by these models.

This work investigates the influence of different models employed in event generation on the event selection for the VBF $H \to W^+W^- \to \ell^+\nu_\ell\ell'^-\bar{\nu}_{\ell'}$ process, following the analysis shown in [155, 157].

4.2. Signal and Background Processes

Since the Higgs mass is not known, different Higgs masses are compared. To cover the most likely Higgs masses in the standard model, the masses $m_{\mathrm{H}} = 120, 140, 160, 180, 200$ GeV are investigated.

There are a lot of background processes for the VBF signal, especially processes with two real W bosons and two or more jets, $W^+W^- + 2$ jets and $t\bar{t}$ +jets. The $WW + 2j$ pair production has to be divided into two samples, the QCD production consisting of contributions $\propto \alpha_S^2 \alpha^2$ and the electroweak production $\propto \alpha^4$. The latter also is a vector boson fusion process and therefore shows similar jet kinematics, making this process an irreducible background.

In addition, processes that produce two oppositely charged leptons and jets can contribute to the backgrounds. Here Z + 2 jets is an important process, due to the large cross section, this process is also possible in vector boson fusion, requiring special attention. Furthermore, $b\bar{b} + 2$ jets and $\tau^+\tau^- +$ jets can contribute to the background.

For the generation of the processes LesHouches files were created with `vbfnlo` and MADGRAPH/MADEVENT which then were showered with HERWIG++ 2.4.2 and PYTHIA 6.4.21. This setup was chosen in order to study the influence of the different models used for parton shower, hadronization and underlying event between the two generators independent of uncertainties stemming from the matrix element calculation in the two generators. In case of the $t\bar{t}$+jets sample the three subsamples $t\bar{t}$, $t\bar{t} + 1$ jet and $t\bar{t} + 2$ jets contribute and thus a matched sample should be employed. However, as of today, the generation of a matched sample is not feasible within HERWIG++. Therefore, only the sample with the biggest contribution at matrix element level, the $t\bar{t} + 1$ jet sample was generated using MADGRAPH/MADEVENT, whereas additional jets can be added by the parton shower or the underlying event. It is clear that this is a simplification but as the goal of this study is to show the influence of the different models in event generation, this subsample can provide a benchmark for the complete set of contributions.

The cross sections for signal and background have been calculated at NLO with `vbfnlo` and MCFM, where the calculation is available, otherwise the LO cross section from MADEVENT is used. Their values can be found in Table 4.1.

Further backgrounds are QCD jet production and W + jets, since a QCD process can fake leptons in the detector. It is however not possible to introduce this into a pure Monte Carlo study without detector simulation and is not expected to be largely influenced by the MC generator used. Therefore, the processes which can only contribute to the backgrounds through fake leptons are not considered in this work.

Process		Cross section [fb]
VBF Higgs	$m_\mathrm{H} = 120$ GeV	13.27
	$m_\mathrm{H} = 140$ GeV	47.70
	$m_\mathrm{H} = 160$ GeV	82.71
	$m_\mathrm{H} = 180$ GeV	75.05
	$m_\mathrm{H} = 200$ GeV	52.83
$WW + 2j$	(QCD)	$38.79 \cdot 10^3$
	(EWK)	28.04
$t\bar{t} + j$		$31.32 \cdot 10^3$
$Z + 2j$	(QCD)	$423.57 \cdot 10^3$
	(EWK)	$1.21 \cdot 10^3$
$\tau^+\tau^- + 2j$		$25.82 \cdot 10^3$
$b\bar{b} + 2j$		$809.71 \cdot 10^6$

Table 4.1.: Cross sections times branching ratios for the signal and background processes used in the analysis.

4.3. Analysis

The analysis starts with the final state of the generated events at hadron level. Here all particles that would end in the calorimeter and thereby contribute to jets, namely hadrons and photons, are collected. This collection is then turned into jets using the k_T algorithm with a jet radius of $R = 0.6$. This is the choice used in [157], therefore this was employed in this study as well. In addition, the leptons are collected and stored. Furthermore, the missing transverse energy $\not{E}_\mathrm{T}$ is obtained by taking the vector sum of the jets above 5 GeV and leptons, corresponding to visible energy deposits in a detector. The absolute value of the negative of the resulting vector is then $\not{E}_\mathrm{T}$.

In principle it is also possible to calculate $\not{E}_\mathrm{T}$ from the neutrinos in the event, since in a Monte Carlo study this information is also present. However, the determination of this quantity in a real detector is necessarily imprecise, whereas the Monte Carlo events of course provide all information to get a perfect balancing in transverse momentum. By removing the softer contributions, the smearing normally found in events can at least partially be taken into account.

4.3.1. Forward Jet Tagging

As the VBF process is characterized by two outgoing hard quarks, the event selection starts by selecting events with two forward jets. First, all jets in the event are sorted by their transverse energy E_T. This choice was employed in [157] therefore it was used here as well. The first two jets, that means the hardest jets
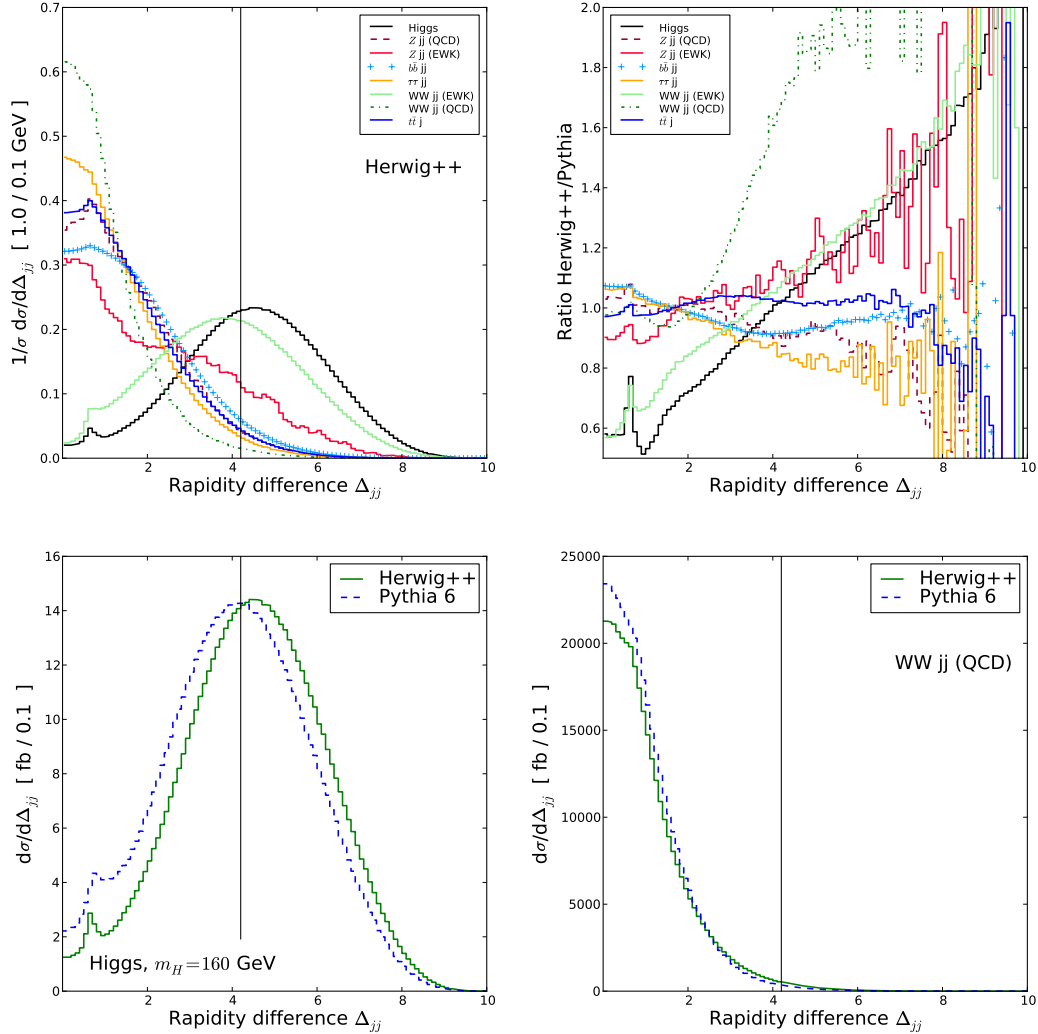
Figure 4.1.: $|\Delta y_{jj}|$ of the two hardest jets in the event. Top left shows all processes simulated with HERWIG++, top right shows the ratio of the HERWIG++ and PYTHIA sample. Bottom left shows the distribution for the Higgs sample with $m_{\mathrm{H}} = 160$ GeV, bottom right the W^+W^- + jets sample.

in the event, should be energetic,

$$E_{\mathrm{T},1} > 50 \text{ GeV} , \quad E_{\mathrm{T},2} > 30 \text{ GeV} \tag{4.1a}$$

and well separated in rapidity and fall in opposite detector hemispheres,

$$|\Delta y_{jj}| > 4.2 , \quad y_1 \cdot y_2 < 0 . \tag{4.1b}$$

This requirement is a direct consequence of the special VBF topology. In addition, to suppress events where the second of these two jet stems from the underlying
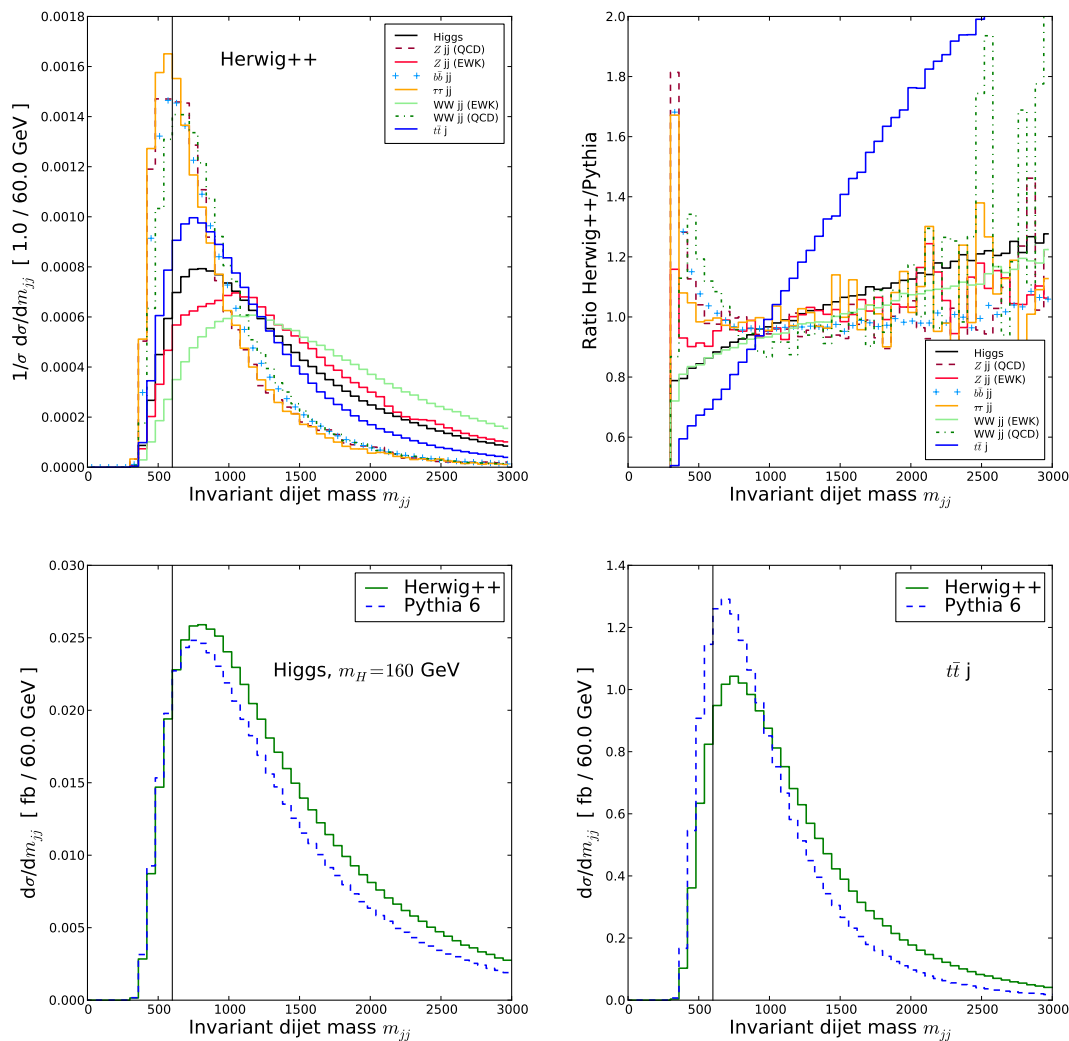
Figure 4.2.: Invariant mass m_{jj} of the two hardest jets in the event. Top left shows all processes simulated with HERWIG++, top right shows the ratio of the HERWIG++ and PYTHIA sample. Bottom left shows the distribution for the Higgs sample with $m_{\mathrm{H}} = 160$ GeV, bottom right the $t\bar{t} +$ jets sample.

event or pile-up, a large invariant mass of the two hardest jet is required,

$$m_{jj} > 600 \text{ GeV} . \tag{4.1c}$$

If the two hardest jet in an event pass these selection criteria, the event is kept for further analysis and the two jets are denoted *tagging jets*.

It can be seen clearly in Fig. 4.1-4.3 that the various cuts are indeed a very powerful handle to suppress especially QCD-induced backgrounds. While most of the background processes show a similar behavior in PYTHIA and HERWIG++, there are some significant differences visible. The description of the rapidity separation is different especially for the vector boson fusion processes, be it the signal
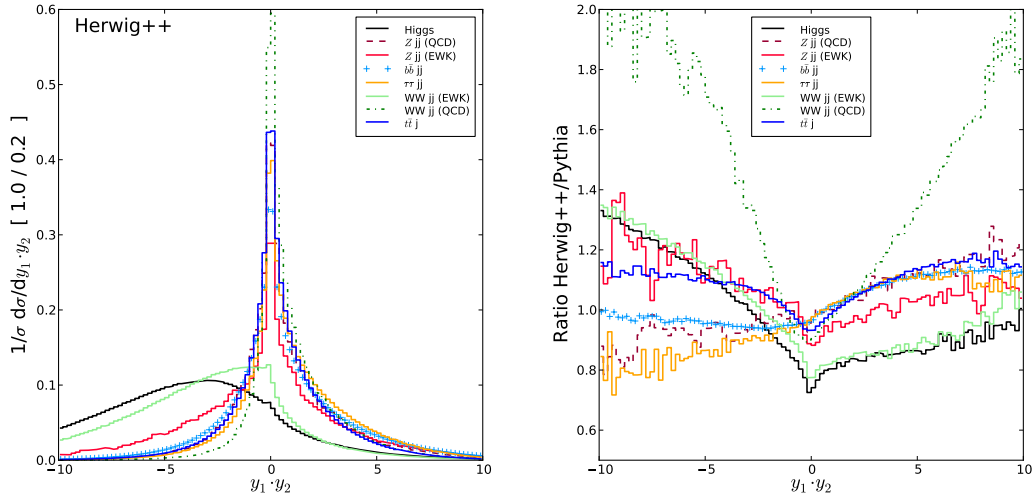
Figure 4.3.: $y_1 \cdot y_2$ of the two hardest jets in the event. On the left all processes simulated with HERWIG++ are shown, the right side shows the ratio of the HERWIG++ and PYTHIA sample.

or the electroweak W^+W^- + jets or Z+jets process. It can be observed that for the electroweak processes the two tagging jets in the PYTHIA samples tend to lie closer to each other than the tagging jets in HERWIG++. This shows the influence of the parton shower employed, as both samples start from the same matrix element provided by the Les Houches files.

The minor peak seen at ≈ 0.6 in the rapidity separation distributions Fig. 4.1 is an artefact from technical cuts at parton level and the jet finding. For the matrix element calculation, some minimal cuts need to be applied to guarantee a finite result, as the cross section can diverge for close jets. In addition, the jet algorithm will cluster particles closely to each other into a jet, therefore it is to be expected that rapidity separations below the jet radius used are very rare.

A similar behavior can be seen in the invariant mass of the tagging jet pair, here again the distribution in the PYTHIA sample is shifted to smaller values with respect to the HERWIG++ sample. This can also be explained by the fact that the tagging jets in the PYTHIA sample lie closer to each other, resulting in a smaller invariant mass of the pair.

The discrepancies present in the rapidity separation and the invariant mass already show an interesting difference in the parton shower models employed. The radiation in the electroweak PYTHIA tends to fall in the central region, pulling the tagging jets with it, whereas the HERWIG++ sample is more in the forward region with a corresponding shift of jets in this direction.

On the other hand, the QCD samples tend to lie closer to each other after the different showers. Some differences can be seen, the W^+W^- + 2 jets sample differs in the rapidity separation for large values of Δy but on the other hand

shows a good agreement on the rather steeply falling slope before. The $t\bar{t} + 1$ jet samples agree quite well in Δy, but exhibit differences in the invariant mass of the tagging jet pair. This might result from a different treatment of the radiation of heavy quarks used in the two event generators used. While PYTHIA employs an approximation of the splitting kernels for massive objects, HERWIG++ features the full treatment of these radiations, which might account for the differences seen here. It is possible that the approximation used in the PYTHIA sample ceases to be useful in the special case of the VBF topology.

The differences in the jet kinematics resulting from the different treatment by the parton shower corresponds to differences in the event selection. As the jets are closer to each other in the electroweak PYTHIA samples, more events are rejected by the forward jet cuts since these cuts especially aim at selecting largely separated jet pairs.

4.3.2. B-tagging

After the forward jet cuts, imposing a b jet veto on the tagging jets is useful to further suppress the $t\bar{t}$ background. This process will contain two b quarks from the top quark decay, and it is likely that at least one of the tagging jets emerges from one of these b jets. The signal however is expected to contain only a very small number of b quarks at matrix element level. This is due to the fact that the b quark density in the proton is very small compared to the lighter quarks. The identification of the b jets, the b tagging, requires information from the tracking system for secondary vertex information. As a tracker only covers the central rapidity region, it is not possible to tag forward b jets.

Therefore an event is discarded if at least one of the tagging jets has a positive b tag. Since the tagging jets are separated largely in rapidity, at least one tagging jet is likely to fall outside the region where b tagging is feasible.

Since this analysis is a pure Monte Carlo study without detector simulation, there is no information about vertices and other input objects used in b tagging. Therefore, it is not possible to compare the b tagging efficiencies predicted by the generators in this study.

To gain an estimate on the importance of this selection, a very simple approach to b tagging is used. The b quark four momentum from the matrix element is stored and for each jet the R separation to the b quarks is calculated. A jet is denoted a b jet when its rapidity is in the rapidity region covered by the tracker, $y < 2.5$ and its R separation to a b quark is smaller than $\Delta R < 0.2$.

Fig. 4.4 shows the R separation between the b quarks and the nearest jet for the two samples that have b quarks in the matrix element for each event. The peak at low values shows that the proposed naive b tagging indeed matches exactly one jet to most of the b quarks. Therefore this is a reasonably good approximation for this kind of study. Of course, this is a very crude way of simulating a b jet veto but already the differences perceptible in the $b\bar{b}$ samples shows that the b jets are simulated differently in the two generators.
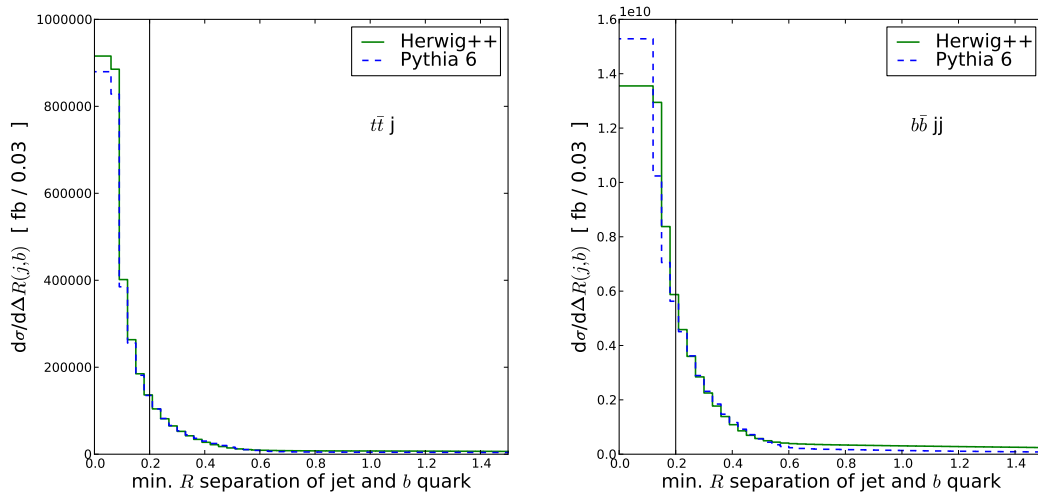
Figure 4.4.: ΔR of the b quarks to the nearest jet in the event. On the left this is shown for the $t\bar{t}$ sample, the right side shows this distribution for the $b\bar{b}$+jets sample.

4.3.3. Central Jet Veto

The VBF process is a color singlet exchange, therefore the region between the two tagging jets is expected to be free of hard QCD radiation. As all additional emissions at tree level originate from the external partons, they are most likely to be either close to the tagging jets or along the beam axis.

This can be understood by the structure of the splitting kernel for QCD branchings, Eq. (1.24), which favors small angle radiation. As a result, additional jets are most likely to be close to other jets. This can especially be observed for jets in QCD processes which tend to be close to other jets. In processes where a colored particle is exchanged, small angle radiation can happen along the exchanged objects as well and also cover the regions between other jets.

In conclusion, the region between the tagging jets in VBF events is expected to be free of hard hadronic activity whereas QCD induced processes are supposed to exhibit a lot of this. Therefore, rejecting events where much activity is present in the gap region can effectively separate the signal from its QCD backgrounds. There are several possible ways of implementing such a Central Jet Veto (CJV), they all aim at rejecting events with hard central jets, where the definitions of "hard" and "central" vary. In any case a detailed understanding of the additional jets found both in the signal as well as the backgrounds is needed.

As the CJV depends on the position of the additional jets in rapidity, this is of course the first thing to study. For the study of additional jets, objects with $p_{\rm T} > 20$ GeV are considered. The rapidity of the third hardest jet is shown in Fig. 4.5. It shows whether the jet tends to lie in the forward rapidity region or not. However, it does not show the position of the third jet with respect to the
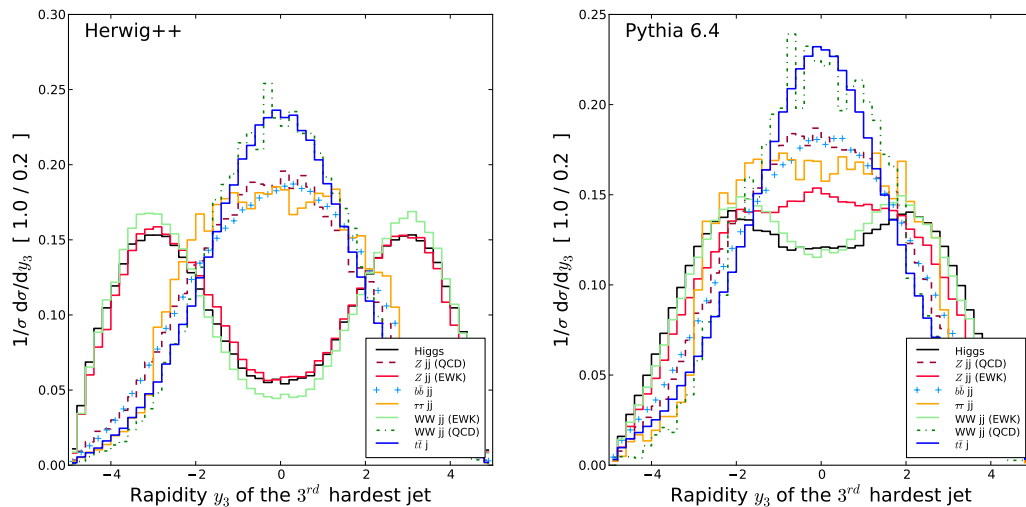
Figure 4.5.: Rapidity of the third hardest jet in events which pass the forward jet cuts, Eq. 4.1. On the left this is shown for all samples generated with HERWIG++, the right side shows this distribution for all samples generated with PYTHIA,

two tagging jets and therefore would lead to the event being vetoed or not. It is therefore desirable to have observables that provide a more detailed insight into this.

One useful observable is

$$y^* = y_3 - \frac{1}{2} \cdot (y_1 + y_2) \ , \tag{4.2a}$$

it shows the rapidity of the third jet centered on the position of the two tagging jets.

Distributions of this quantity are shown in Fig. 4.6. If y^* is around zero, the additional jet falls in the rapidity gap, if it has a large value, the additional jet falls around the tagging jets or outside the rapidity gap. However, this observable does not show the relative position of the additional jet with respect to the tagging jets, that is if a jet is actually between them or if it is outside. Since this is a crucial point for a central jet veto, it is useful to consider a further observable,

$$z^* = \frac{y^*}{|y_1 - y_2|} \ . \tag{4.2b}$$

The normalization of y^* on the actual size of the rapidity gap now provides this additional information. In case the additional jet has the same rapidity as one of the tagging jets, this results in $|z^*| = \frac{1}{2}$. If the additional jet is between the tagging jets, then $|z^*| < \frac{1}{2}$ and $|z^*| > \frac{1}{2}$ if it is outside the two tagging jets.

The distributions for all these observables show major differences, especially in the description of the electroweak samples by HERWIG++ and PYTHIA. It can
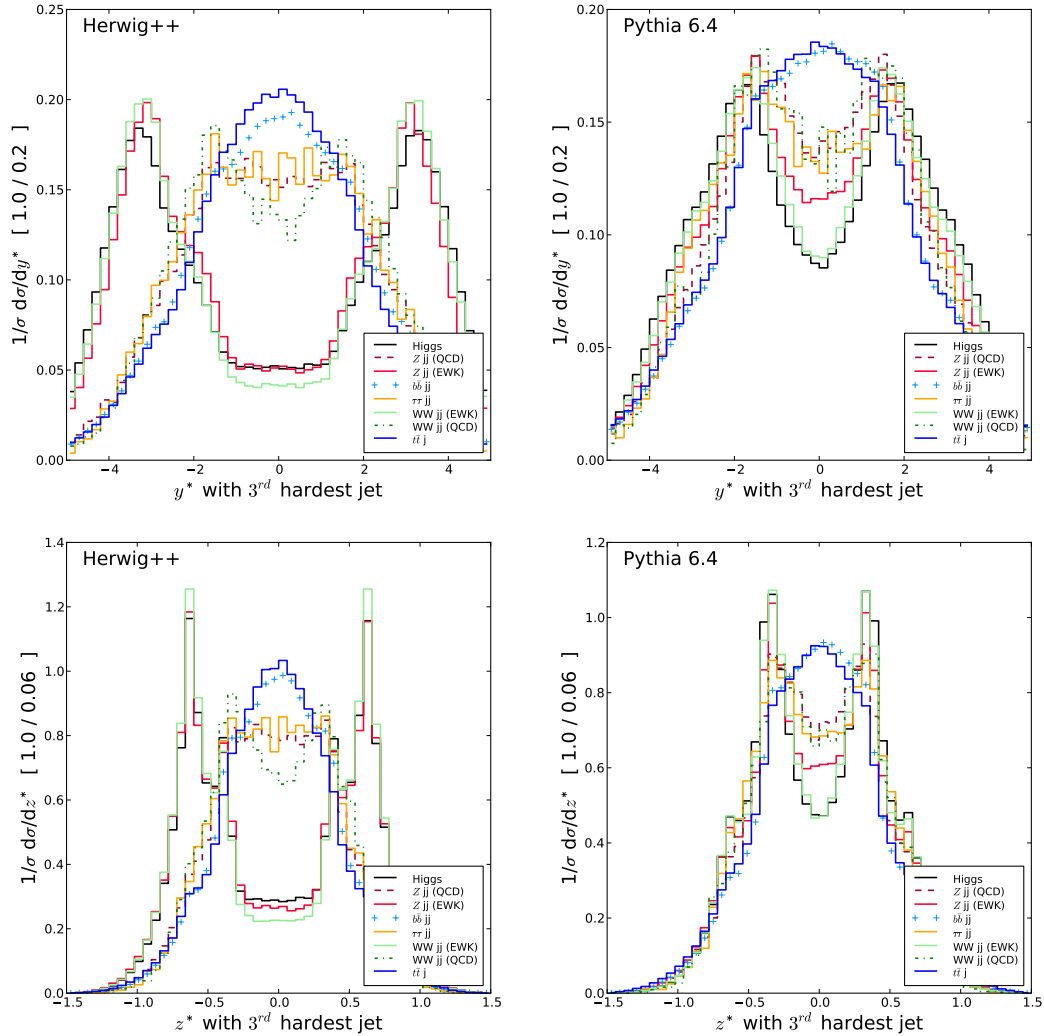
Figure 4.6.: y^* (upper row) and z^* (lower row) calculated from the third hardest jet in events which pass the forward jet cuts, Eq. 4.1. On the left this is shown for all samples generated with HERWIG++, on the right all samples generated with PYTHIA are shown.

be already seen from the rapidity distributions, Fig. 4.5 that the third jet in the HERWIG++ samples tends to lie much more outward than those in the PYTHIA sample.

This gets clearer when regarding y^*, Fig. 4.6, upper row. This observable indeed is able to provide a detailed insight into the position of the additional jet, central for the QCD samples, forward for the electroweak samples simulated with HERWIG++ and somewhere in between for the electroweak samples in PYTHIA. However, the distributions for electroweak samples in PYTHIA follow quite closely the ones of the QCD samples.
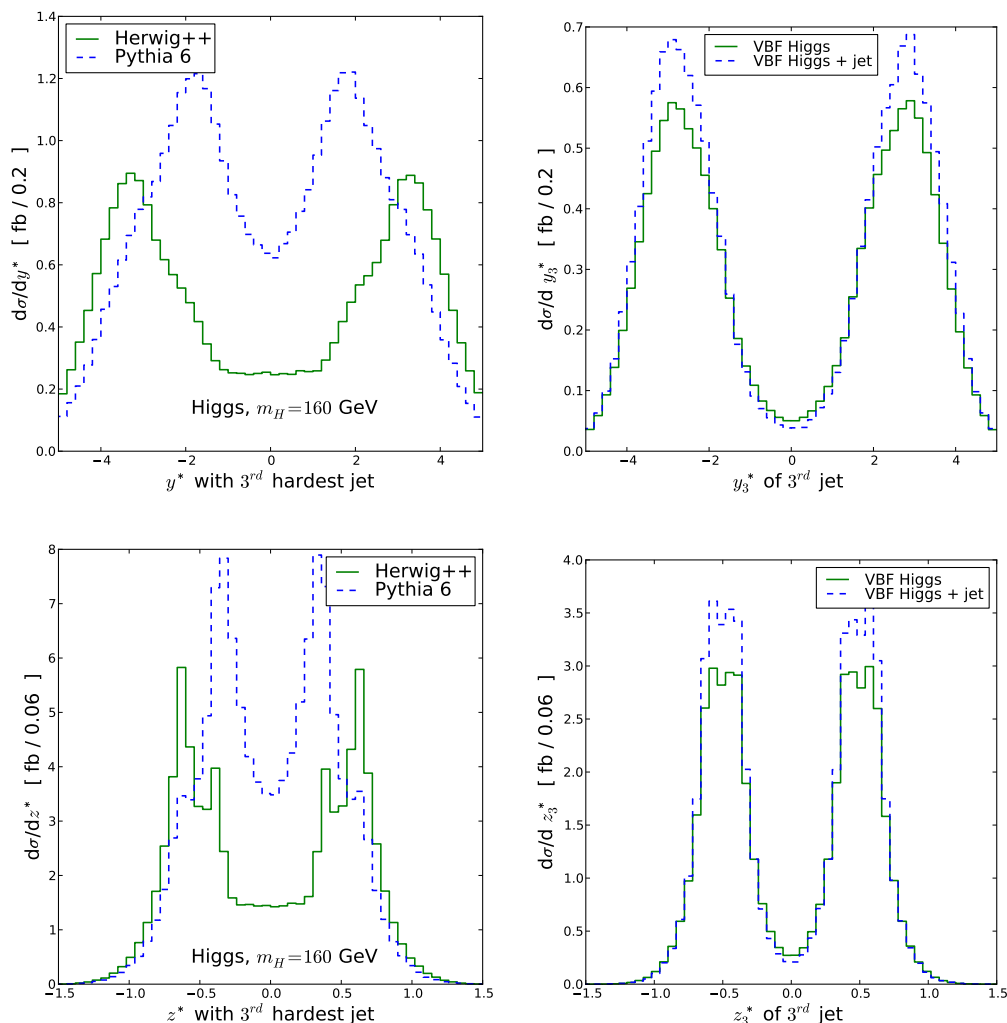
Figure 4.7.: y^* (upper row) and z^* (lower row) calculated from the third hardest jet in Higgs events which pass the forward jet cuts, Eq. 4.1. On the left this is shown for the samples generated with HERWIG++ and PYTHIA, the right side shows the next-to-leading order QCD distributions at parton level.

The different behavior can be seen in even more detail in the distributions for z^*, Fig. 4.6, lower row. Here it is obvious that most of the events from QCD processes indeed fall into the rapidity gap, thus can be reduced significantly by a veto on such central jet activity. However, the description of the electroweak samples is not so unambiguous. The descriptions of HERWIG++ and PYTHIA agree with each other in so far as the majority of the additional jets is in the vicinity of the tagging jets, but the complete picture is very different. The majority of the additional jets in the electroweak HERWIG++ samples lies outside the tagging jet, while in the PYTHIA samples they are on the inside of the tagging jets. Due to
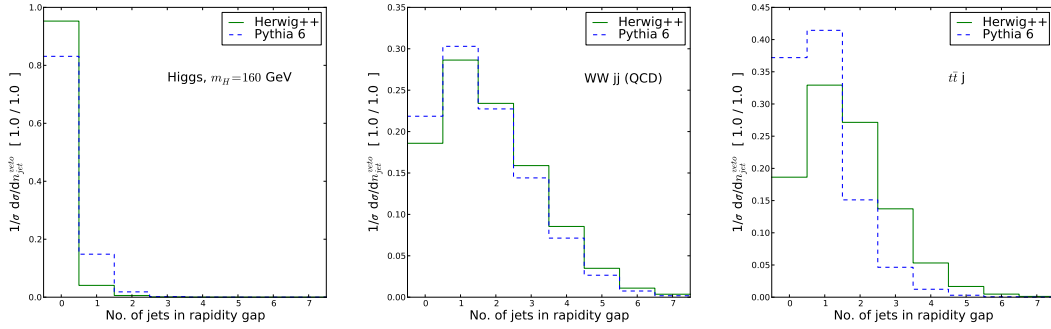
Figure 4.8.: Number of jets falling in the rapidity gap. The left plot shows the signal, the central plot the QCD W^+W^-+jets background, the right hand side shows the $t\bar{t}$ sample.

this shift, the electroweak PYTHIA samples are more similar to the QCD samples.

It is interesting to note when regarding the distributions for z^*, that there are four distinct peaks observable close to the position of the tagging jets. The position of these peaks can be explained by the properties of the jet finding algorithm. The jet algorithm causes the region around the hard tagging jets to be free of other jets, so in the rapidity region of the tagging jets only a reduced amount of activity is found. The rapidity difference between the tagging jets by which y^* was divided to obtain z^* is about 4.5. The jet resolution parameter was set to be $R = 0.6$. The peaks in the z^* distribution now can be found within the distance d to the tagging jet positions, which in this distribution were found to be $\pm\frac{1}{2}$ with

$$ d \approx \frac{R}{\langle |y_1 - y_2| \rangle} \approx \frac{0.6}{4.5} = 0.13 \ , $$

which fits quite well with the found peak positions.

It is not expected that the additional jets are described accurately by the parton shower, as this only provides an approximation valid for soft and collinear jets. In addition, there are more jets expected not associated with the hard process but stemming from the underlying event or pile-up. However, the major contribution to the differences is indeed due to the parton shower models employed [158].

It is now interesting to compare these observables with a NLO QCD prediction for Higgs + 3 jets production at parton level. Fig. 4.7 shows y^* and z^* for the signal with $m_{\text{Higgs}} = 160$ GeV and illuminates the difference between the two parton shower models. The discrepancies between the HERWIG++ and PYTHIA sample can be clearly seen. It is interesting to observe that the NLO QCD prediction seems to provide a compromise between the two generators. The outer slope of the HERWIG++ sample follows quite well that of the NLO prediction, however, in close proximity to the tagging jets this breaks down. The inner slope of the distributions is much lower in the HERWIG++ sample, while it is symmetric in the NLO case. The PYTHIA sample shows the inverse of this behavior, the outer

slope is much lower than the inner one. In addition, the very central region in the NLO sample exhibits much less activity than both fully hadronized samples, while here again a difference between the two generators can be found, HERWIG++ being lower. This central activity which is not present in the NLO distributions stems in parts from the underlying event, as has been shown in [158]. However even without the MPI contributions the PYTHIA sample contains about twice the amount of hard central jets.

With these observables, it is possible to construct a central jet veto to remove QCD backgrounds. A sensible choice for the implementation is to calculate y_i^* for all additional jets i with transverse momentum $p_{T,i} > 20$ GeV and veto events where at least one of the additional jets fulfills

$$|y_i^*| < 2.0 \ . \tag{4.3}$$

That way, all jets that fall in the central rapidity region are considered , whereas forward jets, outside of the rapidity gap do not contribute. Fig. 4.8 shows the number of additional jets with $p_T > 20$ GeV in the signal sample and two backgrounds. On the one hand, it can be seen clearly that the VBF sample contains much less additional central jets than the QCD samples, therefore reducing the amount of vetoed events, as is intended. On the other hand, for the VBF sample and the $t\bar{t}$ sample the number of these additional jets differs between the two generators considered, which, of course, influences the veto efficiency.

In conclusion it is clear that using the information obtained by showering normal matrix elements is not sufficient to gain a reliable estimate of the central jet veto. It can be seen that already the parton shower approximation is not able to provide a consistent description of the hard central activity, leaving alone all the uncertainties associated with a jet veto stemming from the scale of the underlying event or the amount of pile-up. Therefore, it is necessary to allow for large uncertainties in this part of a VBF Higgs search.

In a fully simulated or real event, it is not so obvious if the additional jets are really the most promising candidates for a veto on central activity. Since the underlying event and pile-up can form soft jets, the veto efficiency can fluctuate with small changes in the jet definition. Possibly, a check based on tracks or the energy flow in the central region can provide more insight. However, this is beyond the scope of this work, as this information is not present in the pure Monte Carlo simulations.

4.3.4. Lepton Kinematics

The preselection of VBF events with the leptonic final state described here starts with the lepton selection at trigger level. An event is considered to be a candidate if there are two leptons, electrons or muons, in the event to fire the di-lepton trigger. The values for the transverse momentum required to fire the dilepton trigger are taken from [157].
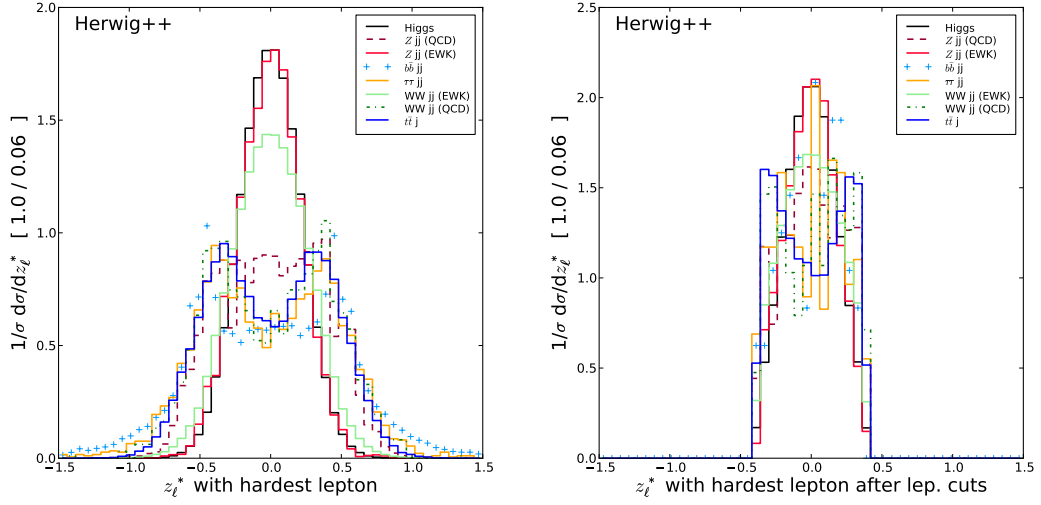
Figure 4.9.: z_l^* of the harder lepton in the event. Left this observable is shown before
            the lepton cuts (4.4), right after the cuts.

For the event selection, this means that two opposite charged leptons in the
acceptance region of the tracker are required, satisfying the trigger requirements,

$$p_{T,1} > 26 \text{ GeV} \wedge p_{T,2} > 10 \text{ GeV} \tag{4.4a}$$

or

$$p_{T,1} > 20 \text{ GeV} \wedge p_{T,2} > 12 \text{ GeV} . \tag{4.4b}$$

The threshold on the transverse momentum of the second lepton needs to be
low, since for Higgs masses below 160 GeV one W boson is necessarily off-shell.
In addition, to exploit the specific features of the VBF signal, the leptons are
required to fall inside the rapidity gap, well separated from the tagging jets,

$$y_{j,\text{lo}} + 0.6 < \eta_l < y_{j,\text{hi}} - 0.6 . \tag{4.4c}$$

Here $y_{j,\text{lo}}$ and $y_{j,\text{hi}}$ are the tagging jets with the lower and higher rapidity respec-
tively. Furthermore, only good quality leptons are taken into account, i.e. leptons
well separated from jets, therefore the leptons are additionally required to be clear
of any jet in the event by

$$\Delta R(j,l) > 0.7 . \tag{4.4d}$$

This last cut is especially important to suppress backgrounds with a fake lepton
coming from a QCD jet, as for example in a W + jets sample.

As in the case for central jets, it is interesting to observe the position of the
leptons relative to the tagging jets. Of course, the observables used there can
be used for the leptons as well, by replacing the rapidity of the third jet by the
pseudorapidity of the leptons,

$$z_\ell^* = \left(\eta_\ell - \frac{1}{2} \cdot (y_1 + y_2) \right) / \Delta y_{12} . \tag{4.4e}$$

Here η_ℓ denotes the pseudorapidity of the two leptons, y_1, y_2 are the rapidities of the two tagging jets and Δy_{12} is their rapidity separation. This observable is shown in Fig. 4.9 before and after the cuts described in this section. It can be clearly seen that the cuts serve well to keep only the very central leptons with a good separation from the tagging jets. In this observable no big difference between the two generator samples can be observed. This is not surprising, since the lepton information in most samples is already present at the level of the Les Houches events, therefore, there is only little contribution from the showering and hadronization generators used.

The only samples where the lepton information is not already present in the Les Houches files are the $t\bar{t}$ + jet, $\tau^+\tau^-$ + 2 jets and $b\bar{b}$ + 2 jets samples. In the top quark sample the decays of the heavy quarks are generated by the Monte Carlo programs, these decays are however quite well understood and the two different implementations do not show big differences as far as this study is concerned. The τ sample contains the τ leptons in the Les Houches files which are decayed by the event generators. Here there are some differences, since HERWIG++ is able to take the full spin correlations into account while PYTHIA has to rely on external packages like TAUOLA [78] for this. The energy and transverse momentum of the τ decay products however are nonetheless similar, but there might be some differences due to angular cuts on leptons. However, as far as this study is concerned, no such effect could be observed.

The biggest uncertainty can be found in the $b\bar{b}$ sample. Here particles found in the Les Houches files do not decay directly. Instead, the b quarks hadronize and the B hadrons in turn decay. So the details of the B hadron decay implementations determine if an event has leptons in the final state. However, this is handled differently in the two generators. HERWIG++ includes the possibility to take spin correlations into account for all decays and incorporates a huge amount of different decay modes with an easy way of steering these. Therefore in the HERWIG++ case only the leptonic decay modes of B hadrons were turned on where available to increase the statistic uncertainty. The corresponding cross section in turn is smaller than the one used in the PYTHIA sample, where it is not possible to turn the different B hadron decays off that easily. As a result, there are large differences in the amount of leptons stemming from the B hadron decays. This shows the importance of understanding this background in detail, using further information for example from track and vertex reconstruction to investigate if leptons stem from a secondary vertex. In addition, in both cases the leptons are quite soft and not well isolated. Therefore, even if the discrepancy between the different B hadron decay models is quite large initially, this background is reduced drastically in both samples.

4.3.5. Further Kinematic Constraints

There are further observables useful for distinguishing the signal from backgrounds. The overall balance in transverse momentum $p_{\mathrm{T}}^{\mathrm{balance}}$ in the event can be used in
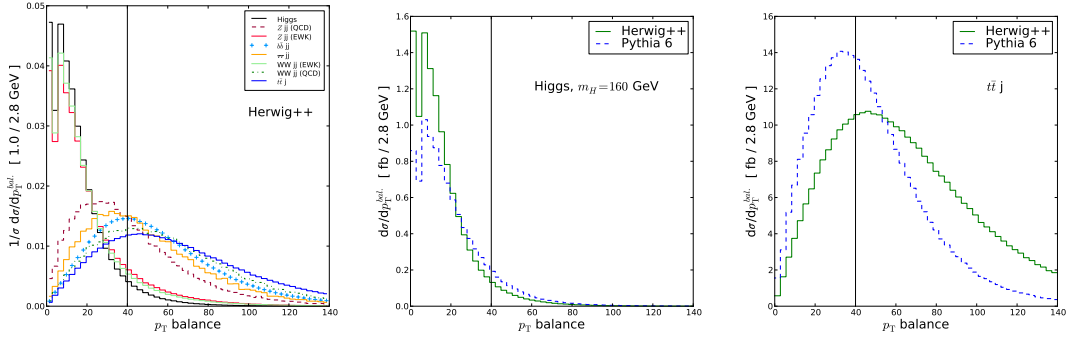
Figure 4.10.: The $p_\mathrm{T}^\mathrm{balance}$ of the events as described in Eq. 4.5a. The left plot shows all processes simulated with HERWIG++, the middle one shows the distribution for the Higgs sample with $m_\mathrm{H} = 160$ GeV, right the $t\bar{t}$ + jets sample.

the event selection as well. It is obtained by calculating the vector sum of the transverse momenta of the two tagging jets, the leptons and the missing energy. Since this includes all relevant objects expected in signal events, this sum should be balanced. The events are therefore required to have

$$p_\mathrm{T}^\mathrm{balance} = \left| \mathbf{p}_{\mathrm{T},\mathrm{j_1}} + \mathbf{p}_{\mathrm{T},\mathrm{j_2}} + \mathbf{p}_{\mathrm{T},\ell_1} + \mathbf{p}_{\mathrm{T},\ell_2} + \not{E}_\mathrm{T} \right| < 40 \text{ GeV} \qquad (4.5\mathrm{a})$$

Fig. 4.10 shows that this is indeed a well discriminating observable. The $t\bar{t}$ sample has more activity in the event and therefore the leptons are not balanced by the two hardest jets. However, the signal events are balanced to a very good extent. Again, differences can be observed when comparing the two generators. As the PYTHIA Higgs sample exhibits more additional jet activity, it is not surprising to see that the events are not as balanced than that in the HERWIG++ sample. The opposite holds for the $t\bar{t}$ sample, here the HERWIG++ samples are less balanced.

The W bosons from the Higgs decay are produced close to threshold and are almost at rest in the Higgs frame. Therefore, the charged lepton and the neutrino from a W decay are almost back-to-back in this frame with equal energies. As a result, the invariant masses of the two charged leptons and of the neutrinos are approximately equal, $m_{\ell\ell} \approx m_{\nu\nu}$ and neither can exceed half the Higgs boson mass. In the lab frame the small dilepton invariant mass favors a small angle between the two charged leptons.

Therefore there are two possible cuts on the charged leptons to reduce especially the Z and the electroweak W^+W^- backgrounds. First, the invariant mass of the lepton pair is required to be

$$m_{\ell\ell} < 80 \text{ GeV} . \qquad (4.5\mathrm{b})$$

This cut removes most of the potential contributions from the Z peak, which would yield a significant contribution due to its large cross section otherwise. In addition,
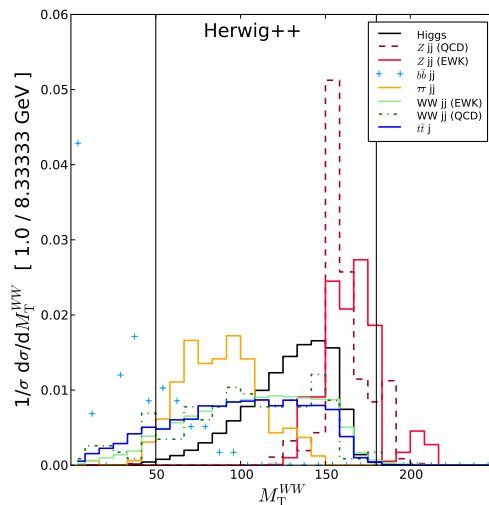
Figure 4.11.: $M_{\mathrm{T},WW}$, all processes simulated with HERWIG++.

the electroweak W^+W^- sample is reduced by this cut, where the invariant mass of the lepton pair is not constrained.

In addition, a cut on the ϕ separation between the two charged leptons also favors the small angle between the two charged leptons,

$$\Delta\phi(\ell\ell) < 2.4 \ . \tag{4.5c}$$

However, in combination with the other lepton cuts, which to some extent also cut on the angle between the leptons, this cut does not yield a useful reduction of the background.

In any case these selection cuts are not likely to be affected much by the event generators used, since for all relevant samples the leptons are already present in the Les Houches file.

The decay channel $H \rightarrow 2\ell + \not{E}_{\mathrm{T}}$ suffers from the fact that no Higgs mass peak can be reconstructed. It is however possible to reconstruct the transverse mass of the Higgs boson as

$$M_{\mathrm{T},WW} = \sqrt{\left(\not{E}_{\mathrm{T}} + p_{\mathrm{T},ll}\right)^2 + \left(\not{E}_{\mathrm{T}} + \mathbf{p}_{\mathrm{T},\mathrm{ll}}\right)^2} \ . \tag{4.5d}$$

The distribution for this observable in the signal sample now is indeed in the region of the Higgs mass and below, as can be expected. For the backgrounds, where no kinematic constraints on the W pair apply, this is different. Therefore, it is sensible to only keep events if

$$M_{\mathrm{T},WW} > 50 \text{ GeV} \quad \text{and} \quad M_{\mathrm{T},WW} < m_{\mathrm{Higgs}} + 20 \text{ GeV} \ . \tag{4.5e}$$

Fig. 4.11 shows this distribution for the HERWIG++ sample, it can be seen that the cuts on $M_{\mathrm{T},WW}$ help to separate the signal from the backgrounds. Especially the processes with a Z boson are affected as well as the $b\bar{b}$ one.

Again, as this is a cut on a quantity composed of the leptons and $\not{E}_T$, its description is very similar in the different generators.

4.3.6. Additional Cuts

To further reduce $b\bar{b}$ and $\tau^+\tau^-$ backgrounds, additional cuts exploiting the correlations between the leptons azimuthal angles and the transverse momentum of the reconstructed Higgs boson, $p_T^{\text{Higgs}} = |\mathbf{p}_{T\ell_1} + \mathbf{p}_{T\ell_2} + \not{E}_T|$ can be employed. Since all the cuts in this section are only based on the lepton kinematics and the missing transverse energy, there is no impact of the parton showering used expected. The only influence of the different generators can come through the decay routines used for B hadron and τ decays, as discussed before.

In both the $b\bar{b}$ and $\tau^+\tau^-$ backgrounds the missing energy stems from neutrinos emitted parallel to the charged leptons. As a result, the $\not{E}_T$ vector lies between the two lepton transverse momentum vectors and therefore close to their sum, $\mathbf{p}_{T\ell\ell} = \mathbf{p}_{T\ell_1} + \mathbf{p}_{T\ell_2}$. As already mentioned, in the Higgs signal the two leptons are likely to be emitted close to each other with the neutrinos recoiling against them. These features can be visualized by the azimuthal angle $\Delta\phi(\ell\ell, \not{E}_T)$ between $\mathbf{p}_{T\ell\ell}$ and $\not{E}_T$. The two backgrounds are concentrated at small values of $\Delta\phi(\ell\ell, \not{E}_T)$ while the signal favors larger values, except when the Higgs has a large transverse momentum, resulting in boosted decay products that are closer to each other.

These correlations are clearly visible in Fig. 4.12. The $\tau\tau$ events mostly contain lepton pairs with small angles between them whereas the $b\bar{b}$ sample only shows low transverse Higgs momenta. The distributions suggest "contour cuts",

$$180/\pi \cdot \Delta\phi(\ell\ell, \not{E}_T) + 1.5 \cdot p_T^{\text{Higgs}} > 180 \qquad (4.6\text{a})$$

and

$$12 \cdot 180/\pi \cdot \Delta\phi(\ell\ell, \not{E}_T) + p_T^{\text{Higgs}} > 360 \qquad (4.6\text{b})$$

to reduce the $b\bar{b}$ and $\tau^+\tau^-$ backgrounds. Here $\Delta\phi(\ell\ell, \not{E}_T)$ is in radians and p_T^{Higgs} in GeV. The lines in Fig. 4.12 depict these cuts.

However, as both the $b\bar{b}$ and the $\tau^+\tau^-$ background were already reduced drastically by previous cuts, it might be possible to drop this cut, as quite a large part of the signal is removed as well. This depends on the understanding of these two backgrounds, a detailed study including detector effects is needed to make a strong statement about this.

A further cut on the missing energy of the remaining events and the transverse momentum of the Higgs is proposed to remove the remaining $b\bar{b}$ background,

$$\not{E}_T > 30 \text{ GeV} \quad \text{if} \quad p_T^{\text{Higgs}} < 50 \text{ GeV} . \qquad (4.6\text{c})$$

However, this could not be reproduced in this analysis, where the $b\bar{b}$ background was effectively removed by the previous cuts. However, as the prediction for this background at hadron level shows to have large uncertainties, it is sensible to keep
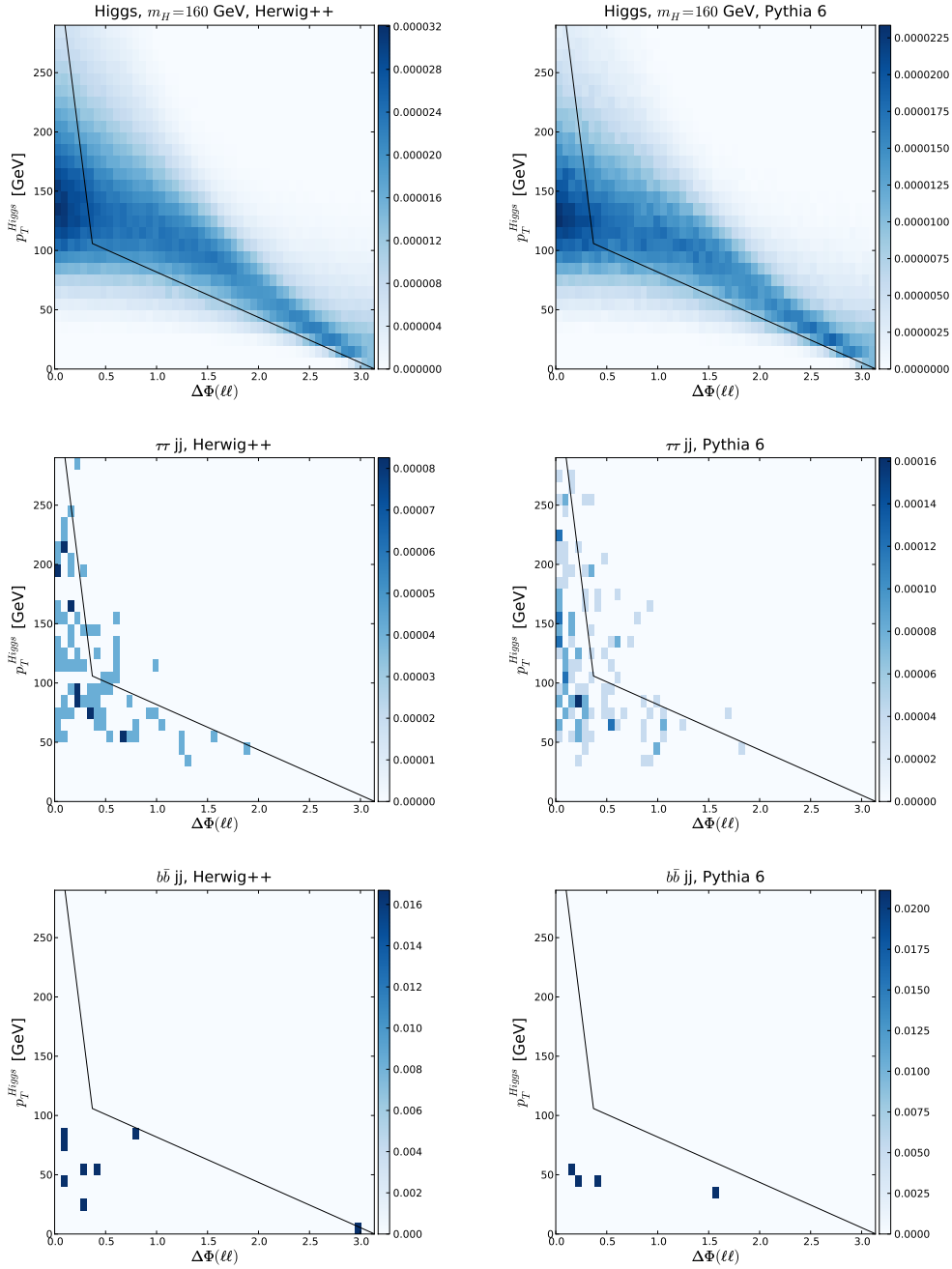
Figure 4.12.: $\Delta\phi(ll, \not{E}_{\mathrm{T}})$ vs $p_{\mathrm{T}}^{\mathrm{H}iggs}$. The top row shows the Higgs sample, the middle row the $\tau^+\tau^-$ and the lower row shows the $b\bar{b}$ samples. The plots on the left show the processes simulated with HERWIG++, right with PYTHIA.

this cut in case the $b\bar{b}$ background turns out to be more dominant. Especially for light Higgs masses this cut might still be important [156, 157].

The only samples affected much by this cut are the Z+2 jet samples, which of course have only little missing transverse energy, as a result of the absence of neutrinos in the event.

A further background, which has not been dealt with so far is the Drell-Yan production of two leptons with additional jets. Since this process has a huge cross section, it is very probable that events from this process will exhibit the VBF topology. As this process shows a distinct peak in the low mass region of the invariant lepton pair mass, a cut on the dilepton mass

$$m_{\ell\ell} > 10 \text{ GeV} \tag{4.6d}$$

is very effective to suppress this. In addition, as in this process there are no neutrinos in the event, all missing energy in these events stems from the uncertainties of the $\not{E}_\mathrm{T}$ determination in the detector. It is therefore possible to reduce this background even further, events with a small missing transverse energy $\not{E}_\mathrm{T} < 30$ GeV are rejected if the two leptons have the same flavor. It is not surprising that this cut does barely affect most of the samples except the Z+jets samples, which are the only ones studied here without $\not{E}_\mathrm{T}$ at the matrix element level as well as a same flavor lepton pair in every event.

A final cut to reduce the $t\bar{t}$ + jets background is based on the sum of the angular separation between the two leptons and that of the combined leptons and the missing transverse energy,

$$\Delta\phi(\ell\ell, \not{E}_\mathrm{T}) + \Delta\phi(\ell\ell) < 3.0 \ . \tag{4.6e}$$

Fig. 4.13 shows the values of $\Delta\phi(\ell\ell, \not{E}_\mathrm{T})$ plotted against $\Delta\phi(\ell\ell)$, with the final cut denoted as a contour plot. This quantity is able to reduce the $t\bar{t}$ and Z backgrounds even further, up to a factor of two for the Z case, while leaving the majority of the signal events.
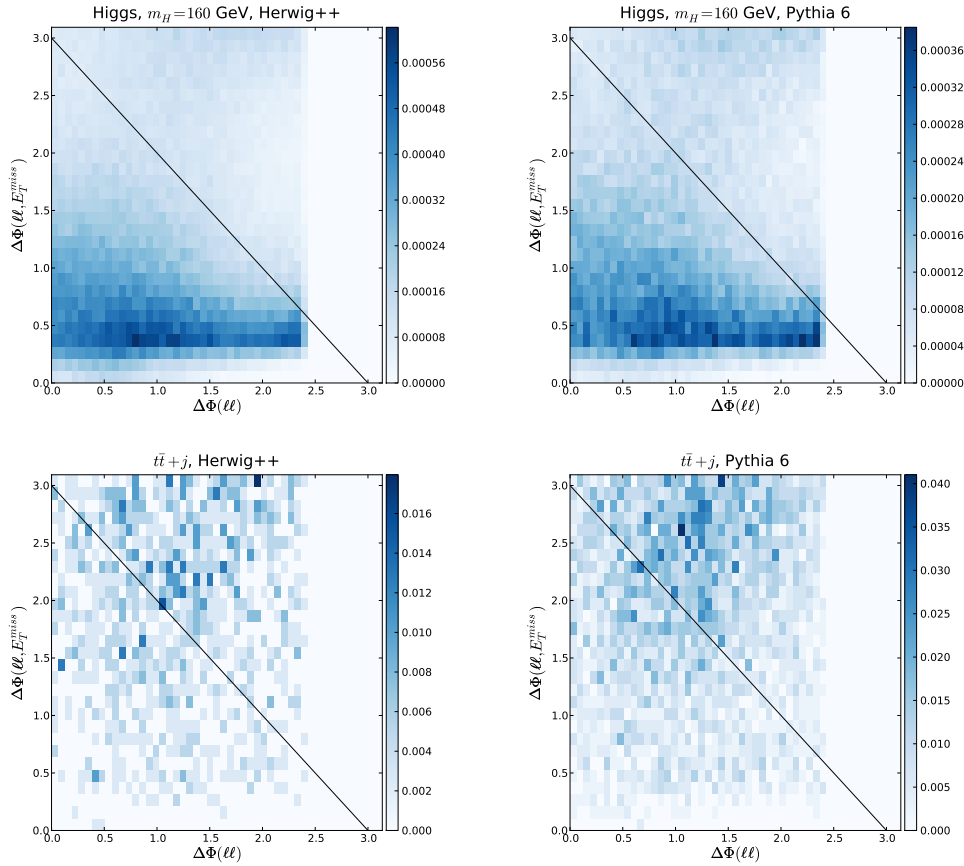
Figure 4.13.: $\Delta\phi(\ell\ell, \not{E}_T)$ vs. $\Delta\phi(\ell\ell)$. The top row shows the Higgs samples, the bottom row the $t\bar{t}$ samples. The plots on the left show the processes simulated with HERWIG++, right with PYTHIA

4.4. Cut Efficiency and Significances

The cross sections after the various cuts are shown in Tab. 4.2 for the HERWIG++ and in Tab. 4.3 for the PYTHIA samples. The effect of the various cuts can be clearly seen, especially their efficiency in reducing the backgrounds.

It is interesting to note that the electroweak backgrounds can be removed almost completely with the cuts, which is achieved essentially by the cuts on the leptons and the missing transverse energy in the events. The QCD backgrounds are reduced by several orders of magnitude in the event selection process. In most cases it is possible to reduce them much below the signal after the full event selection, except for the $t\bar{t}$ background, which remains about the same order of magnitude as the signal.

The differences found in the description of various jet observables by the two generators used also lead to different selection efficiencies when these observables are used to distinguish signal and background processes.

	Higgs	WW (EWK)	WW (QCD)	$t\bar{t}$+jet	$\tau^+\tau^-$jj	$b\bar{b}$jj	Zjj (QCD)	Zjj (EWK)
all events	82.71	28.04	$39 \cdot 10^3$	$31 \cdot 10^3$	$26 \cdot 10^3$	$97.6 \cdot 10^6$	$424 \cdot 10^3$	$1.2 \cdot 10^3$
E_T cuts	61.71	25.04	$35 \cdot 10^3$	$29 \cdot 10^3$	$14 \cdot 10^3$	$69.4 \cdot 10^6$	$174 \cdot 10^3$	797.50
jet rap.cuts	34.90	10.47	396.33	$1.1 \cdot 10^3$	359.17	$3.7 \cdot 10^6$	$6.3 \cdot 10^3$	131.81
all jet cuts	32.15	10.15	321.75	960.98	251.10	$2.8 \cdot 10^6$	$4.5 \cdot 10^3$	123.93
b-tag	32.15	10.15	321.46	958.67	251.10	$2.8 \cdot 10^6$	$4.5 \cdot 10^3$	123.93
P_T-balance cut	30.15	8.99	101.70	257.33	109.92	$1.0 \cdot 10^6$	$2.5 \cdot 10^3$	107.49
Central jet veto	28.72	8.51	18.89	47.93	37.81	$194 \cdot 10^3$	$1.4 \cdot 10^3$	100.05
2 lep.w.opp.charge	28.58	8.46	6.59	38.48	22.04	$68 \cdot 10^3$	$1.4 \cdot 10^3$	99.53
lep. p_T cuts	23.91	5.85	1.70	11.72	1.72	102.47	754.30	83.19
$|\Delta R(j,l)| > 0.7$	23.89	5.84	1.70	11.66	1.72	101.19	753.37	82.99
lep. between jets	23.89	5.84	1.70	11.66	1.72	101.19	753.37	82.99
$m_{ll} < 80$ GeV	18.18	1.72	0.68	4.84	1.71	99.91	24.74	1.83
$\Delta\Phi < 2.4$	14.12	1.50	0.56	4.05	1.39	89.66	23.51	1.32
m_T^{WW}	14.01	1.37	0.48	3.49	1.34	24.34	20.42	1.20
$\Delta\Phi(ll, \not{E}_T), p_{T,H}$	5.09	0.62	0.19	1.55	0.11	1.28	6.31	0.41
$\not{E}_T, p_{T,H}$	5.03	0.62	0.18	1.54	0.11	0.00	5.13	0.40
$m_{ll}, \not{E}_T$	4.71	0.60	0.17	1.44	0.11	0.00	0.08	0.00
$\Delta\Phi(ll, \not{E}_T), \Delta\Phi(ll)$	4.36	0.47	0.13	1.04	0.11	0.00	0.04	0.00

Table 4.2.: Cross sections in femtobarn for the signal with $m_{\text{Higgs}} = 160$ GeV and background processes after the various cuts described before. Samples simulated with HERWIG++.

	Higgs	WW (EWK)	WW (QCD)	$t\bar{t}$+jet	$\tau^+\tau^-$jj	$b\bar{b}$jj	Zjj (QCD)	Zjj (EWK)
all events	82.71	28.04	$39 \cdot 10^3$	$31 \cdot 10^3$	$26 \cdot 10^3$	$810 \cdot 10^6$	$424 \cdot 10^3$	$1.2 \cdot 10^3$
E_T cuts	63.57	25.61	$37 \cdot 10^3$	$28 \cdot 10^3$	$16 \cdot 10^3$	$668 \cdot 10^6$	$244 \cdot 10^3$	850.00
jet rap.cuts	30.17	8.74	233.72	$1.0 \cdot 10^3$	504.38	$38.5 \cdot 10^6$	$9.7 \cdot 10^3$	119.95
all jet cuts	27.31	8.41	196.38	854.46	354.48	$30.1 \cdot 10^6$	$7.2 \cdot 10^3$	111.95
b-tag	27.31	8.41	195.21	851.71	354.48	$30.1 \cdot 10^6$	$7.2 \cdot 10^3$	111.95
P_T-balance cut	24.14	6.54	64.93	397.20	203.64	$14.1 \cdot 10^6$	$4.1 \cdot 10^3$	92.20
Central jet veto	20.06	5.07	14.18	147.75	87.19	$4.1 \cdot 10^6$	$1.7 \cdot 10^3$	62.58
2 lep.w.opp.charge	19.42	4.86	7.30	130.02	40.17	$1.0 \cdot 10^6$	$1.6 \cdot 10^3$	60.16
lep. p_T cuts	15.89	3.33	1.58	35.42	2.75	416.91	786.54	49.71
$|\Delta R(j,l)| > 0.7$	15.87	3.32	1.55	35.23	2.75	416.91	785.99	49.61
lep. between jets	15.87	3.32	1.55	35.23	2.75	416.91	785.99	49.61
$m_{ll} < 80$ GeV	12.47	1.08	0.69	15.48	2.73	403.46	52.01	2.84
$\Delta\Phi < 2.4$	9.50	0.94	0.56	13.08	2.10	403.46	42.61	1.89
m_T^{WW}	9.41	0.82	0.47	11.28	1.94	67.24	39.48	1.66
$\Delta\Phi(ll, \not{E}_T), p_{T,H}$	3.33	0.37	0.20	4.94	0.22	0.00	9.44	0.53
$\not{E}_T, p_{T,H}$	3.29	0.37	0.20	4.92	0.22	0.00	7.81	0.49
$m_{ll}, \not{E}_T$	3.06	0.36	0.20	4.74	0.21	0.00	0.13	0.00
$\Delta\Phi(ll, \not{E}_T), \Delta\Phi(ll)$	2.80	0.27	0.15	3.47	0.20	0.00	0.08	0.00

Table 4.3.: Cross sections in femtobarn for the signal with $m_{\text{Higgs}} = 160$ GeV and background processes after the various cuts described before. Samples simulated with PYTHIA.

All the electroweak samples simulated with PYTHIA show a lower cut efficiency for the forward jet cuts as well as a lower central jet veto efficiency than the samples generated with HERWIG++. This also includes the signal, the only exception is the electroweak Z+jets sample. Here the same differences between the two generators after the forward jet cuts and central jet veto can be observed, but the cross section after all cuts in the PYTHIA sample is larger, due to a larger cut efficiency in the cuts involving $\not{E}_T$.

The other backgrounds show a mixed behavior. The $t\bar{t}$ sample simulated with HERWIG++ after all cuts is more than a factor of two smaller than the PYTHIA one. This is by far the biggest remaining background, the cross section remains of the same order as that of the signal. It is clear that the difference between the two generators affects the resulting significance massively.

The behavior is reversed for the W^+W^-+jets sample, where the HERWIG++
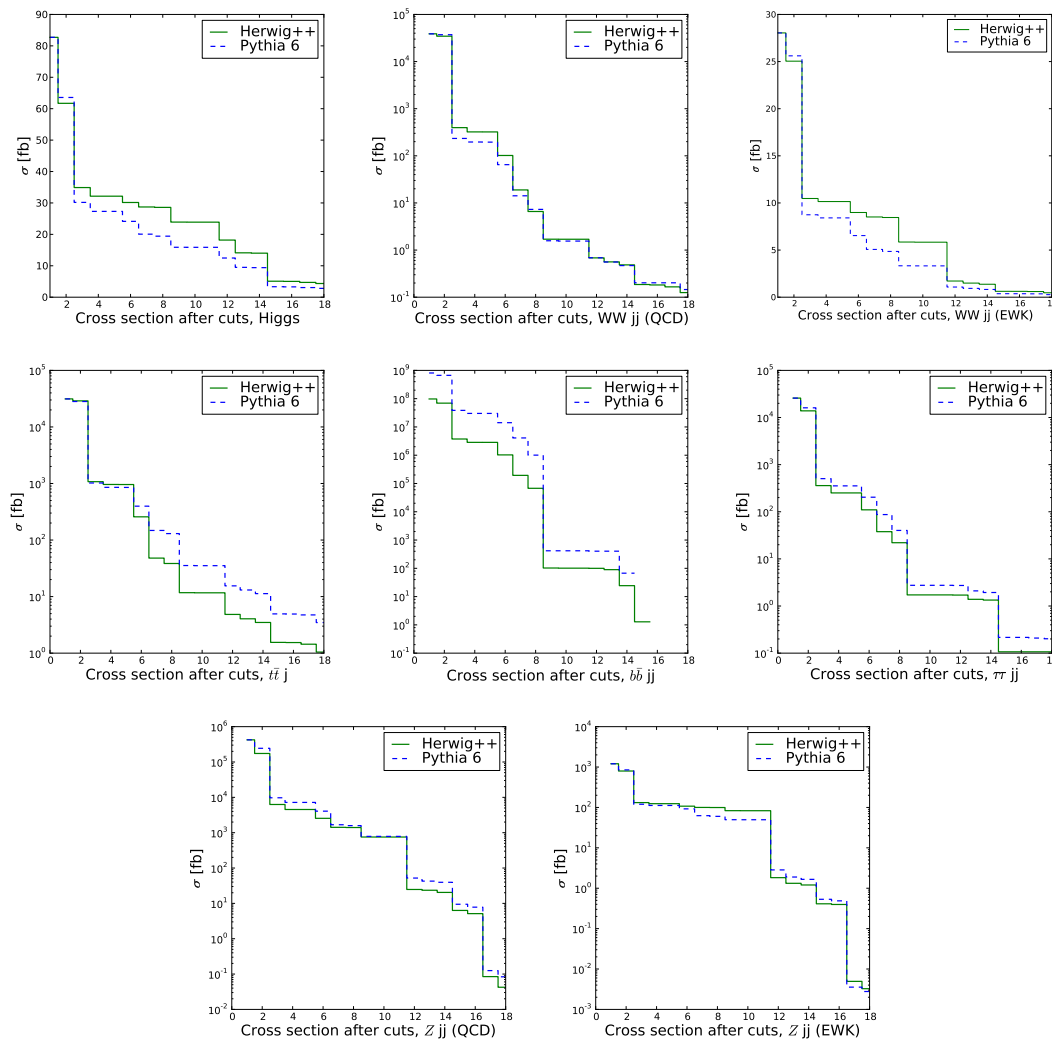
Figure 4.14.: Cross sections of the various processes simulated with Herwig++ and Pythia for a Higgs mass $m_{\mathrm{H}} = 160$ GeV.

sample shows a higher cut efficiency for the forward jet cuts. However, the lepton cuts performed bring the predictions of the two samples close to each other again so that the final cross section after all cuts agrees quite well. The overall background reduction in this process makes the resulting cross section distinctly smaller than the signal and shows that this background is under good control.

The $\tau^+\tau^-$+jets cross section is more affected by the cuts in the Pythia sample as well, resulting in a cross section about a factor two larger than in the Herwig++ case. However, this background as well is under very good control after the cuts, so this difference does not play a big role in the final significance.

A big difference can be observed in the QCD Z+jets production. Here the two generator predictions are quite close for the jet cuts and the central jet veto but

m_{Higgs}	σ_S		σ_B		S/B		$S/\sqrt{B}_{100}$		$\mathcal{L}$ for 5σ	
[GeV]	Hw	Py	Hw	Py	Hw	Py	Hw	Py	Hw	Py
120	0.742	0.404	1.411	3.337	0.526	0.121	6.250	2.213	63.996	510.628
140	2.842	1.476	1.737	4.035	1.636	0.366	21.560	7.346	5.378	46.321
160	4.356	2.805	1.790	4.178	2.434	0.671	32.559	13.721	2.358	13.280
180	4.677	2.460	1.801	4.228	2.597	0.582	34.853	11.965	2.058	17.464
200	3.295	1.731	1.802	4.228	1.829	0.409	24.545	8.419	4.150	35.272

Table 4.4.: Signal and background cross sections, S/B, $S/\sqrt{B}$ for an integrated luminosity of 100 fb^{-1} and luminosity needed for 5σ discovery for the different Higgs masses considered.

differ for cuts on the invariant lepton mass. This is due to soft photon radiation associated with the Z boson decay into leptons. Even though the decay of the Z boson is simulated by MADGRAPH, HERWIG++ is able to add radiative corrections to this decay if the Z boson is present in the Les Houches file. The overall effect of this is small, however as here the tails of the distributions are probed, this can become visible.

The $b\bar{b}$ sample is special in this list, being the only sample which is reduced to zero by the proposed cuts. The two generators differ greatly in their description of this background, but agree that the cuts proposed in [155] are very useful indeed in reducing this background. In addition, if the description found in this study is too optimistic and events pass the cuts, this background could be reduced further with a better understanding of lepton isolation and a veto on leptons stemming from secondary vertices if needed.

A direct comparison for all the processes considered can be seen in Fig. 4.14, where the cross sections after the various cuts are shown graphically for both generators. The numbers on the x axis correspond to the cuts listed in the respective lines in the tables with the cut efficiencies, Tables 4.2 and 4.3.

Table 4.4 shows the combined results for the different Higgs masses. The differences in the description of signal and backgrounds can be seen here as well. The signal cross section in the HERWIG++ samples is larger for all Higgs masses considered here, between about a factor of 1.5 and 2. At the same time the backgrounds show a reciprocal behavior, being between a factor of 1.5 and 2 bigger in the PYTHIA samples.

As a result, the ratio of signal to background S/B is between a factor of two and four larger for the HERWIG++ samples, reaching between $S/B = 2$ and 3 for almost all Higgs masses, except the lightest one at $m_{\mathrm{Higgs}} = 120$ GeV, where the ratio is only about $S/B = 0.7$. In the PYTHIA samples, S/B never exceeds 0.75 and is even lower for $m_{\mathrm{Higgs}} = 120$ GeV. Not surprising, the significance, calculated as $S/\sqrt{B}$ expected is also very different for the two samples. In the table, the predicted significances for an integrated luminosity $\mathcal{L} = 100$ fb^{-1} are shown as well as the integrated luminosity needed for a 5σ excess over background,

which would constitute a discovery.

4.5. Including NLO Parton Shower Merging

The results from the previous section demonstrated the necessity for a better Monte Carlo description of the VBF signal. Especially the additional emissions in the electroweak samples which are crucial for the determination of a central jet veto efficiency should be under better control.

New developments have made it possible to get a better description of these additional emissions. One possibility is to include matrix element corrections into the parton shower, which act in a similar way as the combination with higher level born matrix elements. The cross section prediction is not changed by this method. The built-in VBF matrix element in HERWIG++ contains such a correction, making a better description of additional radiation possible.

In PYTHIA, there is no such correction, which anyway would not help much against a too high level of radiation. However, the program POWHEG implements a NLO QCD calculation of the VBF process matched to the PYTHIA parton shower according to the POWHEG formalism.

These two approaches should provide a better description of at least the hardest additional radiation and therefore get a more consistent description of the central jet activity.

Fig. 4.15 shows the rapidity separation of the two hardest jets after the staggered p_{T} cuts (4.1a) have been applied to them. It can be observed that the peaks of the two distributions lie closer to each other, above the value of 4.2 which is used for the rapidity separation cut. The comparison with the NLO prediction at parton level for the same quantity on the right shows a reasonable agreement. This shows that the overall balancing in the event is now more similar in the two samples and closer to the NLO prediction.

Of course the most interesting observables now are the ones showing the position of the third jet relative to the tagging jets, which give an estimate at how high the central jet veto efficiency for these samples is. Again, the minimum transverse momentum for the additional jets is $p_{\mathrm{T}} > 20$ GeV. Fig. 4.16 shows the distributions for y^* and z^* calculated from the third hardest jet in the upper and lower row respectively.

The distributions are now much closer to each other than in the pure leading order case. Nonetheless still differences in the predictions can be observed which demonstrate the distinct behavior of the two showering approaches. The third jet in the HERWIG++ sample is still more forward, at larger rapidities with respect to the third jet in the PYTHIA sample. However, the matrix element correction does help with the simulation of central jets. The matching with the higher order in PYTHIA reduces the amount of hard central radiation in this sample since the hardest emission is now given by the matrix element and harder emissions from the parton shower are vetoed by the algorithm.
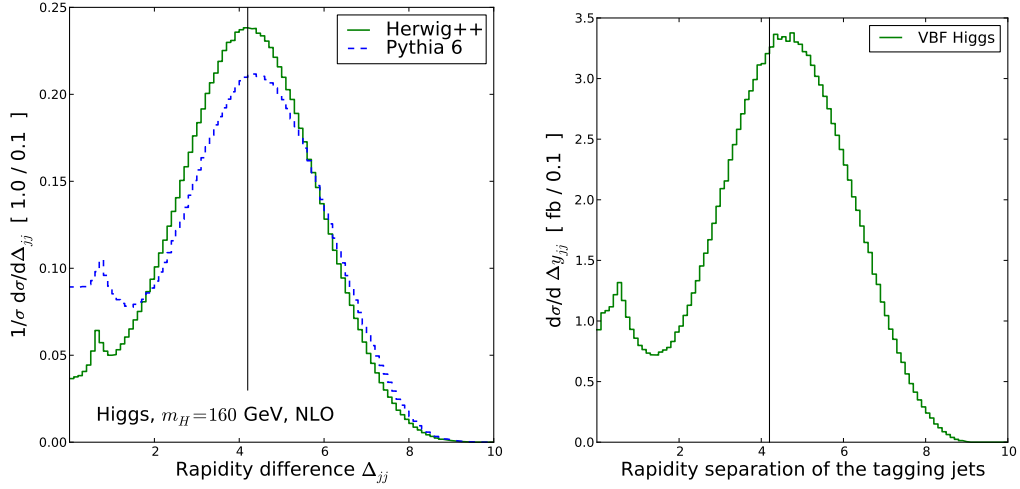
Figure 4.15.: $|\Delta y_{jj}|$ of the two hardest jets in the event. On the left is the simulation with HERWIG++ including matrix element corrections and the PYTHIA + POWHEG sample. The right side shows the prediction from the NLO calculation at parton level.

	Higgs	WW (EWK)	WW (QCD)	$t\bar{t}$+jet	$\tau^+\tau^-$jj	$b\bar{b}$jj	Zjj (QCD)	Zjj (EWK)
all events	82.71	28.04	$39 \cdot 10^3$	$31 \cdot 10^3$	$26 \cdot 10^3$	$97.6 \cdot 10^6$	$424 \cdot 10^3$	$1.2 \cdot 10^3$
E_T cuts	57.77	25.04	$35 \cdot 10^3$	$29 \cdot 10^3$	$14 \cdot 10^3$	$69.4 \cdot 10^6$	$174 \cdot 10^3$	797.50
jet rap.cuts	27.82	10.47	396.33	$1.1 \cdot 10^3$	359.17	$3.7 \cdot 10^6$	$6.3 \cdot 10^3$	131.81
all jet cuts	25.21	10.15	321.75	960.98	251.10	$2.8 \cdot 10^6$	$4.5 \cdot 10^3$	123.93
b-tag	25.21	10.15	321.46	958.67	251.10	$2.8 \cdot 10^6$	$4.5 \cdot 10^3$	123.93
P_T-balance cut	22.84	8.99	101.70	257.33	109.92	$1.0 \cdot 10^6$	$2.5 \cdot 10^3$	107.49
Central jet veto	21.12	8.51	18.89	47.93	37.81	$194 \cdot 10^3$	$1.4 \cdot 10^3$	100.05
2 lep.w.opp.charge	20.90	8.46	6.59	38.48	22.04	$68 \cdot 10^3$	$1.4 \cdot 10^3$	99.53
lep. p_T cuts	16.26	5.85	1.70	11.72	1.72	102.47	754.30	83.19
$|\Delta R(j,l)| > 0.7$	16.25	5.84	1.70	11.66	1.72	101.19	753.37	82.99
lep. between jets	16.25	5.84	1.70	11.66	1.72	101.19	753.37	82.99
$m_{ll} < 80$ GeV	15.67	1.72	0.68	4.84	1.71	99.91	24.74	1.83
$\Delta\Phi < 2.4$	14.74	1.50	0.56	4.05	1.39	89.66	23.51	1.32
m_T^{WW}	11.48	1.37	0.48	3.49	1.34	24.34	20.42	1.20
$\Delta\Phi(ll, \not{E}_T), p_{T,H}$	5.35	0.62	0.19	1.55	0.11	1.28	6.31	0.41
$\not{E}_T, p_{T,H}$	5.33	0.62	0.18	1.54	0.11	0.00	5.13	0.40
$m_{ll}, \not{E}_T$	4.65	0.60	0.17	1.44	0.11	0.00	0.08	0.00
$\Delta\Phi(ll, \not{E}_T), \Delta\Phi(ll)$	4.13	0.47	0.13	1.04	0.11	0.00	0.04	0.00

Table 4.5.: Cross sections in femtobarn for the signal with $m_{\text{Higgs}} = 160$ GeV and background processes after the event selection cuts. Samples simulated with HERWIG++.

The comparison with the NLO predictions at parton level still shows a big difference in the central region, which is mostly due to additional hadronic activity from the underlying event. Here PYTHIA predicts a twice as high level of activity than in the HERWIG++ sample. However, the region around to the tagging jets is now in a reasonable agreement and the overall event number is closer in both samples.

The central jet veto not only considers the third hardest jet in an event but
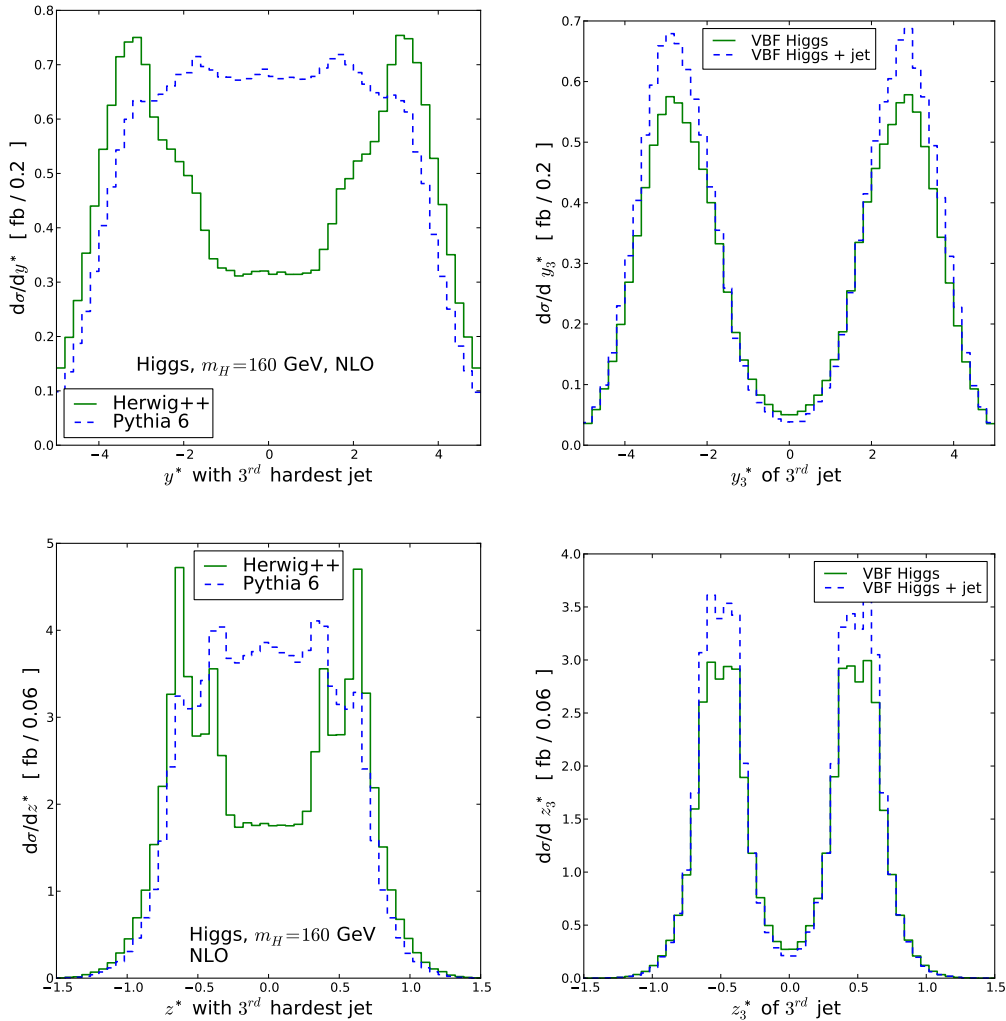
Figure 4.16.: y^* (upper row) and z^* (lower row) calculated from the third hardest jet in Higgs events which pass the forward jet cuts. On the left this is shown for the samples generated with HERWIG++ including matrix element corrections and PYTHIA with combined with `POWHEG`, the right side shows the next-to-leading order QCD distributions at parton level.

all other jets. With a better agreement of the predictions of the third hardest jet provided by the two generators used, it is now interesting to also consider the fourth hardest jet in an event. Of course the predictions of a fourth jet from the parton shower have to be treated with caution, as they will be only accurate in the collinear and soft region. In the case of the VBF topology with the forward jet cuts this does not hold for jets in the central region. On the other hand, the fourth jet from the parton shower or event the matrix element is expected to be soft anyway and therefore the underlying event will play a bigger role in the prediction of this
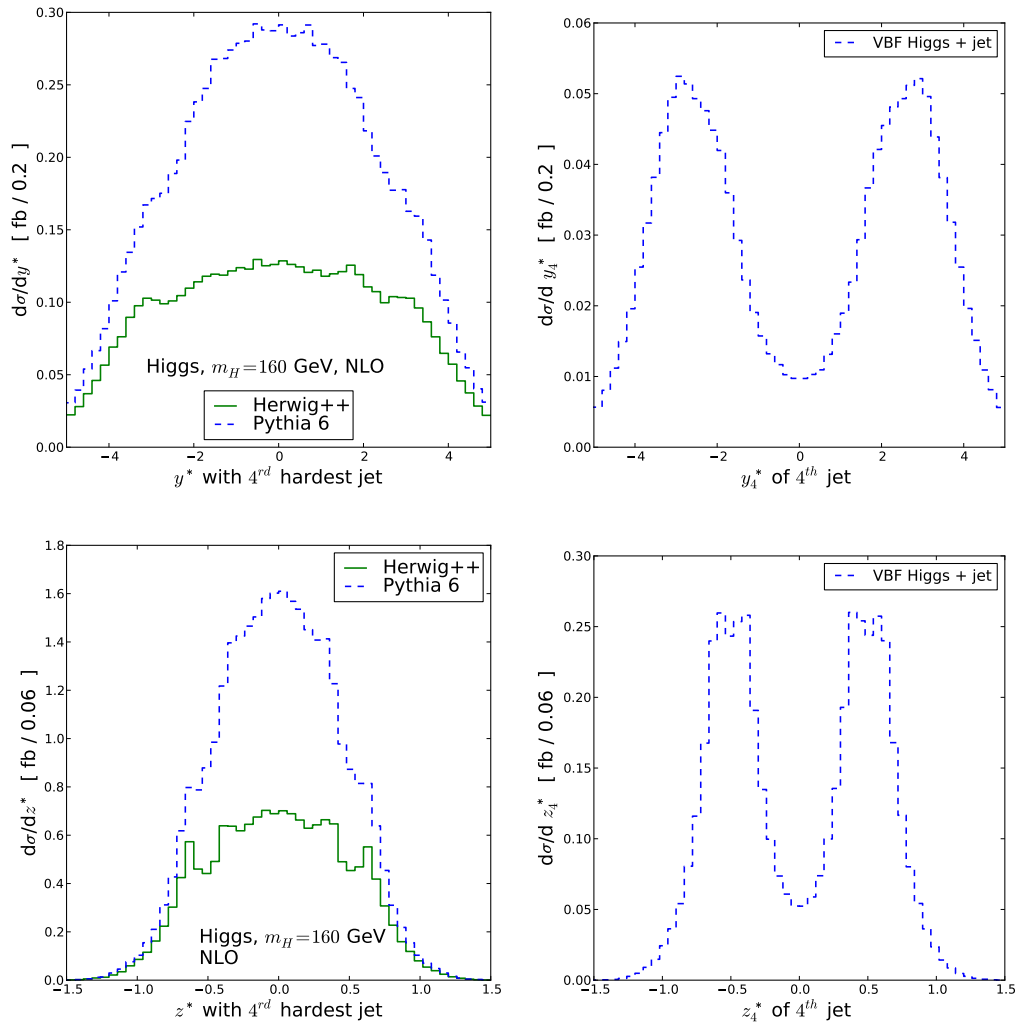
Figure 4.17.: y^* (upper row) and z^* (lower row) calculated from the fourth hardest jet in Higgs events which pass the forward jet cuts. On the left this is shown for the samples generated with HERWIG++ and PYTHIA, the right side shows the leading order QCD distributions at parton level.

jet. A comparison of the predictions by PYTHIA and HERWIG++ with the real emission in the VBF Higgs + 3 jet calculation at NLO is shown in Fig. 4.17. Here the two parton shower predictions show only a minimal resemblance to the LO parton level curve, only in the area around the tagging jets, at $z_4^* \approx \pm 0.5$ some distinguishing features can be observed. The two generators agree in the prediction of the forward jets and both predict a large amount of jet activity in the central region, largely surpassing that found in the matrix element prediction. PYTHIA predicts about twice the number of events with a fourth jet than HERWIG++, which in turn already predicts more than a factor of two more events than the

	Higgs	WW (EWK)	WW (QCD)	$t\bar{t}$+jet	$\tau^+\tau^-$jj	$b\bar{b}$jj	Zjj (QCD)	Zjj (EWK)
all events	82.71	28.04	$39 \cdot 10^3$	$31 \cdot 10^3$	$26 \cdot 10^3$	$810 \cdot 10^6$	$424 \cdot 10^3$	$1.2 \cdot 10^3$
E_T cuts	49.40	25.61	$37 \cdot 10^3$	$28 \cdot 10^3$	$16 \cdot 10^3$	$668 \cdot 10^6$	$244 \cdot 10^3$	850.00
jet rap.cuts	23.59	8.74	233.72	$1.0 \cdot 10^3$	504.38	$38.5 \cdot 10^6$	$9.7 \cdot 10^3$	119.95
all jet cuts	21.67	8.41	196.38	854.46	354.48	$30.1 \cdot 10^6$	$7.2 \cdot 10^3$	111.95
b-tag	21.67	8.41	195.21	851.71	354.48	$30.1 \cdot 10^6$	$7.2 \cdot 10^3$	111.95
P_T-balance cut	19.31	6.54	64.93	397.20	203.64	$14.1 \cdot 10^6$	$4.1 \cdot 10^3$	92.20
Central jet veto	15.95	5.07	14.18	147.75	87.19	$4.1 \cdot 10^6$	$1.7 \cdot 10^3$	62.58
2 lep.w.opp.charge	15.50	4.86	7.30	130.02	40.17	$1.0 \cdot 10^6$	$1.6 \cdot 10^3$	60.16
lep. p_T cuts	11.90	3.33	1.58	35.42	2.75	416.91	786.54	49.71
$|\Delta R(j,l)| > 0.7$	11.89	3.32	1.55	35.23	2.75	416.91	785.99	49.61
lep. between jets	11.89	3.32	1.55	35.23	2.75	416.91	785.99	49.61
$m_{ll} < 80$ GeV	11.49	1.08	0.69	15.48	2.73	403.46	52.01	2.84
$\Delta\Phi < 2.4$	10.79	0.94	0.56	13.08	2.10	403.46	42.61	1.89
m_T^{WW}	8.35	0.82	0.47	11.28	1.94	67.24	39.48	1.66
$\Delta\Phi(ll, \not{E}_T), p_{T,H}$	3.88	0.37	0.20	4.94	0.22	0.00	9.44	0.53
$\not{E}_T, p_{T,H}$	3.87	0.37	0.20	4.92	0.22	0.00	7.81	0.49
$m_{ll}, \not{E}_T$	3.62	0.36	0.20	4.74	0.21	0.00	0.13	0.00
$\Delta\Phi(ll, \not{E}_T), \Delta\Phi(ll)$	3.19	0.27	0.15	3.47	0.20	0.00	0.08	0.00

Table 4.6.: Cross sections in [fb] for the signal with $m_{\text{Higgs}} = 160$ GeV and background processes after the event selection cuts. Samples simulated with PYTHIA.
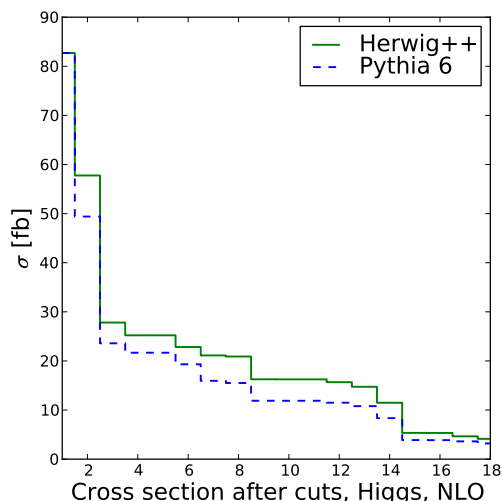
Figure 4.18.: Cross sections of Higgs samples simulated with HERWIG++ and matrix element correction and PYTHIA+ POWHEG for a Higgs mass $m_{\text{H}} = 160$ GeV.

leading order calculation.

This difference is not surprising, as the fourth jet at parton level is expected to follow the tagging jets, as in the case for the third jet, whereas the fourth jet in the full event generators is dominated by the underlying event.

The detailed cross sections after cuts for a Higgs mass of $m_{\text{Higgs}} = 160$ GeV are listed in Tables 4.5 and 4.6.

The two generators now agree better in their description of the Higgs sample,

| m_{Higgs} | σ_S | | σ_B | | S/B | | $S/\sqrt{B}_{100}$ | | $\mathcal{L}$ for 5σ | |
[GeV]	Hw	Py	Hw	Py	Hw	Py	Hw	Py	Hw	Py
120	0.352	0.303	1.411	3.337	0.249	0.091	2.963	1.660	284.765	906.749
140	1.808	1.427	1.737	4.035	1.041	0.354	13.717	7.104	13.286	49.540
160	4.133	3.192	1.790	4.178	2.309	0.764	30.887	15.617	2.621	10.250
180	3.752	2.867	1.801	4.228	2.083	0.678	27.958	13.942	3.198	12.861
200	2.183	1.665	1.802	4.228	1.212	0.394	16.265	8.098	9.450	38.122

Table 4.7.: Signal and background cross sections, S/B, $S/\sqrt{B}$ and required luminosity for a 5σ significance for the different Higgs masses considered, using POWHEG/Matrix element corrections.

this is also illustrated by the graphical representation of the cross section after the various cuts, Fig. 4.18. The rapidity separation cut still yields different cut efficiencies for both the generators, which is not surprising considering the fact that the PYTHIA+ POWHEG sample exhibits a more distinct peak at low values, therefore a larger fraction of the events is cut away.

The central jet veto still yields different veto efficiencies, but not as pronounced as before. This is only to be expected as the distributions of Fig. 4.16 and 4.17 still do not agree. However, the predictions are much closer to each other with this more detailed description of the additional radiation.

The additional cuts bring the two samples closer to each other again, cutting more events in the HERWIG++ sample. As a result, the two cross section agree better with each other after all cuts.

A similar effect can be observed for all Higgs masses considered, the improved simulation leads to a better agreement between the generators considered. However, a perfect agreement can not be found even including the NLO and matrix element corrections.

The complete cross sections and resulting significances can be found in Table 4.7.

Since the backgrounds still differ for the two generators, the resulting ratios S/B and significances are still different, but not that much as in the pure leading order case. The resulting significances now are lower in the HERWIG++ samples and larger in the PYTHIA samples, which is not surprising since that is exactly the behavior of the cross sections. Even though the significances are now more similar in the two generators, the luminosity needed to gain a significance of 5σ differs still up to a factor of two between the two samples.

4.6. Discussion

This study showed that for the understanding of the VBF topology a very detailed understanding of the event simulation is needed. In order to properly describe the

hadronic activity in the vector boson fusion events, higher order matching needs to be employed to gain a consistent description of the jets in the central region. However, even then uncertainties remain with regard to the amount of activity stemming from the underlying event as well as from other collisions in pile-up.

A further important point is the description of top quarks in the parton shower, here the two generators also exhibit big differences. The large uncertainty found in the $t\bar{t}$ + jet sample shows the necessity to include as much of the other $t\bar{t} + n$ jet matrix elements as possible, however, there is no implementation of a matching algorithm to do this in the HERWIG++ shower in the current version. In addition, the implementation of the splitting kernels of massive quark lines which is exact in the HERWIG++ case but only an approximation in PYTHIA might play a role in the prediction of additional jets.

The large differences found in the treatment of the $b\bar{b}$ sample, stemming from the different description of B hadrons show that this needs to be understood in detail as well. The complete reduction of this process in both PYTHIA and HERWIG++ suggests that this background is indeed under good control, but especially the lepton isolation needs to be investigated with regard to this background. Of course, this has to be studied in any case also from data, since both QCD dijet and W+jet events might give rise to fake leptons in their jets. These leptons are also deemed to be removed by lepton isolation cuts.

It is interesting to note the problems encountered with the Z+jets sample, where a discrepancy in the Z mass could be observed.

The discrepancies found in the Monte Carlo description show that it is vital to understand as much of the backgrounds from data as possible. Both $t\bar{t}$ as well as Z+jets have large cross sections and can be studied with early data. In addition, the Z+jets process might offer the possibility to investigate vector boson fusion from data. This would then give a handle on the predictions of the central jet veto efficiency in the signal.

However, in the overall picture both generators show that it is possible to extract the Higgs signal from data and that the proposed cuts indeed allow for a decisive reduction of backgrounds.

Chapter 5

Z+Jets Events in Collision Data

The Z+jets channel is an important background contribution to the VBF Higgs production decaying into two leptons and missing energy. This background has a large cross section and has no neutrinos at matrix element level. Therefore the missing transverse energy is expected to be small in most events, however, with the expected uncertainty on the reconstructed missing transverse energy some events might survive the event selection cuts.

The Z+jets and Drell-Yan backgrounds give rise to two peaks in the invariant mass distribution $m_{\ell\ell}$ of same flavor, opposite sign pairs of leptons. The Drell-Yan process peaks at low values of $m_{\ell\ell}$, corresponding to the photon resonance, the Z + jets background exhibits a peak around the Z boson mass.

The region of interest for the signal as described in the previous section lies between these two peaks and is expected to be distributed around half of the Higgs mass. Therefore, the majority of the Z + jets and Drell-Yan backgrounds can be removed by requiring the invariant mass of same-flavor lepton pairs to be larger than 10 GeV and lower than 80 GeV, as described in Chapter 4.3. This of course only holds for the Higgs mass range between 120 and $\approx$ 200 GeV, for higher Higgs masses the upper bound of 80 GeV is too low. This selection is effective in suppressing the Drell-Yan and Z+jets background significantly. However, even in the dilepton mass region between the peaks, some of this background remains.

Muons are chosen for this validation because they are easier to reconstruct and identify than electrons and therefore have a higher efficiency. In addition the energy and momentum resolution of muons is much better as the muon reconstruction uses the combined information from tracker and muon system. Of course, a similar exercise should be performed including electrons, but due to their more involved reconstruction, this is beyond the scope of this work.

The large cross section of this background allows to determine this background from data, alredy during the first year of LHC operations at 7 TeV a large number of Z + jets events were recorded by the CMS experiment. With these events it is now possible to validate the description of the Z+jets background by Monte Carlo programs in the region where its cross section is large in order to predict

the validity of the description in the signal region of interest. The aim is to fit the available data to Monte Carlo, starting from low mass peak and Z mass peak and use the fitted function as a prediction for the intermediate mass region.

In addition, the electroweak production of Z+ two jets is a vector boson fusion process, as described in Sec. 4.2. This allows to study the behavior of the rapidity gap in VBF process from data if it is possible to separate the electroweak Z+ two jets sample from the QCD one [159, 160].

5.1. Event Selection

The LHC operations at an energy of 7 TeV in 2010 provided an integrated luminosity of 35.9 pb^{-1}, with a large amount of events with muon pairs and jets measured in the CMS experiment [161].

Starting from inclusive quantities, the Monte Carlo description of these events is validated. The dominant part is expected to be Z boson production with jets. Since for the background in VBF processes events with two and more additional jets are relevant, different jet multiplicities need to be studied. This of course requires a matched Monte Carlo sample. However, as currently HERWIG++ is not able to generate a matched sample, only PYTHIA, which is able to simulate a full Z+jets spectrum using the MLM formalism is considered in this validation. A comparison of different Monte Carlo generators however is of major importance and should be performed as soon as HERWIG++ is able to produce inclusive samples.

The samples used in this work were generated using Les Houches files generated with MADGRAPH. Two different PYTHIA tunes, D6T and Z2, were considered in this analysis. D6T employs the virtuality ordered shower and is a relatively old tune, based on measurements at the Tevatron collider and older machines and is using extrapolations in order to make predictions for LHC energies. The tune Z2 uses the parton shower ordered in transverse momentum and was tuned to the first collision data at the LHC. Therefore the description of the underlying event does not rely solely on extrapolations to LHC energies but already is able to properly describe the first minimum bias data obtained at the LHC.

In addition, a $t\bar{t}$ sample generated with POWHEG is included as this is a possible addition to the dimuon sample. As the POWHEG sample relies on the p_T ordered shower, there is no sample available using the D6T tune. However, as this is only expected to be a minor background, the exact implementation of the parton shower is not expected to make a big difference in this case and the $t\bar{t}$ sample is used as background for both Z boson samples.

All events with two opposite sign muons are selected as candidates for the subsequent selection process. The muons have to pass certain quality cuts, which follow the recipe of the CMS Vector Boson Task Force. First, they are required to be so-called global muons, which means they have to be reconstructed from a trajectory starting in the muon system with a matching one in the tracker.
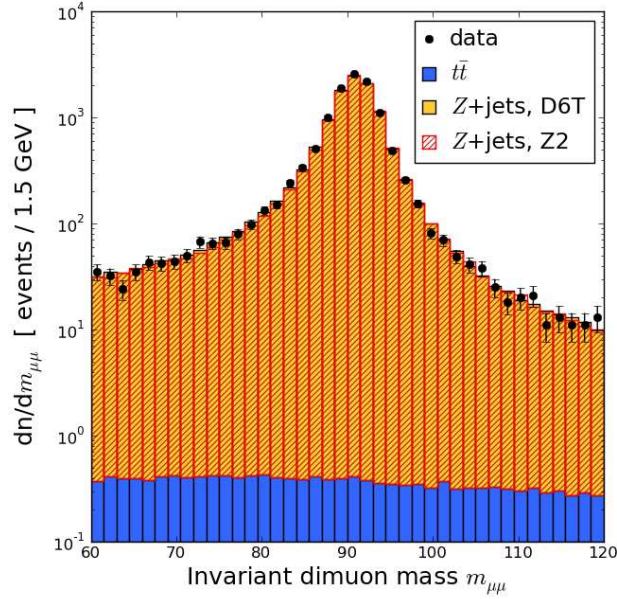
Figure 5.1.: Invariant mass of the same flavor lepton pairs.

This reduces the fake muon rate and gives a higher precision on the momentum reconstruction. In addition, the muons have to be isolated, that means that the activity in a cone around the muon trajectory is small in comparison to the muon transverse momentum. This activity is calculated by summing the energy of tracks and the energy deposits in the electromagnetic and hadronic calorimeters in a cone of radius $R = 0.3$ around the muon trajectory. The isolation criteria used in this work is defined as a relative isolation,

$$\text{Iso}_{\text{rel}}(\mu) = \frac{\sum_{\Delta R < 0.3} p_{\text{T}}^{\text{tracks}} + \sum_{\Delta R < 0.3} p_{\text{T}}^{\text{ECAL}} + \sum_{\Delta R < 0.3} p_{\text{T}}^{\text{HCAL}}}{p_{\text{T},\mu}} < 0.15 \ . \quad (5.1)$$

Furthermore the trajectory needs to contain at least ten hits in the tracker and pixel detector as well as hits in the muon system. The $\chi^2/d.o.f.$ of the fit reconstructing the muon trajectory needs to be smaller than ten. As a kinematic constraint, the muons are required to have a transverse momentum above 20 GeV and a pseudorapidity $|\eta| < 2.1$.

The jets considered in this work are anti-k_{T} Particle Flow jets with a jet resolution parameter of $R = 0.5$. They have to fulfill the so-called *loose jet-ID* requirements [162], which can be summarized to a non-zero charged hadron fraction in the jet. In addition, the transverse momentum is required to be above $p_{\text{T,min}} = 20$ GeV. The jets are then corrected according to the level 2 and 3 corrections specified in [148, 149].
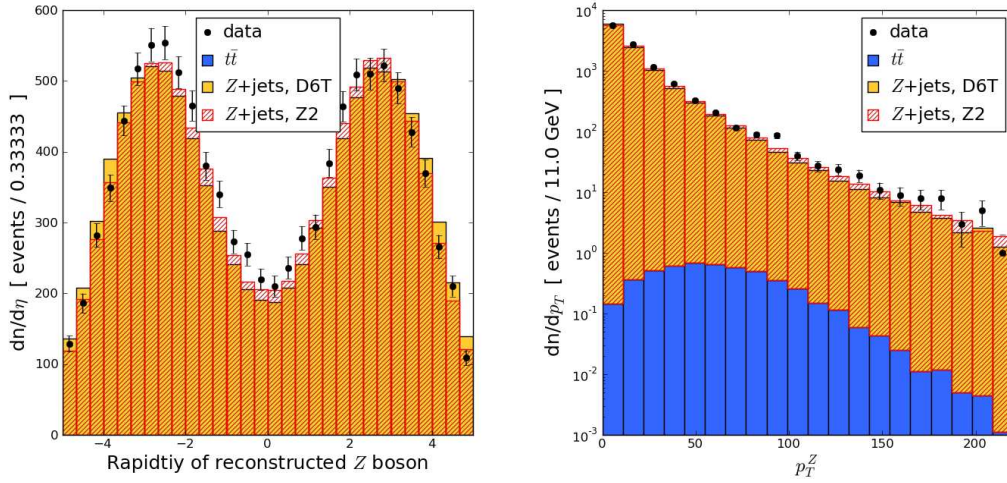
Figure 5.2.: Rapidity (left) and transverse momentum (right) of the Z boson.
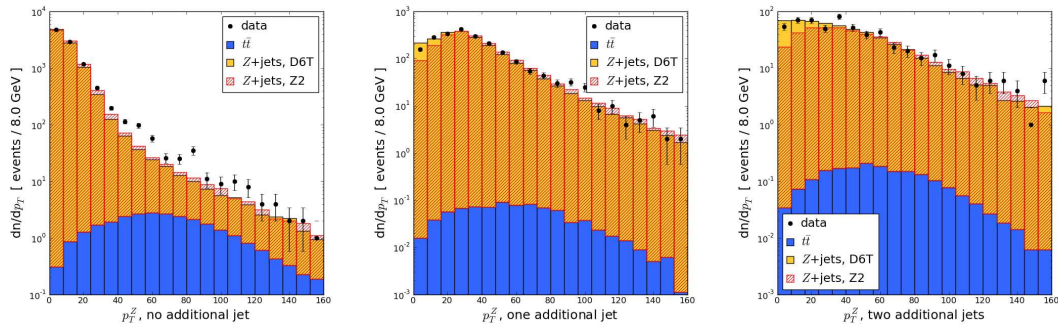
Figure 5.3.: Transverse momentum of the Z boson with no (left), one (central) and two (right) associated jets.

5.2. Z Boson Reconstruction

The selection of events with two reconstructed muons passing the cuts described above with opposite charges leads to 12141 dimuon events in the mass range of 60 GeV $< m_{\ell\ell} <$ 120 GeV. Fig. 5.1 shows the invariant mass of these lepton pairs. In this analysis, events where $m_{\mu^+\mu^-}$ is consistent with the Z boson mass, 80 GeV $< m_{\mu^+\mu^-} <$ 100 GeV, are considered. This is a sensible starting point as in the low-mass region, where the peak from the Drell-Yan contribution is situated, threshold effects from the low transverse momentum of the muons play a role and trigger effects need to be understood in more detail.

The rapidity and the transverse momentum of the reconstructed Z boson are shown in Fig. 5.2. In general, a reasonable agreement between data and Monte Carlo can be observed. It is however interesting to note that the rapidity of the
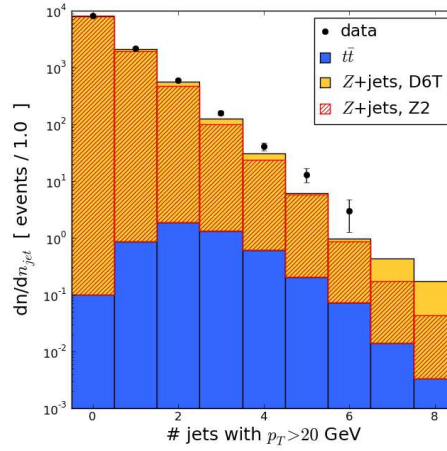
Figure 5.4.: Number of jets in the Z boson events.

Z boson is more accurately described by the sample generated using the Z2 tune, whereas the D6T sample predicts the Z boson more in the forward region.

The transverse momentum of the Z boson is in addition also studied per jet multiplicity. This is shown in Fig. 5.3 for the Z boson with zero, one and two additional jets. Again, the overall shape is described quite well by the Monte Carlo samples, but in the low p_T region, deviations can be seen. Especially the region of low Z boson transverse momentum is sensitive to contributions from the underlying event or other non-perturbative effects. For the region where $p_T^Z < 20$ GeV, none of the two tunes gives an adequate prediction, the D6T sample overshoots the data whereas the Z2 sample predicts not enough events in this region. This shows the quite large uncertainty associated with the non-perturbative contributions dominating for the region of low transverse momentum. Even though the Z2 tune includes a more detailed description of the non-perturbative models describing the underlying event, it does not fully agree with the Z boson spectrum. This shows that here more effects need to be taken into account.

ratio	Data	MC (D6T)	MC (Z2)
1/0	$0.268 \pm (0.033)$	$0.264 \pm (0.033)$	$0.490 \pm (0.034)$
2/1	$0.274 \pm (0.062)$	$0.270 \pm (0.064)$	$0.490 \pm (0.069)$
3/2	$0.266 \pm (0.121)$	$0.222 \pm (0.131)$	$0.455 \pm (0.147)$
4/3	$0.259 \pm (0.236)$	$0.240 \pm (0.271)$	$0.487 \pm (0.309)$
2/0	$0.073 \pm (0.052)$	$0.071 \pm (0.053)$	$0.240 \pm (0.057)$
3/1	$0.073 \pm (0.101)$	$0.060 \pm (0.111)$	$0.223 \pm (0.124)$
4/2	$0.069 \pm (0.197)$	$0.053 \pm (0.224)$	$0.222 \pm (0.254)$
3/0	$0.020 \pm (0.091)$	$0.016 \pm (0.100)$	$0.109 \pm (0.112)$
4/1	$0.019 \pm (0.178)$	$0.014 \pm (0.204)$	$0.109 \pm (0.230)$
4/0	$5.1 \cdot 10^{-3} \pm (0.2)$	$3.8 \cdot 10^{-3} \pm (0.2)$	$53.2 \cdot 10^{-3} \pm (0.2)$

Table 5.1.: Ratios of the different jet multiplicities.

5.3. Inclusive Jet Observables

To validate the description of the data first inclusive observables constructed from jets are compared before moving to more exclusive ones resembling the VBF topology.

An obvious choice to consider is the number of jets and the ratio of the different jet multiplicities. Fig. 5.4 shows the number of jets, i.e. reconstructed and corrected objects passing the above mentioned loose jet identification cuts with a transverse momentum $p_{\mathrm{T}} > 20$ GeV in the events with a reconstructed Z boson. A good agreement for the low jet multiplicities between data and Monte Carlo can be observed, especially for the D6T tune. The Z2 tune undershoots the amount of events with two and more jets, the D6T tune starts to underestimate the jet multiplicity starting from three additional jets.

This can be seen more clearly regarding the ratios of the different jet multiplicities, shown in Tab. 5.1. The ratio of events with $n + 1$ jets to events with n jets is very stable up to 4 jets and similar for other ratios. Naively, the expectation for the $(n + 1)/n$ ratio would be in the order of α_s, since for an additional jet a further coupling with the strong coupling is needed. The fact that the measured ratio is bigger than that is however not surprising, as also different contributions from PDFs play a role. However, the overall description shows that an additional jet does indeed decrease the cross section by a constant factor to a good approximation.

The ratios of $(n + 1)/n$ jet events are described by the D6T PYTHIA sample quite well, to a lesser extent also by the Z2 tune. Again it can be seen that the relative amount of high jet multiplicities in data is higher than in both PYTHIA samples, with D6T being closer to the data. Here a more detailed examination of the higher jet multiplicities could be interesting, since it is possible that the relatively soft additional jets do not stem from the hard process but from the
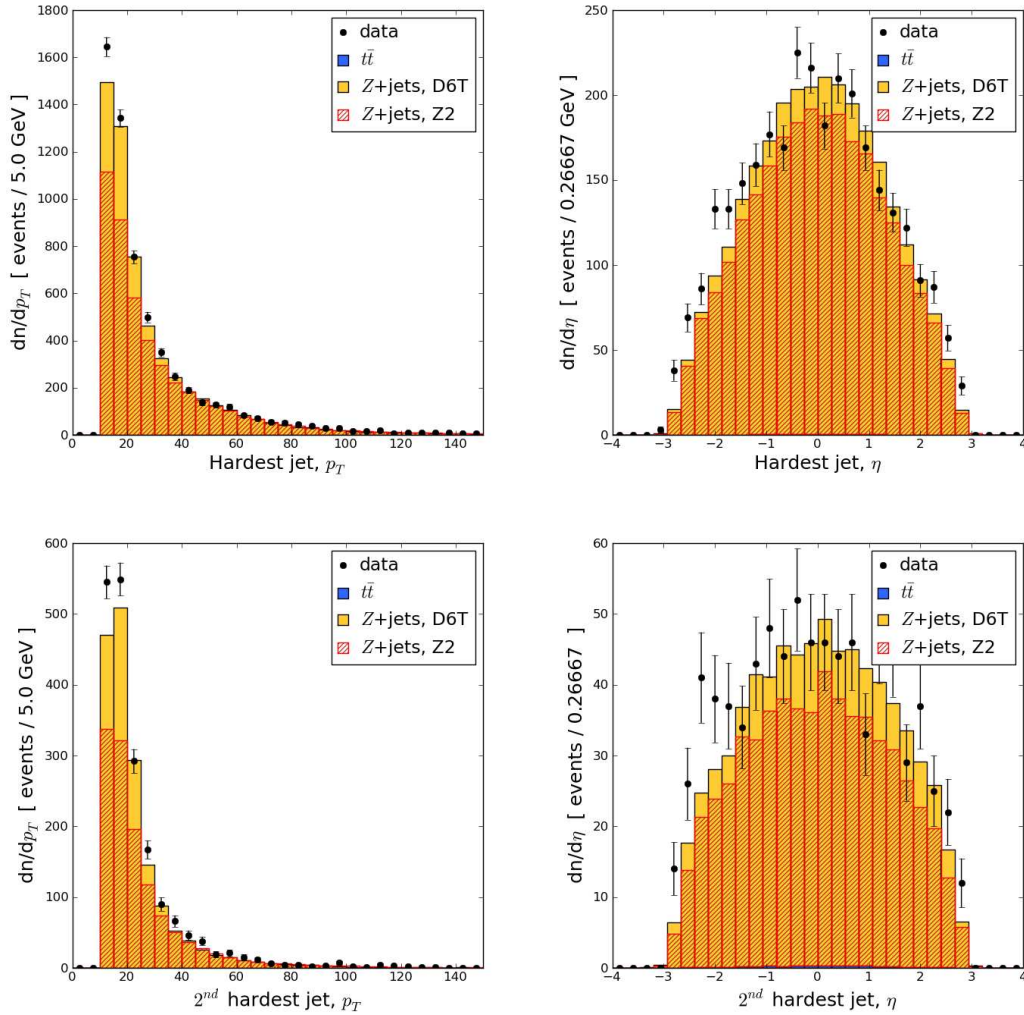
Figure 5.5.: Transverse momentum (left) and rapidity (right) of the hardest (upper row) and 2nd hardest jets in the Z boson events.

underlying event.

In the two Monte Carlo samples the maximum jet multiplicity simulated at matrix element level is three, therefore these samples should in principle be able to describe the same multiplicity in data adequately. The fact that none of the two samples is able to fully describe this accurately shows that non-perturbative models in both PYTHIA tunes need a more detailed understanding.

The transverse momentum and rapidity of the first two jets in the events are shown in Fig. 5.5. The p_T distributions are calculated before the p_T cut, only requiring the loose jet identification including a $p_T > 10$ GeV cut. They show that also in this observable the low region is underestimated by the Monte Carlo samples. Again, Z2 predicts less events over the whole range, whereas D6T agrees

(a) H_{T} calculated from all jets

(b) H_{T} calculated two jet events
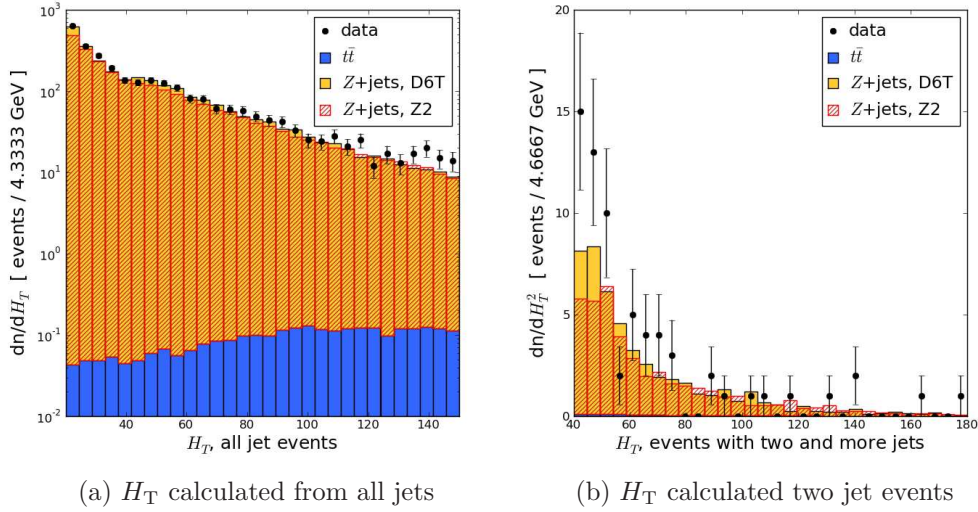
Figure 5.6.: H_{T} calculated from the jets above $p_{\mathrm{T,min}} = 20$ GeV.

better for regions with higher transverse momenta. A similar behavior can be observed in the rapidity distributions. The central rapidity region is described quite well by the D6T tune, however show undershoots the data in the forward regions. The Z2 prediction is again too low over the whole region.

An interesting inclusive observable is H_{T}, the scalar sum of the transverse momenta of the objects in the event. The definition of this quantity is ambiguous, depending on the aim of the study only jets can be considered, or in addition leptons, missing energy or the reconstructed Z boson could be included.

Since the objects of interest in this study are jets, here H_{T} is defined as the scalar sum of the transverse momenta of all the jets with $p_{\mathrm{T}} > 20$ GeV in the event,

$$H_{\mathrm{T}} = \sum_{p_{\mathrm{T}} > 20 \text{ GeV}} p_{\mathrm{T}}^{\mathrm{jet}} . \tag{5.2}$$

The distribution for this quantity is shown in Fig. 5.6. It is steeply falling and shows a good agreement between data and Monte Carlo. Especially D6T gives a very good description, whereas the Z2 sample again undershoots the low region.

In addition, since for the VBF topology at least two jets are needed, the same observable is calculated for events with at least two jets. This shows in more detail the hadronic activity in these events. However, the overall number of these events is quite small, resulting only in a limited description of this observable. But even with the small amount of available data, it can be seen that the distribution in the data follows the prediction from Monte Carlo reasonably well. Nonetheless, the fact that high jet multiplicities are not adequately described by both tunes can be seen, as both Monte Carlo samples predict too few events, again especially in the low region.

(a) Rapidity separation
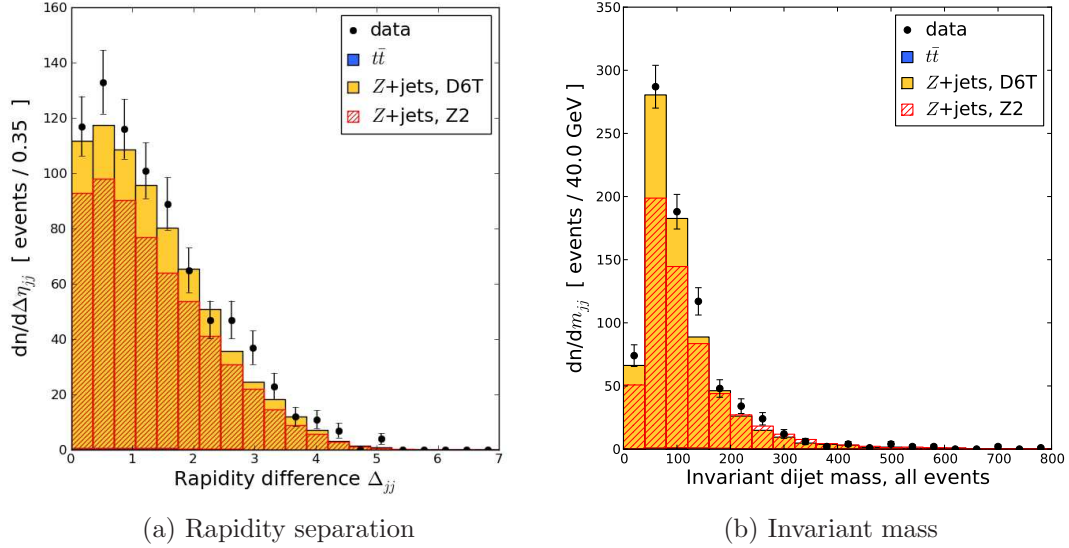
(b) Invariant mass

Figure 5.7.: Rapidity separation and invariant mass of the two hardest jets in the event.
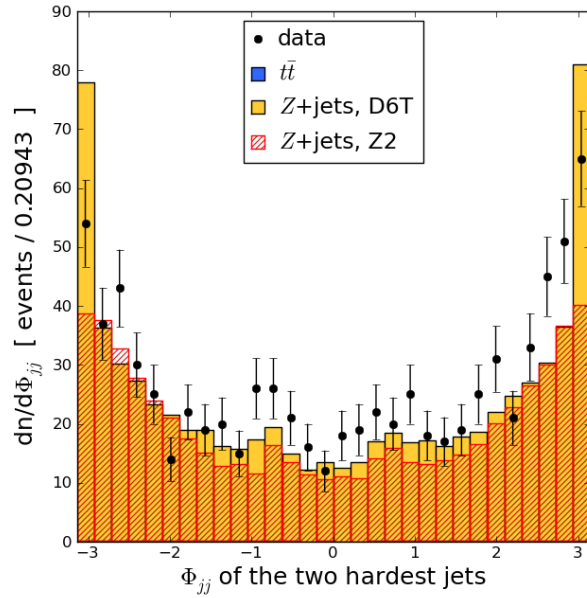
Figure 5.8.: Φ_{jj} between the two hardest jets in the event.
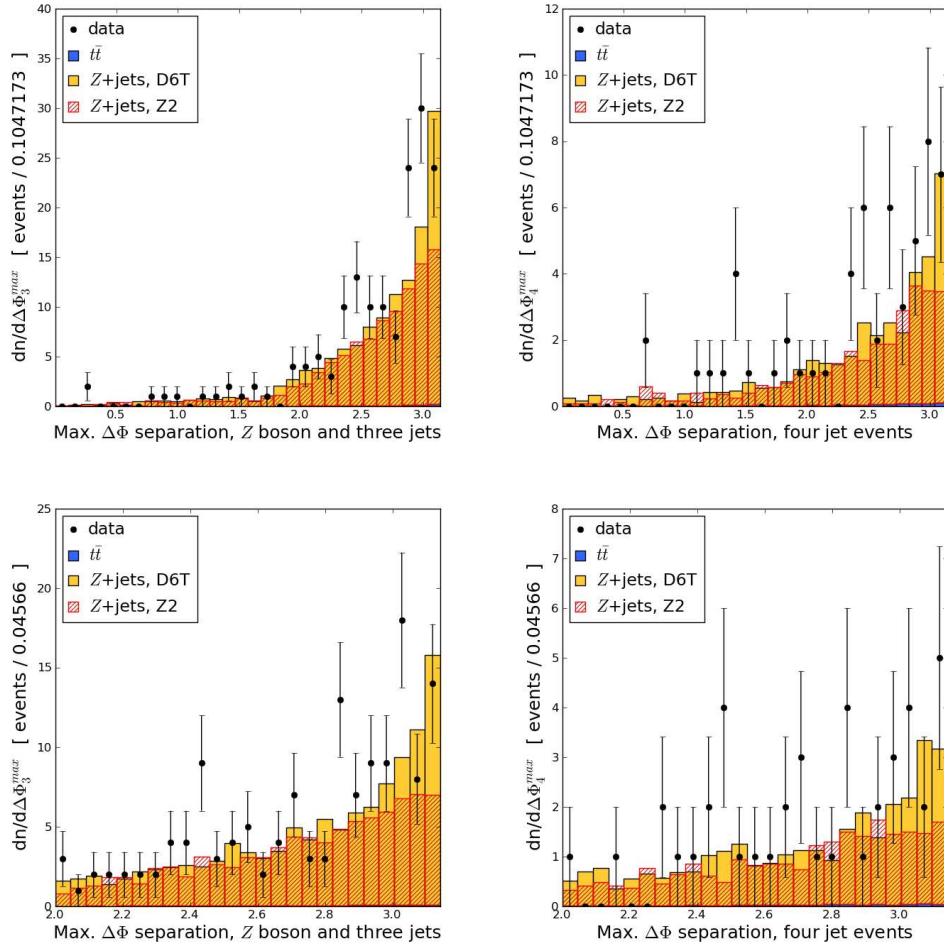
Figure 5.9.: $\varphi_{\max,3}$ (left) and $\varphi_{\max,4}$ (right) calculated from Z+3,4 jet events.

It is interesting to note the contribution from the $t\bar{t}$ background. In this sample each event contains at least two jets, stemming from the b quarks from the top quark decays. Therefore the contribution increases with growing H_T. However, the overall contribution remains very small.

In the case of events with two and more jets with possible VBF contributions, important quantities are the invariant mass of the two hardest jets in the event and the rapidity separation between them. As described in Sec. 4.3, cuts on these quantities can be used to remove the QCD induced backgrounds in VBF events.

The rapidity separation between the two hardest jets is shown in Fig. 5.7a. Again, the Monte Carlo sample is in relatively good agreement with the measured data, with similar shortcomings as noted before. This is a steeply falling distribution, since most of the jets stem from QCD production, and therefore lie close to each other. This is a further demonstration of the usefulness of a cut requiring large rapidity separations to suppress QCD induced backgrounds.

The invariant mass of the two hardest jets is shown in Fig. 5.7b. This distribution shows a peak at low values and then drops rapidly, leaving the bulk of the events below 400 GeV. As in the case of the rapidity separation, this is a useful observable to cut on, reducing the background significantly. Again, D6T gives a better description of the data than Z2.

Further observables sensitive to the description of multijet events can be constructed by probing the angles between the jets and the reconstructed Z boson. In the case of two and more jets in the event, there are at least three objects emerging from the hard process. The angular distribution between these objects can give insight into the underlying process. For events with two and more jets, the Φ_{jj} observable is of interest, as this allows to probe the $\mathcal{CP}$ nature of the Higgs boson coupling [163].

It is defined as

$$\Phi_{jj} = \begin{cases} \varphi_{j_1} - \varphi_{j_2} & \text{if } y_{j_1} \geqslant y_{j_2} \\ \varphi_{j_2} - \varphi_{j_1} & \text{if } y_{j_1} < y_{j_2} \end{cases} \tag{5.3}$$

where φ_{j_1} and φ_{j_2} are the azimuthal angles of the two tagging jets. The resulting angle is mapped on the interval $(-\pi, \pi]$. The sorting in rapidity allows to avoid the averaging when calculating the angular separation, making the observable sensitive to the underlying coupling in the Higgs case.

This quantity is shown in Fig. 5.8. It is interesting to note that the D6T sample predicts very sharp peaks in this distribution at $\pm\pi$ corresponding to an increased amount of back-to-back jets which is not that distinct in the data. The Z2 sample on the other hand predicts too few events, exhibiting barely any peak at all in the back-to-back region. In the central region, none of the samples predicts enough activity.

For three and four jets, the observables

$$\varphi_{\max,3} = \max_{i,j \in \mathrm{Z,jet}} \Delta\varphi_{i,j} \quad \text{with } n_{jets} = 3 \tag{5.4}$$

and

$$\varphi_{\max,4} = \max_{i,j \in \mathrm{jet}} \Delta\varphi_{i,j} \quad \text{with } n_{jets} = 4 \tag{5.5}$$

can be introduced. They allow to study the couplings involved, especially $\varphi_{\max,4}$ is also sensitive to double parton scattering, that is two hard interactions in one proton proton collision [164].

Fig. 5.9 shows the distributions for these two observables. As currently the number of three and four jet events is rather small, this observable is not very illuminating. Nonetheless, also in this case the Monte Carlo description by the D6T sample is acceptable within errors. The Z2 sample again predicts a number of events that is too low. The lower two plots show only the region of large angles, which would exhibit a distinct increase in the presence of double parton scattering events. It is obvious, that with the currently available data, no such effect is visible.

5.4. Exclusive Quantities

In the VBF analysis, hard cuts are applied on the rapidity separation and invariant mass of the two hardest jets. Therefore, this kinematic region needs to be studied in more detail, as a good description of the Z + jets background is needed especially in this kinematic region. This is of course a difficult venture, as these cuts are designed such that among others this process has only a small cross section in the cut region.
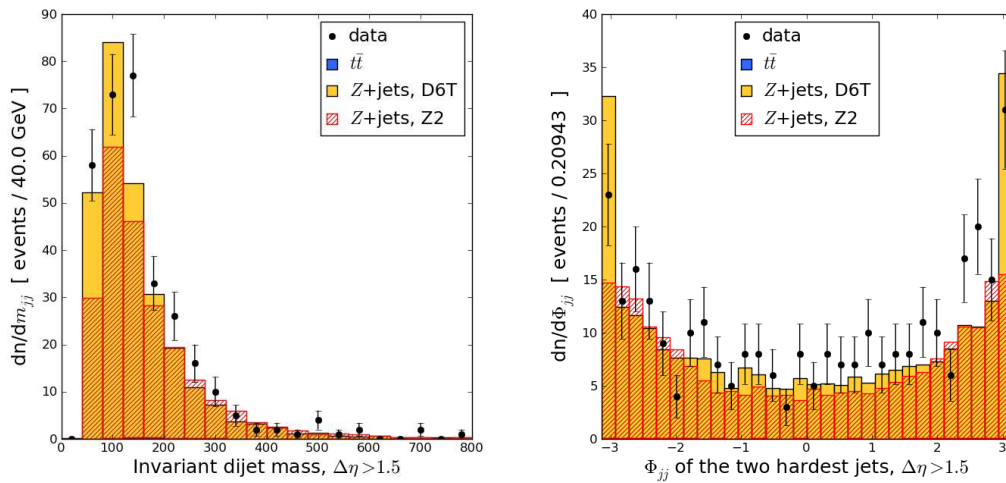
Figure 5.10.: Invariant mass of the hardest jet pair (left) and Φ_{jj} (right), $\Delta\eta_{jj} > 1.5$.

To circumvent the limited amount of statistics, the validation of VBF-like topologies starts with smaller rapidity separation cuts. First, the cut $\Delta\eta_{jj} > 1.5$ is studied. This small cut already removes quite a number of events and gives the possibility to study the activity between the jets.

The invariant mass of the hardest jet pair is shown in Fig. 5.10 on the left. As can be expected, the low mass region is affected by the cuts on the rapidity separation, as jet pairs with a larger angular separation have a higher invariant mass. This is described quite well by the D6T sample, again the Z2 sample is too low in its prediction.

The Φ_{jj} observable after this cut is very similar to the one without a cut on the rapidity separation. Here again the distribution peaks at values $\pm\pi$, and again the D6T sample somewhat overshoots the data at these peaks but gives a good overall description. Not surprisingly, the Z2 sample does not predict enough events over the whole range.

The observables y^* and z^* introduced in Eq. (4.2) can now be used to study both the position of the reconstructed Z boson and of additional jets relative to the position of the two hardest jets.
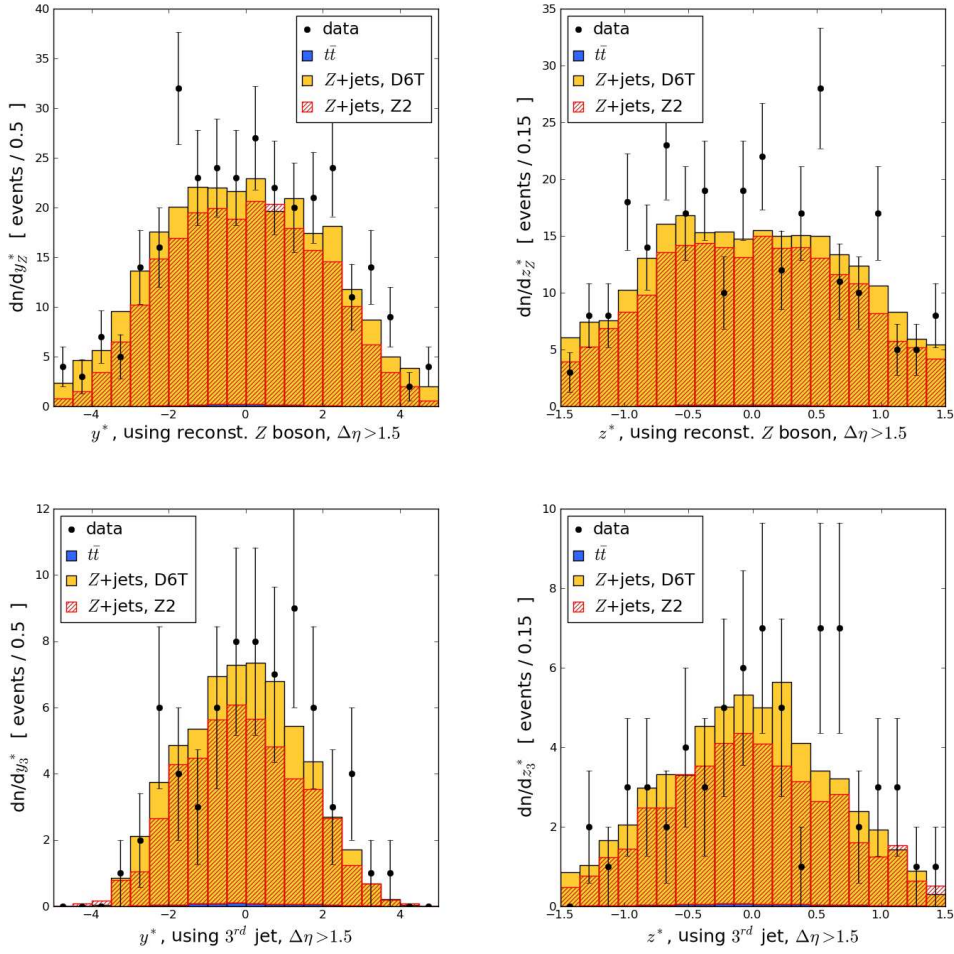
Figure 5.11.: y^* (left) and z^* (right) calculated from the reconstructed Z boson (upper row) and from third jets (lower row), $\Delta\eta_{jj} > 1.5$.

The distributions for these two observables obtained from the two hardest jets and the reconstructed Z boson are shown in Fig. 5.11. It can be seen that the Z boson lies preferably between the two jets. Keeping in mind that the minimum rapidity separation between the two jets is only 1.5, the distributions of y^* show that many of the Z bosons and additional jets lie outside of this gap. This gets more clear from the distributions of z^*, where a value $|z^*| > 0.5$ denotes a Z boson or jet outside the rapidity gap defined by the two hardest jets.

From the distributions it can be seen that the reconstructed Z bosons tend to lie around the tagging jets but not necessarily between them in rapidity. This can be explained by Z bosons balanced by a hard jet which results in a similar rapidity with an opposite ϕ angle. Additional jets now are most likely to be close to the hardest jet, so the Z boson is balanced against a two-jet system. This behavior is present both in data and Monte Carlo events.
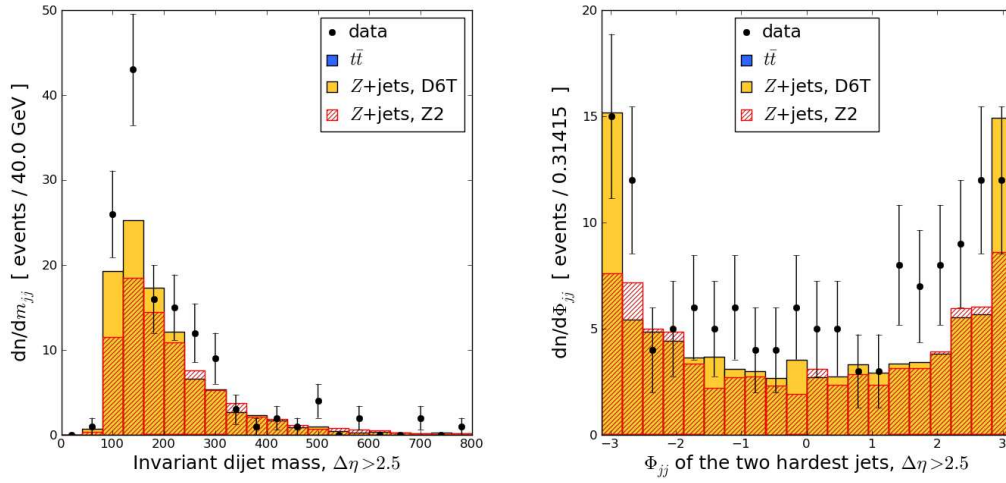
Figure 5.12.: Invariant mass of the hardest jet pair (left) and Φ_{jj} (right), $\Delta\eta_{jj} > 2.5$.

The additional jets tend to lie between the two hardest jets, as can be expected in QCD jet events. The z^* observable shows this in detail, both in data and Monte Carlo.

The description given by the D6T sample is in quite good agreement with the data, the Z2 prediction is again too small. Especially for z_3^*, calculated from events with three jets, this is to be expected already from the low jet multiplicity. The overall shape however is described quite well.

With the agreement found in the observables with the rapidity separation cut of $\Delta\eta_{jj} > 1.5$ it is interesting to explore the rapidity separation further. Even though this will mean a significant decrease in the number of events, it can nonetheless give a first impression of the description in this area.

Applying the cut $\Delta\eta_{jj} > 2.5$ reduces the amount of available events even further, but still some preliminary studies can be performed.

Of course the observables considered so far are as well of interest after this stricter cut. Fig. 5.12 shows the invariant mass of the jet pair and Φ_{jj}. Not surprisingly, the invariant mass of the jet pair peaks at a higher value, the low-mass region is even more reduced compared to the distribution with the $\Delta\eta_{jj} > 1.5$ cut. The distributions show a reasonable agreement between data and Monte Carlo simulation. The angular separation Φ_{jj} is again similar to the distributions for lower rapidity cuts, again exhibiting peaks at $\pm\pi$.

The distributions for y^* and z^*, Fig. 5.13 calculated from events with this rapidity separation are plagued by low statistics. The Z boson rapidity is predicted to be close to the two hardest jets, which can be seen explicitly from z^*, which peaks around $z^* \pm 0.5$. The data seems to agree with this prediction, however, the low number of events does not allow to make a strong statement about this.

The same observables calculated with additional jets have even less statistics,
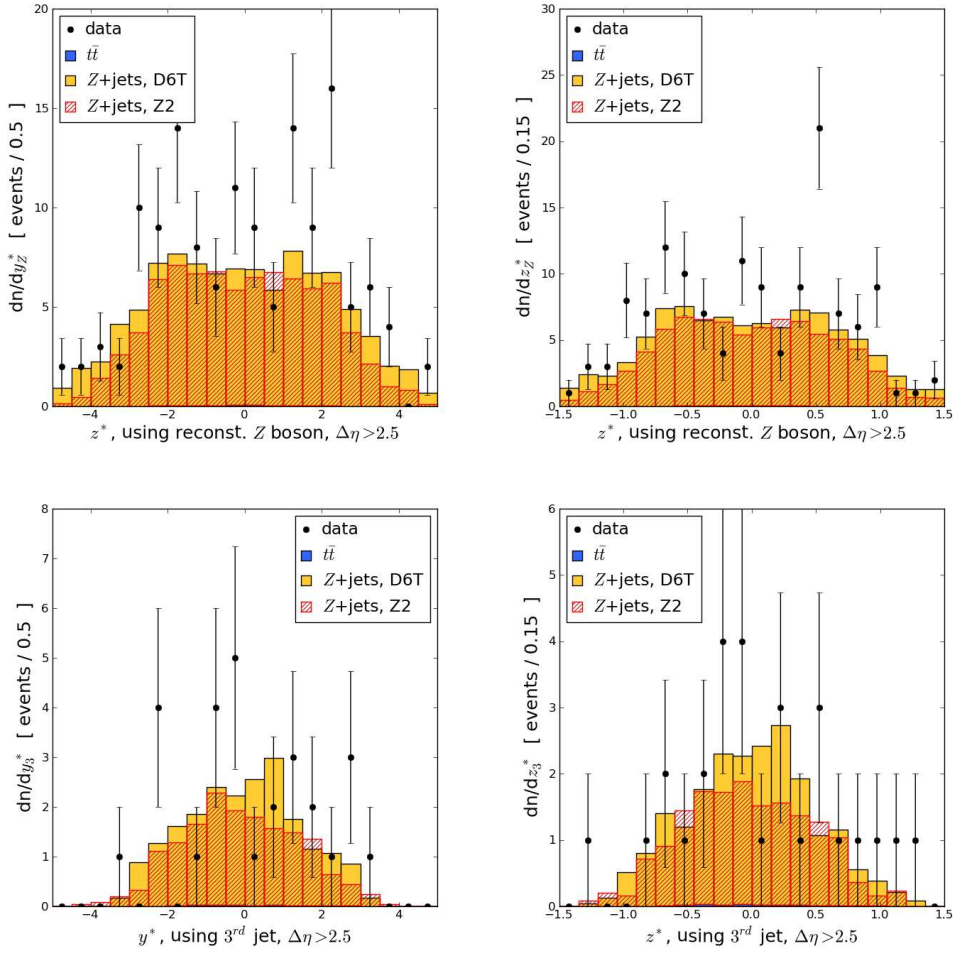
Figure 5.13.: y^* (left) and z^* (right) calculated from the reconstructed Z boson (upper row) and from third jets (lower row), $\Delta\eta_{jj} > 2.5$.

as only about 20% of the events have a third jet. However, even with the small number of events, it can be seen that with increasing rapidity gap the additional jets prefer to fall into this gap.

5.5. Full VBF Cuts

The low number of events even after the reduced $\Delta\eta_{jj} > 2.5$ cut shows that it does not make any sense to study distributions for even stricter cuts.

However, there are some events passing full vector boson fusion jet cuts, that is the cuts on the transverse momentum used so far, in addition

$$\Delta\eta_{jj} > 4 \,, \qquad m_{jj} > 600 \text{ GeV} \quad \text{and} \quad \eta_1 \cdot \eta_2 < 0 \,. \qquad (5.6)$$
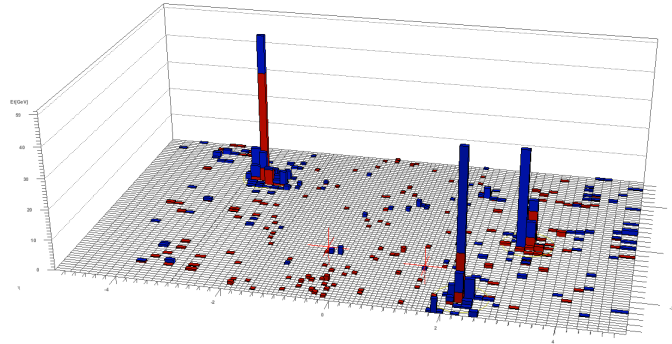
Figure 5.14.: Illustration of the deposited energy in the electromagnetic (red) and
               hadronic (blue) calorimeter as a function of η and ϕ, called "lego plot"
               of the first Z event passing VBF cuts, recorded on September 23, 2010.
               The circles show the position of jets, the crosses denote muons.
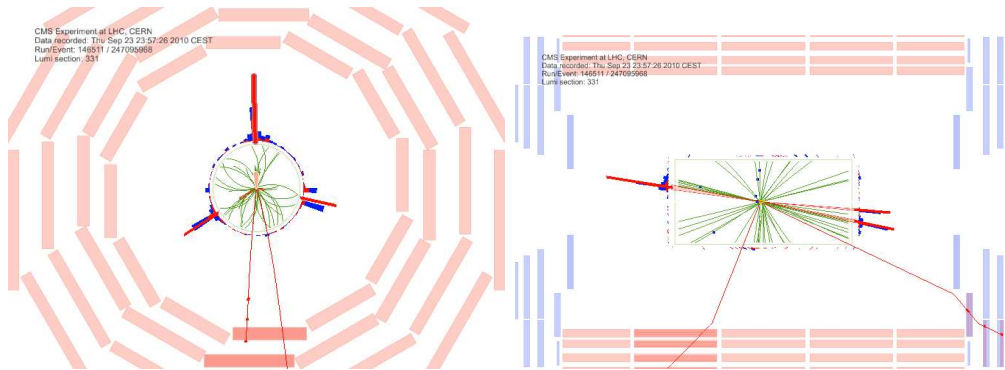
Figure 5.15.: Projection of the first Z event passing VBF cuts to the r-ϕ plane (left)
               and the r-z plane (right).

In the data sample considered, there were two events passing these cuts. The
meta information of these events is listed in Tab. 5.2. As an illustration, event
displays of these events are shown in Fig. 5.14–5.16 and Fig. 5.17 - 5.19.

The events show the typical behavior expected in a VBF event, jets widely
separated in rapidity with only little hadronic activity in the central region. The
muons assumed to stem from the Z boson fall in the gap. They are denoted by
red crosses in the lego plots, Fig. 5.14 and 5.17.

The first event has basically no sizeable activity in the gap region, whereas in
the second event, there is a central jet, approximately balancing the Z boson.

It is interesting to note that in both events the second hardest jet is accompanied
by another jet with approximately the same rapidity but a different azimuthal
angle.
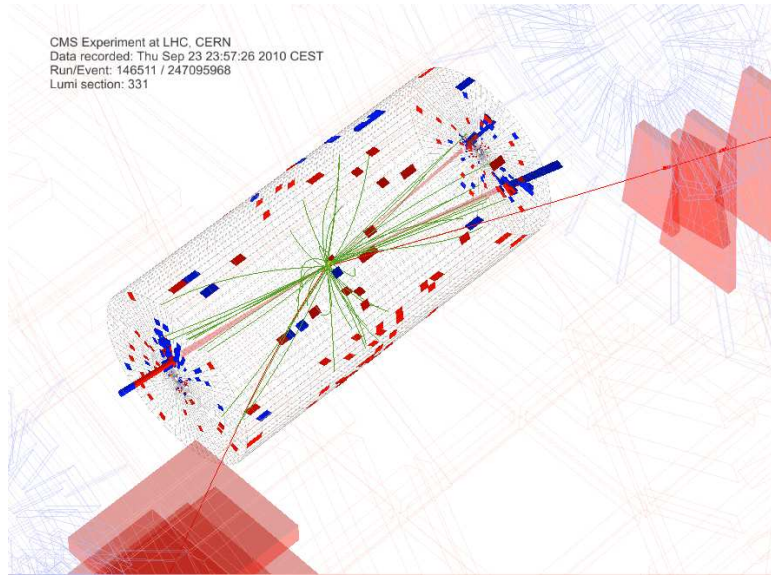
Figure 5.16.: 3D view of the first Z event passing VBF cuts. Detector components without a minimum contribution are not shown.
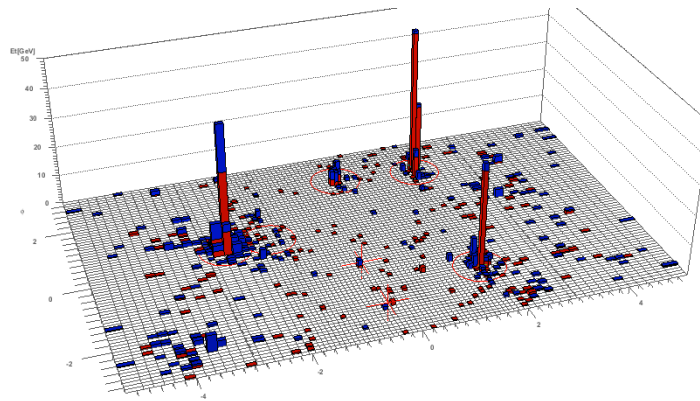
Figure 5.17.: Illustration of the deposited energy in the electromagnetic (red) and hadronic (blue) calorimeter as a function of η and ϕ, called "lego plot" of the second Z event passing VBF cuts, recorded on October 12, 2010. The circles show the position of jets, the crosses denote muons.

Run	Lumi Section	Event	Date
146511	331	247095968	09/23/2010
147757	270	227568519	10/12/2010

Table 5.2.: Information about the two events passing the strict VBF cuts from Eq. (5.6).
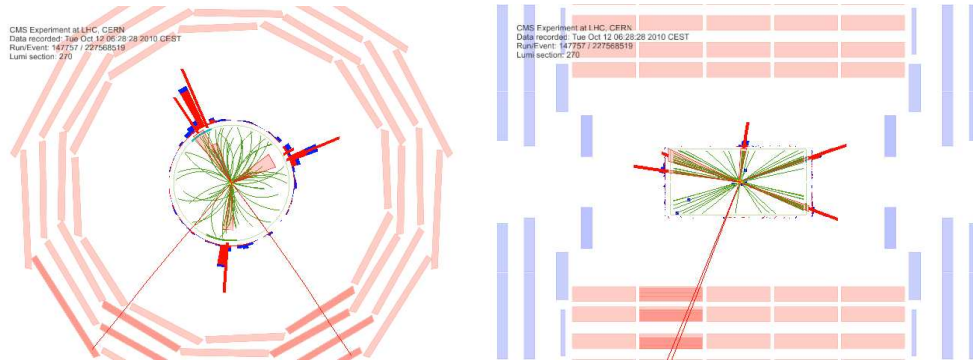
Figure 5.18.: Projection of the second Z event passing VBF cuts to the r-ϕ plane (left) and the r-z plane (right).
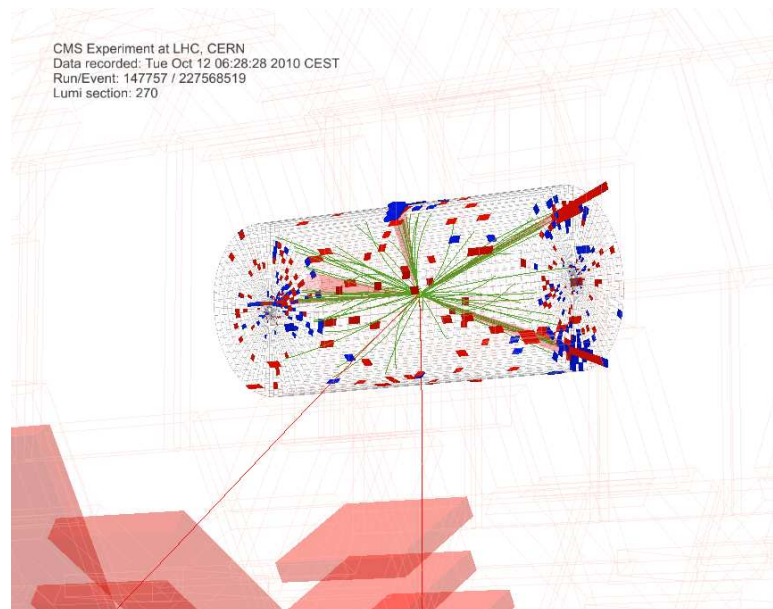
Figure 5.19.: 3D view of the second Z event passing VBF cuts. Detector components without a minimum contribution are not shown.

5.6. Subjet Analysis
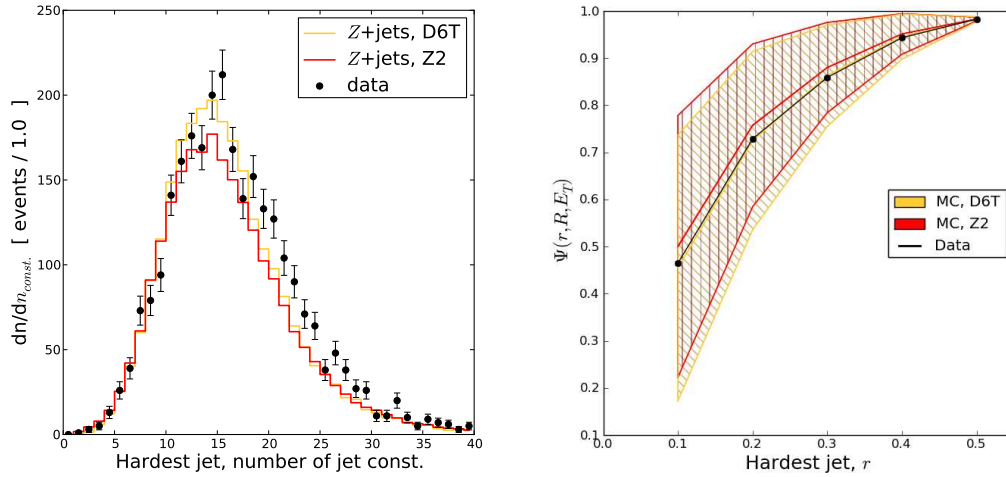
Figure 5.20.: Number of jet constituents and $\Psi(r, R, E_\mathrm{T})$ of the hardest jet in a Z
event.

To investigate the jets found in in the Z boson events, their inner structure can
be studied. One interesting information is the number of constituents of jet. In
addition, the distribution of the energy inside the jet is of interest. This can be
studied using the fractional E_T profile $\Psi(r, R, E_\mathrm{T})$, defined as the average fraction
of the jet transverse energy that lies inside a coaxial inner cone of radius $r < R$.
This observable reflects the distribution of the jet energy inside the jet and might
be an indicator of the nature of the jets, as jets stemming from the hard process
and parton showering might have a different internal structure as jets stemming
from the underlying event or pile-up.

The distributions of the number of jet constituents and energy flow Ψ for the
three hardest jets are shown in Fig. 5.20 - 5.22. It would be preferable to study
the energy flow in different rapidity and energy bins, as it is usually performed,
however, due to the low statistics, this is not possible here so all jets are studied
together.

A reasonably good agreement can be found for all the distributions, the shapes
agree quite well. The number of jet constituents peaks for all jets considered
around 15, which is properly described by both Monte Carlo samples. However,
the Monte Carlo samples both slightly underestimate the number of jets with
more than 15 constituents.

Regarding the profiles for $\Psi(r, R, E_\mathrm{T})$, a difference between the two Monte Carlo
samples used is visible. All distributions exhibit a large spread, denoted by the
shaded regions. This is not surprising, given the wide range of rapidity and
transverse momentum the jets have. However, the mean value of each bin has
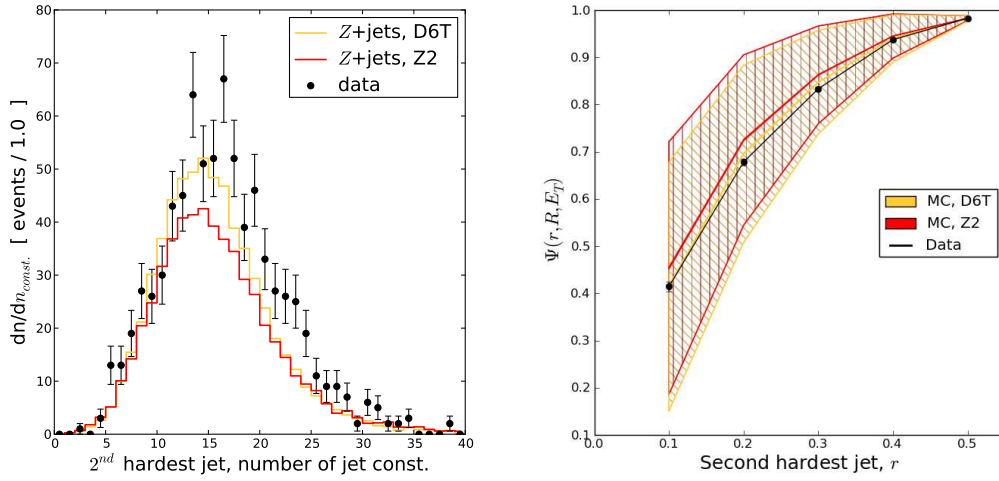
Figure 5.21.: Number of jet constituents and $\Psi(r, R, E_\mathrm{T})$ of the 2$^\mathrm{nd}$ hardest jet in a Z
           event.
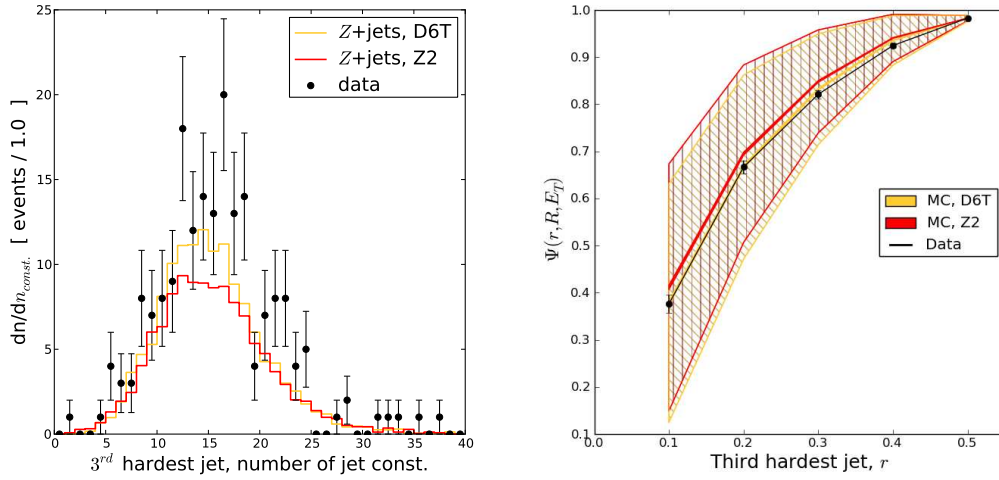
Figure 5.22.: Number of jet constituents and $\Psi(r, R, E_\mathrm{T})$ of the 3$^\mathrm{rd}$ hardest jet in a Z
           event.

a very small error, denoted by the central band in the Monte Carlo samples and
the error bars in the data. The D6T sample shows an excellent agreement with
the data, the central values and errors lie practically on top of each other. Only
for the second and third jet, the agreement is not as perfect over the whole range,
but still a very good description of the data is achieved.

   The Z2 sample on the other hand does not provide a similarly good description.
The predicted curve for the central value lies higher than the curves for data and

the D6T sample over the whole range. This can be observed for all three jets. This is an indication that here the central part of the jets is more energetic than in the data, giving an enhancement in the $R = 0.1$ bin. Since the curve of the Z2 sample stays above the others, it can be deduced that the activity in the intermediate regions of R are similar in Z2 and the data. In conclusion, the outer area of the jet is less energetic in the jets found in the Z2 sample.

The distributions of the number of jet constituents and the jet energy flow show that the D6T tune on the one hand is able to describe the high energetic jets quite well, whereas the differences between data and the Z2 sample show that this tune has problems predicting the detailed distribution of energy.

5.7. Energy and Charge Density in the Gap Region
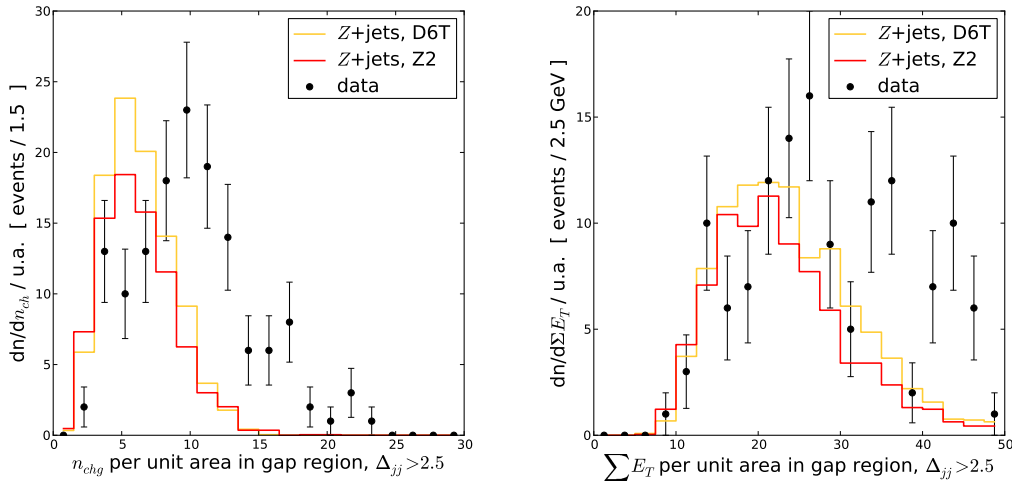
Figure 5.23.: Charged multiplicity (left) and $\sum E_\mathrm{T}$ (right) per unit area in the "gap" region in Z events.

Besides studying the distributions of additional jets it is also possible to study the overall hadronic activity in the gap region. A possible way to do so can be borrowed from the measurement of the underlying event. Here the charged density and the sum of transverse energy in regions without much hard activity are studied in relation to the hardest jet in the event.

In a similar fashion it is possible to measure the activity in the rapidity region between the two tagging jets. This is done for events where $\Delta\eta_{jj} > 2.5$ is fulfilled which is equivalent to a pronounced gap. To avoid the region of the tagging jets, only particles in the strip given by the pseudorapidity region

$$\eta_\mathrm{low} + 0.5 < \eta < \eta_\mathrm{high} - 0.5 \tag{5.7}$$
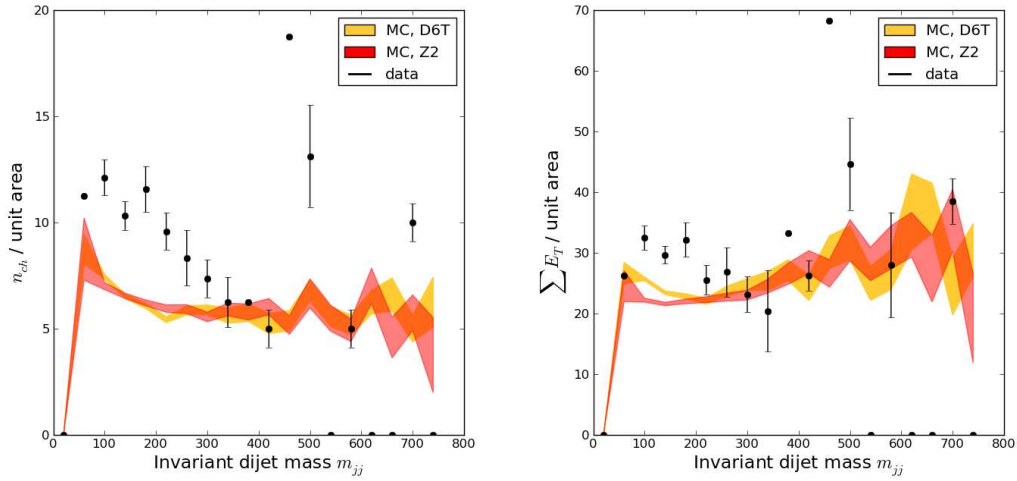
Figure 5.24.: Mean values of the charged mulitplicity (left) and $\sum E_{\mathrm{T}}$ (right) per unit area in the "gap" region in Z events.

are considered. Here η_{low} is the lower rapidity of the two tagging jets, η_{high} is the higher one. The number of charged objects n_{ch} and the sum of the transverse energies of all objects $\sum E_{\mathrm{T}}$ falling in the gap region per unit area in η and ϕ are shown in Fig. 5.23. For both observables, the Monte Carlo samples predict too low values, especially in the $\sum E_{\mathrm{T}}$ distribution. This shows that the topologies considered here are not very well described in both tunes studied. The Z2 tune which incorporates the most recent measurements of the underlying event would be expected to perform better for such observables, especially for the charged multiplicity, however, in this topology this is not the case.

In reminiscence of the p_{T} dependence in which the charged multiplicity and transverse energy sum are measured in two-jet events it is also interesting to study them here relative to the invariant mass of the tagging jet pair. In the underlying event measurements the hardest jet denotes the overall scale of the event, similar in the Z+jet events the invariant mass of the jet pair also is related to the event scale. Since in this study the area considered is not fixed, the final multiplicity is divided by the actual area of the gap present in the event. The distributions for the mean values quantities are shown in Fig. 5.24. It is not surprising that these distributions as well show differences between data and Monte Carlo. In the charged multiplicity, the data again overshoots the predicted values. The sum of the transverse energies however shows a better agreement. Nonetheless, the data is again higher than the prediction.

The study of the central activity performed here is of course only preliminary. A more detailed examination is beyond the scope of this work. However, even this small check shows that the rapidity gap region is not well described by both samples considered.

5.8. Conclusion

This chapter evaluated the description of Z boson events associated with jets by two different PYTHIA tunes. Especially the phase space region of relaxed vector boson fusion cuts is of interest, as the process is a background to Higgs production in vector boson fusion.

The overall agreement between data and Monte Carlo was reasonably well for most observables. However, especially in the phase space regions where non-perturbative effects play an important role, differences can be observed. Here especially the sample produced using the Z2 tune predicts too low values, whereas the sample obtained with D6T is generally in better agreement.

Detailed studies of the jet energy flow show an excellent agreement for the D6T sample and a reasonable description provided by the Z2 one. The activity in the rapidity gap is underestimated by both tunes.

Boosted Higgs Search

New developments in jet physics, namely the recent works on subjet analysis following the improvements in jet clustering revive decay channels that were discarded before as too crowded with backgrounds. Among these are Higgs-Strahlung HV as well as associated production H$t\bar{t}$. A similar case is the decay of a heavy Higgs into two Z bosons where one decays leptonically and one hadronically.

For Higgs masses above 140 GeV the branching ratio to vector boson pairs becomes sizeable. Here the so-called "gold plated mode" H $\to$ ZZ$^* \to 4\ell$ results in a very clean final state and allows for a Higgs boson discovery up to $m_\mathrm{H} = 600$ GeV based on 10 fb^{-1} at $\sqrt{s} = 14$ TeV [19].

In this mass region roughly 30% of the Higgs bosons decay to Z bosons, see Fig. 1.1. The charged lepton mode can be complemented by H $\to$ ZZ$^* \to \ell^+\ell^-\nu\bar{\nu}$ [165]. Unfortunately, the fact that only 6% of the Z bosons decay to electrons or muons means that this gold plated mode is strongly limited statistically. Another possibility using H $\to$ ZZ is based on the fact that 15% of Z bosons decay to $b\bar{b}$ pairs. However, searching for this channel by imposing one or two additional b-tags with a limited b-tagging efficiency will also suffer from a low statistical precision. Allowing for one of the Z bosons to decay hadronically and hence including the 60% hadronic Z decays increases the expected number of events.

The semi-leptonic channel

$$pp \to \mathrm{H} \to \mathrm{ZZ} \to (\ell\ell)\,(jj) \tag{6.1}$$

has not been given the attention it deserves in the context of heavy Higgs searches. This can be partly understood because it is very difficult to compete with the clean leptonic final state, and as additional backgrounds like Z + jets and leptonically decaying $t\bar{t}$ make the extraction of the semi-leptonic signal events a difficult task.

However, recent developments of subjet techniques [44, 99, 100, 101] change this assumption. If a heavy resonance (H) decays to intermediate resonances (Z) which subsequently decay to quarks, the final-state quarks will be highly collimated. Thus, the hadronic Z decays can be collected in a so-called "fat jet".

It has been shown for gauge bosons [166], Higgs bosons [44, 47, 167, 168, 169, 170], and top quarks [47, 100, 171] that a successful QCD background rejection can be achieved based on kinematic patterns of subjets inside the fat jet. The experimental signature in Eq. (6.1) requires to first reconstruct the leptonically decaying Z boson from the two leptons and the hadronically decaying Z boson using subjet techniques and then to combine the hadronic Z boson with a leptonic Z decay to form a Higgs resonance. This work has already been published in [172].

6.1. Leptonic HZZ Decay: The Gold Plated Mode

To compare the semi-leptonic ZZ channel with the purely leptonic mode over the entire Higgs mass range the results for the four-muon final state of [173] are reproduced and a good agreement can be found, as can be seen in Fig. 6.1.

Throughout this work the total rate for the gluon-fusion Higgs signal and the backgrounds are normalized to the next-to-leading order predictions. The NLO signal cross sections were obtained by scaling the LO value from Pythia 6.4.22 with a K-factor obtained from HIGLU [174]. The transverse momentum distribution of the Higgs boson simulated with Pythia 6.4 approximates the full calculation with POWHEG very well [175]. The inclusive signal also includes Vector boson fusion. The NLO corrections to this production process are known to be small, see Sec. 1.2.2, so within errors K=1.0 is assumed.

The dominating background for the four-muon signature is continuum ZZ production. This background was simulated using MadEvent and Pythia 6.4. Its NLO cross section including the branching ratio was calculated with MCFM, giving 7.39 pb at 7 TeV and 19.02 pb at 14 TeV.

The analysis presented in [173] starts with selecting four central and sufficiently hard muons,

$$|y_\mu| < 2.5, \qquad \begin{aligned} p_{\mathrm{T},\mu} &> 7 \text{ GeV} \qquad \text{for } |y_\mu| < 1.1 \\ p_{\mathrm{T},\mu} &> 13 \text{ GeV} \qquad \text{for } |y_\mu| > 1.1. \end{aligned} \tag{6.2}$$

The muons have to be isolated, that is the hadronic transverse energy in a cone of $R = 0.3$ around the lepton has to be $E_\mathrm{T}^{\mathrm{hadronic}} < 0.1 \cdot E_\mathrm{T}^\mu$. Events with at least four isolated muons passing the staggered p_T cuts

$$p_{\mathrm{T},\mu} > 15, 15, 12, 8 \text{ GeV} \tag{6.3}$$

are selected.

The Z bosons are reconstructed by combining two oppositely charged isolated muons, and requiring for every such combination

$$m_{\mu^+\mu^-} > 15 \text{ GeV} \tag{6.4}$$

and for the pair closest to the nominal Z boson mass

$$m_\mathrm{Z} - 10 \text{ GeV} < m_{\mu\mu} < m_\mathrm{Z} + 10 \text{ GeV}. \tag{6.5}$$
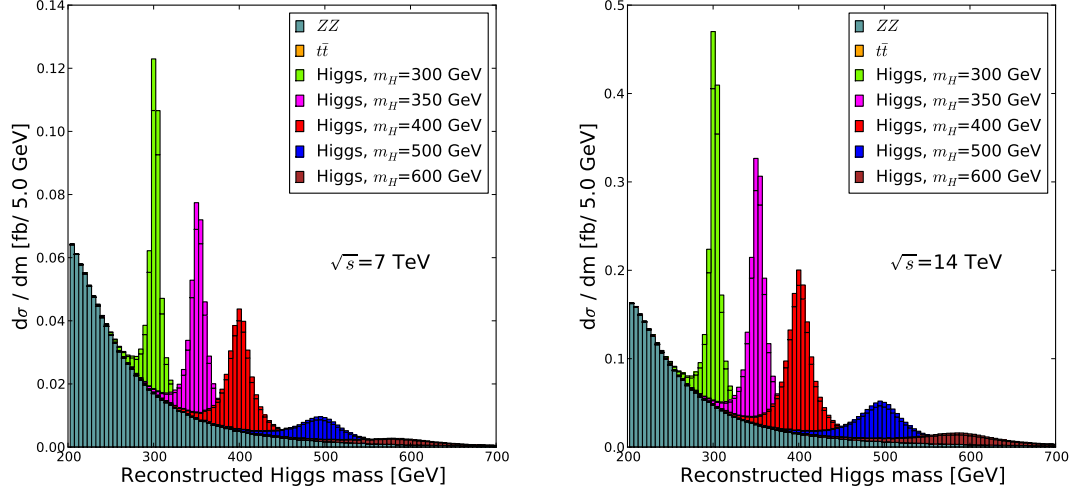
Figure 6.1.: Invariant mass distribution of the reconstructed Z bosons in the leptonic channel at 7 TeV (left) and 14 TeV (right) collider energy.

m_{H} [GeV]	7 TeV				14 TeV			
	σ_S [fb]	σ_B [fb]	S/B	$S/\sqrt{B}_{10}$	σ_S [fb]	σ_B [fb]	S/B	$S/\sqrt{B}_{10}$
300	0.35	0.21	1.7	2.4	1.39	0.56	2.5	5.9
350	0.35	0.19	1.8	2.5	1.52	0.53	2.9	6.6
400	0.28	0.10	2.7	2.7	1.34	0.31	4.4	7.6
500	0.11	0.05	2.1	1.5	0.65	0.18	3.7	4.9
600	0.05	0.03	1.4	0.8	0.30	0.12	2.5	2.7

Table 6.1.: Signal and background cross sections for the purely leptonic H $\rightarrow$ ZZ analysis. The final significance is computed for 10 fb^{-1}.

For this analysis five different Higgs-boson masses were considered. Because the Higgs decay width grows very fast with the Higgs mass, see Fig. 1.1b, the mass windows for the reconstruction are chosen as

$$(300 \pm 30,\ 350 \pm 50,\ 400 \pm 50,\ 500 \pm 70,\ 600 \pm 100)\ \text{GeV}. \qquad (6.6)$$

The mass windows are completely dominated by the physical Higgs width. Detector effects like the lepton or jet energy scale will have only little effect, which means the windows for reconstructed Higgs mass can be kept for the leptonic and the semi-leptonic analysis.

The purely leptonic channel is very clean and with four relatively hard muons not plagued by large background rates or large background uncertainties. Systematic errors should not be a problem since for $\sqrt{s} = 14$ TeV an outstanding

signal-to-background ratio of $S/B > 1$ can be found over the whole mass region. The results for collider energies of 7 TeV and 14 TeV are listed in Table 6.1. The main distinguishing feature between signal and background is the four-muon invariant mass which is show in Fig. 6.1. Its signal shape is clearly distinguishable from the background, which makes this channel a save bet for a data driven sideband analysis. While the significances shown for 7 TeV running will hardly give evidence for a heavy Higgs, at an energy of 14 TeV a discovery based on a modest integrated luminosity should not be a problem.

6.2. The Semi-Leptonic Channel

For the semi-leptonic signature $pp \to \text{H} \to jj\ell\ell$, the dominant backgrounds are $\text{Z} + \text{jets}$, ZZ, $t\bar{t}$ and WZ. Again, signal and backgrounds were normalized to the NLO cross sections using K-factors obtained by HIGLU, `vbfnlo` and MCFM. The values used are listed in Table 6.2.

The ZZ background corresponds to the numbers quoted in Section 6.1.

It is possible to pursue in the semi-leptonic case a similar search strategy as in the leptonic case. Again, the two muons are checked for their compability with the Z boson mass and a similar check is performed on the jets. If the jet pair which is closest to the nominal Z boson mass is compatible with it, the four momenta are combined to reconstruct the Higgs boson momentum.

However, the amount of backgrounds with two muons and two or more jets is much larger than in the four muon case. Especially the Z + jets background has a large cross section compared to the signal and makes a search directly following the leptonic channel futile. The invariant mass of the reconstructed Z boson pair is shown in Fig. 6.2. The effect of the overwhelming backgrounds is obvious.

It is however possible to make use of the kinematic configuration of a heavy Higgs decay. If a heavy Higgs boson decays to two Z bosons, the Higgs mass generates sizeable kinetic energy for the Z bosons. Figure 6.3 shows that 70% of the leading Z bosons have $p_\text{T} > 150$ GeV for $m_\text{H} = 400$ GeV. The geometric distance between the Z decay jets is roughly $\Delta R_{j_1,j_2} \simeq 2m_\text{Z}/p_\text{T}$, which means that the inclusive Cambridge-Aachen (C-A) jet algorithm, described in section 1.8.2, with $R = 1.2$ should be able to collect all Z decay products in a *fat jet*.

This analysis is a Monte Carlo study and was performed at hadron level, that is

Process	Cross section at 14 TeV	Cross section at 7 TeV
Z + jets $p_{\text{T}_\text{jet}} > 100$ GeV	33.91 pb	9.94 pb
$t\bar{t}$	875 pb	157.50 pb [176]
WZ	43.44 pb	17.31 pb [128]

Table 6.2.: NLO cross sections for signal and backgrounds in the semileptonic $\text{H} \to \text{ZZ}$ analysis for 7 and 14 TeV
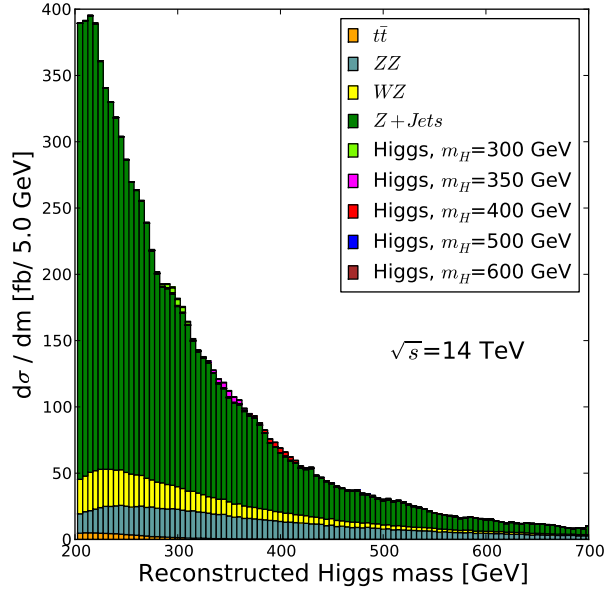
Figure 6.2.: Invariant mass distribution of the reconstructed Z bosons in the semi-
leptonic channel at 14 TeV collider energy. The signal consists of two parts.
In every bin the top part shows the contribution of the VBF production
process and the lower part the gluon fusion production process.

no detector simulation was used. To take a finite detector resolution into account,
all final state particles after showering and hadronization are grouped into detector
cells of size $\Delta\eta\times\Delta\phi = 0.1\times0.1$. This simulates the finite resolution and thresholds
of a calorimeter. Then all particles in a cell are combined and the total three-
momentum is re-scaled such that each cell has zero invariant mass. Only cells
with energy above 0.5 GeV are considered further.

These "calorimeter cells" are then clustered into jets using the C-A algorithm
with $R = 1.2$.

Event selection starts with the identification of exactly two isolated muons with

$$p_\mathrm{T} > 15 \text{ GeV} \quad \text{and} \quad |\eta| < 2.5 \ . \tag{6.7}$$

This muon pair is supposed to stem from the leptonically decaying Z boson, there-
fore its invariant mass has to match $m_\mathrm{Z} \pm 10$ GeV. Due to the excellent muon
identification and precise momentum measurement the presence of such a muon
pair can also be used for triggering the events.

In the next step all events with a fat jet, that is a jet supposed to contain all
the decay products of the hadronically decaying Z boson, are selected. Since the
Z boson needs to be boosted for this to happen, only hard jets are considered. In
addition, all Z boson decay products need to be found with a good energy and
angular resolution in order to provide an exact measurement. Since a jet with a
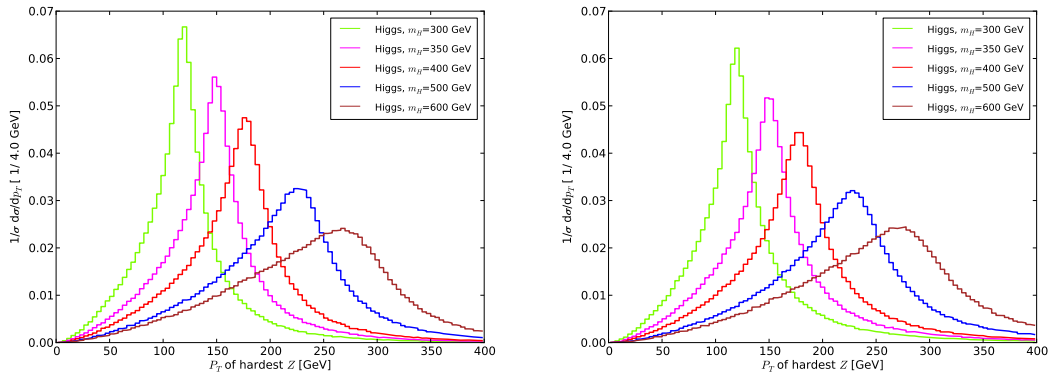
Figure 6.3.: p_T distribution of the leading Z boson for different Higgs masses m_H at 7 (left) and 14 (right) TeV center-of-mass energy.

radius as big as 1.2 covers an area corresponding approximately to a circle with radius 1.2 the fat jet needs to be central. The complete *fat jet criteria* thus reads

$$p_{\mathrm{T}_j} > 150 \text{ GeV} \quad \text{and} \quad |y_{\text{fat jet}}| < 2 \ . \tag{6.8}$$

That way most of the objects clustered into the fat jet are in regions of good calorimetric acceptance.

The hadronic Z is reconstructed following the prescription from [44]. The fat jet is investigated for a mass drop and undergoes jet filtering if the mass drop condition is met. As described in Sec. 1.8.3, the clustering of the jet is undone and the heavier of the two protojets is checked for a significant decrease in mass $m_{j_1} < \mu m_j$, where m_{j_1} denotes the mass of the heavier clustering object and m_j the mass of the original jet.

If the mass drop condition is not met, this unclustering continues with the heavier protojet until either the mass drop condition is fulfilled or if this does not happen when all clustering has been undone the event is removed. In this analysis the mass drop parameters are $\mu = 0.67$ and $y_{\text{cut}} = 0.09$. Varying $\mu = 0.33 - 0.67$ does not improve $S/\sqrt{B}$.

After the mass drop condition is met, the fat jet is filtered as described in Sec. 1.8.3: the constituents of the two subjets which survive the mass drop condition are recombined with the finer resolution $R_{\text{filt}} = \min(0.3, \Delta R_{j_1,j_2}/2)$ and the three hardest filtered subjets are required to give $m_\mathrm{Z}^{\text{rec}} = m_\mathrm{Z} \pm 10$ GeV.

The advantages of this method compared with the direct search for two jets stemming from the Z boson decay are twofold. First, the restriction on boosted Z bosons allows for a focused search which does not suffer much from combinatoric backgrounds, since both jets are supposed to lie in the region of the fat jet. Second, the combination of mass drop and filtering automatically chooses a suitable jet radius R_{filt} on an event-by-event basis. Since R_{filt} is based on the distance of the two assumed subjets, this choice will most likely cluster these two objects into
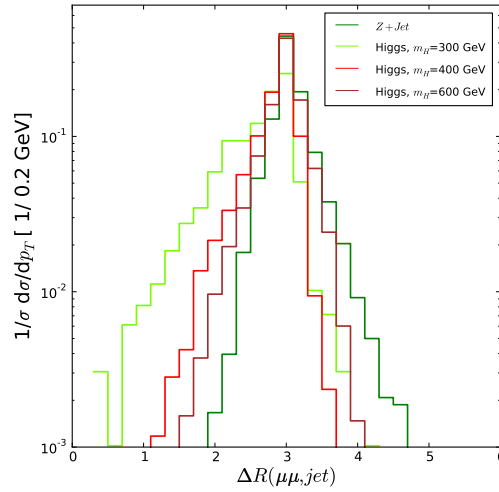
Figure 6.4.: $\Delta R(Z, j)$ between the Z boson reconstructed from the muon pair and the fat jet.

two separate jets. This prevents losses due to a too small or too large jet radius.

If both Z bosons in the signal are correctly reconstructed their invariant mass peaks around the Higgs boson mass,

$$m_{\mathrm{H}}^2 = (p_{\mathrm{Z,lep}} + p_{\mathrm{Z,had}})^2.$$

The shape of the m_{H} distribution is determined by the width of the Higgs boson and the ability of the algorithm to remove underlying event and initial state radiation from the hadronic Z reconstruction.

In practice, such an analysis would be combined with a likelihood fit or other elaborate statistical methods, taking into account systematic uncertainties. This is beyond the scope of this work, especially since this should include all experimental uncertainties which cannot be estimated in this Monte Carlo study. The choice of Higgs mass windows used here, Eq. (6.6), should give a conservative estimate of the prospects of such an analysis.

The subjets on which the analysis relies are close collimated jets which will have a significant experimental resolution uncertainty. As the subjet analysis is a new method for jet reconstruction, the experimental systematics are as yet unknown. This uncertainty will be dominant in this analysis and has to be determined in the context of an experiment and cannot be estimated in this pure Monte Carlo study.

After reconstructing the Higgs boson from a leptonic and a hadronic Z boson, S/B can be further improved by requiring a maximum angular separation of $\Delta R_{\mathrm{ZZ}} < 3.2$. For Z + jets the angular separation of the reconstructed leptonic Z and the fake-Z from QCD jets often becomes large, to accomodate the large
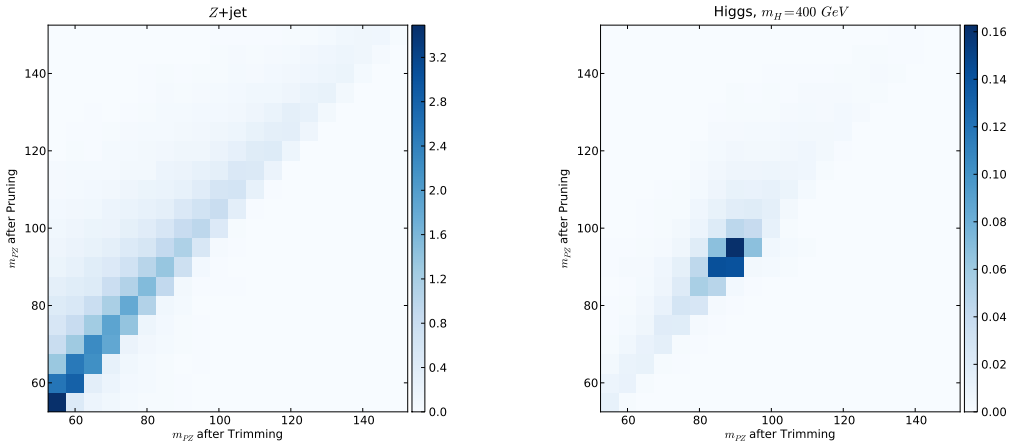
Figure 6.5.: Mass of the trimmed and pruned fat jet for the Z+jet (left) and the $m_\mathrm{H} =$ 400 GeV sample.

invariant (Higgs) mass. This is illustrated in Fig. 6.4. A similar effect could be achieved by scaling the p_T cut on the hardest jet to higher values for larger Higgs masses.

For different Higgs masses, it might prove useful to apply further cuts to reduce the Z+jets contributions even more. Also a pre-selection obtained with jets using a smaller jet radius is possible, using kinematic constraints specially chosen for the Higgs mass considered. Among these are cuts on the ϕ separation of the leptonic Z boson and the hardest jet as well as the ratio $p_{\mathrm{T},2}/p_{\mathrm{T},1}$ of the two hardest jets. In both cases, the cuts should favor events where the leptonically decaying Z boson is balanced with a hard jet, without hard additional jets.

The exact nature of such additional cuts should in addition also take the the finite experimental resolution into account.

It has been shown that a combination of pruning and trimming, described in Sec. 1.8.3, helps discriminating the decay products of a color singlet resonance from QCD jets [168]. This asymmetry between the trimmed and pruned jet is shown in Fig. 6.5 for the Z+jet background and the $m_\mathrm{H} = 400$ GeV sample. A difference in the reconstructed jet mass in the Z+jet background is clearly visible whereas the Higgs sample does not exhibit such a big difference. All events passing the two Z tags and the Higgs mass reconstruction are re-processed using pruning and trimming on the massless cells of the event [168]. For the pruning, the C-A algorithm is used. The asymmetry parameter is $\min(p_{\mathrm{T},i}, p_{\mathrm{T},j})/p_{\mathrm{T},i+j} >$ 0.1. For the trimming, the anti-k_T algorithm [139] was used to define the fat jet and the inclusive k_T algorithm [138] with a small cone $R = 0.2$ for the subjet recombination. During trimming, subjets with $p_{\mathrm{T,subjet}} > 0.03 \cdot p_{\mathrm{T,fat\ jet}}$ are kept.

Only events where the pruned and trimmed masses of the leading jet are in the range $m_\mathrm{Z} \pm 10$ GeV are accepted in this final selection step.

m_H [GeV]	300		400		500		600	
σ [fb]	σ_S	σ_B	σ_S	σ_B	σ_S	σ_B	σ_S	σ_B
selection	3.37/0.89	907.3	8.89/0.97	907.3	4.91/0.70	907.3	2.19/0.46	907.3
Z^{had}	0.79/0.22	27.11	3.81/0.42	27.11	2.36/0.35	27.11	1.11/0.25	27.11
m_H^{rec}	0.46/0.17	1.02	3.35/0.35	9.50	1.98/0.28	10.53	0.88/0.20	8.08
ΔR_{ZZ}	0.45/0.17	1.00	2.99/0.35	7.93	1.52/0.28	6.52	0.60/0.15	3.82
prun/trim	0.29/0.12	0.39	2.02/0.24	3.97	1.11/0.18	3.33	0.46/0.12	1.97
S/B	1.03		0.57		0.39		0.30	
$S/\sqrt{B}_{10}$	2.0		3.6		2.2		1.3	
selection	17.97/3.83	6200	46.18/4.64	6200	29.48/3.87	6200	15.08/2.90	6200
Z^{had}	3.80/1.00	180.0	18.03/2.03	180.0	13.49/1.98	180.0	7.24/1.62	180.0
m_H^{rec}	2.21/0.76	6.56	15.50/1.65	61.47	11.27/1.56	69.09	5.75/1.24	54.16
ΔR_{ZZ}	2.18/0.76	6.45	13.94/1.55	52.22	8.98/1.35	45.14	4.19/0.98	27.89
prun/trim	1.34/0.48	2.10	8.96/1.07	19.21	6.32/1.00	18.01	3.15/0.77	11.83
S/B	0.87		0.52		0.41		0.33	
$S/\sqrt{B}_{10}$	4.0		7.2		5.5		3.6	

Table 6.3.: Signal and backgrounds for the semi-leptonic fat-jet analysis for a collider energy of 7 TeV (upper) and 14 TeV (lower). The expected significance is calculated for 10 fb^{-1}.

Table 6.3 shows the results for the semi-leptonic analysis for each of these steps. The gluon fusion and weak boson fusion signal rates and the background cross sections are given separately. After the reconstruction of the leptonic Z and requiring $p_{\text{T}} > 150$ GeV for the leading jet, the Z+jets background still exceeds the signal by roughly a factor 1000. The hadronic Z reconstruction in combination with the Higgs mass condition reduces this background significantly and improves the ratio to typically $S/B \gtrsim 1/10$. Especially for a heavy Higgs boson, the ΔR_{ZZ} cut proves efficient against the Z+jets background. Finally, the combined pruning and trimming on the hadronic Z improves S/B over the whole considered Higgs mass range. The significance quoted can be even further improved by including electrons in leptonic Z reconstruction.

It is interesting to track the relative contributions of the gluon fusion and the weak boson fusion contributions to the inclusive signal. For small Higgs masses at 14 TeV collider energy, the acceptance cuts yield a 80%-20% balance of the two channels. This enhancement as compared to the total rates is due to the generally larger Higgs transverse momentum in weak boson fusion, even if there is no cut on the tagging jets. For intermediate masses the weak boson fusion contribution drops to a 90%-10% ratio, because the Higgs transverse momentum of $p_{\text{T,H}} = \mathcal{O}(m_W)$ does not help to significantly boost the Z decay products. Both channels are pushed far into their $p_{\text{T,H}}$ tails by the acceptance cuts. For large Higgs masses the relative rate of weak boson fusion as compared to gluon fusion increases because of a logarithmic enhancement. This effect increases the relative weight of weak boson fusion back to 80%-20%. Of the different cuts only the hadronic Z reconstruction shows a bias towards weak boson fusion, because the
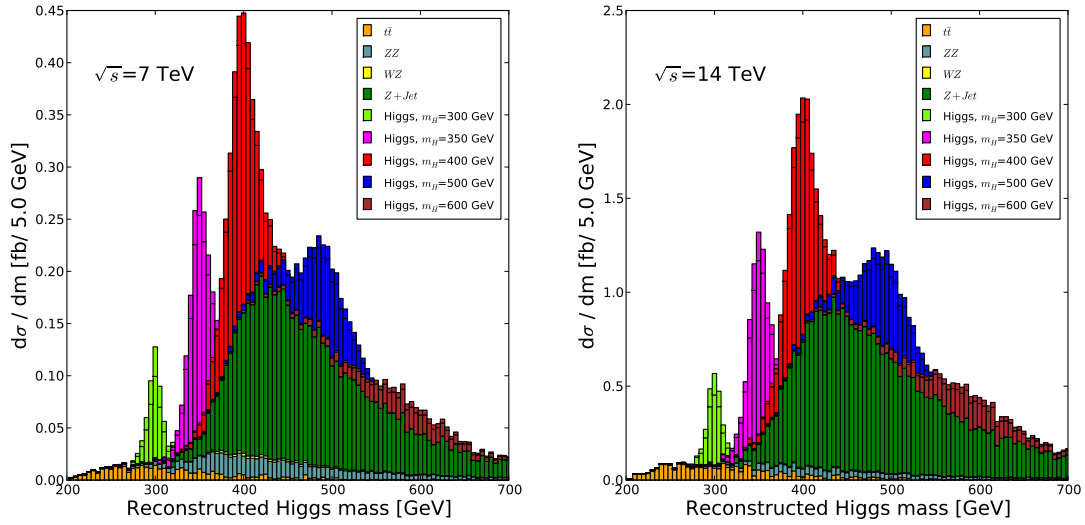
Figure 6.6.: Invariant mass distribution of the reconstructed Z bosons, m_{ZZ}, in the semi-leptonic channel at 7 TeV (left) and 14 TeV (right) center-of-mass energy. A cut for the maximum angular separation of the Z bosons has been applied, $\Delta R(Z_{\mathrm{lep}}, Z_{\mathrm{had}})$, as well as the combined usage of pruning and trimming. The signal consists of two parts. In every bin the top part shows the contribution of the VBF production process and the lower part the gluon fusion production process.

fat jet reconstruction is expected to benefit from the lower jet activity in this channel [47]. The final contribution from weak boson fusion ranges from 15% for $400 \text{ GeV} \leq m_{\mathrm{H}} \leq 500 \text{ GeV}$ to 30% for smaller or larger Higgs masses. This weak boson fusion contribution could be a major handle for improving the results shown using advanced analysis methods. While here none of the kinematic features are used to suppress backgrounds a neural net could clearly include them.

In Fig. 6.6 the reconstructed Higgs masses after pruning and trimming are shown. The signal excess over backgrounds is clearly visible for $m_{\mathrm{H}} = 300 - 500 \text{ GeV}$. Requiring boosted Z bosons with a large angular separation slightly shapes the dominant Z + jets background and generates a maximum around 450 GeV. This shows the need for a good understanding of this background, ideally from a data-driven method.

As also shown in Table 6.3, the cross sections for $\sqrt{s} = 7$ TeV are too small to allow for a Higgs discovery with early data. However, in new physics scenarios with a modified ggH coupling this might change. A straightforward example is a chiral fourth generation for which electroweak precision data favors Higgs masses between 300 and 500 GeV [177]. Its loop contribution enhances the ggH coupling by roughly a factor of three. For an early LHC run at 7 TeV collecting 1 fb^{-1} integrated luminosity this semi-hadronic analysis could then give 15 signal versus 4 background events for $m_{\mathrm{H}} = 400$ GeV.

The analysis shown is a search experiment with a small number of signal events,

for a 400 GeV Higgs about 20 events at 7 TeV and 89 events at 14 TeV for an integrated luminosity of $\mathcal{L} = 10$ fb^{-1} are expected. The statistical uncertainty would be small compared to the expected experimental jet energy scale uncertainties. As the reconstructed width in the four lepton analysis is about a factor of 10 smaller than in the 2 lepton, 2 jet study, a hundredfold number of events would be required to be competitive with the pure leptonic analysis. This analysis can provide significance for an already assumed Higgs mass found in the four lepton channel, thus boosting the Higgs detection in the combination.

6.3. Measuring Spin and $\mathcal{CP}$ from Semi-Hadronic ZZ Decays

To claim the discovery of the Higgs boson it is not sufficient to be able to reconstruct a mass peak or suchlike. Besides establishing a signal also the the properties of the resonance found have to be measured. Among these are the couplings to different particles, especially the gauge bosons of the electro-weak theory and the spin- and $\mathcal{CP}$-properties of the resonance.

In view of the possibility to discover a heavy resonance X using boosted Z-Bosons it is now interesting to investigate the attainable extent of sensitivity to the spin and $\mathcal{CP}$ quantum numbers of this resonance in this analysis. To arrive at a reliable assessment, the analysis for the Higgs search is redone for several scenarios with different quantum numbers for the resonance X. This analysis has already been published [178], this presentation follows the one in the publication.

The mass and the production modes of X, as well as its production cross section are fixed to be similar to the SM Higgs boson expectation. This is done by normalizing the cross section to SM Higgs production at the parton level.

On the one hand, this approach can be motivated by referring to unitarity constraints: Curing the growth of both the $VV \rightarrow VV$ and $q\bar{q} \rightarrow WW$ scattering amplitudes by a *singly-dominating* additional resonance fixes the overall cross section to be of the order of the SM as is shown in e.g. [179, 180] for non-trivial examples.

On the other hand, it is useful to focus on an experimental situation, which favors the SM expectation, but leaving $\mathcal{CP}$ and spin properties as an open question. For this reason, additional dependencies of the cross section on the width of X are also not included. The width is, in principle, an additional, highly model-dependent parameter, which can be vastly different from the SM Higgs boson width, e.g. in models with EWSB by strong interactions [181, 182], or in so-called hidden-valley models [183]. Instead, for this work the SM Higgs boson width was straightforwardly adopted, which then turns the resonance considered here into a "Higgs look-alike", as it is denoted in [18].

6.3.1. Details of the Analysis

Spin- and $\mathcal{CP}$-Sensitive Observables

The angles used to determine spin and $\mathcal{CP}$ properties of a heavy resonance are described in Sec. 1.2.1.

There is a small drawback when carrying over the definitions of Eq. 1.17 from the purely leptonic decay channels to the considered semi-hadronic final state: When dealing with $X \to \ell^+\ell^-\ell'^+\ell'^-$, it is always possible to unambiguously assign a preferential direction for the lepton pairs by tagging their charge. This allows to fix a convention for the helicity angles, as well as for the relative orientation of the decay planes via a specific ordering of the three-momenta when defining the normal vectors in Eq. 1.17. Considering semi-hadronic X decays, there is a two-fold ambiguity, which affects the angular distributions. Even worse, p_{T}-ordered hard subjets, dug out from the *fat jet* during the subjet analysis can bias the distributions, as more central jets tend to be harder. So in order to be able to calculate the helicity angles, an ordering scheme which avoids these shortcomings has to be found. An efficiently working choice on the inclusive parton level is provided by imposing rapidity-ordering

$$y(j_\alpha) < y(j_\beta)\,, \tag{6.9}$$

which is reminiscent of the $\mathcal{CP}$-sensitive Φ_{jj} observable in vector boson fusion [163]. This choice, however, does not remove all ambiguities. The orientation of the decay planes, Eq. 1.17e, is not fixed by ordering the jets according to Eq. 6.9. The unresolved ambiguity results in averaging $\cos\Phi$ and $\cos(\pi-\Phi)$ over the event sample, leaving a decreased sensitivity in the angle $\Phi \in [0, \pi]$. This is discussed in more detail in Sec. 6.4.

Simulation of signal and background events

The signal events $pp \to X \to \mathrm{ZZ} \to \ell^+\ell^- jj$ for the various $\mathcal{CP}$ scenarios are simulated using MADGRAPH/MADEVENT [127], which was slightly modified to fit the purpose of this work. In particular these modifications include supplementing additional HELAS [123] routines and modifications of the MADGRAPH-generated code to include the vertex structures and subprocesses that are under investigation. The implementation was validated against existing spin correlation results of Refs. [6, 17]. The partonic production modes were chosen to be dependent on the quantum numbers of the particle X,

$$X = 0^\pm : \quad gg \to X \to \mathrm{ZZ} \to \ell^+\ell^- jj\,, \tag{6.10a}$$

$$X = 1^\pm : \quad q\bar{q} \to X \to \mathrm{ZZ} \to \ell^+\ell^- jj\,, \tag{6.10b}$$

$$X = 2^+ : \quad gg \to X \to \mathrm{ZZ} \to \ell^+\ell^- jj\,, \tag{6.10c}$$

where g denotes the gluon, and $q, j = (u, d, s, c)$ represents the light constituent quarks of the proton. The bottom quark contributions are negligibly small.

While in the light of the effective theory language of Ref. [17], this specific choice can be considered as a general assumption of this analysis, the partonic subprocesses of Eq. 6.10 reflect the dominant production modes at the LHC. In particular, the production of an uncolored vector particle 1^- from two gluons via fermion loops is forbidden by Furry's Theorem [184], while a direct ggZ' coupling is ruled out by Yang's theorem [185].

The effective operators that are included for the production and the decay of X do not exhaust all possibilities either, see again Ref. [17] for the complete set of allowed operators. Yet, the set of operators adopted here are general enough to serve as benchmarks adequately highlighting the features of objects X with different spins and $\mathcal{CP}$ quantum numbers in a comparative investigation in Sec. 6.4. The effective couplings of X to the SM Z bosons appearing in the calculation of the matrix elements in Eq. (6.10) are derived from the effective vertex function. For the scalar case, suppressing the color indices, they read [186],

$$\mathcal{L}_{\mu\nu}^{ZZX} = c_1^s\, g_{\mu\nu} + \frac{c_2^s}{m_Z^2}\epsilon_{\mu\nu\rho\delta}\, p_1^\rho\, p_2^\delta\,. \tag{6.11a}$$

For a vectorial X, the vertex function follows from the generalized Landau-Yang theorem [188]

$$\mathcal{L}_{\mu\nu\rho}^{ZZX} = c_1^v\left(g_{\mu\rho}\, p_{1,\nu} + g_{\nu\rho}p_{2,\mu}\right) - c_2^v\,\epsilon_{\mu\nu\rho\delta}\left(p_1^\delta - p_2^\delta\right)\,, \tag{6.11b}$$

while for tensorial X, the vertex function [187]

$$\mathcal{L}_{\mu\nu\rho\delta}^{ZZX} = c_1^t\left(p_{1,\nu}\, p_{2,\rho}\, g_{\mu\delta} + p_{1,\rho}\, p_{2,\mu}\, g_{\nu\delta} + p_{1,\rho}\, p_{2,\delta}\, g_{\mu\nu} - \frac{1}{2}m_X^2\, g_{\mu\rho}\, g_{\mu\delta}\right) \tag{6.11c}$$

is included to this comparison.

From Eqs. 6.11, the (off-shell) decays $X, X_\rho, X_{\rho\delta} \to Z_\mu(p_1)Z_\nu(p_2)$ can be determined by contracting with the final state Z bosons' effective polarization vectors $\epsilon_\mu^*(p_1), \epsilon_\nu^*(p_2)$, which encode the Breit-Wigner propagator and the respective Z decay vertex.

The spin- and $\mathcal{CP}$-dependence of the X production from quarks via the effective Lagrangian in the vectorial scenario [123] is included

$$\mathcal{L}^{q\bar{q}X} = \bar{\Psi}_q\gamma^\mu\left(g_L^v\, \mathbb{P}_L + g_R^v\, \mathbb{P}_R\right)\Psi_q\, X_\mu\,, \tag{6.12a}$$

where

$$\mathbb{P}_{L,R} = \frac{1}{2}\left(\mathbb{1} \mp \gamma_5\right)\,, \tag{6.12b}$$

project to left- and right-handed fermion chirality as usual. Defining $g_{1,2}^v = g_R^v \pm g_L^v$, the vectorial and axial couplings can be steered via $g_{1,2}^v$. For the gluon-induced production of the scalar X case in Eq. 6.10, the interaction vertices can be computed from

$$\mathcal{L}^{ggX} = -\frac{1}{4}\left(g_1^s\, G^{\mu\nu}G_{\mu\nu}\, X + g_2^s\, G^{\mu\nu}\widetilde{G}_{\mu\nu}\, X\right)\,, \tag{6.12c}$$

$J^{\mathcal{CP}}(X)$	production Eq. 6.12	decay Eq. 6.11
0^+	$g_1^s \neq 0,\ g_2^s = 0$	$c_1^s \neq 0,\ c_2^s = 0$
0^-	$g_1^s = 0,\ g_2^s \neq 0$	$c_1^s = 0,\ c_2^s \neq 0$
1^+	$g_1^v = 0,\ g_2^v \neq 0$	$c_1^v = 0,\ c_2^v \neq 0$
1^-	$g_1^v \neq 0,\ g_2^v = 0$	$c_1^v \neq 0,\ c_2^v = 0$
2^+	$g_1^t \neq 0$	$c_1^t \neq 0$

Table 6.4.: Definition of the scenarios considered for the comparison in Sec. 6.4.

where $\widetilde{G}_{\mu\nu}$ is the Hodge dual of the non-abelian $SU(3)$ field strength tensor $G^{\mu\nu}$. For the production of the tensor particle X from gluons, again the vertex function quoted in Eq. 6.11c is assumed. This choice corresponds to graviton-like coupling, which, when taken to be universal, is already heavily constrained by Tevatron data (see e.g. [189] for recent D$\varnothing$ searches). The $X = 2^+$, however, still represents a valid candidate for a spin and $\mathcal{CP}$ analysis.

In the following the five scenarios of Table 6.4 are considered in the comparison in Sec. 6.4. The parton level Monte Carlo results for observables of Eq. 1.17 are plotted in Figs. 6.7-6.11 of Sec. 6.4. From a purely phenomenological point of view, the strategy to normalize the parton level cross sections to the SM Higgs production at next-to-leading order as was done before effectively removes the dependence on the process-specific combinations of the parameters $c_{1,2}^{s,v}, c_1^t$ and $g_{1,2}^{s,v}, g_1^t$, as well as the dependence on the initial state parton distribution functions on the considered spin- and $\mathcal{CP}$-sensitive angles. At the same time, the distinct angular correlations will induce different signal efficiencies for the different particles $X = J^{\mathcal{CP}}$, when the signal sample is confronted with the selection cuts of the subjet analysis. In this approach, these naturally communicates to the final state after showering and hadronization.

In principle, the s-channel signal adds coherently to the continuum ZZ production and their subsequent decay. The t-channel Feynman graphs are considered as part of the background and the resulting interference terms are discarded, which is admissible in the vicinity of the resonance. The effect of the interference on the angular distributions at the parton level for inclusive generator-level cuts was explicitly checked and excellent agreement for the invariant X mass window around the resonance was found, which is later applied as a selection cut in the subjet analysis.

The MadEvent-generated signal events are processed further with Herwig++ for parton showering and hadronization. As Herwig++ includes spin correlations to the shower, the unphysical contamination of the backgrounds' angular distribution by simulation-related shortcomings is minimized. The results were also compared to Pythia 6.4 to assess the systematic uncertainties and find reasonable agreement for the net efficiencies after all analysis steps have been carried out. This can be seen in detail in Tab. 6.5 and the discussion of the next section.

	0^+		0^-		1^-		1^+		2^+	
	P	H	P	H	P	H	P	H	P	H
Raw	1.00		1.00		1.00		1.00		1.00	
Cuts	0.41	0.53	0.35	0.47	0.28	0.40	0.29	0.42	0.31	0.40
Hadr.Z	0.22	0.29	0.16	0.22	0.16	0.22	0.16	0.23	0.15	0.19
m_X	0.17	0.22	0.12	0.16	0.12	0.17	0.13	0.18	0.11	0.15
ΔR_{ZZ}	0.15	0.20	0.11	0.14	0.10	0.14	0.10	0.14	0.10	0.13
Tr+Pr	0.10	0.13	0.07	0.09	0.07	0.10	0.07	0.10	0.06	0.08

	$Z+$ jets		ZZ		$t\bar{t}$	
	P	H	P	H	P	H
Raw	1.00		1.00		1.00	
Cuts	0.15	0.17	0.24	0.36	0.02	0.01
Hadr.Z	4.2×10^{-3}	6.5×10^{-3}	0.02	0.03	1.2×10^{-3}	0.8×10^{-3}
m_X	1.6×10^{-3}	2.2×10^{-3}	4.7×10^{-3}	7.0×10^{-3}	2.3×10^{-4}	1.6×10^{-4}
ΔR_{ZZ}	1.3×10^{-3}	1.9×10^{-3}	3.7×10^{-3}	5.7×10^{-3}	2.0×10^{-4}	1.3×10^{-4}
Tr+Pr	4.7×10^{-4}	5.7×10^{-4}	1.9×10^{-3}	2.9×10^{-3}	7.8×10^{-5}	4.2×10^{-5}

Table 6.5.: Cut flow comparison of the MADEVENT signal event when processed either with PYTHIA 6.4 (referred to as P) or HERWIG++ (denoted by H) for the X states of Tab. 6.4. Starting from the showered sample on calorimeter level (Raw), we apply the selection cuts (Cuts), the hadronic Z reconstruction requirements, the X mass reconstruction (m_X), the S/B-improving requirement on ΔR_{ZZ}, and trimming and pruning (Tr+Pr). The selection criteria are described in detail in Sec. 6.2.

6.4. Results and Discussion

In Figs. 6.7-6.12 the angles at matrix element level of Eq. 1.17 are shown after various steps of the analysis have been carried out. In addition, there is also a comparison of the full hadron level result and Monte Carlo truth, i.e. using the shower's particle information.

Comparing the two shower and hadronization approaches of PYTHIA 6.4 and HERWIG++ for the process efficiencies in Table 6.5 shows substantial discrepancies at intermediate steps of this analysis. After the entire analysis has been carried out this translates into a systematic uncertainty of $\sim 30\%$ of the total cross sections. This is not a too large disagreement as both programs rely on distinct philosophies and approaches, which typically result in sizable deviations when compared for identical Monte Carlo input. The plots in Figs. 6.7-6.12 show distributions obtained with HERWIG++.

Regarding the angular distributions, it is immediately clear that the chosen selection criteria, Eqs. 6.7-6.8, do heavily affect the $\mathcal{CP}$ sensitive angular distributions of Eqs. 1.17. Retaining a signal-over-background ratio of approximately 0.5, however, does not allow to relax the p_T cut on the fat jet. This cut turns out to be lethal to some of the angular distributions. Referring, e.g., to $\cos\theta^\star$, plotted in
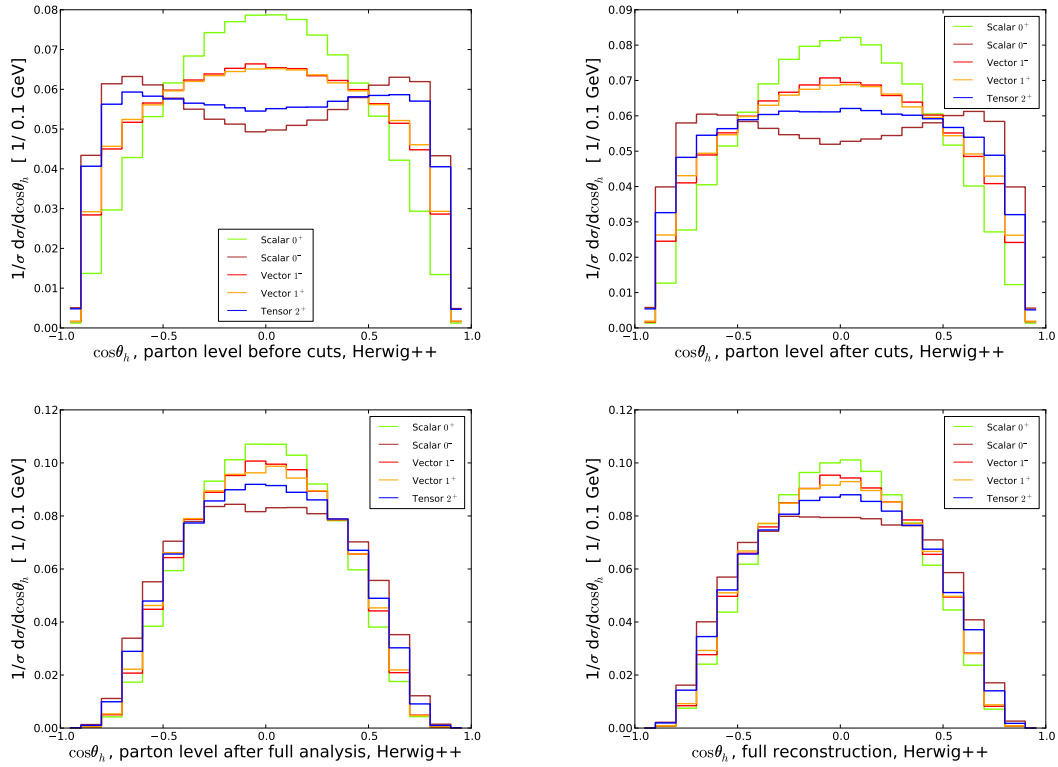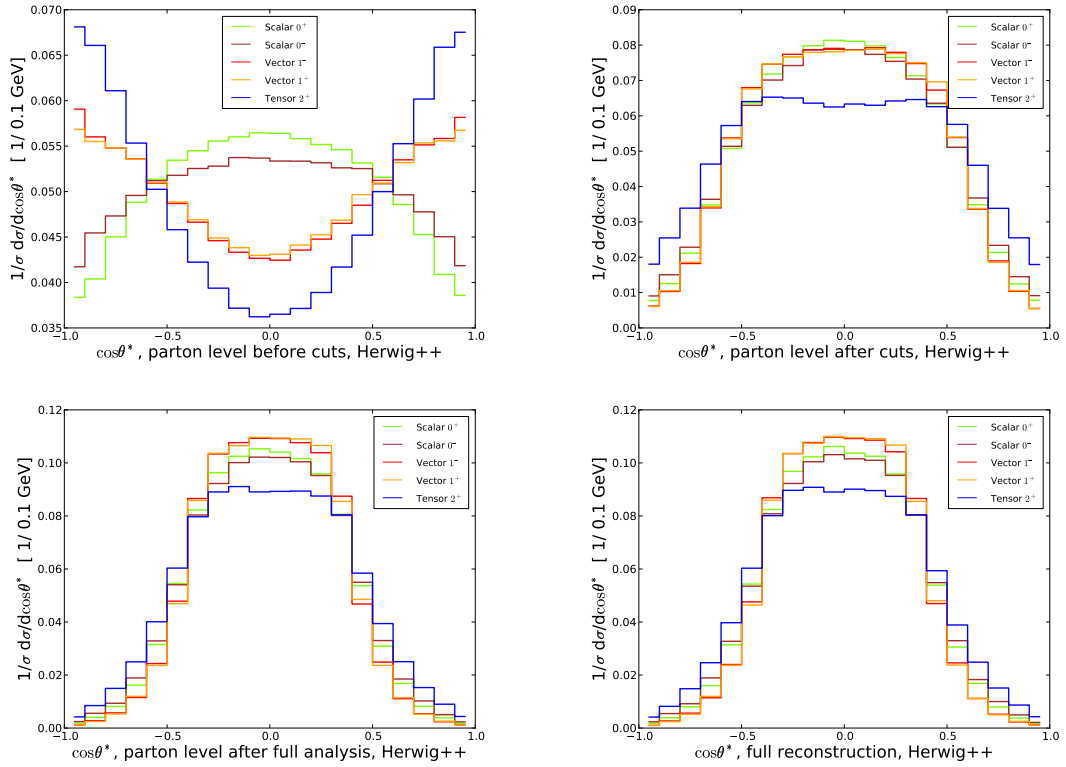
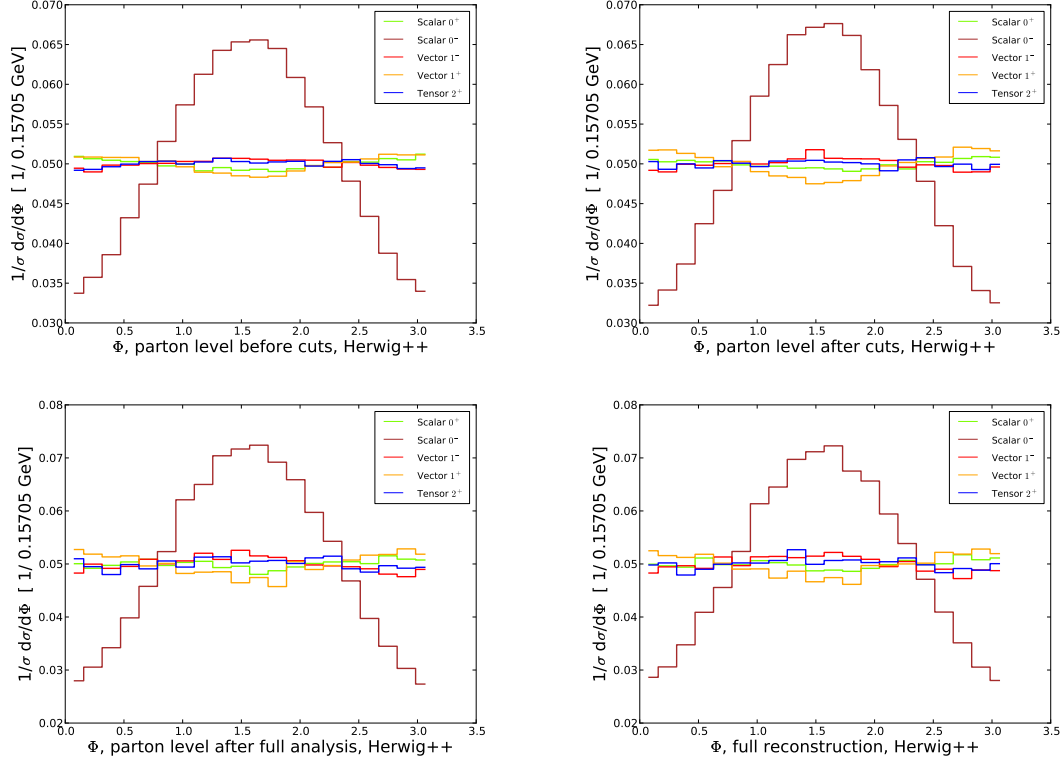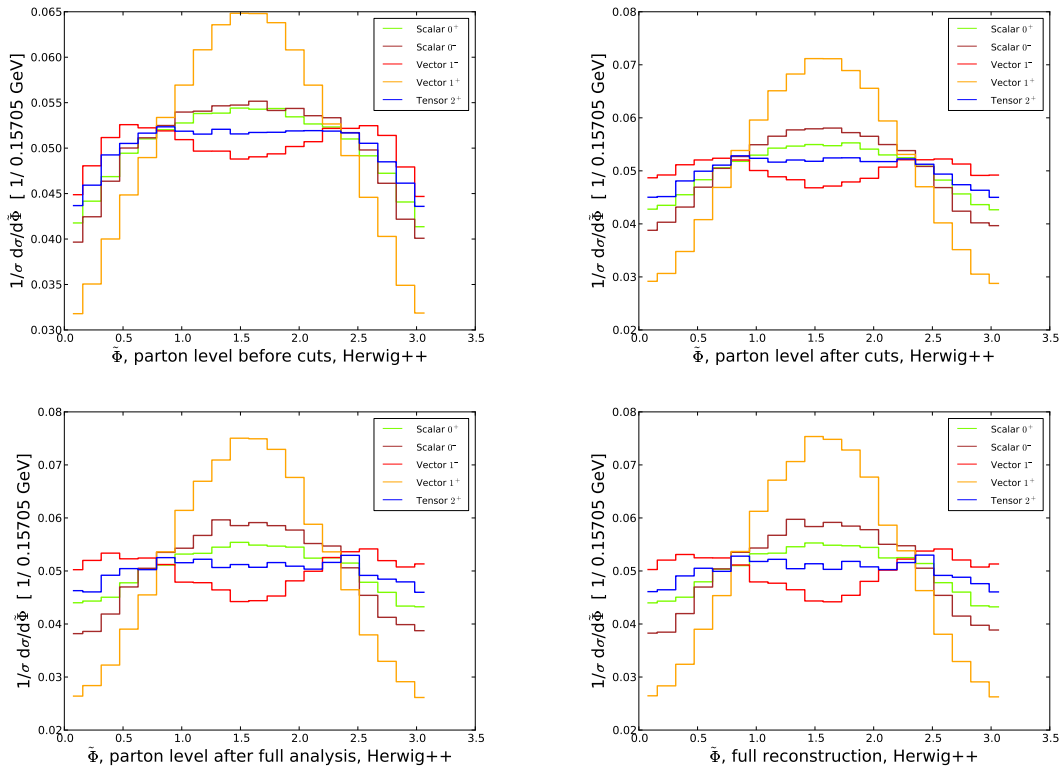Figure 6.7.: Cosine of the helicity angle θ_h, Eq. 1.17c, calculated from the hadronically decaying Z at different steps of the analysis: Inclusive Monte Carlo generation level (top, left), Monte Carlo generation level including selection cuts Eqs. 6.7-6.8 (top, right), after the full subjet analysis including Monte Carlo truth information (bottom, left), and after the full analysis (bottom, right).

Fig. 6.9, it can be found that the fat jet criteria, Eq. 6.8, force the distribution into reflecting extremely hard, central decay products. It is of course not very surprising that the decay products can be found in the central region as the basic idea of using boosted Z bosons focuses on the requirement of all decay products lying close in the η-ϕ-plane. However, this removes essentially all discriminating features from the differential distribution $d\sigma/d\cos\theta^\star$, that show up for $|\cos\theta^\star| \gtrsim 0.5$ at the (inclusive) Monte Carlo event generation level. This is also reflected in the distinct acceptance level of the different $J^{\mathcal{CP}}$ samples, shown in Tab. 6.5. It is interesting to note that, throughout, the fully hadronic distributions are in very good agreement with the Monte Carlo-truth level.

Most of the sensitivity found in the observable $\tilde{\Phi}$ for the signal sample, can be carried over to the hadron-level. Yet, the angular pattern is known to be sensitive to the X's mass scale, tending to de-correlate for larger X masses (see e.g. [17]).

As already pointed out in Sec. 6.3.1, the ambiguity in $\cos\Phi$ smears out the an-
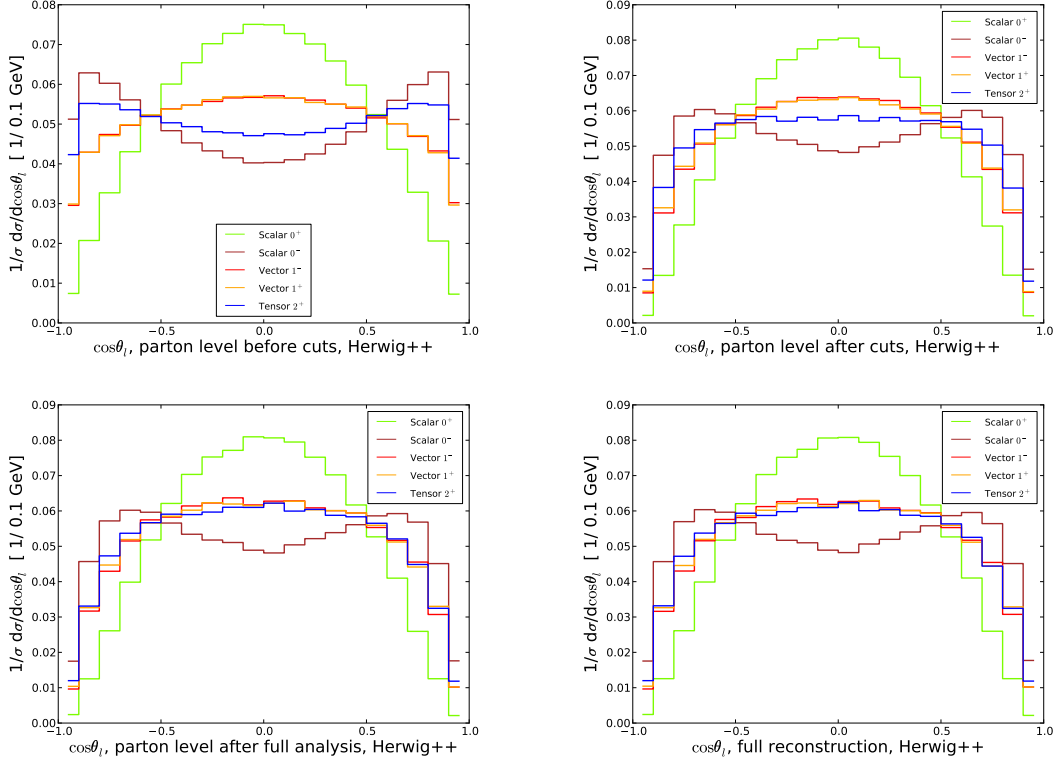
Figure 6.8.: Cosine of the helicity angle θ_ℓ, Eq. 1.17c, calculated from the leptonically decaying Z at different steps of the analysis: Inclusive Monte Carlo generation level (top, left), Monte Carlo generation level including selection cuts Eqs. 6.7-6.8 (top, right), after the full subjet analysis including Monte Carlo truth information (bottom, left), and after the full analysis (bottom, right).

gular correlations quite a lot in Fig. 6.10. This comes not as too large limitation of the angle's sensitivity for a $\mathcal{CP}$-odd scalar particle X. For $X = 0^-$, the distribution peaks at $\Phi = \pi/2$, and is also rather symmetrical around $\pi/2$. This leaves after the subjet analysis the helicity angles of Eq. 1.17c and $\tilde\Phi$ as three sensitive angles out of five not taking into account the background distribution.

Crucial to obtaining angular correlations after all, is the capability of the analysis to reconstruct both of the Z rest frames (and from them the X rest frame). This is already clear from the angles' definition in Eq. 1.17, and, again, this is not an experimental problem considering the purely leptonic channels. For the angles Φ and $\theta^\star$ decorrelate (with the exception of 0^-) due to the selection criteria, a bad rest frame reconstruction would not be visible in these observables immediately. This is very different in the case of the helicity angles. Quite obviously, given a good hadronically decaying Z rest frame reconstruction, the *identical* leptonic helicity angle can be applied as invoked for the measurement in $X \to ZZ \to 4\ell$;

Figure 6.9.: Cosine of the angle $\theta^\star$, Eq. 1.17d, calculated from the hadronically decaying Z at different steps of the analysis: Inclusive Monte Carlo generation level (top, left), Monte Carlo generation level including selection cuts Eqs. 6.7-6.8 (top, right), after the full subjet analysis including Monte Carlo truth information (bottom, left), and after the full analysis (bottom, right).

this angle has been referred to as θ_ℓ, previously. The only difference compared to the purely leptonic analysis is that here a partly hadronic system is consulted to construct the reference system, in which the leptonic helicity angle θ_ℓ is defined.

Indeed, the subjet analysis described in Sec. 6.2 is capable of giving a very good reconstruction of the hadronically decaying Z boson rest frame, while sufficiently reducing the backgrounds. This allows to carry over most of the central sensitivity of the angular distributions in Fig. 6.8 to the fully simulated final state. However, the hadronically-defined helicity angle, displayed in Fig. 6.7, also suffers badly from the subjet analysis. It is interesting to note that the bulk of the modifications of $\cos\theta_h$ do not arise from the restrictive selection criterion Eq. 6.8, but from symmetry requirements among the subjets in the mass-drop procedure. Thus, the subjets which provide a significant mass drop are biased towards $\theta_h \simeq 90°$.

A remaining key question that needs to be addressed is whether the potentially sensitive angles θ_ℓ, Φ, and $\tilde\Phi$ exhibit visible spin- and $\mathcal{CP}$-dependent deviations when the background distribution is taken into account. These angles including

Figure 6.10.: Angle Φ, Eq. 1.17d, calculated from the hadronically decaying Z at different steps of the analysis: Inclusive Monte Carlo generation level (top, left), Monte Carlo generation level including selection cuts Eqs. 6.7-6.8 (top, right), after the full subjet analysis including Monte Carlo truth information (bottom, left), and after the full analysis (bottom, right).

the backgrounds are shown in Fig. 6.12. The backgrounds' $\tilde{\Phi}$ distribution largely mimics the 1^+ shape under the subjet analysis' conditions, so it is not possible to claim sensitivity unless the background distribution is very well known. This also accounts for the Φ distribution in a milder form. While here the background is flat to good approximation, S/B limits the sensitivity to the shape deviations, which are ameliorated due to the different signal efficiencies. However, the distribution remains sensitive to the $X = 0^-$ shape. $pp \to X \to \mu^+\mu^- jj$ remains sensitive to the $\mathcal{CP}$ quantum number of a scalar particle X in the $\cos\theta_\ell$ distribution, which is opposite in shape comparing to the background distribution. The distributions for the PYTHIA sample for these observables show the same behavior for the backgrounds and can be found in Appendix C.

It is interesting to note that for one observable, $\cos\theta_h$, the predictions of PYTHIA and HERWIG++ differ for the Z+jet background. The effect can be seen from Fig. 6.13, the background in PYTHIA follows the distribution found in the leptonic counterpart with two distinct peaks, whereas HERWIG++ predicts one central

Figure 6.11.: Angle $\tilde{\Phi}$, Eq. 1.17e, calculated from the hadronically decaying Z at different steps of the analysis: Inclusive Monte Carlo generation level (top, left), Monte Carlo generation level including selection cuts Eqs. 6.7-6.8 (top, right), after the full subjet analysis including Monte Carlo truth information (bottom, left), and after the full analysis (bottom, right).

peak without any structure. This can be understood by considering the nature of this observable. This angle is defined in the plane of the hadronic Z decay products. For the Z+jet process however, the two subjets found do not stem from one resonance but from the parton shower of one hard jet. So this observable seems to be sensitive to the inner structure of the jet and therefore also the shower evolution. A subjet analysis taking this observable or similar ones into account might give insights into the QCD evolution inside jets.

In this spin analysis, only an X mass $m_X = 400$ GeV was considered, a choice which is quite close to the lower limit of the mass range, where the boosted analysis is applicable. Some remarks concerning this analysis for different X masses and widths are due. The boost requirements and the centrally-required selection cuts do affect the angular distributions in a X mass-independent manner. The remaining angles are then qualitatively determined by the goodness of reconstruction, which becomes increasingly better for heavier X masses, keeping the width fixed.
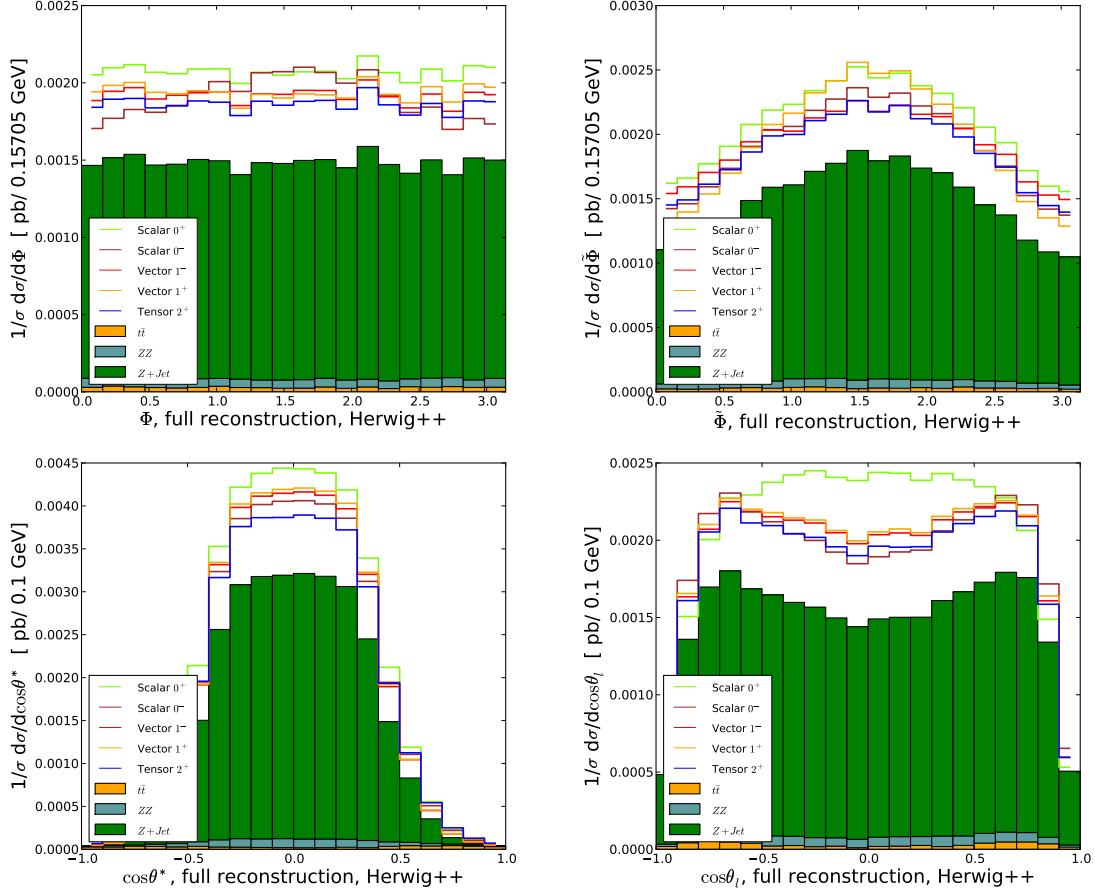
Figure 6.12.: The spin and $\mathcal{CP}$ sensitive angles Φ (top, left), $\tilde{\Phi}$ (top, right), $\cos\theta^*$ (bottom, left) and $\cos\theta_\ell$ (bottom, right) including the shape of the backgrounds, simulated with HERWIG++.

In case of the SM Higgs boson, the width is proportional to m_H^3 due to the enhanced branching of the Higgs to longitudinally-polarized Zs. With the resonance becoming width-dominated, the mass reconstruction still remains sufficiently effective; S/B, however, increasingly worsens. For these mass ranges, the analysis is sensitive to the experimental methods that recover the resonance excess. Additionally, from a theoretical perspective, there are various models known in the literature where a heavy resonance becomes utterly narrow or exceedingly broad [180, 190]. The former yields, depending on the (non-SM) production cross section, a better mass reconstruction, while the latter case is again strongly limited by S/B, cf. Fig. 6.12. For any of these EWSB realizations, the method shown should be modified accordingly, taking into account all realistic experimental algorithms, techniques, and uncertainties as well as all model-dependent parameters.
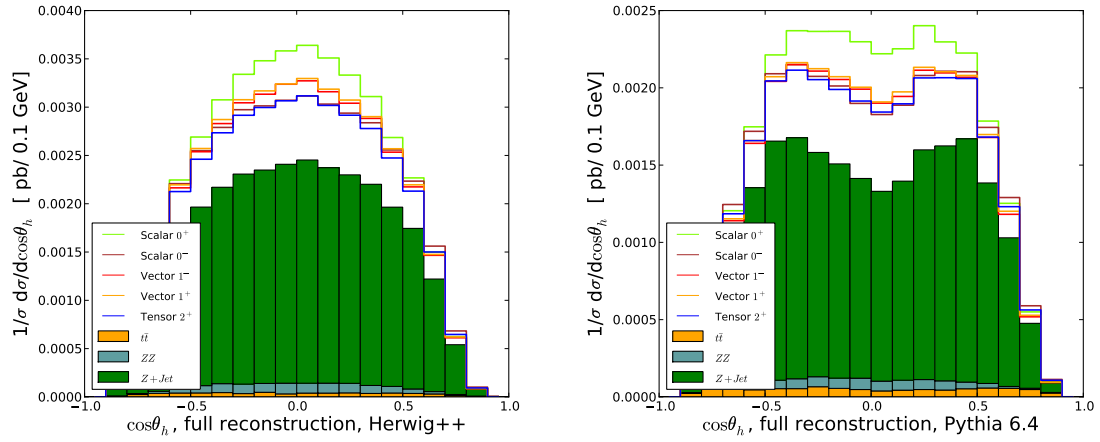
Figure 6.13.: The spin and $\mathcal{CP}$ sensitive angles $\cos\theta_{\text{had.}}$ including the shape of the backgrounds, simulated with HERWIG++ and PYTHIA 6.

6.5. Summary and Conclusions

This work shows that fat jet techniques allow to extract semi-leptonic H $\rightarrow$ ZZ decays at the LHC. To discriminate the signal from the large Z + jets background a combination of mass drop searches and filtering based on large light-flavor C-A jets is used. For Higgs masses between 350 GeV and 500 GeV a successive reconstruction of the two Z bosons and the Higgs boson extracts the inclusive signal at the 5σ level based on $10\,\text{fb}^{-1}$ at a $\sqrt{s} = 14\,\text{TeV}$ LHC. Using additional information on the QCD structure of the event by employing a combined pruning/trimming analysis yields typical signal-to-background ratios $S/B \sim 1/2$.

Comparing these results to the purely leptonic ZZ channel at 14 TeV collider energy the leptonic signal on the one hand achieves $S/B > 1$ while the semi-leptonic analysis only reaches $S/B \sim 0.33 - 0.87$. On the other hand, this is compensated by the larger number of signal events in the semi-hadronic channel. The semi-hadronic channel, which has received only little attention before, can have as much statistical significance as the purely leptonic "gold plated" mode. Heavy Higgs boson detection might greatly benefit from the orthogonal strength of this semi-leptonic ZZ $\rightarrow \ell\ell jj$ search, especially if the LHC operations will continue at energies lower than the design value.

In addition, the performance of new jet techniques when applied to the analysis of spin- and $\mathcal{CP}$-sensitive distributions of a heavy resonance resembling the SM in the overall rate in $pp \rightarrow \mu^+\mu^- jj$ was explored. A detailed investigation of the angular correlations was performed and the limitations specific to this approach were identified, resulting from the boosted and central kinematical configurations. It is self-evident, that a QCD-dominated final state cannot compete with a leptonic final state in terms of signal purity, higher order- and shower uncertainties, *per se*. These uncertainties are inherent to any current discussion related to jet physics.

Nonetheless, it has been shown that potential "no-go theorems" following from huge underlying event and QCD background rates for $pp \to X \to \text{ZZ} \to \ell^+\ell^- jj$ can be sufficiently ameliorated to yield an overall sensitivity to the $\mathcal{CP}$ property of a singly-produced scalar resonance. Given that the cross section of the semi-hadronic decay channel is approximately ten times larger compared to $X \to 4\ell$, the performed subjet analysis qualifies to at least supplement measurements of the purely leptonic decay channels.

A question that has not been addressed in this work is the potential application of the presented strategy to signatures, which do not resemble the SM at all. Electroweak symmetry breaking by strong interactions is likely to yield a large rate of longitudinally polarized electroweak bosons due to modified $X\,\text{ZZ}$ and $X\bar{q}q$ couplings [181, 182]. Measuring the fraction of longitudinal polarizations, which can be inferred from the Z's decay products' angular correlation as proposed recently in Ref. [191], should benefit from the methods presented in this work. This is in particular true for new composite operators, such as a modification of the Higgs kinetic term [182], inducing asymmetric angular decay distributions of the leptons. In addition, this analysis is also applicable to the investigation of iso-vectorial resonances (see e.g. Ref. [190]) in $pp \to \text{WZ}$, with the W decaying to hadrons, and $\text{Z} \to \mu^+\mu^-$.

Conclusion

The search for the Higgs boson is one of the major tasks of the Large Hadron Collider. However, it is a very challenging undertaking since the Higgs boson production processes suffer from large backgrounds and the Higgs mass itself is unknown. Since the Higgs mass determines the branching ratios for the decay of the Higgs boson, the final state which is sought for strongly depends on the Higgs mass considered.

The coupling of vector bosons to the Higgs boson plays a crucial role in both production as well as decay of the Higgs boson. On the one hand, Vector Boson Fusion plays an important role as Higgs production process since it both has a comparatively large cross section and allows to measure the Higgs couplings to vector bosons directly. On the other hand, for Higgs masses above 160 GeV the Higgs boson decays predominantly into pairs of vector bosons.

In this work, three aspects of vector boson coupling to the Higgs boson were considered. First, a generator study investigating the influence of different models used in Monte Carlo generators on the VBF selection of both signal and background in the channel $H \rightarrow WW \rightarrow 2\ell\,\not{E}_T$ was performed. In addition, the Monte Carlo description of the Z boson and jets background was validated with the collision data taken by the CMS experiment in the LHC operations in 2010. Finally, a novel search for a heavy Higgs boson in the decay channel $H \rightarrow ZZ \rightarrow 2\ell\,2j$ was developed.

The special event topology of Higgs production via Vector Boson Fusion allows to suppress background contributions effectively via the use of a forward jet selection and a veto on central jets. The exact description of the signal events by Monte Carlo event generators is important for the search strategies employed. It was shown that leading order predictions combined with parton showers are not able to describe the central jet veto correctly, with differences of a factor of two between the two models compared. The inclusion of higher order corrections improved the agreement between the Monte Carlo predictions, but still the discrepancy is sizeable. This demonstrates the need for a validation of the available Monte Carlo tools with collision data to reduce the existing uncertainties.

The LHC operations in 2010 provided a large number of Z boson events. This makes a validation of the Monte Carlo description of the Z boson plus jets back-

ground to the VBF search with data feasible. Starting from inclusive quantities, the description of the measured data is evaluated, which then is extended to more exclusive ones, closer to the topologies relevant for Higgs searches. A reasonable agreement between data and the two Monte Carlo samples used was found, however, especially in observables where non-perturbative corrections play an important role the Monte Carlo generators have shortcomings. Especially the activity in the rapidity gap region in two-jet events was underestimated by both samples, so more tuning is needed.

The Higgs decay channel $H \rightarrow ZZ \rightarrow 2\ell 2j$ has not received much attention in the past since the Z boson and jet backgrounds were deemed to be too large. However, the Z bosons stemming from a heavy Higgs boson decay are naturally boosted. This allows to cluster all decay products from a hadronic Z boson decay into one large jet and use subjet techniques to remove QCD contaminations. This allows to revive the semi-leptonic $H \rightarrow ZZ$ as a Higgs search channel for Higgs boson masses above 300 GeV. In addition, it is possible to use the channel in order to study the spin and $\mathcal{CP}$ properties of the Higgs found with this method.

A

QCD – a non abelian gauge theory

QCD is a non-abelian gauge theory with gauge group $SU(3)$. $SU(3)$ is a Lie group and so the generators of the group τ^a satisfy the corresponding Lie-algebra $su(3)$[1]

$$\left[\tau^a, \tau^b\right] = i f^{abc} \tau^c \tag{A.1}$$

where the numbers f^{abc} are called the *structure constants*. They obey the *Jacobi identity*

$$f^{ade} f^{bcd} + f^{bde} f^{cad} + f^{cde} f^{abd} = 0 \ , \tag{A.2}$$

which follows from the generators satisfying the identity

$$\left[\tau^a, [\tau^b, \tau^c]\right] + \left[\tau^b, [\tau^c, \tau^a]\right] + \left[\tau^c, [\tau^a, \tau^b]\right] = 0 \ . \tag{A.3}$$

The generators t^a in the fundamental representation of $su(N)$ obey the relations

$$t_N^a t_N^a = C_N \cdot, \qquad C_N = \frac{N^2 - 1}{2N}, \qquad \mathrm{Tr}[t_N^a t_N^b] = \frac{1}{2}\delta^{ab} \ . \tag{A.4}$$

In the adjoint representation the generators T^a are given by the totally antisymmetric structure constants as

$$(T^c)_{ab} = -i f^{abc}, \qquad \mathrm{Tr}[T^c T^d] = f^{abc} f^{abd} = C_A \delta^{cd}, \quad C_A = N \tag{A.5}$$

Constructing a Lagrangian density that is invariant under local $SU(3)$ transformations yields

$$\mathcal{L}_{\mathrm{QCD}} = \bar{q}(i\slashed{\partial} - m_q)q - g_s \bar{q}\gamma^\mu T^a q A_\mu^a - \frac{1}{4}F^{\mu\nu,a} F_{\mu\nu}^a \tag{A.6}$$

with

$$F_{\mu\nu}^a = \partial_\mu A_\nu^a - \partial_\nu A_\mu^a - g_s f^{abc} A_\mu^b A_\nu^c \ . \tag{A.7}$$

---

[1]here and in the following no distinction between upper and lower indices is made, since in $su(N)$ the Cartan-metric can always be chosen as δ_{ab}

The quantization of this theory is usually done by means of path integrals which needs the insertion of a gauge-fixing term which in covariant gauges can be chosen to be

$$\mathcal{L}_{\text{gauge fixing}} = -\frac{1}{2\xi}(\partial_\mu A^\mu)^2 \tag{A.8}$$

as well as the insertion of Grassman-valued ghost-fields c_a to absorb unphysical polarizations of the gluon field:

$$\mathcal{L}_{\text{ghost}} = \partial_\mu \bar{c}^a \tilde{D}^\mu_{ab} c^b \tag{A.9}$$

with $\tilde{D}^\mu_{ab}$ being the covariant derivative in the adjoint representation

$$\tilde{D}^\mu_{ab} = \partial^\mu \delta_{ab} - g f_{abc} A^{c,\mu} \ . \tag{A.10}$$

Appendix B

Les Houches Event files

The Les Houches Event files consist of two kinds of common blocks that are embedded into an XML structure.

B.1. User process run information: HEPRUP

The general information about the generated events is stored in this `common` block.

```
integer        MAXPUP
parameter (   MAXPUP=100  )
integer        IDBMUP, PDFGUP, PDFSUP, IDWTUP, NPRUP, LPRUP
double precision  EBMUP, XSECUP, XERRUP, XMAXUP
common /HEPRUP/  IDBMUP(2), EBMUP(2), PDFGUP(2), PDFSUP(2),
+                IDWTUP, NPRUP, XSECUP(MAXPUP), XERRUP(MAXPUP),
+                XMAXUP(MAXPUP), LPRUP(MAXPUP)
```

First, there are informations about the beam particles, what particles there are (`IDBMUP`), their energy (`EBMUP`) and in the case of hadrons the PDF sets used in the calculation (`PDFGUP, PDFSUP`).

Then there is a switch (`IDWTUP`) telling the SHG if the events are weighted and if the SHG is supposed to produce unweighted events or not.

Finally, there is a list of the `NPRUP` different processes stored in the file and for each process the cross section (`XSECUP`), its error (`XERRUP`), the maximal weight (`XMAXUP`) and a number `LPRUP` identifying the process is stored.

Only the most general informations are included here in order to obtain a general structure.

B.2. User process event information: HEPEUP

For each event in the final state of the calculation there is the HEPEUP common
block in which the necessary information concerning this event is stored.
```
 integer       MAXNUP
 parameter (   MAXNUP=500 )
 integer       NUP, IDPRUP, IDUP, ISTUP, MOTHUP, ICOLUP
 double precision  XWGTUP, SCALUP, AQEDUP, AQCDUP,
                   PUP, VTIMUP, SPINUP
 common /HEPEUP/  NUP, IDPRUP, XWGTUP, SCALUP, AQEDUP, AQCDUP,
+                 IDUP(MAXNUP), ISTUP(MAXNUP), MOTHUP(2,MAXNUP),
+                 ICOLUP(2,MAXNUP), PUP(5,MAXNUP), VTIMUP(MAXNUP),
+                 SPINUP(MAXNUP)
```
First, there is the size of the common block given by the number of particles NUP.
This is followed by information about the event, the process IDPRUP, the weight
XWGTUP, the scale SCALUP at which the running couplings and PDFs have been
evaluated and the values of the coupling constants used (AQEDUP, AQCDUP).

Then for each of the NUP particles the relevant informations are stored. These
consist of the information what kind of particle there is (IDUP[1]), the status of the
particle (ISTUP), specifying whether the particle is in- or outgoing or an internal
resonance, the mother particles (MOTHUP) and the color flow (ICOLUP). Then there
is the five-momentum[2] of the particle (PUP), the invariant lifetime VTIMUP and the
spin information SPINUP.

B.3. XML structures in Les Houches event files

The data in the HEPRUP and HEPEUP common blocks has to be stored in one single
file. In addition to the data stored in these blocks a user might want to add
additional program- specific information on how the events were generated or
other totally different data. For this an XML-like framework is used to store
this additional data and to distinguish it from the compulsory one in the common
blocks. The Les Houches File created that way is no "real" XML document by
the standard of this file format, since the common blocks contain data which is not
structured by XML standard, so no validating is possible.

The resulting structure for the files is:

---

[1]Numbered by the convention of the particle data group

[2]The first four components are the usual components of a four-momentum vector, $p_x, p_y, p_z, E,$
the fifth is the invariant mass squared

```
<LesHouchesEvents version="1.0">
<!--
  # optional information in completely free format,
  # except for the reserved end tag (see next line)
-->
<header>
  <!-- individually designed XML tags, in fancy XML style -->
</header>
<init>
  compulsory initialization information - HEPRUP data
  # optional initialization information
</init>
<event>
  compulsory event information - HEPEUP data
  # optional event information
</event>
(further <event> blocks, one for each event)
</LesHouchesEvents>
```

The tags must all be alone in their respective line, especially the `<init>`, `<event>` tags, since their position defines the points after which the compulsory data in the `common` blocks is stored. The `LesHouchesEvents` block defines the root element of the XML document, it shows the standard and version of the file. Additional information can be written in the `<!-- ... -->` and `<header>` ... `</header>` blocks. The data in the `<!-- ... -->` block is XML "comment" style, so it can be arbitrarily formatted, since it is ignored by XML parsers, whereas data in the `<header>` ... `</header>` block has to be based on XML syntax.

This structure is open to future as well as individual extensions, it is for example possible to add additional information in the attribute part of the elements containing the `common` blocks, since `<init` , `<event` followed by a blank and further text on the same line should be treated equivalent to `<init>`, `<event>` tags, any comment or information can follow after the compulsory initialization or event information before the respective end tag.

B.4. Sample Les Houches File

```
<LesHouchesEvents version="1.0">

<!--

File generated with VBFNLO - parton level MC program (LO)

pp -> H jj -> mu+ mu- jj


Higgs + 2 jets production in vector boson fusion with Higgs

decay into mu+ mu-.

Process is implemented at LO and NLO QCD.

Anomalous coupling parameters can be set in "anom_HVV.dat".

## Number of Events :  22702397

-->

<init> 2212   2212   7.000000E+03   7.000000E+03   0   0   10042   10042   2   1

  2.035589E-04   3.448832E-08   1.741728E-07   102

</init>

<event>

  7   102   1.058494E-08   6.360184E+01   7.554144E-03   1.376638E-01

      3   -1   0   0   501     0   0.0000000000E+00   0.0000000000E+00   7.7127008479E+02
                               7.7127008479E+02   0.0000000000E+00   0.0E+00   9.0E+00
     -1   -1   0   0     0   502   0.0000000000E+00   0.0000000000E+00  -4.7510403211E+02
                               4.7510403211E+02   0.0000000000E+00   0.0E+00   9.0E+00
      4    1   1   2   501     0   4.0431488591E+01   2.4829448551E+00   6.6093340603E+02
                               6.6217357052E+02   0.0000000000E+00   0.0E+00   9.0E+00
     -2    1   1   2     0   502  -5.1764506989E+01  -3.2480996279E+01  -4.3649404954E+02
                               4.4075121621E+02   0.0000000000E+00   0.0E+00   9.0E+00
     25    2   1   2     0     0   1.1333018398E+01   2.9998051424E+01   7.1726696188E+01
                               1.4344933017E+02   1.2001946086E+02   0.0E+00   9.0E+00
    -13    1   5   0     0     0  -3.3939222322E+01   7.0199312873E+00  -1.8970000138E+01
                               3.9509633665E+01   0.0000000000E+00   0.0E+00  -1.0E+00
     13    1   5   0     0     0   4.5272240721E+01   2.2978120137E+01   9.0696696326E+01
                               1.0393969650E+02   0.0000000000E+00   0.0E+00   1.0E+00

</event>

:
:

</LesHouchesEvents>
```
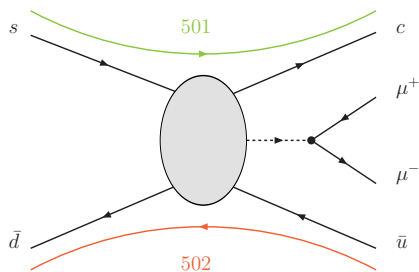

Figure B.1.: Schematic description of first event. The blob marks the VBF process producing the Higgs.

CP Angles Simulated with PYTHIA

The CP sensitive angles Φ, $\tilde{\Phi}$, θ^* and $\cos\theta_\ell$. Signal and backgrounds simulated using PYTHIA.
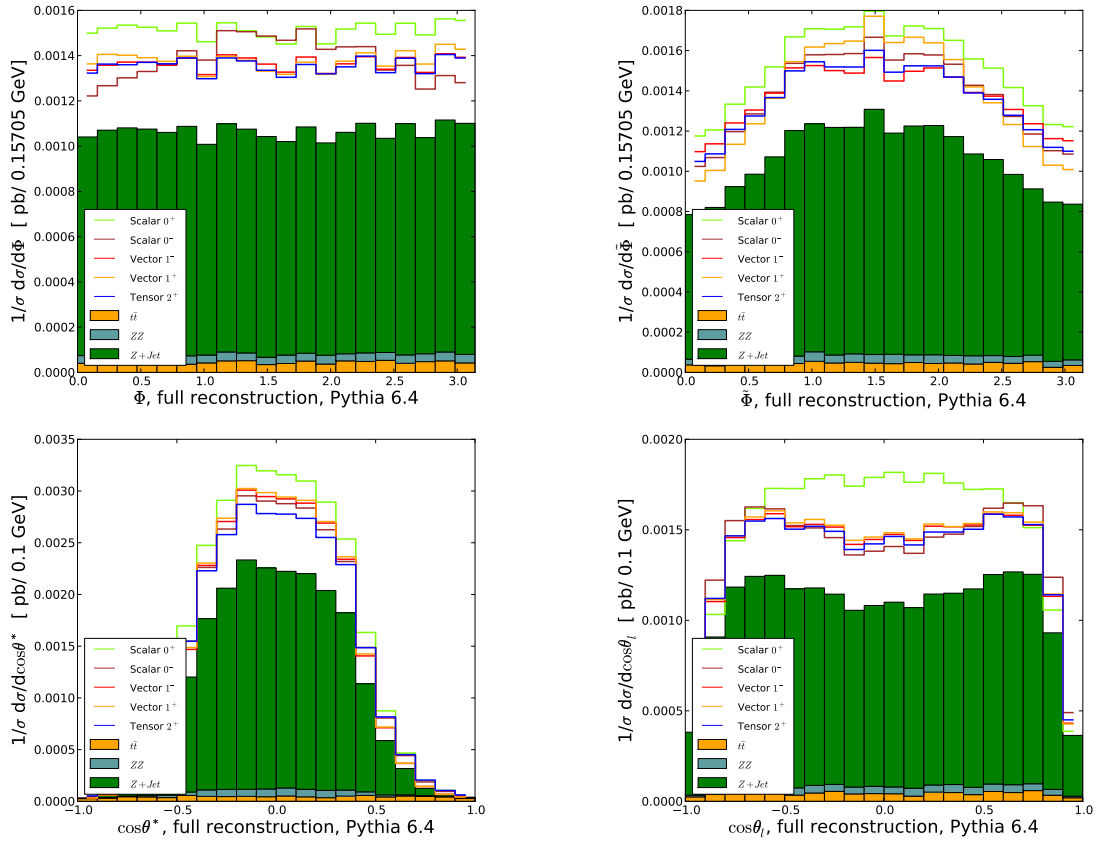
Figure C.1.: The spin and $\mathcal{CP}$ sensitive angles Φ (top, left), $\tilde{\Phi}$ (top, right), $\cos\theta^*$ (bottom, left) and $\cos\theta_\ell$ (bottom, right) including the shape of the backgrounds, simulated with PYTHIA.

List of Figures

List of Tables

Bibliography

[1] M. E. Peskin and D. V. Schroeder, "An Introduction To Quantum Field Theory," *Reading, USA: Addison-Wesley (1995) 842 p*

[2] L. H. Ryder, "Quantum Field Theory," *Cambridge, Uk: Univ. Pr. (1985) 443p*

[3] S. Glashow, Nucl. Phys. 22 (1961) 579; S. Weinberg, Phys. Rev. Lett. 19 (1967) 1264; A. Salam, in "Elementary Particle Theory", ed. N. Svartholm, Almqvist and Wiksells, Stockholm (1969) p. 367.

[4] P.A.M. Dirac, Proc. Roy. Soc. Lond. A114 (1927) 243; P. Jordan and W. Pauli, Z. Phys. 47 (1928) 151; W. Heisenberg and W. Pauli, Z. Phys. 56 (1929) 1; S. Tomonaga, Progr. Theor. Phys. 1 (1946) 27; J. Schwinger, Phys. Rev. 73 (1948) 416; R. Feynman, Phys. Rev. 76 (1949) 749.

[5] E. Fermi, Nuovo Cim. 11 (1934) 1; *ibid.* Z. Phys. 88 (1934) 161; R. Feynman and M. Gell-Mann, Phys. Rev. 109 (1958) 193.

[6] A. Djouadi, Phys. Rept. **457** (2008) 1

[7] P.W. Higgs, Phys. Rev. Lett. 13 (1964) 508; *ibid.* Phys. Rev. 145 (1966) 1156; F. Englert and R. Brout, Phys. Rev. Lett. 13 (1964) 321; G.S. Guralnik, C.R. Hagen and T. Kibble, Phys. Rev. Lett. 13 (1965) 585; T. Kibble, Phys. Rev. 155 (1967) 1554.

[8] B. W. Lee, C. Quigg and H. B. Thacker, Phys. Rev. D **16**, 1519 (1977).

[9] N. Cabibbo, L. Maiani, G. Parisi and R. Petronzio, Nucl. Phys. B158 (1979) 295; R. Dashen and H. Neuberger, Phys. Rev. Lett. 50 (1983) 1897; D. Callaway, Nucl. Phys. B233 (1984) 189; P. Hasenfratz and J. Nager, Z. Phys. C37 (1988) 477; J. Kuti, L. Lin, and Y. Shen, Phys. Rev. Lett. 61 (1988) 678; R. Chivukula and E. Simmons, Phys. Lett. B388 (1996) 788.

[10] M. Lindner, M. Sher and H.W. Zaglauer, Phys. Lett. 228B (1989) 139; M. Sher, Phys. Lett. B317 (1993) 159; *ibid.* Phys. Lett. B331 (1994) 448; G.

Altarelli and I. Isidori, Phys. Lett. B337 (1994) 141; J.A. Casas, J.R. Espinosa and M. Quiros, Phys. Lett. B342 (1995) 171; J. Espinosa and M. Quiros, Phys. Lett. B353 (1995) 257.

[11] The LEP Collaborations (ALEPH, DELPHI, L3 and OPAL), the LEP Electroweak Working Group and the SLD Heavy Flavour Group, *A combination of preliminary Electroweak measurements and constraints on the Standard Model*, hep-ex/0412015; `http://lepewwg.web.cern.ch/LEPEWWG`.

[12] FERMILAB-CONF-11-044-E
`http://www-d0.fnal.gov/Run2Physics/WWW/results/prelim/HIGGS/H106/H106.pdf`

[13] S. Dittmaier *et al.* [LHC Higgs Cross Section Working Group], arXiv:1101.0593 [hep-ph].

[14] C. P. Buszello, I. Fleck, P. Marquard and J. J. van der Bij, Eur. Phys. J. C **32** (2004) 209.

[15] C. P. Buszello, P. Marquard and J. J. van der Bij, [arXiv:hep-ph/0406181].

[16] S. Y. Choi, D. J. . Miller, M. M. Muhlleitner and P. M. Zerwas, Phys. Lett. B **553** (2003) 61, R. M. Godbole, D. J. . Miller and M. M. Muhlleitner, JHEP **0712** (2007) 031, P. S. Bhupal Dev, A. Djouadi, R. M. Godbole, M. M. Muhlleitner and S. D. Rindani, Phys. Rev. Lett. **100** (2008) 051801.

[17] Y. Gao, A. V. Gritsan, Z. Guo, K. Melnikov, M. Schulze and N. V. Tran, Phys. Rev. D **81**, 075022 (2010). [arXiv:1001.3396 [hep-ph]].

[18] A. De Rujula, J. Lykken, M. Pierini, C. Rogan and M. Spiropulu, Phys. Rev. D **82** (2010) 013003.

[19] J.-C. Chollet et al., ATLAS note PHYS-NO-17 (1992), L. Poggioli, ATLAS Note PHYS-NO-066 (1995);, D. Denegri, R. Kinnunen and G. Roullet, CMS-TN/93-101 (1993), I. Iashvili R. Kinnunen, A. Nikitenko and D. Denegri, CMS TN/95-076, D. Bomestar et al., Note CMS TN-1995/018, C. Charlot, A. Nikitenko and I. Puljak, CMS TN/95-101, G. Martinez, E. Gross, G. Mikenberg and L. Zivkovic, ATLAS Note ATL-PHYS-2003-001 (2003).

[20] N. Cabibbo and A. Maksymowicz, Phys. Rev. **137**, B438 (1965) [Erratum-ibid. **168**, 1926 (1968)].

[21] A. Bredenstein, A. Denner, S. Dittmaier and M. M. Weber, Phys. Rev. D **74** (2006) 013004.

[22] Q. H. Cao, C. B. Jackson, W. Y. Keung, I. Low and J. Shu, Phys. Rev. D **81** (2010) 015010.

[23] T. L. Trueman, Phys. Rev. D **18** (1978) 3423, J. R. Dell'Aquila and C. A. Nelson, Phys. Rev. D **33** (1986) 80.

[24] KNakamura *et al.* [Particle Data Group Collaboration], J. Phys. G **G37** (2010) 075021.

[25] J. C. Collins and D. E. Soper, Phys. Rev. D **16** (1977) 2219.

[26] R. Boughezal, [arXiv:0908.3641 [hep-ph]].

[27] D. Graudenz, M. Spira and P. M. Zerwas, Phys. Rev. Lett. **70** (1993) 1372. M. Spira, A. Djouadi, D. Graudenz and P. M. Zerwas, Nucl. Phys. B **453** (1995) 17

[28] M. 1. Kramer, E. Laenen and M. Spira, Nucl. Phys. B **511** (1998) 523

[29] Y. Schroder and M. Steinhauser, JHEP **0601** (2006) 051 K. G. Chetyrkin, J. H. Kuhn and C. Sturm, Nucl. Phys. B **744** (2006) 121

[30] R. V. Harlander and W. B. Kilgore, Phys. Rev. Lett. **88**, 201801 (2002) C. Anastasiou and K. Melnikov, Nucl. Phys. B **646**, 220 (2002) V. Ravindran, J. Smith and W. L. van Neerven, Nucl. Phys. B **665**, 325 (2003)

[31] A. Pak, M. Rogal and M. Steinhauser, arXiv:0907.2998 [hep-ph].

[32] S. Actis, G. Passarino, C. Sturm and S. Uccirati, arXiv:0809.1301 [hep-ph]; S. Actis, G. Passarino, C. Sturm and S. Uccirati, arXiv:0809.3667 [hep-ph].

[33] C. Anastasiou, G. Dissertori and F. Stockli, JHEP **0709** (2007) 018

[34] T. Figy, C. Oleari and D. Zeppenfeld, Phys. Rev. D **68** (2003) 073005 C. Oleari and D. Zeppenfeld, Phys. Rev. D **69** (2004) 093004 B. Jager, C. Oleari and D. Zeppenfeld, JHEP **0607** (2006) 015

[35] T. Han, G. Valencia and S. Willenbrock, Phys. Rev. Lett. **69** (1992) 3274

[36] M. Ciccolini, A. Denner, S. Dittmaier, Phys. Rev. Lett. **99** (2007) 161803. M. Ciccolini, A. Denner, S. Dittmaier, Phys. Rev. **D77** (2008) 013002.

[37] P. Bolzoni, F. Maltoni, S. -O. Moch, M. Zaro, Phys. Rev. Lett. **105** (2010) 011801.

[38] D. Zeppenfeld, R. Kinnunen, A. Nikitenko and E. Richter-Was, Phys. Rev. **D62**, 013009 (2000) D. Zeppenfeld, in *Proc. of the APS/DPF/DPB Summer Study on the Future of Particle Physics (Snowmass 2001)* ed. N. Graf, eConf **C010630**, P123 (2001) A. Belyaev and L. Reina, JHEP **0208**, 041 (2002)

[39] H. Chehime and D. Zeppenfeld, "'Rapidity gaps' A New tool to find the Higgs?," C93-02-21; A. Duff and D. Zeppenfeld, Phys. Rev. D **50** (1994) 3204

[40] T. Figy, V. Hankele, D. Zeppenfeld, JHEP **0802** (2008) 076.

[41] S. L. Glashow, D. V. Nanopoulos and A. Yildiz, Phys. Rev. D **18** (1978) 1724. T. Han and S. Willenbrock, Phys. Lett. B **273** (1991) 167.

[42] O. Brein, A. Djouadi and R. Harlander, Phys. Lett. B **579**, 149 (2004)

[43] M. L. Ciccolini, S. Dittmaier and M. Kramer, Phys. Rev. D **68** (2003) 073003

[44] J. M. Butterworth, A. R. Davison, M. Rubin and G. P. Salam, Phys. Rev. Lett. **100**, 242001 (2008).

[45] M. Duhrssen, S. Heinemeyer, H. Logan, D. Rainwater, G. Weiglein, D. Zeppenfeld, [hep-ph/0407190].

[46] S. Dawson, C. Jackson, L. H. Orr, L. Reina and D. Wackeroth, NLO QCD corrections," Phys. Rev. D **68** (2003) 034022

[47] T. Plehn, G. P. Salam, M. Spannowsky, Phys. Rev. Lett. **104**, 111801 (2010).

[48] R. K. Ellis, W. J. Stirling and B. R. Webber, "QCD and collider physics," Camb. Monogr. Part. Phys. Nucl. Phys. Cosmol. **8** (1996) 1.

[49] G. Dissertori, I. G. Knowles and M. Schmelling, "Quantum Chromodynamics" *Oxford, UK: Clarendon (2003) 538 p*

[50] H. D. Politzer, Phys. Rev. Lett. **30** (1973) 1346-1349. D. J. Gross, F. Wilczek, Phys. Rev. Lett. **30** (1973) 1343-1346.

[51] W. Giele, E. W. N. Glover, I. Hinchliffe, J. Huston, E. Laenen, E. Pilon, A. Vogt, S. Alekhin *et al.*, [hep-ph/0204316]. M. R. Whalley, D. Bourilkov, R. C. Group,

[52] H. Plothow-Besch, Comput. Phys. Commun. **75** (1993) 396-416.

[53] `http://hepdata.cedar.ac.uk/pdf/pdf3.html`

[54] V. N. Gribov and L. N. Lipatov, Sov. J. Nucl. Phys. **15** (1972) 438 [Yad. Fiz. **15** (1972) 781].
G. Altarelli and G. Parisi, Nucl. Phys. B **126** (1977) 298.
Y. L. Dokshitzer, Sov. Phys. JETP **46** (1977) 641 [Zh. Eksp. Teor. Fiz. **73** (1977) 1216].

[55] M. Bengtsson and P. M. Zerwas, Phys. Lett. B **208** (1988) 306.

[56] R. Odorico, Nucl. Phys. B **172** (1980) 157.
A. Bassetto, M. Ciafaloni and G. Marchesini, Phys. Rept. **100** (1983) 201.
Y. L. Dokshitzer, G. Marchesini and B. R. Webber, Nucl. Phys. B **469** (1996) 93

[57] G. Marchesini and B. R. Webber, Nucl. Phys. B **238** (1984) 1.
G. Marchesini and B. R. Webber, Nucl. Phys. B **310** (1988) 461.
S. Catani, B. R. Webber and G. Marchesini, Nucl. Phys. B **349** (1991) 635.

[58] J. Frenkel and J. C. Taylor, Nucl. Phys. B **116** (1976) 185.

[59] T. Sjostrand, [arXiv:0911.5286 [hep-ph]].

[60] F. Caravaglios, M. L. Mangano, M. Moretti, R. Pittau, Nucl. Phys. **B539** (1999) 215-232.

[61] S. Catani, F. Krauss, R. Kuhn, B. R. Webber, JHEP **0111** (2001) 063.

[62] T. Plehn, [arXiv:0810.2281 [hep-ph]].

[63] S. Frixione, B. R. Webber, JHEP **0206** (2002) 029.

[64] P. Nason, JHEP **0411** (2004) 040. S. Frixione, P. Nason, C. Oleari, JHEP **0711** (2007) 070.

[65] R. D. Field and R. P. Feynman, Phys. Rev. D **15** (1977) 2590.R. D. Field and R. P. Feynman, Nucl. Phys. B **136** (1978) 1.R. P. Feynman, R. D. Field and G. C. Fox, Phys. Rev. D **18** (1978) 3320.

[66] T. Sjostrand and M. Bengtsson, Comput. Phys. Commun. **43** (1987) 367.

[67] R. D. Field and S. Wolfram, Nucl. Phys. B **213** (1983) 65.
S. Wolfram, CALT-68-740;
T. D. Gottschalk, Nucl. Phys. B **239** (1984) 325.
T. D. Gottschalk, Nucl. Phys. B **239** (1984) 349.

[68] F. Becattini, [arXiv:0901.3643 [hep-ph]].

[69] P. Hoyer, P. Osland, H. G. Sander, T. F. Walsh, P. M. Zerwas, Nucl. Phys. **B161** (1979) 349. A. Ali, E. Pietarinen, G. Kramer, J. Willrodt, Phys. Lett. **B93** (1980) 155. A. Ali, J. G. Korner, G. Kramer, J. Willrodt, Nucl. Phys. **B168** (1980) 409.

[70] X. Artru, Phys. Rept. **97** (1983) 147.

[71] T. Sjostrand,
RX-981-LUND;B. Andersson, G. Gustafson and T. Sjostrand, Phys. Scripta **32** (1985) 574.
E. Norrbin and T. Sjostrand, Eur. Phys. J. C **17** (2000) 137

[72] B. R. Webber, Nucl. Phys. B **238** (1984) 492.

[73] UA1 Collab., Albajar, C. *et al.* (1988). *Nucl. Phys.* **B309**, 405. UA2 Collab., Appel, J. A. *et al.* (1985). *Phys. Lett.* **B165**, 441. UA2 Collab., Bagnaia, P. *et al.* (1985). *Phys. Lett.* **B154**, 338. UA2 Collab., Ansari, R. *et al.* (1987). *Phys. Lett.* **B194**, 158.

[74] G. J. Alner *et al.* [UA5 Collaboration], Phys. Rept. **154** (1987) 247. G. J. Alner *et al.* [UA5 Collaboration], Nucl. Phys. B **291** (1987) 445.

[75] V. A. Abramovskii, O. V. Kancheli, V. N. Gribov,

[76] F. E. Paige, S. D. Protopopescu, H. Baer, X. Tata, [hep-ph/0312045]. P. Aurenche, F. W. Bopp, R. Engel, D. Pertermann, J. Ranft, S. Roesler, Comput. Phys. Commun. **83** (1994) 107-123. [hep-ph/9402351].

[77] J. M. Butterworth, J. R. Forshaw and M. H. Seymour, Z. Phys. C **72** (1996) 637 [arXiv:hep-ph/9601371].

[78] S. Jadach, J. H. Kuhn and Z. Was, Comput. Phys. Commun. **64** (1990) 275.

[79] D. Grellscheid and P. Richardson, arXiv:0710.1951 [hep-ph].

[80] M. Gigg and P. Richardson, Eur. Phys. J. C **51** (2007) 989 [arXiv:hep-ph/0703199]. M. A. Gigg and P. Richardson, arXiv:0805.3037 [hep-ph].

[81] D. R. Yennie, S. C. Frautschi, H. Suura, Annals Phys. **13** (1961) 379-452.

[82] P. Golonka and Z. Was, Eur. Phys. J. C **45** (2006) 97

[83] K. Hamilton, P. Richardson, JHEP **0702** (2007) 069.

[84] R. Kleiss and W. J. Stirling, Nucl. Phys. B **385** (1992) 413.

[85] E. P. Venugopal and B. R. Holstein, Phys. Rev. D **57** (1998) 4397 [arXiv:hep-ph/9710382]. Phys. Scripta **T99** (2002) 55 [arXiv:hep-ph/0112150].

[86] D. J. Lange, Nucl. Instrum. Meth. A **462** (2001) 152.

[87] `http://www.ippp.dur.ac.uk/~richardn/particles/`

[88] G. C. Blazey *et al.*, [arXiv:hep-ex/0005012].

[89] G. Sterman and S. Weinberg, Phys. Rev. Lett. **39** (1977) 1436.

[90] S. Catani, Y. L. Dokshitzer, M. Olsson, G. Turnock and B. R. Webber, Phys. Lett. B **269** (1991) 432. S. D. Ellis and D. E. Soper, Phys. Rev. D **48** (1993) 3160 S. Catani, Y. L. Dokshitzer, M. H. Seymour and B. R. Webber, Nucl. Phys. B **406** (1993) 187.

[91] G. P. Salam and G. Soyez, JHEP **0705** (2007) 086

[92] J. M. Butterworth, J. P. Couchman, B. E. Cox and B. M. Waugh, Comput. Phys. Commun. **153** (2003) 85 [arXiv:hep-ph/0210022].

[93] M. Cacciari and G. P. Salam, Phys. Lett. B **641** (2006) 57 M. Cacciari, [arXiv:hep-ph/0607071].

[94] Y. L. Dokshitzer, G. D. Leder, S. Moretti and B. R. Webber, JHEP **9708** (1997) 001 M. Wobisch and T. Wengler, [arXiv:hep-ph/9907280].

[95] M. Cacciari, G. P. Salam and G. Soyez, JHEP **0804** (2008) 063

[96] D. Krohn, J. Thaler and L. T. Wang, JHEP **0906** (2009) 059

[97] M. H. Seymour, Z. Phys. **C62** (1994) 127-138.

[98] M. Cacciari, G. P. Salam and G. Soyez, JHEP **0804** (2008) 005

[99] S. D. Ellis, C. K. Vermilion and J. R. Walsh, Phys. Rev. D **80** (2009) 051501

[100] S. D. Ellis, C. K. Vermilion and J. R. Walsh, [arXiv:0912.0033 [hep-ph]].

[101] D. Krohn, J. Thaler and L. T. Wang, JHEP **1002** (2010) 084

[102] "Large Electron-positron Collider - LEP."
`http://public.web.cern.ch/public/en/research/lep-en.html`.

[103] CERN Editorial Board. *LHC Design Report - Volume I: The LHC Injector Chain*, 2004. CERN-2004-003-V-1.

[104] CERN Editorial Board. *LHC Design Report - Volume II: The LHC Infrastructure and General Services*, 2004. CERN-2004-003-V-2.

[105] CERN Editorial Board. *LHC Design Report - Volume III: The LHC Main Ring*, 2004. CERN-2004-003-V-3.

[106] "CMS Luminosity - Public Results."
`https://twiki.cern.ch/twiki/bin/view/CMSPublic/LumiPublicResults2010`.

[107] `http://press.web.cern.ch/press/PressReleases/Releases2008/PR14.08E.html`

[108] `https://edms.cern.ch/file/973073/1/Report_on_080919_incident_at_LHC__2_.pdf`

[109] "ATLAS: technical proposal for a general-purpose pp experiment at the Large Hadron Collider at CERN," Tech. Rep. CERN/LHCC 94-43, Geneva, 1994.

[110] CMS Collaboration, "The Compact Muon Solenoid Technical Proposal," Tech. Rep. CERN/LHCC 94-38 , Geneva, 1994.

[111] ALICE Collaboration, "ALICE Technical Proposal," Tech. Rep. CERN/L-HCC 2001-021, 2001.

[112] LHCb Collaboration, "LHCb Technical Proposal," Tech. Rep. CERN/L-HCC 98-004, 1998.

[113] LHCf Collaboration, "Technical design report of the LHCf experiment". Tech. Rep. CERN-LHCC-2006-004, 2006.

[114] TOTEM Collaboration, "TOTEM: Technical design report". Tech. Rep. CERN-LHCC-2004-002, 2004.

[115] J. Phys. Conf. Ser. **219** (2010) 032040.
JINST **5** (2010) T03016.

[116] CMS Collaboration, "The Tracker System Project Technical Design Report". No. CERN/LHCC 2000-016, 2000.

[117] CMS Collaboration, "The Electromagnetic Calorimeter Technical Design Report". No. CERN/LHCC 97-033.

[118] CMS Collaboration, "The Hadron Calorimeter Project Technical Design Report". No. CERN/LHCC 97-032.

[119] CMS Collaboration, "The Muon Project Technical Design Report". No. CERN/LHCC 97-032.

[120] CMS Collaboration, "The Trigger and Data Acquisition Project, Volume I: The Level-1 Trigger Technical Design Report". No. CERN/LHCC 2000-038 .

[121] CMS Collaboration, "The Trigger and Data Acquisition Project, Volume II: Data Acquisition and High Level Trigger Technical Design Report". No. CERN/LHCC 2002-026 .

[122] K. Arnold, M. Bahr, G. Bozzi, F. Campanario, C. Englert, T. Figy, N. Greiner, C. Hackstein *et al.*, Comput. Phys. Commun. **180** (2009) 1661-1670.
`http://www-itp.physik.uni-karlsruhe.de/~vbfnloweb`

[123] H. Murayama, I. Watanabe and K. Hagiwara, KEK-91-11;

[124] G. P. Lepage, CLNS-80/447;

[125] J. R. Andersen, T. Binoth, G. Heinrich, J. M. Smillie, JHEP **0802** (2008) 057.

[126] A. Bredenstein, K. Hagiwara, B. Jager, Phys. Rev. **D77** (2008) 073004.

[127] F. Maltoni and T. Stelzer, JHEP **0302** (2003) 027

[128] J. M. Campbell and R. K. Ellis, Phys. Rev. D **60**, 113006 (1999);
J. M. Campbell and R. K. Ellis, arXiv:1007.3492 [hep-ph];
`http://mcfm.fnal.gov/`.

[129] T. Sjostrand, S. Mrenna and P. Z. Skands, JHEP **0605**, 026 (2006).

[130] S. Gieseke, D. Grellscheid, K. Hamilton, A. Papaefstathiou, S. Platzer,
P. Richardson, C. A. Rohr, P. Ruzicka *et al.*, [arXiv:1102.1672 [hep-ph]].
M. Bahr, S. Gieseke, M. A. Gigg, D. Grellscheid, K. Hamilton, O. Latunde-
Dada, S. Platzer, P. Richardson *et al.*, Eur. Phys. J. **C58** (2008) 639-707.

[131] HERWIG 6.5, G. Corcella, I.G. Knowles, G. Marchesini, S. Moretti, K.
Odagiri, P. Richardson, M.H. Seymour and B.R. Webber, JHEP 0101 (2001)
010

[132] S. Gieseke, P. Stephens and B. Webber, JHEP **0312** (2003) 045

[133] S. Catani, S. Dittmaier, Z. Trocsanyi, Phys. Lett. **B500** (2001) 149-160.

[134] P. Richardson, JHEP **0111** (2001) 029

[135] L. Lönnblad, Comput. Phys. Commun. **118** (1999) 213.
M. Bertini, L. Lonnblad and T. Sjostrand, Comput. Phys. Commun. **134**
(2001) 365

[136] S. Alioli, P. Nason, C. Oleari, E. Re, JHEP **1006** (2010) 043.

[137] M. Cacciari, G. P. Salam and G. Soyez, `http://fastjet.fr`

[138] S. D. Ellis and D. E. Soper, Phys. Rev. D **48**, 3160 (1993).

[139] M. Cacciari, G. P. Salam and G. Soyez, JHEP **0804**, 063 (2008).

[140] E. Boos *et al.*, [arXiv:hep-ph/0109068].

[141] J. Alwall *et al.*, Comput. Phys. Commun. **176** (2007) 300

[142] `http://www.w3.org/XML/`
`http://www.xml.org/`

[143] M. Dobbs, J. B. Hansen, Comput. Phys. Commun. **134** (2001) 41-46.

[144] `http://root.cern.ch/`

[145] `http://wwwasd.web.cern.ch/wwwasd/paw/`

[146] G. L. Bayatyan, M. Della Negra, Fo, A. Herv, and A. Petrilli, *CMS comput-
ing: Technical Design Report. Technical Design Report CMS*. CERN, Geneva,
2005. Submitted on 31 May 2005. 49

[147] CMS Collaboration, Offset Energy Correction for Cone Jets, CMS Physics Analysis Summary CMS-PAS-JME-09-003 (2009). 50

[148] CMS Collaboration, Determination of the Relative Jet Energy Scale at CMS from Dijet Balance, CMS Physics Analysis Summary CMS-PAS-JME-08-003 (2009). 51

[149] CMS Collaboration, Calibration of the absolute jet energy scale with Z + jet events at CMS, CMS Physics Analysis Summary CMS-PAS-JME-09-009 (2009). 51

[150] Esen, S. and Landsberg, G., MC Truth L4 EMF-Based Factorized Jet Corrections in CMS, CMS Analysis Note (2009). 51

[151] Cammin, J., Flavor Specific Jet Energy Corrections and Closure Tests for Factorized Jet Energy Corrections, CMS Analysis Note (2009). 51

[152] M. Heinrich et. al., Non-perturbative Corrections to Inclusive Jet Spectra at 10 TeV, . 51, 54, 55, 118

[153] CMS Collaboration, Jet Corrections to Parent Parton Energy, CMS Physics Analysis Summary CMS-PAS-JME-08-002 (2008). 51

[154] CMS Collaboration, Plans for Jet Energy Corrections at CMS, CMS Physics Analysis Summary CMS-PAS-JME-07-002 (2008). 51

[155] D. L. Rainwater, D. Zeppenfeld, Phys. Rev. **D60** (1999) 113004.

[156] N. Kauer, T. Plehn, D. L. Rainwater, D. Zeppenfeld, Phys. Lett. **B503** (2001) 113-120.

[157] CMS NOTE 2007/011

[158] V. Mauch, Diploma Thesis, IEKP IEKP-KA/2008-27
http://www-ekp.physik.uni-karlsruhe.de/pub/web/thesis/iekp-ka2008-27.pdf

[159] D. Green, [hep-ex/0502009].

[160] P. Govoni, C. Mariotti, [arXiv:1001.4357 [hep-ph]].

[161] V. Khachatryan *et al.* [CMS Collaboration], JHEP **1101** (2011) 080.

[162] CMS AN 2010-003

[163] V. Hankele, G. Klamke, D. Zeppenfeld and T. Figy, Phys. Rev. D **74** (2006) 095001

[164] E. Maina, JHEP **1101** (2011) 061

[165] R. N. Cahn and M. S. Chanowitz, Phys. Rev. Lett. **56**, 1327 (1986).

[166] J. M. Butterworth, J. R. Ellis and A. R. Raklev, JHEP **0705**, 033 (2007); T. Han, D. Krohn, L. T. Wang and W. Zhu, JHEP **1003**, 082 (2010); ATLAS Collaboration CERN-OPEN-2008-020.

[167] ATLAS Collaboration, ATL-PHYS-PUB-2009-088, ATL-COM-PHYS-2009-345.

[168] D. E. Soper and M. Spannowsky, JHEP **1008**, 029 (2010)

[169] G. D. Kribs, A. Martin, T. S. Roy and M. Spannowsky, Phys. Rev. D **81**, 111501 (2010); G. D. Kribs, A. Martin, T. S. Roy and M. Spannowsky, [arXiv:1006.1656 [hep-ph]].

[170] C. R. Chen, M. M. Nojiri and W. Sreethawong, [arXiv:1006.1151 [hep-ph]]; A. Falkowski, D. Krohn, J. Shelton, A. Thalapillil and L. T. Wang, [arXiv:1006.1650 [hep-ph]].

[171] G. Brooijmans, ATL-PHYS-CONF-2008-008 and ATL-COM-PHYS-2008-001, Feb. 2008 J. Thaler and L. T. Wang, JHEP **0807**, 092 (2008); D. E. Kaplan, K. Rehermann, M. D. Schwartz and B. Tweedie, Phys. Rev. Lett. **101**, 142001 (2008); L. G. Almeida, S. J. Lee, G. Perez, G. Sterman, I. Sung and J. Virzi, Phys. Rev. D **79**, 074017 (2009); L. G. Almeida, S. J. Lee, G. Perez, I. Sung and J. Virzi, Phys. Rev. D **79**, 074012 (2009);

[172] C. Hackstein and M. Spannowsky, Phys. Rev. D **82** (2010) 113012

[173] M. Aldaya et al., CMS NOTE 2006/106.

[174] M. Spira, Nucl. Instrum. Meth. A **389**, 357 (1997).

[175] S. Alioli, P. Nason, C. Oleari and E. Re, JHEP **0904**, 002 (2009).

[176] M. Cacciari, S. Frixione, M. L. Mangano, P. Nason and G. Ridolfi, JHEP **0809**, 127 (2008)

[177] G. D. Kribs, T. Plehn, M. Spannowsky and T. M. P. Tait, Phys. Rev. D **76**, 075016 (2007).

[178] C. Englert, C. Hackstein and M. Spannowsky, Phys. Rev. D **82** (2010) 114024

[179] M. Duhrssen, S. Heinemeyer, H. Logan, D. Rainwater, G. Weiglein and D. Zeppenfeld, Phys. Rev. D **70** (2004) 113009, R. Lafaye, T. Plehn, M. Rauch, D. Zerwas and M. Duhrssen, JHEP **0908** (2009) 009, S. Bock, R. Lafaye, T. Plehn, M. Rauch, D. Zerwas and P. M. Zerwas, Phys. Lett. B **694** (2010) 44.

[180] A. Birkedal, K. Matchev and M. Perelstein, Phys. Rev. Lett. **94** (2005) 191803, H. J. He *et al.*, Phys. Rev. D **78** (2008) 031701, C. Englert, B. Jager and D. Zeppenfeld, JHEP **0903** (2009) 060.

[181] M. S. Chanowitz and M. K. Gaillard, Nucl. Phys. B **261** (1985) 379,

[182] G. F. Giudice, C. Grojean, A. Pomarol and R. Rattazzi, JHEP **0706** (2007) 045, J. R. Espinosa, C. Grojean and M. Muhlleitner, JHEP **1005** (2010) 065.

[183] M. J. Strassler and K. M. Zurek, Phys. Lett. B **651** (2007) 374.

[184] W. H. Furry, Phys. Rev., **51**, 125 (1937).

[185] C. N. Yang, Phys. Rev. **77** (1950) 242.

[186] W. Buchmuller and D. Wyler, Nucl. Phys. B **268** (1986) 621, K. Hagiwara, R. D. Peccei, D. Zeppenfeld and K. Hikasa, Nucl. Phys. B **282** (1987) 253.

[187] K. Hagiwara, J. Kanzaki, Q. Li and K. Mawatari, Eur. Phys. J. C **56** (2008) 435.

[188] W. Y. Keung, I. Low and J. Shu, Phys. Rev. Lett. **101** (2008) 091802.

[189] V. M. Abazov *et al.* [The DØ Collaboration], Phys. Rev. Lett. **104** (2010) 241802.

[190] J. Bagger *et al.*, Phys. Rev. D **49** (1994) 1246, J. Bagger *et al.*, Phys. Rev. D **52** (1995) 3878, C. Englert, B. Jager, M. Worek and D. Zeppenfeld, Phys. Rev. D **80** (2009) 035027.

[191] T. Han, D. Krohn, L. T. Wang and W. Zhu, JHEP **1003** (2010) 082.

Danksagung